

# UC San Diego

## UC San Diego Electronic Theses and Dissertations

**Title**

Electrochemical implications of defects in carbon nanotubes

**Permalink**

<https://escholarship.org/uc/item/6mc5489t>

**Author**

Hoefer, Mark

**Publication Date**

2012

Peer reviewed|Thesis/dissertation

UNIVERSITY OF CALIFORNIA, SAN DIEGO

**Electrochemical Implications of Defects in Carbon Nanotubes**

A dissertation submitted in partial satisfaction of the  
requirements for the degree  
Doctor of Philosophy

in

Materials Science and Engineering

by

Mark Hoefer

Committee in charge:

Professor Prabhakar Bandaru, Chair  
Professor Sungho Jin  
Professor Clifford Kubiak  
Professor Shirley Meng  
Professor Michael Tauber

2012



Copyright  
Mark Hoefer, 2012  
All rights reserved.

The dissertation of Mark Hoefer is approved, and it is acceptable in quality and form for publication on microfilm and electronically:

---

---

---

---

---

Chair

University of California, San Diego

2012

## DEDICATION

I dedicate this thesis to my family, friends, and colleagues for their support.

## TABLE OF CONTENTS

Signature Page . . . . .	iii
Dedication . . . . .	iv
Table of Contents . . . . .	v
List of Figures . . . . .	viii
List of Tables . . . . .	xviii
Acknowledgements . . . . .	xix
Vita and Publications . . . . .	xx
Abstract of the Dissertation . . . . .	xxi
1 Introduction . . . . .	1
2 Carbon Nanotube Synthesis . . . . .	3
2.1 Background . . . . .	3
2.1.1 Role of Substrate, Supporting, and Catalyst Layers . . . . .	3
2.1.2 Role of Feed Gases on Defect Density and CNT Morphology . . . . .	6
2.1.2.1 Influence of Carbon Source on Defect Density . . . . .	6
2.1.2.2 Changes in CNT Morphological due to Nitrogen . . . . .	6
2.2 Experimental Synthesis of CNTs . . . . .	7
2.2.1 Substrate Preparation . . . . .	7
2.2.2 Thermal Chemical Vapor Deposition (CVD) . . . . .	8
2.3 Results and Conclusions . . . . .	8
3 Carbon Nanotube Defects . . . . .	11
3.1 Point Defects . . . . .	11
3.1.1 Intrinsic Point Defects . . . . .	12
3.1.2 Extrinsic Point Defects . . . . .	14
3.2 One-Dimensional Defects: Intrinsic and Extrinsic . . . . .	16
3.3 CNT Morphological Dependency on Defects . . . . .	17
3.4 Manipulating Band Structure With Extrinsic Defects . . . . .	18
3.4.1 General Description of CNT Electronic Band Structure . . . . .	18
3.4.2 n and p-type CNT Doping . . . . .	21
3.4.3 Introduction to Raman Spectroscopy . . . . .	23
3.5 Experimental Methods for Manipulating Defects . . . . .	25
3.5.1 Reactive Ion Etching . . . . .	26
3.5.2 Hydrogen Exposure and Metal Deposition . . . . .	31

3.6	The Influence of Defects as Determined Through Raman Spectroscopy	33
3.6.1	Structural Differences in As Produced CNTs	35
3.6.2	Generating Defects with Argon Plasma	39
3.6.2.1	Tailoring Defects in Hollow CNTs	39
3.6.2.2	Ineffectiveness of Inducing Defects in Bamboo CNTs	46
3.6.3	Passivating Effects of Hydrogen	46
3.6.3.1	Hydrogen Plasma Irradiation: Simultaneous Defect Formation and Passivation	48
3.6.3.2	Hydrogen Reactivity in Thermal CVD	50
3.6.4	Influence of Chlorine Ion Charge State on Defects	53
3.6.5	n-Doping Through Magnesium Deposition	55
3.7	Summary of Treatment Effects on Raman Spectroscopy	59
4	Electrochemistry	61
4.1	Background	61
4.1.1	Fundamentals of Cyclic Voltammetry	61
4.1.2	Electrochemical Impedance Spectroscopy (EIS): Equivalent Circuit Design	70
4.1.3	Chronopotentiometry	76
4.2	Experimental Setup	78
4.2.1	Cyclic Voltammetry	78
4.2.2	Electrochemical Impedance Spectroscopy	81
4.3	Effects of Defects on Electrochemistry	81
4.3.1	Influence of Intrinsic Defects on Electron Transfer Kinetics	84
4.3.2	Defect Manipulation in Hollow Carbon Nanotubes	88
4.3.2.1	Increasing Reaction Site Density Through Argon Plasma Irradiation	89
4.3.2.2	Influence of Hydrogen Treatments on Charge Transfer Kinetics	94
4.3.2.3	Effects of Chlorine Plasma Reactions at Defects on Reaction Kinetics	101
4.3.2.4	Effects of Magnesium Deposition on Double-Layer Capacitance	104
4.4	Summary of Electrochemical Performance	107
5	CNT Based Capacitor Design and Implementation	109
5.1	Testing Methods for Exploring Pseudocapacitance Longevity	110
5.2	Device Characterization Results	110
5.2.1	Influence of Source Current on Pseudocapacitance	110
5.2.2	Increasing Capacitance with Concentration	113
5.2.3	Performance Increases through Defect Manipulation	114
5.3	Summary and Conclusions of CNT Capacitor Performance	116

6	Conclusions and Potential Future Work . . . . .	118
---	---	-----

## LIST OF FIGURES

Figure 1.1:	Diagram of CNTs, where the rolling direction can lead to armchair or zig-zag edges and determined the semiconducting or metallic behavior of CNTs as illustrated by Meo et al.[1] . . . . .	1
Figure 2.1:	Diagram illustrating the basic experimental design for a thermal CVD system. MFC indicates mass flow controller. . . . .	4
Figure 2.2:	Fe catalyst layer of 5 nm post annealing at 650 °C for 10 minutes. A few CNTs are present due to residual carbon on the furnace tube from previous growth runs. . . . .	4
Figure 2.3:	Diagram originally presented by Kumar and Ando illustrating tip (top) and base (bottom) growth models with Ni and Fe catalysts, respectively. The effect of substrate-catalyst interactions on the growth model can be understood through changes in the contact angle between the two layers.[2] . . . . .	5
Figure 2.4:	Diagram illustrating the mechanism of bamboo type CNTs as presented by Lin et al.[3] . . . . .	7
Figure 2.5:	SEM images of hollow type CNTS taken from (a) top and (b) side orientations to determine CNT growth uniformity and length. (c) is an image of the CNT diameter. (c) is a typical image of bamboo type CNTs. . . . .	9
Figure 2.6:	TEM images of (a) hollow type and (b) bamboo type CNTS to confirm morphology. . . . .	10
Figure 3.1:	Jahn-Teller distortion as a result of a single vacancy illustrated originally by Banhart et al.[4] . . . . .	12
Figure 3.2:	(a) Diagram illustrating a Stone-Wales defect originally illustrated by Banhart et al.[4] (b) Bond rotation energy as a function of bond angle for graphene originally illustrated by Li et al.[5] (c) Bends in CNT sidewall that illustrate not hexagonal pairing. . . .	13
Figure 3.3:	Bond rotation resulting from a carbon adatom dimer (red), which leads to an inverse Stone-Wales defect originally illustrated by Lusk et al.[6] . . . . .	14
Figure 3.4:	Au and Pt clusters on a CNT, and the associated energies of the metals compared to the Fermi energy of the CNT originally illustrated by Choi et al.[7] . . . . .	15
Figure 3.5:	(a) Covalently bound PEG polymer to a SWCNT originally illustrated by Sun et al.[8] (b) Noncovalently bound N-succinimidyl-1-pyrenebutanoate to a SWCNT originally illustrated by Zhao et al.[9]	15
Figure 3.6:	Various edge-plane configurations with the edge atoms in red: (a) armchair (b) Reconstructed armchair (c) zig-zag (d) Reconstructed zig-zag adapted from Banhart et al.[4] . . . . .	16

Figure 3.7:	(a) Hollow Type CNT. (b) Y-Junction from Hollow Type CNTs originally illustrated by Zhang et al. and Bandaru et al.[10, 11] (c) Coiled Hollow Type CNT originally illustrated by Zhang et al.[10] (d) Bamboo Type CNT. (e) Herringbone Type CNT originally illustrated by Rodriguez et al.[12] . . . . .	17
Figure 3.8:	Graphene sheet indicating the CNT chiral vector ( $C_h$ ) originally illustrated by Odom et al.[13] . . . . .	19
Figure 3.9:	(a) Band structure of a graphene sheet.[14] (b) The reduced BZ of a graphene sheet. (d) Overlap of the reduced BZ's of graphene and semiconducting SWCNTs (solid lines). (c) Overlap of the reduced BZ's of graphene and metallic SWCNTs (solid lines). . . . .	19
Figure 3.10:	A sample electronic DOS for a SWCNT where $V$ and $C_n$ indicate the valence and conduction bands, respectively and $E_{n,n}$ indicates the band gap. . . . .	21
Figure 3.11:	Sample illustrations of delocalized bonding in (a) CNTs, (b) boron doped CNTs, (c) nitrogen doped CNTs. . . . .	22
Figure 3.12:	DOS of a (a) boron doped SWCNT and a (b) nitrogen doped SWCNTs adapted from the illustrations presented by Louie. [14] . . .	23
Figure 3.13:	The phonon band structure (left) and the phonon DOS (right) for a SWCNT adapted from Dresselhaus et al.[15] . . . . .	24
Figure 3.14:	Different scattering events in CNTs. $\mathbf{k}$ and $\mathbf{q}$ are the wavevector of the electron and phonon vector, respectively. Incident resonance occurs when the excitation laser energy matches a real electronic transition, while scattered resonance occurs when the excitation laser energy is equal to the electronic transition energy plus the phonon energy. Furthermore, the dashed lines indicate elastic scattering events originating from defects. Illustrated originally published by Dresselhaus et al.[15] . . . . .	25
Figure 3.15:	(a) Atom displacements for the G and D/D' bands. (b) Changes in the G-peak position and G/D peak intensities with increasing bond disorder. nc-graphite is nanocrystalline graphite, a-C is $sp^2$ amorphous carbon, ta-C is $sp^3$ amorphous carbon originally illustrated by Robertson.[16] . . . . .	26
Figure 3.16:	Diagram that outlines the important features of the Trion etcher. The lower plate has a CNT covered substrate. . . . .	27
Figure 3.17:	Concentration profiles of $H^+$ , $H_2^+$ , and $H_3^+$ in plasma generated from pure $H_2$ . Originally plotted by Nunomura et al.[17] . . . . .	29
Figure 3.18:	Concentration profiles of $Cl_2$ , $Cl$ , $Cl_2^+$ , $Cl^+$ , $Cl^{2+}$ , $Cl^-$ , and $e^-$ in plasma generated from pure $Cl_{2,0}$ stock feed with respect to (a) pressure as illustrated by Ono et al. and (b) power as illustrated by Meeks et al.[18, 19] . . . . .	30
Figure 3.19:	Vapor pressure profiles of Be(●) and Mg(■) as a function of temperature. . . . .	33



Figure 3.20:	(a) Full Raman spectrum of as produced CNTs. (a) First order fitted Raman spectra of as produced CNTs. The peak assignments reflect those found in the literature. . . . .	34
Figure 3.21:	Diagram illustrating the impact of edge-plane orientation on the D peak and the total defect density. Labels 1 and 2 correspond to the armchair and zig-zag configurations respectively, and label 3 corresponds to the basal plane of graphite. The figure was adapted from Cancando et al.[20] . . . . .	35
Figure 3.22:	Raman spectra of first order peaks of AP CNTs growth with (a) ethylene and (b) acetylene carbon sources. . . . .	36
Figure 3.23:	G (red), D (black), D' (green) peak positions for HCNTs grown with (a) acetylene and (b) ethylene carbon sources. Peak widths with respect to (c) acetylene and (d) ethylene carbon sources. Comparison of edge plane defects to all defects for CNTs growth with (e) acetylene and (f) ethylene carbon sources. . . . .	37
Figure 3.24:	(a) Fitted Raman spectra of a typical BCNT. The D' peak could not be resolved. (b) G (red) and D (black) peak positions and (c) peak widths for BCNTs growth with an acetylene and ammonia mixture. . . . .	38
Figure 3.25:	(a) G (red), D (black), and D' (green) peak positions (x) and (b) peak full width half maximum values $\omega$ for several RIE (50-150 W) and ICP (0-50 W) powers and 60 s exposure time. . . . .	40
Figure 3.26:	G (red), D (black), and D' (green) (a) peak positions (x), (b) peak full width half maximum values ( $\omega$ ), and (c) relative edge plane density for all RIE and ICP powers, exposure times, and pressures used as a function of defect density. . . . .	41
Figure 3.27:	(a) Typical Raman spectra for CNTs exposed to Ar plasma with differing RIE powers. The RIE power was incrementally increased from 50 to 150 W in 50W intervals. The exposure time for all samples was 60 s, with a pressure of 60 mTorr. (b) Peak position shifts, (c) change in peak shifts for the G (red), D (black), and D' (green) peaks, and (d) intensity ratios for the different RIE powers. The reference value for the various parameters was calculated by taking the average and standard deviation of all AP samples. . . . .	43
Figure 3.28:	Illustrative diagram describing the random formation of edge-plane-like defect in CNTs as a result of changing the RIE power, where the red atoms in (a) depict initial defect locations and the blue atoms in (b) illustrate new defect locations as a result of carbon sputtering. . . . .	44

Figure 3.29:	(a) Typical Raman spectra for CNTs exposed to Ar plasma with differing ICP powers. For all treated samples, the ICP power was incrementally increased from 0 to 150 W in 50W intervals, with a concurrent use of 50 W of RIE power. The exposure time for all samples was 60 s, with a pressure of 60 mTorr. G (red), D(black), and D' (green)(b) peak position shift, (c) change in peak width, and (d) intensity ratios for CNTs exposed to Ar plasma with differing ICP powers. The reference value for the various parameters was calculated by taking the average and standard deviation of all AP samples. . . . .	45
Figure 3.30:	Illustrative diagram describing non-random edge-plane-like defect formation in CNTs as a result of changing the ICP power, where the red atoms in (a) depict the initial defect locations and the blue atoms in (b) illustrate new defect locations. . . . .	46
Figure 3.31:	(a) Typical spectra of BCNTs exposed to Ar plasma as a function of exposure time. The pressure and RIE power used were 30 mTorr and 100 W, respectively. Changes in the D (black) and G (red) peak (b) positions and (c) widths with respect to the defect density. (d) Comparison of the changes in $\frac{I_D}{I_G}$ with increases in Ar exposure time between HCNTs and BCNTs. . . . .	47
Figure 3.32:	(b) Typical Raman spectra for CNTs exposed to H <sub>2</sub> plasma with differing RIE powers. The RIE power was incrementally increased from 0 to 150 W in 50W intervals. The exposure time for all samples was 60 s, with a pressure of 10 mTorr. G (red), D (black), and D' (green) (b) peak position shift, (c) change in peak width, and (d) intensity ratios for CNTs exposed to H <sub>2</sub> plasma. The reference value for the various parameters was calculated by taking the average and standard deviation of all AP samples. . . . .	49
Figure 3.33:	(a) Typical Raman spectra for CNTs exposed to H <sub>2</sub> plasma with differing RIE powers. The ICP power was incrementally increased from 0 to 100 W in 50W intervals with a RIE power of 50W. The exposure time for all samples was 60 s, with a pressure of 10 mTorr. G (red), D (black), and D' (green) (b) peak position shift, (c) change in peak width, and (d) intensity ratios for CNTs exposed to H <sub>2</sub> plasma. The reference value for the various parameters was calculated by taking the average and standard deviation of all AP samples. . . .	51
Figure 3.34:	G (red), D (black), and D' (green) (b) peak position shift, (c) change in peak width, and (d) intensity ratios for CNTs exposed to H <sub>2</sub> plasma. The RIE power was incrementally increased from 0 to 150 W in 50W intervals. The exposure time for all samples was 60 s, with a pressure of 10 mTorr. The reference value for the various parameters was calculated by taking the average and standard deviation of all AP samples. . . . .	52

Figure 3.35:	EDS spectra of CNTs exposed to $\text{Cl}_2$ for 180 s at 240 mTorr and a RIE power of 50 W. . . . .	53
Figure 3.36:	(a) Typical Raman spectra for a total power of 200 W at a pressure of 10 mTorr. (b) Peak position shift, (c) change in peak width for the G (red), D (black), and D' (green) peaks, and (d) intensity ratios for CNTs exposed to $\text{Cl}^+$ ions in the plasma. The exposure times were 60, 120, and 240 s. . . . .	54
Figure 3.37:	(a) Typical Raman spectra for a total power of 50 W at a pressure of 240 mTorr. (b) Peak position shift, (c) change in peak width for the G (red), D (black), and D' (green) peaks, and (d) intensity ratios for CNTs exposed to $\text{Cl}^-$ ions in the plasma. The exposure times were 60, 120, and 240 s. . . . .	56
Figure 3.38:	SEM images of a wafer (a) prior and (b) post Mg deposition. Image (c) is a higher magnification image illustrating the presence of deposited Mg metal on the CNTs and Si wafer. (d) illustrates the successful removal of excess Mg from the Si wafer. . . . .	57
Figure 3.39:	(a) Typical Raman spectra of CNTs treated with Mg, Mg + HCl + CPD, and HCl + CPD. (b) Peak position shift, (c) change in peak width for the G (red), D (black), and D' (green) peaks, and (d) intensity ratios for CNTs exposed to Mg vapor at different temperatures and total pressures. The error bars indicated the standard deviation between different trials. . . . .	58
Figure 4.1:	(a) CV triangular waveform. (b) Current response to triangular waveform for a one $e^-$ transfer. $i_b$ and $i_{lim}$ are the baseline and limiting currents, respectively. . . . .	62
Figure 4.2:	CV illustrating irreversible electron transfer and adsorption of the redox couple during the anodic sweep, adapted from Kissinger et al.[21, 22] . . . . .	65
Figure 4.3:	(a) $\Psi$ as a function of E. Dashed lines indicate reversibility and the Roman Numerals represent different scan rates, where I, II, III, and IV correspond to $\Lambda = 10, 1, 0.1$ , and $0.01$ , respectively. (b) $\Xi$ as a function of $\log(\Lambda)$ for different values of $\alpha$ . Dashed lines indicate total irreversibility. Illustrations originally published by Matsuda et al. and Bard et al.[22, 23] . . . . .	67
Figure 4.4:	Illustration of the double-layer, where d indicates the distance from the electrode surface. $\Phi$ indicates the potential at the surface(s), inner Helmholtz plane (IHP), and outer Helmholtz plane (OHP). Past the OHP, the diffuse layer begins, which extends into the bulk solution. The smaller (green) circles are solvent molecules. . . . .	67
Figure 4.5:	Illustrative CV curve demonstrating how the experimental CV curves were used to measure the difference components of the total current. . . . .	69

Figure 4.6:	(a) The waveform of the applied dc and ac signals. (b) The resulting ac current response to the ac applied potential, indicating the phase shift between the two. (c) Example of frequency response for $ Z $ and $\phi$ of an electrochemical system. . . . .	71
Figure 4.7:	The equivalent circuit of the electrochemical system under investigation. $R_s$ is the solution resistance, $R_{ct}$ is the charge transfer resistance, $C_{dl}$ is the double-layer capacitance, $Z_W$ is the Warburg impedance. . . . .	72
Figure 4.8:	(a) The equivalent circuit as $\omega \rightarrow \infty$ . (b) Nyquist plot of the equivalent circuit shown in (a). . . . .	73
Figure 4.9:	Nyquist plot of when $\omega \rightarrow 0$ (diffusion limited regime). The intercept can be used to determine $R_s$ , $R_{ct}$ , $\sigma$ and $C_{dl}$ . . . . .	74
Figure 4.10:	Nyquist plot indicating the knee frequency, where the kinetic regime transitions to the diffusion regime. . . . .	75
Figure 4.11:	Nyquist plot where $Z_W$ is replaced by $C_p$ , but remains in series with $R_{ct}$ to demonstrate a transition to ideal capacitor behavior. . . . .	75
Figure 4.12:	(a) Square waveform used for cyclic constant current chronopotentiometry. (b) Resulting voltage response to current waveform for an ideally polarizable capacitor in series with a resistor. ESR is the equivalent series resistance and is calculated experimentally by $R_{ESR} = \frac{V_{ESR}}{ i_1 - i_2 }$ . In electrolytic capacitors, $R_{ESR}$ is a combination of the current collector resistance, $R_s$ , $R_{ct}$ , and contact resistance at the terminal leads. The value of $R_{ESR}$ is critical for high power applications since large resistances can lead to heating and expansion of the electrolyte, causing the capacitor to fail. . . . .	76
Figure 4.13:	(a) Measured potential as a function of time for reversible and irreversible systems with reference to $E^{0'}$ . (b) Measured potential as a function of time, concentration, and source current for reversible systems. . . . .	77
Figure 4.14:	Experimental CV setup used for working electrode (WE) characterization. The counter electrode used was a Pt wire and reference electrode was a saturated calomel electrode (SCE). . . . .	79
Figure 4.15:	Experimental two electrode setup used for device characterization. The reference (Ref) and counter electrode (CE) leads were electrically connected and attached to one capacitor electrode and the working electrode (WE) leads were connected to the second capacitor electrode. . . . .	80
Figure 4.16:	CV plots as a function of concentration and scan rate for (a), (c) potassium ferricyanide and (b), (d) ruthenium hexaamine trichloride in 1.0 M $KCl_{aq}$ , respectively. Pt was the working electrode. . . . .	82
Figure 4.17:	Plots of $i_p$ as functions of scan rate and redox couple concentration to determine reversibility. (a) and (b) are for potassium ferricyanide. (c) and (d) are for ruthenium hexaamine trichloride. . . . .	83

Figure 4.18: The redox couple was 6 mM ruthenium hexaamine trichloride in 1 M KCl, where a scan rate of 100 mV/s was used. . . . .	84
Figure 4.19: CV plots for AP CNTs with respect to scan rate for (a) potassium ferricyanide and (b) ruthenium hexaamine trichloride. CV plots with respect to changes in the concentration of (c) potassium ferricyanide ( $K_3Fe(CN)_6$ ) and (d) ruthenium hexaamine trichloride ( $Ru(NH_3)_6Cl_3$ ). The supporting electrolyte was 1.0 M KCl for all solutions. . . . .	85
Figure 4.20: Peak capacitances as functions of (a) the inverse of the square-root of the scan rate and (b) redox couple concentration. $\Delta E_p$ as a function of (c) scan rate to determine reversibility. . . . .	86
Figure 4.21: CV plots of (a) BCNTs and (b) HCNTs with respect to different argon irradiation times, illustrating the changes in the current normalized to the total surface area of the CNTs. The potassium ferricyanide concentration was 3mM in 1 M KCl and the scan rate was 20 mV/s. Changes in (c) double-layer and (d) peak capacitances for BCNTs and HCNTs as a function of RIE irradiation time. The RIE experimental conditions were 30 mTorr, 100 W, with a gas flow rate of 30 SCCM. . . . .	87
Figure 4.22: The effects of Ar plasma irradiation time on electron transfer kinetics are evident for HCNTs and comparatively minute for BCNTs when 3mM of potassium ferricyanide is used with a scan rate of 20 mV/s. . . . .	88
Figure 4.23: CV scans as a function of scan rate for a HCNT working electrode treated with Ar plasma at 100W RIE. N denotes the nominal area of $0.25\text{ cm}^2$ . . . . .	89
Figure 4.24: Plots of $C_p$ normalized to the nominal area ( $0.25\text{ cm}^2$ ) as functions of $\frac{1}{\sqrt{v}}$ for Ar plasma exposure using (a) RIE only and (b) 50W RIE with ICP. (c) and (d) illustrate the shifts in the peak positions with RIE and ICP treatments, respectively. The redox couple used is potassium ferricyanide. The error bars in the figure represent the standard deviation between different trials. . . . .	90
Figure 4.25: Contact angle measurements with Ar plasma exposed CNTs. The exposure time for (a) was 30 s, and for (b) was 180s. The difference in the wetting angle in (a) is believed to result from non-uniform Ar plasma exposure of the CNT wafer. . . . .	91
Figure 4.26: Typical Nyquist (a) and (b) Bode plots for Ar plasma treated CNTs with an $5\text{ mV}_{RMS}$ AC signal and a DC offset of 0 V with respect to the open circuit voltage. . . . .	92
Figure 4.27: Peak and double-layer capacitance normalized to the nominal wafer ( $A_N = 0.25\text{ cm}^2$ ) area for (a) RIE Ar treatments and (b) ICP Ar treatments. The scan rate and potassium ferricyanide concentration were 50 mV/s and 10 mM, respectively. . . . .	93

Figure 4.28: Determination of the non-edge-plane contribution to the average $k^\circ$ for ICP and RIE Ar plasma treatments. . . . .	95
Figure 4.29: CV scans as a function of (a) scan rate and (b) $K_3Fe(CN)_6$ concentration for a HCNT working electrode treated with $H_2$ plasma at 100W RIE. N denotes the nominal area of $0.25\text{ cm}^2$ . . . . .	95
Figure 4.30: Plots of $C_p$ normalized to the nominal area ( $0.25\text{ cm}^2$ ) as functions of $\frac{1}{\sqrt{v}}$ for $H_2$ plasma exposure using (a) RIE only and (b) 50W RIE with ICP. (c) and (d) illustrate the shifts in the peak positions with RIE and ICP treatments, respectively. The redox couple used is 10 mM $K_3Fe(CN)_6$ in 1.0 M KCl. (e) and (f) illustrate the dependence of $C_p$ and $\Delta E_p$ on concentration for RIE treated CNTs. The error bars in the figure represent the standard deviation between different trials. . . . .	96
Figure 4.31: Peak and double-layer capacitance normalized to the nominal wafer (N) area ( $0.25\text{ cm}^2$ ) for (a) RIE $H_2$ treatments and (b) ICP $H_2$ treatments. The scan rate and potassium ferricyanide concentration were 50 mV/s and 10 mM, respectively. . . . .	97
Figure 4.32: Typical Nyquist (a) and (b) Bode plots for $H_2$ plasma treated CNTs with an 5 mV <sub>RMS</sub> AC signal and a DC offset of 0 V with respect to the open circuit voltage. . . . .	98
Figure 4.33: Determination of the non-edge-plane contribution to the average $k^\circ$ for ICP and RIE $H_2$ plasma treatments. . . . .	99
Figure 4.34: (a) CV scans as a function of scan rate for a HCNT working electrode treated with $H_2$ gas in the CVD reactor at 300 °C. (b) Plots of $C_p$ normalized to the nominal area ( $0.25\text{ cm}^2$ ) as a function of $\frac{1}{\sqrt{v}}$ . (c) illustrates the shifts in the peak positions with scan rate. (d) illustrate the dependence of $C_p$ and $C_{dl}$ on defect density at 50 mV/s. The error bars in the figure represent the standard deviation between different trials. . . . .	100
Figure 4.35: (a) CV scans as a function of scan rate for a HCNT working electrode treated with $Cl_2$ plasma with a RIE power of 50 W at 240 mT for times of 60, 120, and 240 s. (b) Plots of $C_p$ normalized to the nominal area ( $0.25\text{ cm}^2$ ) as a function of $\frac{1}{\sqrt{v}}$ . (c) illustrates the shifts in the peak positions with scan rate. (d) illustrate the dependence of $C_p$ and $C_{dl}$ on defect density at 50 mV/s. The error bars in the figure represent the standard deviation between different trials. . . . .	102

Figure 4.36:	(a) CV scans as a function of scan rate for a HCNT working electrode treated with $\text{Cl}_2$ plasma with a RIE power of 200 W and an ICP power of 100 W at 10 mT for times of 60, 120, and 240 s. (b) Plots of $C_p$ normalized to the nominal area ( $0.25 \text{ cm}^2$ ) as a function of $\frac{1}{\sqrt{v}}$ . (c) illustrates the shifts in the peak positions with scan rate. (d) illustrate the dependence of $C_p$ and $C_{dl}$ on edge-plane-like defect density at 50 mV/s. The error bars in the figure represent the standard deviation between different trials. . . . .	103
Figure 4.37:	Determination of the non-edge-plane contribution to the average $k^\circ$ for ICP and RIE $\text{Cl}_2$ plasma treatments. . . . .	104
Figure 4.38:	(a) CV scans as a function of scan rate for a HCNT working electrode treated with Mg evaporated at $415^\circ\text{C}$ and a total pressure of 10 Torr. (b) Plots of $C_p$ normalized to the nominal area ( $0.25 \text{ cm}^2$ ) as a function of $\frac{1}{\sqrt{v}}$ . (c) illustrates the shifts in the peak positions with scan rate. (d) illustrate the dependence of $C_p$ and $C_{dl}$ on defect density at 50 mV/s. The error bars in the figure represent the standard deviation between different runs on the same substrate. . . . .	105
Figure 4.39:	(a) Bode and (b) Nyquist plots of a typical Mg exposed CNTs in 10 mM potassium ferricyanide with DC bias of 0 V versus the open circuit potential and a AC voltage of $5 \text{ mV}_{RMS}$ . The circuit model for these fits was similar to that of Figure 4.7, yet the Warburg element was replaced with a bounded Warburg element. . . . .	106
Figure 4.40:	Determination of the non-edge-plane contribution to the average $k^\circ$ for Mg treatment. . . . .	107
Figure 5.1:	Schematic of CNT capacitor based device. All materials used were non-metallic to prevent the capacitor from short circuiting, and silicon O-rings were used at all joints to prevent the leakage of electrolyte onto the back contact pad and out of the cell. ACRYL denotes acrylic. . . . .	109
Figure 5.2:	(a) CV plot for the AP-AP CNT capacitor device. (b) Galvanostatic plots for the same CNT device as a function of different source currents after 1000 cycles. $\tau$ is the time associated with faradaic reactions described by Equation (4.35). . . . .	112
Figure 5.3:	CNT capacitor performance with respect to the number of cycles for different source currents. $[K_3Fe(CN)_6] = 10 \text{ mM}$ in $1.0 \text{ M KCl}$ . . . . .	112
Figure 5.4:	(a) CV plots for a CNT capacitor device comprised of two as produced (AP) CNT electrodes at different $K_3Fe(CN)_6$ concentrations in $1.0 \text{ M KCl}$ . (b) Galvanostatic plots for the same CNT capacitor device as a function of $K_3Fe(CN)_6$ concentration after 1000 cycles, when a current of 1 mA is sourced. . . . .	114

Figure 5.5:	(a) CV and (b) galvanostatic plots for a AP-AP CNT capacitor device at 100 mM $K_3Fe(CN)_6$ concentration after 1000 cycles with a source current of 10 mA. (a) Plot of peak separation as a function of redox couple concentration, illustrating the effects of high redox couple concentration. . . . .	115
Figure 5.6:	(a) Galvanostatic plot after 2000 cycles illustrating the effects of Ar plasma exposure for $[K_3Fe(CN)_6] = 100$ mM and a source current of 10 mA. (b) Nyquist plot of the Ar-Ar CNT device for $[K_3Fe(CN)_6] = 100$ mM and a $DC_{offset}$ of 0.6 V. . . . .	116



## LIST OF TABLES

Table 3.1:	Ionization Processes in Argon Plasmas. [24, 25] . . . . .	28
Table 3.2:	Trion Process Variables: Ar Plasma . . . . .	28
Table 3.3:	Ionization Processes in Hydrogen Plasmas. [17, 26] . . . . .	29
Table 3.4:	Trion Process Variables: H <sub>2</sub> Plasma . . . . .	29
Table 3.5:	Ion Reaction Processes in Chlorine Plasmas. [18, 19] . . . . .	30
Table 3.6:	Trion Process Variables: Cl <sub>2</sub> Plasma . . . . .	31
Table 3.7:	Hydrogen CVD Variables . . . . .	32
Table 3.8:	Magnesium Deposition Variables . . . . .	33
Table 4.1:	CV Concentrations . . . . .	80
Table 4.2:	Redox Couple Performance . . . . .	82
Table 4.3:	EIS and $V_d$ Analysis: Ar Plasma . . . . .	93
Table 4.4:	EIS and $V_d$ Analysis: H <sub>2</sub> Plasma . . . . .	98
Table 5.1:	Capacitor Cycling Characterization . . . . .	111

## ACKNOWLEDGEMENTS

I am very thankful to have been able to work with numerous people, who have provided support during the course of this work. I would like to acknowledge my advisor, Professor Prabhakar Bandaru for his the support and valuable discussions during the course of my graduate research. I wish to also acknowledge the other committee members for their time and input: Professor Sungho Jin, Professor Clifford Kubiak, Professor Shirley Meng and Professor Michael Tauber. Professor Frank Talke was also very generous in providing access to his lab for Raman spectrometry.

In addition, I would also like to acknowledge my fellow graduate student colleagues at UCSD. Ralf Brunner (Talke Lab) and Christian Deck (Vecchio Lab) provided guidance and help with carbon nanotube synthesis and Raman measurements at the start of this work. Chinung Ni of the Bandaru group was also an invaluable source of help for the chemical vapor deposition system design and initial nanotube growth characterization. Aaron Sathrum (Kubiak Lab) provided valuable insight on capacitor device design that was integral to the final portion of my research. Hesham Khalifa, Paothep Pichanusakorn, and Max Aubain have been an important source of support and inspiration throughout my entire graduate career.

None of this research would have been possible without the invaluable support and guidance of my parents, Carolyn and Walter. I would also like to thank Melanie Zeisig for her understanding and patience during the final portion of this work.

Chapters 2, 3, and 4, in part, are a reprint of the material as it appears in “Defect engineering of the electrochemical characteristics of carbon nanotube varieties”, in *Journal of Applied Physics*, v.108, n.3, pp.034308, 2010, Hoefer, M. A.; Bandaru, P. R. The dissertation author was the primary investigator and author of this paper.

## VITA

2006	B. S. in Chemical Engineering University of California, San Diego
2007	M. S. in Materials Science and Engineering University of California, San Diego
2011	Ph. D. Materials Science and Engineering University of California, San Diego

## PUBLICATIONS

Jeffrey, N. A., Saito, H., Hoefer, M., Bandaru, P. R., “Tailoring the Electrochemical Behavior of Multiwalled Carbon Nanotubes Through Argon and Hydrogen Ion Irradiation”, *Electrochemical and Solid-State Letters*, v.11, n.4, K35-K39, 2008.

Hoefer, M. A., Nichols, J., Bandaru, P. R., “The Role of Defects in Carbon Nanostructures Probed through Ion Implantation and Electrochemistry.”, *Materials Research Society Conference Proceedings*, Symposium JJ, Fall Session, 2008.

Hoefer, M., Bandaru, P. R., “Determination and enhancement of the capacitance contributions in carbon nanotube based electrode systems”, *Applied Physics Letters*, v.95, n.18, 183108, 2009.

Hoefer, M., Bandaru, P. “Defect Engineering of the Electrochemical Characteristics of Carbon Nanotubes for Catalytic Applications.”, *Materials Research Society Conference Proceedings*, Symposium Y, Spring Session, 2009.

Hoefer, M. A., Bandaru, P. R., “Defect engineering of the electrochemical characteristics of carbon nanotube varieties”, *Journal of Applied Physics*, v.108, n.3, 034308, 2010.

## ABSTRACT OF THE DISSERTATION

### **Electrochemical Implications of Defects in Carbon Nanotubes**

by

Mark Hoefer

Doctor of Philosophy in Materials Science and Engineering

University of California, San Diego, 2012

Professor Prabhakar Bandaru, Chair

The electrochemical behavior of carbon nanotubes (CNTs) containing both intrinsic and extrinsically introduced defects has been investigated through the study of bamboo and hollow multi-walled CNT morphologies. The controlled addition of argon, hydrogen, and chlorine ions in addition to atomic hydrogen and magnesium vapor was used for varying the charge and type of extrinsic defects. To quantify changes in the CNTs upon treatment, Raman spectroscopy and electrochemical techniques were employed.

It was indicated from Raman spectroscopy, cyclic voltammetry, electrochemical impedance spectroscopy, and chronopotentiometric experiments that the electrochemical response of hollow type CNTs could be tailored more significantly compared to bamboo type CNTs, which have innately high reactive site densities and are less amenable to

modification. Total defect density and edge-plane-like defect concentrations monitored through Raman spectroscopy were used to correlate changes in the electrochemical response of the CNT electrodes as a function of treatment.

The implementation of CNT electrodes in a prototypical electrolytic capacitor device was then explored and characterized. Dependencies on source current and redox couple concentration were evaluated, as well as changes in the total capacitance as a function of treatment. Cyclability studies were also performed as a function of source current magnitude to evaluate the longevity of the faradaic currents which typically decrease over time in other similar capacitors.

This thesis then concludes with an overall summary of the themes and findings of the research presented in this work.

# 1 Introduction

Carbon nanotubes (CNTs) have been postulated for a variety of uses in recent years due to their theoretically impressive mechanical, electrical, and optical properties. For example, the tensile strength of CNTs has been measure to be 63 GPa,  $\sim 100$  times greater than steel, and the theoretical maximum current density is  $\sim 5 \times 10^9 \frac{A}{cm^2}$ , which is more than 1,000 times larger than that of copper.[27, 28] Numerous studies have been conducted that manipulate different CNT synthesis parameters to gain a comprehensive understanding of how these parameters affect CNT growth mechanism, CNT geometry, chirality, semiconducting or metallic character, and length. However, regardless of the synthesis method, CNT uniformity has been extremely difficult to control. Therefore, much effort has been focused on methods to purify CNT mixtures. Ultimately, the focus of CNT research is to characterize the variety of CNTs morphologies and conducting types as well as the CNT synthesis methods to evaluate their potential (commercial) use.

To best implement CNTs in commercial devices and to understand the current limitations of transitioning CNTs into commercially viable materials, the CNT growth mechanism and synthesis process must be explored. This thesis will begin with an introduction to the thermal chemical vapor deposition (CVD) synthesis technique and provide an overview of the effects of several growth parameters. Generally, CNTs can be regarded as rolled sheets of graphene, as shown in Figure 1.1. Changes in the growth parameters can lead to different CNT morphologies, affect the length and relative intrinsic defect density, as well as determine the structural and electrical properties of the CNTs.

Once a general understanding of the growth mechanism and synthesis process has been established, potential applications can be explored. One such application is explained in this work, which involves around using defective CNTs as electrodes in supercapacitors. In this instance, the inherent imperfections generated during CVD growth and those subsequently added to the CNTs through various processes, can significantly improve the capacitive performance of CNT electrodes. To characterize the CNTs and understand structure-property relationships, the following techniques are used: Raman Spectroscopy, scanning and transmission electron microscopy (SEM/TEM), electrochemical impedance spectroscopy (EIS), cyclic voltammetry (CV), and galvanostatic

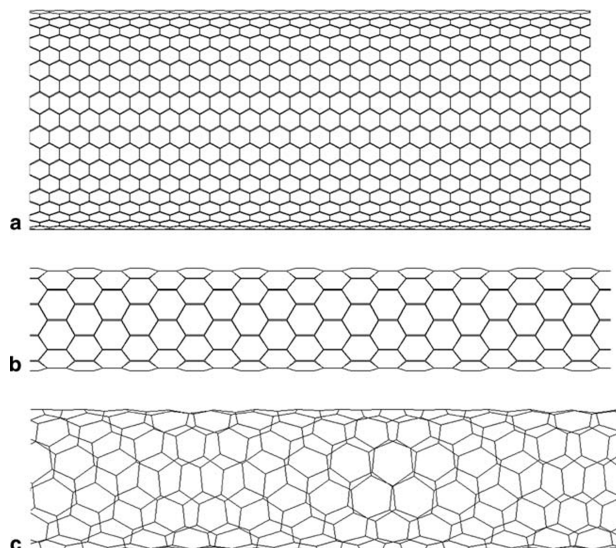


**Figure 1.1:** Diagram of CNTs, where the rolling direction can lead to armchair or zigzag edges and determined the semiconducting or metallic behavior of CNTs as illustrated by Meo et al.[1]

charging/discharging (GALV).

Several different methods were used to generate defects in CNTs and induce structural and electronic change. To best understand how different treatments change the CNTs, Raman spectroscopy was used as it provides much information on both the electronic and structural states. A review of defects and the influence that they have on the electronic band structure will be given. Raman spectroscopy does not fully characterize how the CNTs will perform electrochemically and cannot be used quantitatively. To quantify changes in the CNTs and correlate those changes in the Raman spectra, the CV, EIS, GALV electrochemical techniques were employed. Each of these techniques will be described in detail and provide complimentary and unique results that quantify charge transfer and diffusion related processes that are present in electrochemistry.

Finally, a description of the performance of CNTs as capacitors will be given. By creating CNT based devices, the potential of CNTs to act as electrodes can be evaluated. Methods to improve upon the present performance will also be described. While characterization prior to implementing CNT electrodes in devices is useful, a true test of performance comes through the use of the CNTs on the device level. Many unforeseen problems typically arise when issues such as form factor, heat dissipation, chemical

compatibility, and reproducibility are explored for real world applications. A final summary of the findings will then be presented along with some concluding remarks about potential future research directions.



## 2 Carbon Nanotube Synthesis

Carbon nanotubes have been grown through a variety of different methods, including thermal chemical vapor deposition (CVD), plasma enhanced CVD, arc discharge, and laser ablation. Each of these methods has its own advantages and limitations, but all allow for the growth of CNTs with a large variety of mechanical, optical, and electronic properties. For instance, when using thermal CVD, the feed gas composition determines the useful pressure, temperature, and flow of gases to effectively grow CNTs.[2, 29–36] Changes in these and many other parameters can lead to a wide variety of CNT growth rates, CNT lengths, diameters, chirality, and quality. As a result, a plethora of research has been focused in an effort to define key process parameters that can lead to reproducible growth of high quality, defect free CNTs.

In this work, much effort was focused on the growth of CNTs, via thermal CVD, on conducting substrates for the purpose of using them as electrochemical electrodes. It was found that several factors are important to understanding CNT growth. In the following sections, the roles of feed gas composition and substrate will be explained with reference to CNT morphology and overall growth quality. A general description of CNT formation theory will also be given.

### 2.1 Background

A CNT can be simply regarded as a rolled sheet of graphene that formed into a tube as illustrated in Chapter 1, Figure 1.1. The underlying formation processes depend on a complex relationship between catalyst and reactant gas properties. In a thermal CVD setup, shown schemtically in Figure 2.1, feed gases are introduced into the CVD reactor, after which they are heated to promote decomposition on the catalyst surface. Upon decomposition, carbon atoms adsorb onto the surface of the catalyst particles, which then begin to diffuse along the surface of and subsequently dissolve into the catalyst. Such processes increase the concentration of carbon in the catalyst material until supersaturation is attained and carbon begins to precipitate out of the catalyst particle and CNTs start to grow. If the CNT density is large enough, the CNTs are naturally supported through van der Waals forces that cause the CNTs to vertically align instead of forming a tangled network, creating an array of CNTs.

Using this reaction scheme it is seen that there are several factors that are generally applicable to CNTs grown via thermal CVD: control over catalyst density and

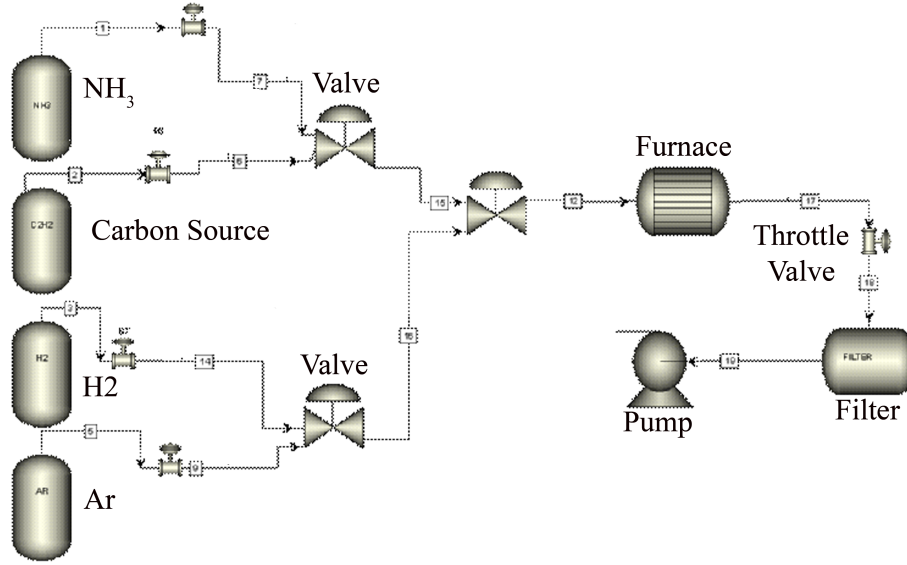


**Figure 2.1:** Diagram illustrating the basic experimental design for a thermal CVD system. MFC indicates mass flow controller.

activity, carbon source decomposition rate, and carbon solubility in the catalyst layer. If these parameters can be effectively controlled, CNT growth can more reproducible.

### 2.1.1 Role of Substrate, Supporting, and Catalyst Layers

Careful control of the catalyst properties is most likely the single most important factor in thermal CVD growth of CNTs. In this work, a thin layers of catalyst metals, such as Ni, Fe, and Ag, were deposited on Si wafers. Upon heating these substrates during the growth process, the thin metal film breaks down resulting from surface energy minimization, to form catalyst islands as shown in Figure 2.2.

The growth temperature, annealing rate, thickness of the catalyst film, composition of the underlying layers, and the surface energy mismatch between the underlying layers and the catalyst metal have a large impact on the size and composition of the catalyst islands. [37–39] For instance, by annealing the thin film at a faster rate and then promptly starting the growth, the catalyst islands do not have enough time to coalesce and form larger island particles. Furthermore, if the surface energies between the catalyst particles and the underlying layers are greatly mismatched, the contact angle between the catalyst islands and the underlying layers is larger and also affect the shape

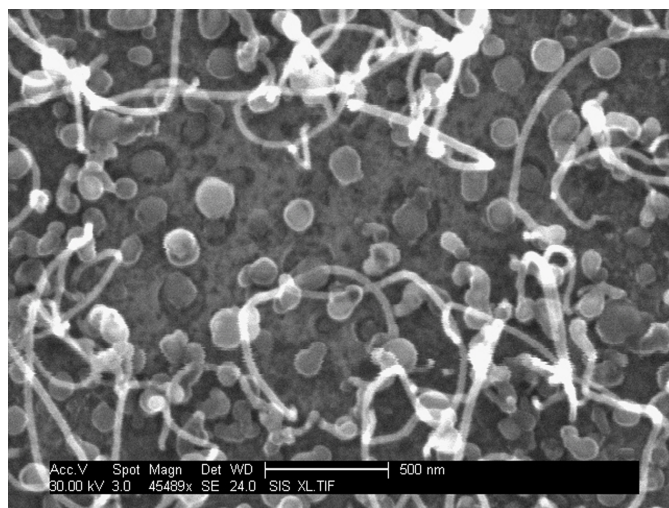


**Figure 2.2:** Fe catalyst layer of 5 nm post annealing at 650 °C for 10 minutes. A few CNTs are present due to residual carbon on the furnace tube from previous growth runs.

and size of the catalyst islands as well as the growth mechanism shown in Figure 2.3. [2]

However more important is the composition of the catalyst and underlying supporting structure, due to their effect on carbon solubility and catalyst activity. Initial research utilizing the thermal CVD process often involved depositing a variety of transition metals, such as Fe, Co, and Ni, on silicon wafers.[40] Of these metals, iron was a promising candidate due to the preferential formation of graphite instead of Fe carbide. One pitfall of using iron in conjunction with a silicon substrate is the possible formation of iron-silicides, which lowers the solubility of carbon in iron. [39, 41] Recent studies that have yielded ultra long CNTs grown on Si wafers, have utilized barrier layers to prevent the mixing of Fe and Si layers. [29, 31, 35, 36] The most widely used of these barrier layers are silicon and aluminum oxides. Typically, a ~500 nm layer of silicon oxide is electron beam evaporated or thermally grown on the Si wafer to act as a diffusion barrier. Aluminum oxide is then deposited or thermally grown from a thin film of deposited aluminum on top of the silicon oxide layer to help better control catalyst size. The aluminum oxide layer is typically ~1-10 nm in thickness. By using these two oxide layers the usable growth temperature range could be increased to accommodate a larger variety of carbon sources since the catalyst layer is protected from undesirable mixing

with the substrate.

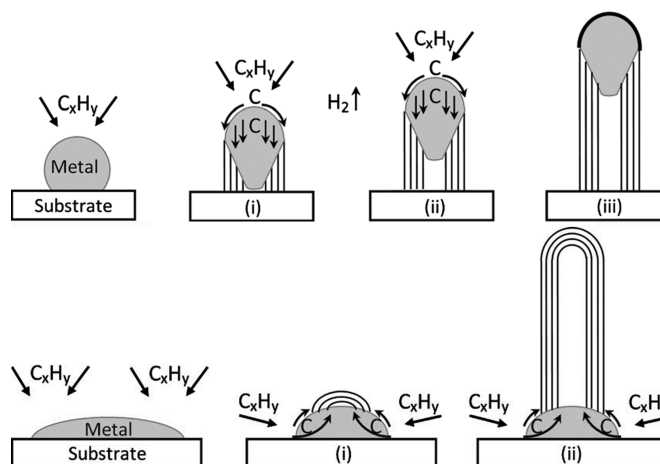


**Figure 2.3:** Diagram originally presented by Kumar and Ando illustrating tip (top) and base (bottom) growth models with Ni and Fe catalysts, respectively. The effect of substrate-catalyst interactions on the growth model can be understood through changes in the contact angle between the two layers.[2]

For the purpose of this research, supporting oxide layers were not considered, since they are insulating and detract from using CNTs as electrodes in electrochemical experiments. Since the substrate and catalyst used were Si and Fe, respectively, care must be taken when selecting the feed gas composition and growth temperature since these parameters determine the carbon decomposition rate and thus determine the life-time of catalytic activity. A balance must be found between the optimal hydrocarbon decomposition temperature that simultaneously reduces the formation of transition metal silicides when using Si as a substrate. Several research groups have attempted growth on other conducting substrates such as copper, but the quality of CNTs is typically poor due to cracking of the substrate and alloy formation upon annealing.[37]

## 2.1.2 Role of Feed Gases on Defect Density and CNT Morphology

### 2.1.2.1 Influence of Carbon Source on Defect Density

A variety of carbon feed gas sources have been used in thermal CVD, ranging from low molecular weight hydrocarbons such as methane and acetylene to liquid sources such as benzene and ethanol. These carbon sources are often mixed with a car-

rier gas typically consisting of a mixture of argon and hydrogen to reduce the partial pressure of the carbon source and limit its decomposition.[42] The addition of hydrogen prevents the sintering of the catalyst layer and reduces native oxide, such as iron oxide, to the pure metal state to prevent the loss of catalytic ability and increase the solubility of carbon.[43, 44]

Larger molecular weight hydrocarbons would also require higher growth temperatures than lighter hydrocarbons due to their larger heat capacities.[42] A greater degree of saturation also increases the growth temperature, as seen with carbon sources of similar molecular weight, such as ethylene compared to acetylene, since they are less reactive.[45–47]

In this work, acetylene and ethylene were used as the carbon feed stock gases. Acetylene gas is much more reactive than ethylene gas and can be used with lower growth temperatures. However, due to its high reactivity, the decomposition of acetylene occurs much faster than the catalyst can support, inducing early catalyst poisoning. Catalyst poisoning is the loss of catalytic activity and results in the inability of the catalyst to support hydrocarbon decomposition. Catalyst poisoning is often accompanied by the formation of amorphous carbon on the surface of the catalyst, as well.

Conversely, ethylene decomposition is more stable decomposition at elevated temperatures, which promotes longer growth times and helps inhibit catalyst poisoning. The higher temperature decomposition also promotes higher bulk and surface diffusion of carbon, increasing the growth rate of CNTs. These effects have important effects on the quality and structure of the produced CNTs and will be explored in Section 3.6.1.

### **2.1.2.2 Changes in CNT Morphological due to Nitrogen**

When CNTs are grown with only carbon and hydrogen containing species, the resulting CNTs have a hollow core with various numbers of tube walls. As was shown in Figure 2.3, CNT tube walls grow at the edges of the catalyst islands, leaving the core of the CNT hollow. The reason behind this mechanism is based on the faster surface diffusion of carbon compared to the bulk diffusion. The much slower bulk diffusion of carbon effectively prevents graphitic precipitation at the center of the catalyst to occur at the same rate as the precipitation at the edges of the catalyst.[3, 48, 49] Therefore an initial cap of the CNT is formed, but further bulk precipitation is not favored.

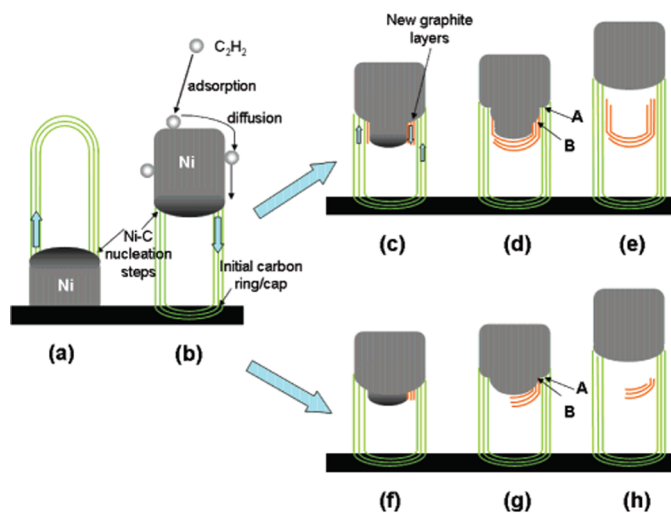


**Figure 2.4:** Diagram illustrating the mechanism of bamboo type CNTs as presented by Lin et al.[3]

If passivation is prevented through the use of nitrogen containing compounds such as ammonia and pyridine, high rates of bulk and surface diffusion of the carbon feed stock through the catalyst particle are achieved and bamboo type CNTs are formed. These types of CNTs have periodic graphitic planes that are angled away from the nanotube axis of the MWCNT and form compartment-like structures. Figure 2.4 illustrates the mechanism behind the compartmentalization of these CNTs. The compartments are defect rich providing an interesting contrast to less defective hollow CNTs, and will be explained in detail in Section 3.3 and investigated through Raman spectroscopy and electrochemistry in Sections 3.6.1 and 4.3.1, respectively.

Since the growth of CNTs involves the culmination of several simultaneous processes, the importance of feed gas composition, temperature, pressure along with the catalyst properties is critical for achieving and maintaining growth via thermal CVD. The problems of preventing catalyst poisoning and sustaining growth to achieve bulk production of CNTs are still being investigated today.

## 2.2 Experimental Synthesis of CNTs

### 2.2.1 Substrate Preparation

The surface of the substrates were prepared by following the same general sequence of steps described below. Initially, 3 inch n-doped Si wafers with a resistivity of  $\sim 1\text{-}10\text{ m}\Omega\text{-cm}$  were cleaned by sequentially sonicating the wafers in isopropyl alcohol, acetone, and water. A catalyst layer of either 3, 5, or 7 nm of Fe was then deposited with a Temescal BJD 1800 e-beam evaporator. The base pressure prior to evaporation was always less than  $6 \times 10^{-6}$  Torr. Square contact pads with side lengths of 1 mm were then patterned onto the other side of the side wafer. The pads consisted of a 10 nm Ti adhesion layer and 60 nm of Ag. Finally, the wafer was diced into squares with side length of 5 mm.

### 2.2.2 Thermal Chemical Vapor Deposition (CVD)

To begin the CNT growth, the substrates with Fe catalyst were placed near the center of the tube furnace that composes the reactor. The ports on both sides of the furnace were then shut and clamped closed. The mechanical vacuum pump was then turned on until a pressure lower than 100 mTorr was attained. Once the pressure stabilized, Ar gas was flown into the furnace. The flow rate was controlled by mass flow controllers (MFCs) with a typical value for Ar of 350 SCCM. A throttle valve downstream from the furnace was then closed and feedback controlled to allow the system to fill with Ar until a pressure of 750 Torr was attained and maintained. After reaching this pressure, the tube furnace was turned on with a ramp rate of  $50\text{ }^{\circ}\text{C}/\text{s}$ . Once the growth temperature was reached, which ranged between 600 and 750  $^{\circ}\text{C}$ , hydrogen gas or a mixture of  $\text{H}_2$  and  $\text{NH}_3$  gases were added to the feed gas stream for 10min with a typical total flow rate of 210 SCCM to reduce any iron oxide. After the 10 min period, either  $\text{C}_2\text{H}_2$  or  $\text{C}_2\text{H}_4$  was finally added to the feed gas stream. The flow rates were varied from 20 to 200 SCCM in an effort to obtain the an optimal flow rate for each gas type. The carbon source was left on for a specific time period, typically 10 min, after which the hydrogen and carbon source were stopped. The tube furnace was then turned off and allowed to cool to room temperature, while Ar gas was allowed to flow during the entire cooling down process. A vast range of different flow rates, growth temperatures, and times were

used to understand how the growth changed with variations in these parameters.

### 2.3 Results and Conclusions

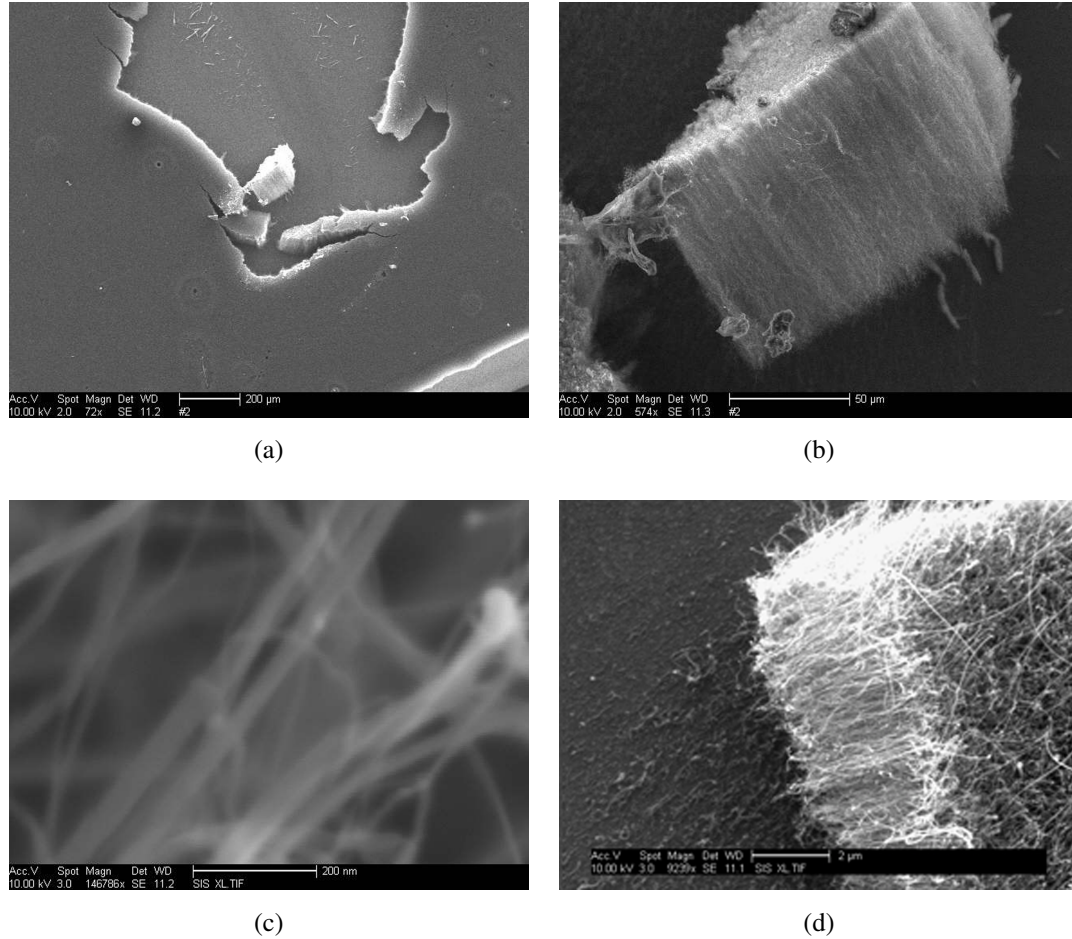


**Figure 2.5:** SEM images of hollow type CNTs taken from (a) top and (b) side orientations to determine CNT growth uniformity and length. (c) is an image of the CNT diameter. (c) is a typical image of bamboo type CNTs.

To characterize the impact that the changes in conditions and post growth treatments described in Chapter 3, Section 3.5 have on CNT growth, a Phillips XL30 environmental scanning electron microscope (ESEM) and a JEOL transmission electron microscope (TEM) were used to image the CNTs. The SEM was also equipped with an energy dispersive spectroscopy (EDS) detector. Since these tools can only be used to determine CNT lengths and diameters they must be used in conjunction with Ramam



spectroscopy (Section 3.6) and electrochemical techniques (Section 4.3) to gain a full understanding of how the CNT electronic and structural properties change.

For many as-produced (AP) CNTs and for all of those that were treated post growth, three unique SEM images were taken. Typical SEM from these views are shown in Figure 2.5. As can be seen from Figure 2.5d, the SEM cannot be used to distinguish CNT morphology since the resolution of  $\sim 10$  nm is not high enough to resolve features of this size. To determine the CNT morphology, TEM must therefore be used. Figure 2.6 shows TEM images to confirm the morphology of the CNTs treated with and without ammonia gas during the growth process.

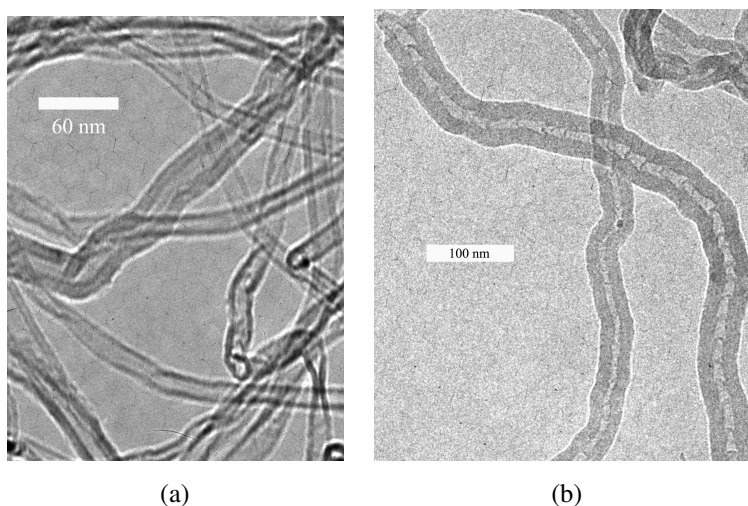


**Figure 2.6:** TEM images of (a) hollow type and (b) bamboo type CNTs to confirm morphology.

Successful and repeatable CNT fabrication is a complex undertaking that involves many different components. The ability to change the various processing parameters, however, allows for the growth of CNTs with a variety of different physical features. The implications of such changes in the growth conditions can be major, as they can affect the mechanical, optical properties, and electrical properties of the CNTs. The uniformity of the CNTs therefore becomes important when using the CNTs in device based applications.

Chapter 2, in part, is a reprint of the material as it appears in “Defect engineering of the electrochemical characteristics of carbon nanotube varieties”, in Journal of

Applied Physics, v.108, n.3, pp.034308, 2010, Hoefer, M. A.; Bandaru, P. R. The dissertation author was the primary investigator and author of this paper.

### 3 Carbon Nanotube Defects

Carbon nanotube defects can be generally defined at any location where the periodic hexagonal arrangement of  $sp^2$  bonded carbon atoms present in a single-layer graphene sheet (crystalline lattice) is perturbed in some way. Defects can be classified by two categories: intrinsic and extrinsic. Intrinsic defects are those that result from structural changes in the lattice without the introduction of impurity atoms. Extrinsic defects are those that involve impurity atoms to induce structural changes.

Historically, research has been focused on obtaining defect free CNTs through synthesis in the hope of being able to experimentally verify the impressive theoretically calculated thermal, electrical and structural properties. Defects do not necessarily hinder the performance of CNTs and in some applications, defects are not only beneficial, but also necessary. One example is a CNT based chemical sensor. Defects in the CNT chemical sensor act as binding locations for sensing functional groups because they are more energetic and subsequently more chemically reactive compared to pristine sites. Typically, functionalization is used to incorporate charged moieties into the CNT based sensor. Carboxyl, ammine, and hydroxyl groups for instance, can increase sensitivity and add specificity to sensing for the appropriate target molecules. Charged moieties could perhaps also achieve similar results. Consequently, one of the goals of this research was to determine if functionalization is necessary to increase the electrocatalytic activity of a CNT electrode or if this can be achieved solely through defect manipulation.

The following sections describe different types of intrinsic and extrinsic defects and how such defects affect the structural properties of CNTs. In addition to structural effects, defects also produce unique changes in the electronic properties of CNTs and an introduction of the electronic band structure and how the band structure can be probed spectroscopically will be provided. The impurity electronegativity and atomic or ionic size can all affect the way in which the impurity interacts with the lattice. Section 3.4.2 will thus provide an introduction to electron deficient (p states) and electron rich (n states) CNTs with a focus on changes in the density of states (DOS). A detailed description of the procedures used in this work to create extrinsic defects will follow in Section 3.5. Finally, the results of various experimental procedures to manipulate CNT defect density and charge will be presented. The majority of work presented in this chapter is used to illustrate that defects can be used to generate regions of charge

density along the CNT.

### 3.1 Point Defects

Due to the low dimensionality of CNTs, some of the defects that are present in three-dimensional crystals such as stacking faults are not possible in CNTs. Lower order defects like point defects however manifest themselves in multi-walled CNTs as Stone-Wales, inverse Stone-Wales defects, vacancies, interstitial adatoms, or lattice impurities. These defects induce changes in the bonding structure of CNTs and can cause re-hybridization of the carbon atoms in addition to inducing local bond strain.

Point defects are entropically necessary and as described in Chapter 2, Section 2.1.2, specific synthesis conditions can change the concentration of defects. One manifestation of different defect concentrations is CNT morphology, where for instance, BCNTs have larger intrinsic defect densities compared to HCNTs as a result of an increased number of edge planes.

#### 3.1.1 Intrinsic Point Defects

When the lattice is missing an atom a vacancy may form. In CNTs, the energy of formation for single vacancies ( $E_{f,SV}$ ) is  $5 - 7\text{ eV}$  depending on the CNT diameter.[4] The dependance of  $E_f$  on diameter arises from differences in curvature for different diameter CNTs. If a single vacancy is created, carbon atoms surrounding the vacancy are at a relatively higher energy state since they are not fully coordinated and have dangling bonds. These higher energy carbon atoms can undergo Jahn-Teller distortions to minimize the local energy, forming a pentagon and a nonagon with one dangling bond remaining, as seen in Figure 3.1. The Jahn-Teller effect is the geometric distortion of non-linear molecules to reach a lower energy state.[4] In graphene and CNTs with low curvature, the energy of formation associated with the Jahn-Teller effect ( $E_{f,JT}$ ) is  $\sim 7\text{ eV}$ , which is relatively large.

Vacancies can also become mobile if enough energy is provided to overcome the migration barrier ( $E_{mb,SV}$ )  $\sim 0.5\text{-}2\text{ eV}$ .[50] The migration barrier is again dependent on the CNT diameter and type. If two vacancies join, a double vacancy is formed with an energy of formation ( $E_{f,DV}$ ) of  $4\text{-}5.5\text{ eV}$ .[50]. In a double vacancy the carbon atoms have no dangling bonds since two pentagons and a heptagon form which are relatively

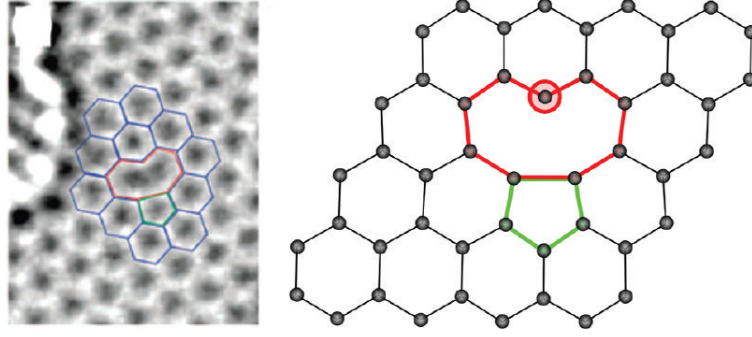


**Figure 3.1:** Jahn-Teller distortion as a result of a single vacancy illustrated originally by Banhart et al.[4]

immobile with a migration barrier ( $E_{mb,DV}$ ) of  $\sim 5$  eV.[50].

Another type of defect, the Stone-Wales defect, occurs when a C-C bond rotates and is a unique property of graphitic systems. As illustrated in Figure 3.2b, the most energetically favorable rotation of the C-C bond is  $90^\circ$ . [5] When both C atoms also rotate, the activation energy ( $E_{f,SW}$ ) increases from  $\sim 5$  eV to  $\sim 10$  eV. [5, 51, 52] As the C-C bond rotates, the local carbons form non-hexagonal rings while maintaining  $sp^2$  hybridization. The non-hexagonal pairings cause bends or kinks along the CNT axis as shown in Figure 3.2c.

### 3.1.2 Extrinsic Point Defects

Defects can also arise from the addition of adatoms on the surface of the lattice. If the adatoms are smaller than the inter-shell spacing of  $\sim 0.35$  nm, they can reside interstitially between the walls of multi-walled CNTs.[53]. If the adatom is carbon and lies interstitially, two new covalent bonds to the surrounding carbons will form and adopt  $sp^3$  character.[4] The binding energy associated with the bond formation ( $E_{b,adatom}$ ) is  $\sim 2$  eV.[54] In the case of carbon adatoms, the migration barrier is 0.4 eV, thus giving them high mobility along the surface of the CNT.[54] If a carbon adatom moves into a vacancy location, it will undergo rehybridization and covalently bond with the surrounding carbon atoms. If only a single vacancy is encountered, rehybridization will effectively re-establish the symmetric hexagonal pairing typical of a pristine CNT. Local bending can also occur if two carbon adatoms meet to form a dimer, which then interacts with the surrounding delocalized  $sp^2$  network to form an inverse Stone-Wales

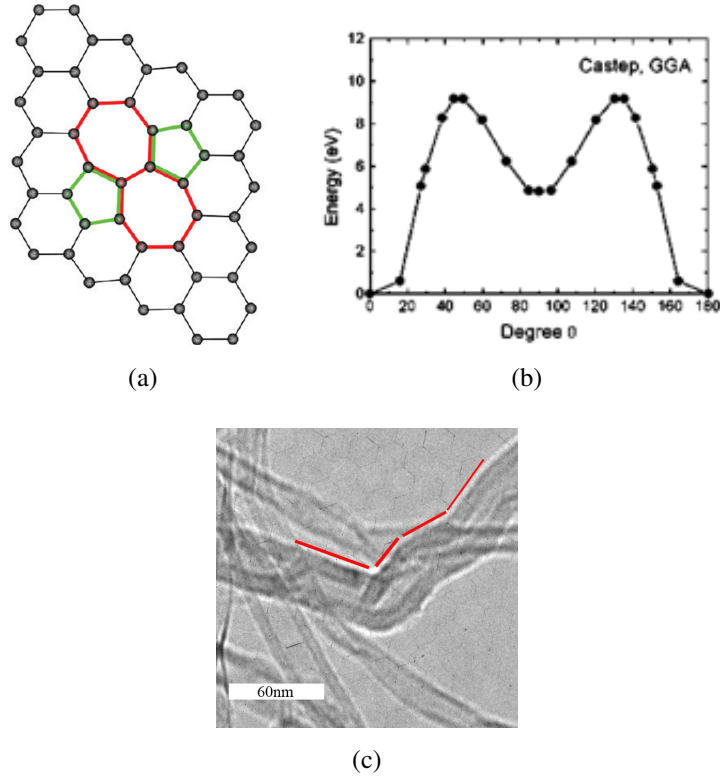


**Figure 3.2:** (a) Diagram illustrating a Stone-Wales defect originally illustrated by by Banhart et al.[4] (b) Bond rotation energy as a function of bond angle for graphene originally illustrated by Li et al.[5] (c) Bends in CNT sidewall that illustrate not hexagonal pairing.

defect, as illustrated in Figure 3.3. The energy of formation for inverse Stone-Wales defects ( $E_{f,iSW}$ ) is  $\sim 7$  eV, which is larger than the energy of a Stone-Wales defect and is less thermodynamically favorable.[4, 6]



**Figure 3.3:** Bond rotation resulting from a carbon adatom dimer (red), which leads to an inverse Stone-Wales defect originally illustrated by Lusk et al.[6]

When adatoms are not carbon, the electronic interaction between the adatom and the local carbon structure varies with the electronic state of the adatom and its size. Depending on the energy of the adatom, it will either physisorb through van der Waals forces or chemisorb through bonding to the CNT surface. Covalently bonding transition metals to the surface of CNTs with electrochemical techniques has been used as a method to identify the location of defects along the surface of the CNT, shown in Figure 3.4.[4, 7, 53] The reduction potential of most metals is  $\sim 2.5$  eV or equivalently  $\sim 2.5$  V compared to the standard hydrogen electrode, therefore if the adatoms are pinned at defects with a larger thermodynamic energy, the adatoms and the defect will bond.

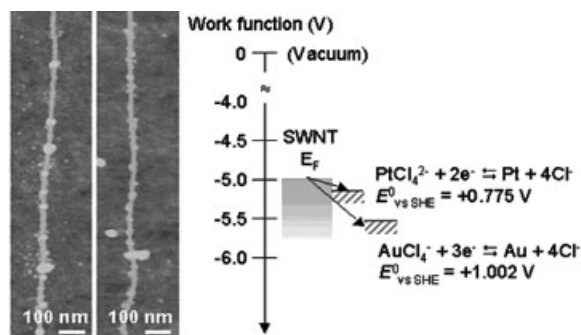


**Figure 3.4:** Au and Pt clusters on a CNT, and the associated energies of the metals compared to the Fermi energy of the CNT originally illustrated by Choi et al.[7]

Bonding to CNTs is not restricted to carbon or foreign adatoms, but can also happen between adparticles at defect sites. An adparticle can be a cluster of atoms or a molecule, which is then either noncovalently or covalently bound to the CNT surface. The mechanism for adparticle attachment is the same as an adatom, yet can only happen on the surface of the outermost CNT shell from geometric considerations. As mentioned at the beginning of this chapter, CNT chemical sensors have utilized functionalization to gain sensing capability. Figure 3.5 illustrates examples of covalently bond PEG molecule and aromatic rings connected to polymers  $\pi$ -bonded to a single walled CNT (SWCNT).

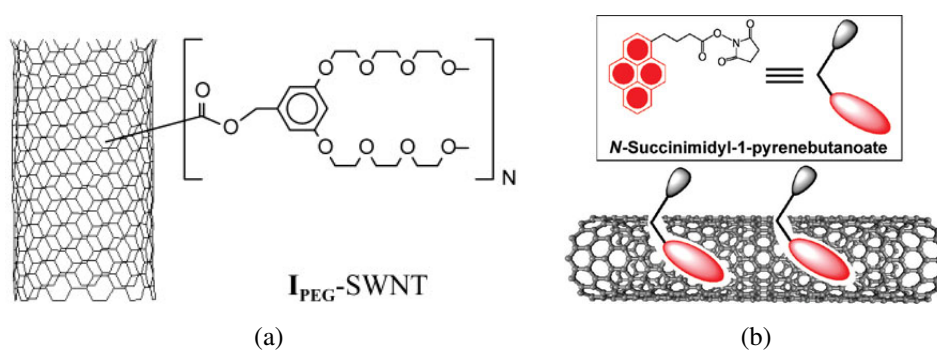


**Figure 3.5:** (a) Covalently bound PEG polymer to a SWCNT originally illustrated by Sun et al.[8] (b) Noncovalently bound N-succinimidyl-1-pyrenebutanoate to a SWCNT originally illustrated by Zhao et al.[9]

Another type of point defect observed in CNTs occurs when foreign atoms add as substitutional impurities into the CNT lattice. Thermodynamically stable substitu-



tional impurities in CNTs tend to be similar in atomic size and have a similar number of valence electrons as carbon, such as Group III and Group V boron or nitrogen.[55] However, when coupled with vacancies, a broader variety of substitutions can occur. Transition metals can also form strong covalent bonds,  $E_{b,metal} \sim 2-8$  eV, at vacancy sites by coordinating with dangling bonds.[4, 55, 56]

### 3.2 One-Dimensional Defects: Intrinsic and Extrinsic

The most commonly observed one dimensional defect in CNTs is an edge plane defect, which resembles the edge plane of a graphene sheet. At an edge plane defect varied bond orderings and bonding configurations can occur. If only bond reordering occurs without the addition of vacancies or other atoms, the armchair (Figure 3.6a) and zig-zag (Figure 3.6c) configurations are formed. These configurations are the most stable of the four depicted in Figure 3.6 since they have the fewest dangling bonds. If vacancies are present on the edge, then variations of the armchair and zig-zag configurations can occur as illustrated in Figures 3.6b and 3.6d.

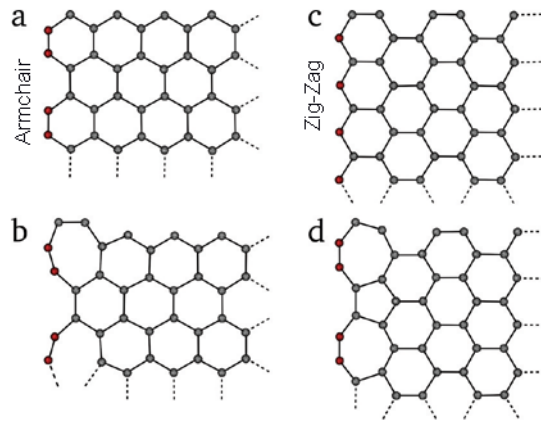


**Figure 3.6:** Various edge-plane configurations with the edge atoms in red: (a) armchair (b) Reconstructed armchair (c) zig-zag (d) Reconstructed zig-zag adapted from Banhart et al.[4]

The dangling bonds present at the edge plane can be passivated by various atoms or compounds giving rise to different bond strains and hybridizations that each have varying effects on the delocalized  $\pi$  bonding and local geometries. An example of passivation is accomplished with hydrogen, where hydrogen bonds to a lone pair and adds

$sp^3$  character to local geometry. However if other elements or compounds are present, a large variety of different edge plane configurations can occur. A quick survey of the current literature reveals that many experiments have been performed to open the caps of CNTs and create edge planes.[57, 58] Since end cap removal typically involves strong oxidizers, the edge carbons can then undergo oxidation to form carboxyl functional groups upon end cap removal. The carboxyl groups can in turn undergo further reactions such as PEG addition that was previously illustrated in Figure 3.5a. If an adatom or adparticle resides interstitially between two walls in a MWCNT at the edge, then the tube walls can be linked together through bonding as demonstrated by Agrawal et al and Picozzi et al.[59, 60]

### 3.3 CNT Morphological Dependency on Defects

All defects mentioned in Sections 3.1 and 3.2 can be present in CNTs and may also effect CNT geometry by causing bending and varied edge plane stacking. When these defects reach a critical concentration the macroscopic CNT structure will be unique, characterizing the CNT morphology. Figure 3.7 illustrates some of the different CNT morphologies and defect dependent structures.

Hollow type CNTs illustrated in Figure 3.7a, are essentially straight with no interruption in the CNT lattice along the tube axis. This geometric phenomenon implies that either the separation between defects is relatively large such that no change in curvature exists or unlikely situation where the sum of all the defects cancel each other, rendering the CNT straight. Utilizing Raman spectroscopy (Section 3.4.3) it can be determined that hollow type CNTs can be relatively defect free. In some cases, the defect density can approach the limiting case of highly ordered pyrolytic graphite (HOPG), which has no defects.

Both the Y-junction CNT shown in Figure 3.7b and the coiled CNT shown in Figure 3.7c are hollow type CNTs. The defect carbons maintain a strained  $sp^2$  hybridization through Stone-Wales type rotations and form complimentary pentagon and heptagon rings. The pentagon-heptagon pairing creates a local contraction in the tube radius at the center of the defect, forcing the other atoms radially outward. When this phenomenon occurs at two locations that are in close enough proximity, the CNT tube axis branches outward forming a Y-junction. When the defect density is more extensive,

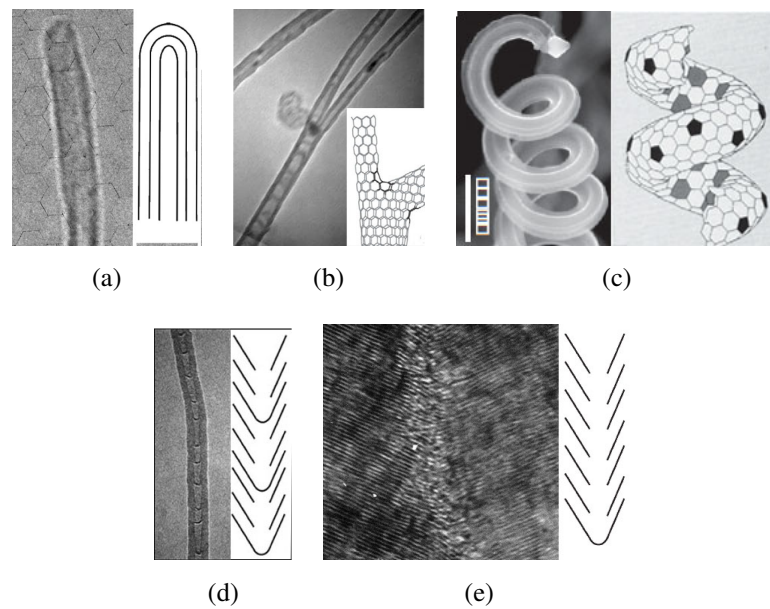


**Figure 3.7:** (a) Hollow Type CNT. (b) Y-Junction from Hollow Type CNTs originally illustrated by Zhang et al. and Bandaru et al.[10, 11] (c) Coiled Hollow Type CNT originally illustrated by Zhang et al.[10] (d) Bamboo Type CNT. (e) Herringbone Type CNT originally illustrated by Rodriquez et al.[12]

complementary pairing of pentagon-hexagon rings can lead to a twisting or coiling of the CNT, where coil radius is dependent on the defect density and the pitch is dependent on van der Waals forces.[61] In coiled CNTs, the inner part of the coil will consist mainly of rings with less than six sides to accommodate the higher curvature. Conversely, the outer part of the coil will consist mainly of rings with greater than six sides to accommodate a lower curvature.

The last two CNT types in Figure 3.7, bamboo and herringbone, have significantly different morphologies than hollow type CNTs. The insets of Figures 3.7d and 3.7e reveal that the sidewalls are formed by stacking layers of conical formations on top of each other, where the outermost surface of the CNT is essentially stacked layers of edge-planes. Since edge-planes are highly defective, these two CNT morphologies have inherently much larger defect densities than hollow type CNTs. In bamboo type CNTs, there is a periodic compartmentalization along the CNT axis that is not present in herringbone type CNTs. The compartment cap is formed through a large concentration of non-hexagonal polygon pairings resulting from Stone-Wales type rotations that give rise to high curvature, similar to the end caps of hollow type CNTs.[62]

### **3.4 Manipulating Band Structure With Extrinsic Defects**

Both intrinsic and extrinsic defects can be created in CNTs post synthesis with adatom, adparticle, vacancy, or substitutional impurity introduction. The methods for creating these defects will be categorized into two general groups: (1) irradiation with electrons or ions, and (2) chemical treatments. As mentioned in Section 3.3, edge-plane and adparticle defects can be generated through wet chemistry by oxidizing CNT end caps. Edge-planes and vacancies as well as substitutional impurities can also be created with irradiation.[63–68] The ways in which the defects are introduced and the type of atoms or ions that are involved play a crucial role in how the defects interact with the electronic structure of CNTs. For instance, the electronegativity and ionization potential of an adatom can determine, to a first order approximation, whether or not the adatom has a propensity for drawing electrons away or donating electrons to the surrounding bonds. The injection or withdrawal of electrons into the  $\pi$  bonds will be termed doping.

### 3.4.1 General Description of CNT Electronic Band Structure

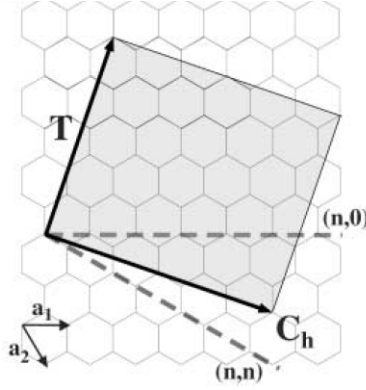


**Figure 3.8:** Graphene sheet indicating the CNT chiral vector ( $C_h$ ) originally illustrated by Odom et al.[13]

Carbon nanotubes have unique electronic structure that arises from strong in-plane  $\sigma$  bonds, an extensive delocalized  $sp^2$  network and a range of diameter dependent curvatures. As described briefly in Chapter 1 and illustrated in Figures 1.1 and 3.8, CNTs are rolled sheets of graphene that can have different chiralities based on the chiral vector ( $C_h$ ). The chiral vector is defined as:

$$C_h = na_1 + ma_2 \equiv (n, m) \quad (3.1)$$

where  $a_1$  and  $a_2$  are the graphene lattice basis vectors illustrated in Figure 3.8 and  $n$  and  $m$  are integers. Using tight binding calculations to determine the 2D band structure, shown in Figure 3.9a, it can be demonstrated that specific  $(n, m)$  indices will result in semiconducting or metallic SWCNTs with different band gap energies.[15, 69, 70] To illustrate this point explicitly, it is convenient to switch to reciprocal space and draw the reduced Brillouin Zone (BZ) for graphene as in Figure 3.9b.

Each of the six corners of the hexagon is a  $\kappa$  point and represents where the  $\pi$  and  $\pi^*$  orbitals overlap. The wavevector ( $\mathbf{k}$ ) is confined to lines in the BZ and its direction is dependent on  $n$  and  $m$  through  $C_h$ , where:

$$C_h \mathbf{k} = 2\pi q \quad (3.2)$$

and  $q$  is an integer. When the reduced BZ's of graphene and SWCNTs are superimposed, the points at which  $\mathbf{k}$  crosses the  $\kappa$  points (Figure 3.9c) indicate  $\pi - \pi^*$  orbital overlap

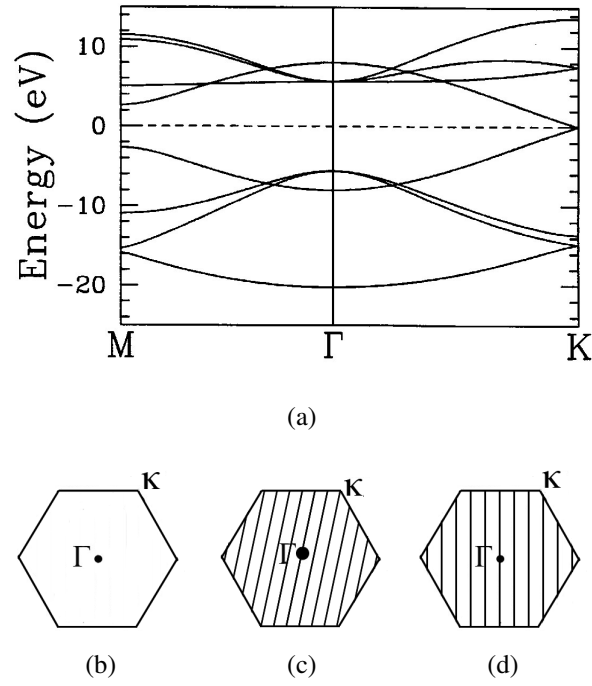


**Figure 3.9:** (a) Band structure of a graphene sheet.[14] (b) The reduced BZ of a graphene sheet. (d) Overlap of the reduced BZ's of graphene and semiconducting SWCNTs (solid lines). (c) Overlap of the reduced BZ's of graphene and metallic SWCNTs (solid lines).

and only a minimal amount of energy is needed to promote electrons the  $\pi$  to  $\pi^*$  orbitals. Conversely, if  $\mathbf{k}$  does not pass through the  $\kappa$  point (Figure 3.9d),  $\pi$  and  $\pi^*$  orbitals do not overlap. When this situation arises, a finite amount energy is needed to excite electrons from the bonding  $\pi$  orbitals into the anti-bonding  $\pi^*$  orbitals. Expressed mathematically;

$$\begin{aligned} n = m & \quad E_{excitation} = 0 \\ n - m = 3j \quad j \text{ is non-zero, } E_{excitation} \text{ is small} \\ n - m \neq 3j \quad E_{excitation} \text{ is large} \end{aligned}$$

Since the delocalization of electrons in the  $\pi$  bonding system is extensive in graphene and CNTs, the  $\pi$  and  $\pi^*$  orbitals can be termed the valence and conduction bands, respectively. In this context, the excitation energy described above is called the band gap between the conduction and valence bands and the  $\kappa$  point energy is the Fermi level energy,  $E_F$ . The size of the band gap depends not only on CNT curvature, but also on defects since defects can interact with the bands through electron withdrawal or donation. Changes in the bands induced by defects can be understood more thoroughly by investigating how the defects perturb the allowable energies or the density of energy states (DOS) near  $E_F$ . The DOS can be calculated from the band structure illustrated in Figure 3.9a with the following relation:

$$DOS \equiv \frac{dN}{dE} = \frac{dN}{dk} \frac{dk}{dE} \quad (3.3)$$

where  $N$  is the number of states,  $E$  is the energy,  $k$  is the wavevector described previously. Although the derivation of  $N$  will not be explicitly given in this work, it is important to note that for 1D materials, the DOS has characteristic spikes originating from  $\frac{dE}{dk} \rightarrow 0$ , as shown in Figure 3.10. The spikes are called van Hove singularities (VHS) and create the majority of interesting electronic properties near  $E_F$ . [15, 71, 72]

Changes in the DOS are especially important in electrochemistry since  $E_F$  represents the chemical potential ( $\mu$ ) in the absence of an external force such as voltage. Structural changes in CNTs originating from defects can therefore be linked through the electronic DOS to changes in  $\mu$  and also changes in bond reactivity. Structural changes in CNTs also cause modulation of phonon characteristics and can be investigated spectroscopically. Utilizing both electrochemistry and spectroscopy allows correlations

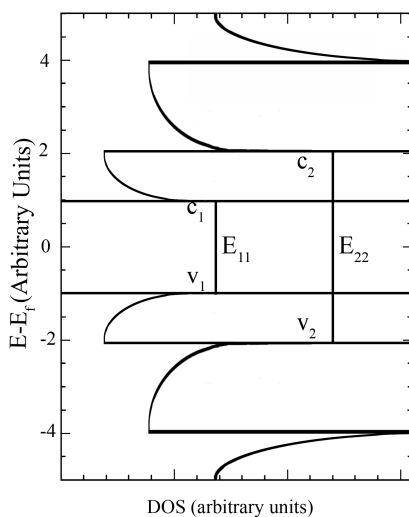


**Figure 3.10:** A sample electronic DOS for a SWCNT where  $V$  and  $C_n$  indicate the valence and conduction bands, respectively and  $E_{n,n}$  indicates the band gap.

to be draw between changes in bond vibrations and chemical reactivity. The next two sections explain modulation of both the electronic and phonon DOS due to defects.

### 3.4.2 n and p-type CNT Doping

When electron deficient moieties are added to CNTs either through bonding, adatom introduction, or substitutional impurity addition as with boron addition, energy levels near the valence band are created that are dependent on the dopant energy. Conversely, if electron rich moieties are added, energy levels near the conduction band are introduced. These two processes can tailor the energy level of  $E_F$  with respect to the conduction band.

Instances of electron donating and withdrawing with respect to carbon in CNTs occur when nitrogen and boron are added in substitutional positions. Nitrogen and boron are approximately the same size as carbon ( $\sim 70$  pm) and can readily act as substitutional impurities in CNTs. Since boron has one less electron than carbon, when boron replaces carbon atoms, as shown in Figure 3.11b, an adjacent carbon is left with an incomplete octet. Electron density shifts to accommodate the loss of the electron creating a partial positive charge on the surrounding carbons and a new defect energy level is created



in the band structure near the valence band. Conversely, if nitrogen is introduced into the lattice (as shown in Figure 3.11c), a new energy level near the conduction band is created since nitrogen has one more electron than carbon. Fluctuations in  $E_F$  change the required energy needed to promote electrons from the valence band to the conduction band as shown in Figure 3.12. Both of the energy levels associated with boron and nitrogen doping in Figure 3.12 are not seen in pristine CNTs.

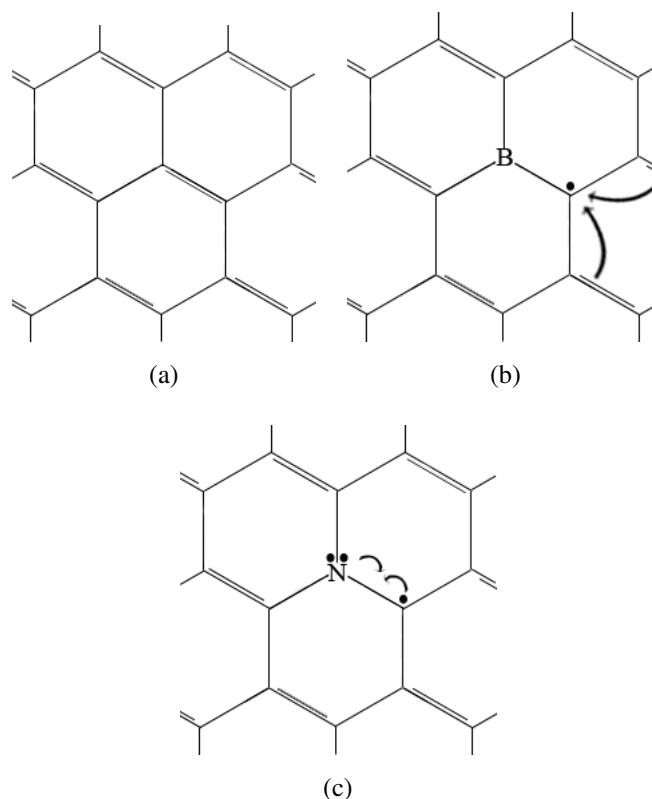


**Figure 3.11:** Sample illustrations of delocalized bonding in (a) CNTs, (b) boron doped CNTs, (c) nitrogen doped CNTs.

Adatoms and adparticles can also cause shifts in the electronic DOS, just as the boron and nitrogen. Due to the higher reactivity of defect sites, adparticles and adatoms can be trapped at defects. Depending on the electronegativity of the adatom or the dipole moment of the adparticle, electron density can be shifted to or away from the  $\pi$  bonds. An example of electrostatic doping arises when exposing CNTs to oxygen. Atmospheric oxygen adds as an adparticle on the CNT, and since it has an electronegativity of 3.44 compared to carbons electronegativity of 2.55 on the Pauling scale, the oxygen shifts

electron density away from the CNT, creating a local positive charge.

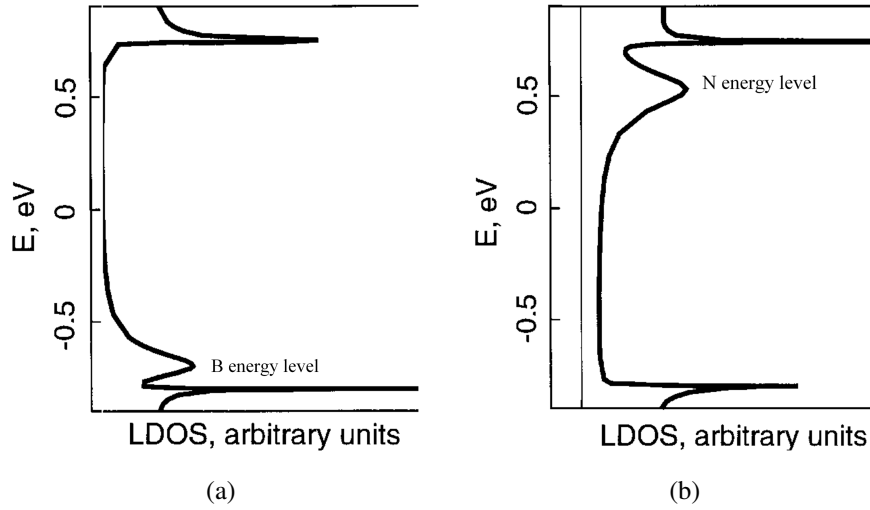


**Figure 3.12:** DOS of a (a) boron doped SWCNT and a (b) nitrogen doped SWCNTs adapted from the illustrations presented by Louie. [14]

Inducing local charged regions along the CNT surface through defect manipulation and doping inherently changes the bonding in CNTs and  $E_F$ . Changes in  $\mu$  dictate the reactivity of CNT bonds and consequently doping can increase electrocatalytic activity.

### 3.4.3 Introduction to Raman Spectroscopy

A change in the electronic DOS has a two-fold effect on bond vibrations. To utilize Raman spectroscopy electromagnetic radiation must be scattered by a crystalline lattice atom or a molecule. A photon of the incident radiation is annihilated and a photon of the scattered radiation is simultaneously created, where the incident photon is scattered either by emitting (Stokes) or absorbing (anti-Stokes) a phonon. The difference in the emitted and incident photon frequencies is equal to the phonon frequency. Changes in  $E_F$  also affect bond vibrations, since the addition or removal of electrons can effectively change the spring constant associated with bond and lattice vibrations. Raman spectroscopy could therefore be a useful tool for understanding vibrational modes and subsequently shifts in electron density arising from defects in CNTs.

As shown in Figure 3.13, CNTs exhibit many phonon modes. However only

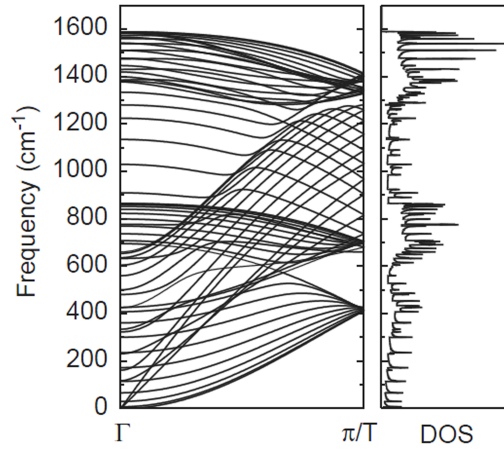


**Figure 3.13:** The phonon band structure (left) and the phonon DOS (right) for a SWCNT adapted from Dresselhaus et al.[15]

some of these modes are Raman active due to selection rules that generally limit the phonon modes to involve only symmetric stretching. In SWCNTs, a unique feature called the radial breathing mode (RBM) in the Raman spectra can be used to determine CNT chirality as the frequency shift associated lattice vibrations is inversely proportional to the diameter of the CNTs. However, when investigating MWCNTs the RBM cannot be determined for three reasons: (1) MWCNTs are themselves comprised of multiple SWCNTs, (2) multiple CNTs with a distribution of diameters are measured, and (3) the Raman signal from the RBM is low unless resonantly enhanced. The first two factors broaden the RBM peaks to where no diameter dependent information can be obtained. For instance, if the MWCNTs have a diameter  $23 \pm 3$  nm and consist of 5 walls, 30 different nominal RBMs should be observed and can be further increased by a greater number of tube walls and larger outer diameter distribution. Furthermore, since the laser wavelength was fixed, the wavelength cannot be changed to enhance the resonance of the RBM mode, which is  $\sim 10\times$  less energetic than other phonon modes in CNTs.[15] However, the information gained through Raman spectra provides an averaged analysis of vibrational modes in MWCNTs.

Of the Raman active modes in CNTs, several scenarios exist that explain how defects affect the phonon modes in all CNTs. Figure 3.14 illustrates first and second-order processes that give rise to the phonon modes in CNTs. The only first order process in

CNTs corresponds to the G-peak and RBM. The G-peak originates from atom displacements along the CNT axis analogous to the in-plane atom displacements of graphene (Figure 3.15a, left), hence the name G-peak. Another important peak in MWCNTs is the defect induced peak or D-Peak that arises from second order processes. The D-peak has been attributed to bond vibrations that result in the radial stretching/contracting of the hexagonal motif.[16] A second defect called the D' peak can also be observed and is attributed to edge planes.[73–77] Finally, second order two phonon processes or harmonics can also be observed in CNTs, but are typically less intense than single phonon processes, especially with highly defective CNTs as the propensity for two identical vibrations to occur decreases with higher defect concentrations.

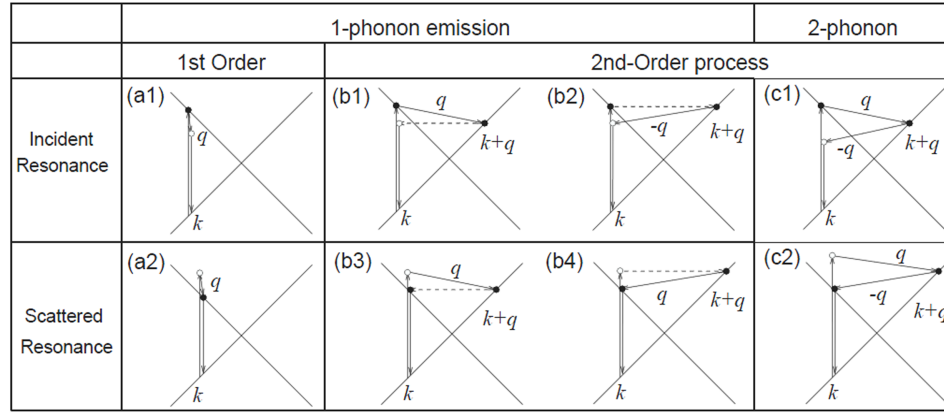


**Figure 3.14:** Different scattering events in CNTs.  $\mathbf{k}$  and  $\mathbf{q}$  are the wavevector of the electron and phonon vector, respectively. Incident resonance occurs when the excitation laser energy matches a real electronic transition, while scattered resonance occurs when the excitation laser energy is equal to the electronic transition energy plus the phonon energy. Furthermore, the dashed lines indicate elastic scattering events originating from defects. Illustrated originally published by Dresselhaus et al.[15]

By monitoring the peak heights, positions, and widths, information can be obtained about the influence of defects on the different bond vibrations. Certain trends have been determined for graphite that illustrate the effects of bond disorder as shown in Figure 3.15b and were applied to CNTs in this thesis.

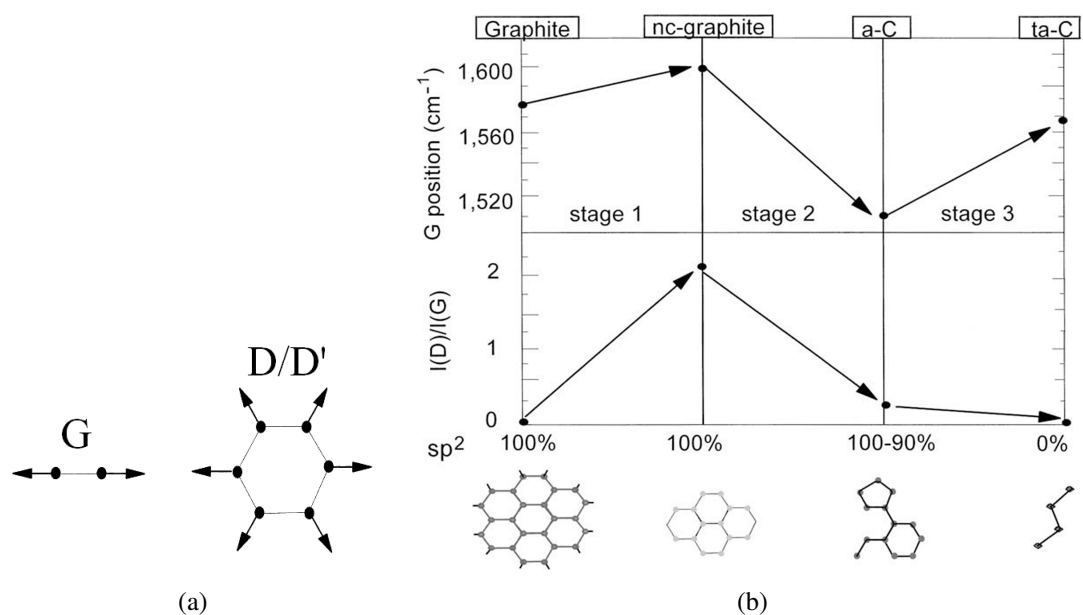


**Figure 3.15:** (a) Atom displacements for the G and D/D' bands. (b) Changes in the G-peak position and G/D peak intensities with increasing bond disorder. nc-graphite is nanocrystalline graphite, a-C is  $sp^2$  amorphous carbon, ta-C is  $sp^3$  amorphous carbon originally illustrated by Robertson.[16]

### 3.5 Experimental Methods for Manipulating Defects

Raman spectroscopy was used to characterize changes in the CNTs for the various treatments. The diffraction limited Raman spectroscopy setup (Renishaw) consisted of a 514.5 nm Ar optically coupled to a microscope which was then focused on the samples. The grating used had 1800 lines/mm, the laser power was measured to be 2.5 mW at the sample, the microscope objective magnification was 80x, and the detector exposure time was 10-30 s. Before and after each set of Raman data was collected, the power at the sample was checked with a power meter and the calibration of the Raman was checked. The calibration was completed by taking a spectra of a polished Si wafer and comparing the experimentally determined peak position to the known value of  $520.4\text{ cm}^{-1}$ . [78] To reduce noise, a minimum intensity value of  $900\frac{\text{counts}}{\text{mWs}}$  was ensured. Between 3 and 5 spectra were taken at different regions of each CNT sample to monitor the uniformity of the treatments.

Two distinct methods were used for introducing defects into CNTs. The first utilized a Trion Reactive Ion Etcher (Trion) and the second utilized the CVD furnace. In both configurations atoms or ions of different elements and molecules were directed towards the CNTs to create defects. Since the two techniques were independently conducted, the following two sections explain the experimental procedures for both processes.

#### 3.5.1 Reactive Ion Etching

The dry etcher could be used in two modes: reactive ion etching (RIE) or with inductively coupled plasma (ICP). A diagram of the Trion dry etcher setup is shown in Figure 3.16.

Initially, the chamber was evacuated to  $\sim 10\text{ mTorr}$ . The gas under investigation was then allowed to flow into the chamber until a certain pressure was reached. Once this pressure was attained, the RIE process was initiated by applying an AC voltage at 13.56 MHz to generate an electromagnetic field between the upper and lower electrode plates. The RIE voltage is applied to the lower plate with a power between 50 and 300 W, which causes the gas molecules to be stripped of their electrons subsequently forming a plasma in the reaction chamber. During the oscillation of the applied volt-

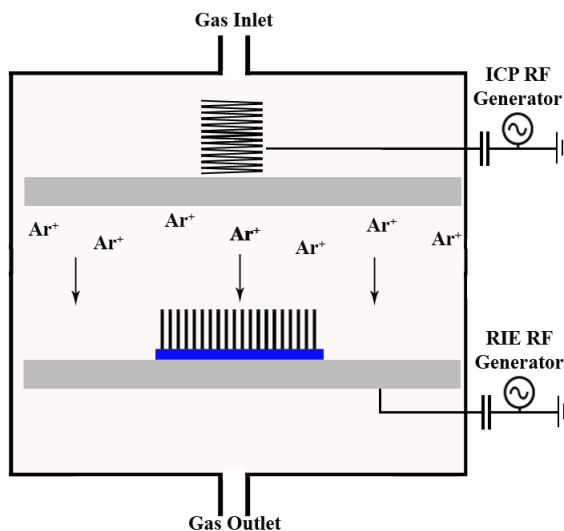


**Figure 3.16:** Diagram that outlines the important features of the Trion etcher. The lower plate has a CNT covered substrate.

age, changes in the electric field cause electrons to be accelerated up and down in the chamber, contacting both the upper and lower electrode plates. Since the lower plate is externally grounded with a capacitor in series with the voltage source, a self generating negative bias between the two electrode plates is formed. When using ICP, another RF voltage source is applied at the same frequency as the RIE RF voltage source to the coils above the top plate, coupling it to the plasma to create higher plasma densities. Once the desired reaction time had elapsed, the RF voltage source(s) were turned off and the chamber was evacuated to  $\sim 10$  mTorr. Once attained the chamber was purged with nitrogen until atmospheric pressure was attained.

The application of either RIE or RIE coupled with ICP power can greatly influence how ions interact with the CNTs through changes in the momentum of the ions in the plasma. If ions could be accelerated towards the CNTs with enough momentum, such that the energy is greater than the bond energy, they could physically (sputter) etch the CNTs by ejecting carbon atoms. The influence of RIE and ICP power on sputtering becomes evident when calculating the momentum ( $\mathbf{p}$ ) of an ion accelerated in an electric field as demonstrated by:

$$\mathbf{p} = m\mathbf{v} = m \left[ \frac{qV_{DC}}{dm} + v_0 \right] \quad (3.4)$$

where  $V_{DC}$  is the self-generating DC voltage,  $m$  is the mass of the charged particle,  $d$  is the distance moved by the charged particle,  $q$  is the magnitude of the charge, and  $v$  is the ion velocity. For the Trion,  $V_{DC}$  can be determined by the following equations:

$$I_{RIE} = I_0 \sin(\omega t) \quad (3.5a)$$

$$V_{DC} \approx \frac{1.3I_0}{e\epsilon_0\omega^2 n_s A} [79] \quad (3.5b)$$

where  $I_{RIE}$  is the current of the RF power supply with a peak current of  $I_0$  and frequency  $\omega$ ,  $e$  is the charge of an electron,  $\epsilon$  is the permittivity of free space,  $n_s$  is the electron density near the powered electrode and  $A$  is the area of the electrode. Since  $V_{DC}$  is inversely proportional to the number of electrons and proportional to  $I_{RIE}$ , increasing the plasma density with ICP decreases ion momentum, while increasing the RIE power increases ion momentum.

**Table 3.1:** Ionization Processes in Argon Plasmas. [24, 25]

Process Description	Reaction
Radical Formation	$e^- + Ar \rightarrow Ar^* + e^-$
Radical Ionization	$e^- + Ar^* \rightarrow Ar^+ + 2e^-$
Atomic Ionization	$e^- + Ar \rightarrow Ar^+ + 2e^-$
Radical-Electron Recombination	$e^- + Ar^* \rightarrow Ar + e^-$
Radical-Radical Recombination	$Ar^* + Ar^* \rightarrow Ar^+ + Ar + e^-$
Radical-Atomic Recombination	$Ar^* + Ar \rightarrow 2Ar$
	$Ar^* + 2Ar \rightarrow 2Ar_2 + Ar$

In addition to sputter etching, reactions can also occur during plasma exposure. Therefore, in this work argon (Ar), hydrogen (H<sub>2</sub>), and chlorine (Cl<sub>2</sub>) gas were used as the working gases to elucidate dependencies of defect creation on polarity, size, and momentum of the ions present in the plasma. Argon was used initially since the plasma chemistry for Ar is relatively simple. Upon initiating the plasma, Ar can undergo the reactions shown in Table 3.1.



Although several reactions are possible, the only ion in the gas mixture is  $\text{Ar}^+$ . The  $\text{Ar}^+$  charge state is highly energetic since the ionization energy of Ar is  $\sim 15.7$  eV. If  $\text{Ar}^+$  would contact a CNT it could potentially strip electron density from the CNTs to reform Ar, which would be energetically favorable. If  $\text{Ar}^+$  would be accelerated towards the CNTs with enough momentum, it could also sputter etch the CNTs as mentioned previously. To understand how plasma density, kinetic energy, and irradiation time would affect both mechanisms, numerous process parameters were used as outlined in Table 3.2.

**Table 3.2:** Trion Process Variables: Ar Plasma

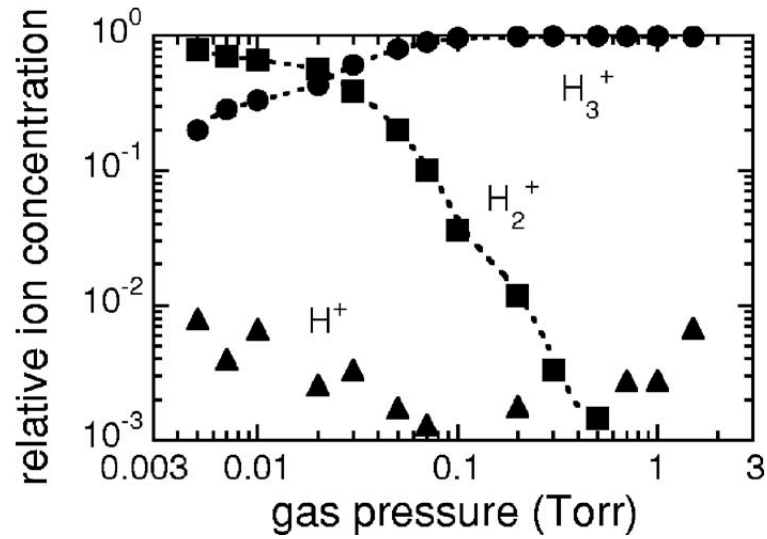
Process Parameter	Range
RIE Power (W)	50, 100, 150
ICP Power (W)	0, 50, 100, 150
time (s)	30, 60, 90, 180
Pressure (mTorr)	30, 45, 60, 90, 120
Flow (SCCM)	30

Hydrogen was also used as a working gas since  $\text{H}_2$  plasma also consists of positively charged ions as shown in Table 3.3. Differences in defect generation rates and types can therefore be attributed to ion size and momentum in addition to any reactions that occur between hydrogen ions and the CNTs. For example, hydrogen can sputter etch the CNTs to create free lone pairs, termed dangling bonds, while undergoing reactions with the same dangling bonds.

As shown in Table 3.3, different positively charged ions of hydrogen can exist that are dependent on the gas pressure as shown in Figure 3.17. The processing parameters were therefore chosen such that a majority of  $\text{H}_2^+$  was present to simplify the comparison between Ar and  $\text{H}_2$  plasmas, shown in Table 3.4.

**Table 3.3:** Ionization Processes in Hydrogen Plasmas. [17, 26]

Process Description	Reaction
Molecular Ionization	$e^- + H_2 \rightarrow H_2^+ + 2e^-$
	$e^- + H_2 \rightarrow 2H + e^-$
Ion Ionization	$e^- + H_2^+ \rightarrow H^+ + H + e^-$
	$H_3^+ + e^- \rightarrow H^+ + 2H + e^-$
Atomic Ionization	$e^- + H \rightarrow H^+ + 2e^-$
Ion-Molecular Recombination	$H_2^+ + H_2 \rightarrow H_3^+ + H$
Ion-Electron Recombination	$H_3^+ + e^- \rightarrow H_2 + H$

**Figure 3.17:** Concentration profiles of  $H^+$ ,  $H_2^+$ , and  $H_3^+$  in plasma generated from pure  $H_2$ . Originally plotted by Nunomura et al.[17]**Table 3.4:** Trion Process Variables:  $H_2$  Plasma

Process Parameter	Range
RIE Power (W)	50, 100
ICP Power (W)	0, 25, 50, 100
time (s)	60
Pressure (mTorr)	10
Flow (SCCM)	30

The final working gas used in this work is chlorine gas ( $\text{Cl}_2$ ). The plasma chemistry for  $\text{Cl}_2$  is similar, yet more complex than for  $\text{H}_2$  plasma, since the ionization and recombination reaction pathways can generate both positively and negatively charged ions, shown in Table 3.5.

**Table 3.5:** Ion Reaction Processes in Chlorine Plasmas. [18, 19]

Process Description	Reaction
Molecular Ionization	$e^- + \text{Cl}_2 \rightarrow \text{Cl}_2^+ + 2e^-$
Dissociative Ionization	$e^- + \text{Cl}_2 \rightarrow \text{Cl}^+ + \text{Cl} + 2e^-$
Ion-Pair Formation	$e^- + \text{Cl}_2 \rightarrow \text{Cl}^+ + \text{Cl}^- + e^-$
Dissociative Attachment	$e^- + \text{Cl}_2 \rightarrow (\text{Cl}_2^-)^* \rightarrow \text{Cl}^+ + \text{Cl}^-$
Atomic Ionization	$e^- + \text{Cl} \rightarrow \text{Cl}^+ + 2e^-$ $e^- + \text{Cl}^+ \rightarrow \text{Cl}^{++} + 2e^-$
Ion-Ion Recombination	$\text{Cl}_2^+ + \text{Cl}^- \rightarrow \text{Cl}_2 + \text{Cl}$ $\text{Cl}^+ + \text{Cl}^- \rightarrow 2\text{Cl}$
Dissociative Recombination	$\text{Cl}_2^+ + e^- \rightarrow 2\text{Cl}$

To quantify any potential differences in the effects between positively and negatively charged ions, control over the process parameters used for chlorine plasma etching were used to limit the ion polarity to one charge type. As can be seen from Figure 3.18, the concentration of the species present in the plasma depends critically on the power and pressure of the reactor. The formation of negatively charged ions is favorable when relatively higher pressures and lower powers are used, while positively charged ions are favored at low pressures and higher powers. Table 3.6 therefore reflects the aim of generating either positively or negatively charged ions.

By using the above process parameters for Ar,  $\text{H}_2$ , and  $\text{Cl}_2$  plasma etching, the defect generation mechanism, defect formation rate, and uniformity dependence on the polarity, size, and momentum of the ions was explored.

### 3.5.2 Hydrogen Exposure and Metal Deposition

To decouple the sputtering and reaction defect generation mechanisms, the CNTs were exposed to hydrogen and magnesium gases in the CVD reactor, shown in Figure

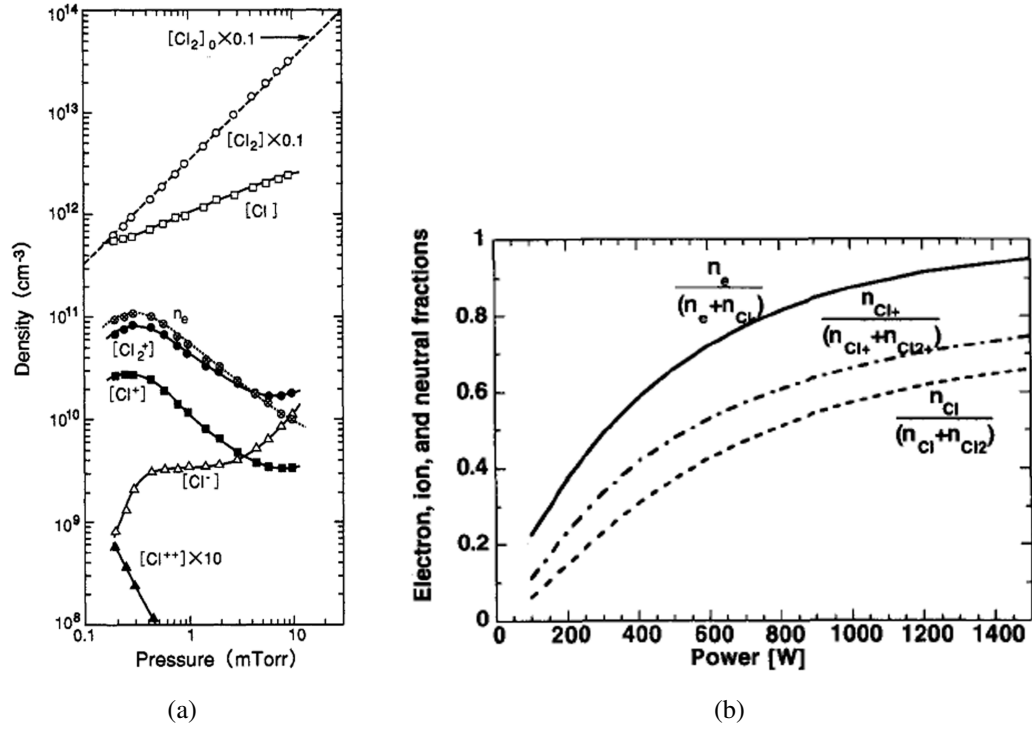


**Figure 3.18:** Concentration profiles of Cl<sub>2</sub>, Cl, Cl<sub>2</sub><sup>+</sup>, Cl<sup>+</sup>, Cl<sup>2+</sup>, Cl<sup>-</sup>, and e<sup>-</sup> in plasma generated from pure Cl<sub>2,0</sub> stock feed with respect to (a) pressure as illustrated by Ono et al. and (b) power as illustrated by Meeks et al.[18, 19]

**Table 3.6:** Trion Process Variables: Cl<sub>2</sub> Plasma

Process Parameter	Range
RIE Power (W)	50, 100, 150, 200
ICP Power (W)	0, 50, 100, 150
time (s)	60, 120, 240
Pressure (mTorr)	10, 60, 240
Flow (SCCM)	30

2.1. Gas exposure in the CVD constitutes relatively low momentum processes compared to plasma irradiation and thus should not involve any sputtering processes. A comparison hydrogen gas used in the Trion and CVD, therefore allows for the direct comparison between reaction and sputter in addition to reaction based processes. The reactivity between CNTs and evaporated Mg was also explored. If reactive Mg, could be used to n dope the CNTs, contrasting the potential p doping of the CNTs through positively charged ion bombardment.

In these experiments, the CVD chamber was initially evacuated to 80 mTorr and then purged for 10 min with Ar. Hydrogen was then fed into the Ar carrier gas stream until a specific total pressure was obtained and maintained for another 20 minutes through the use of a throttle valve. The individual gas flows and total pressure of the gas mixture were chosen such that the  $H_2$  partial pressure was the same as pressure used in the plasma experiments as shown in Table 3.7. Once the pressure was reached, the furnace was heated until a specific temperature and was maintained for a specific time. Subsequently, the  $H_2$  flow was stopped, the chamber was filled with Ar gas until atmospheric pressure was attained and the furnace was allowed to cool to room temperature.

**Table 3.7:** Hydrogen CVD Variables

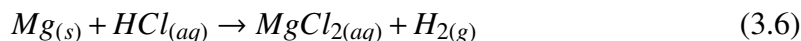
Process Parameter	Range
Temperature ( $^{\circ}C$ )	300, 400, 500
time (min)	10
Total Pressure (Torr)	5
Ar Flow (SCCM)	400
$H_2$ Flow (SCCM)	0, 18

Since the experiments were carried out at elevated temperatures to increase hydrogenation reaction kinetics, controls were first used to determine if any changes in the CNTs would arise from the effects of annealing in Ar gas.[80] The controls consisted of CNTs that were synthesized the same way as the  $H_2$  treated samples, but without plasma processing with  $H_2$  gas. By completing the above procedure for CVD  $H_2$  exposure, the effects of plasma processing induced sputtering coupled with plasma reactions compared to hydrogenation reaction based defect manipulation can be better understood

and quantified.

Magnesium was then used to electron/n dope the CNTs since it is a good electron donor and the deposition method does not involve the acceleration of particles at the CNTs that is be present with plasma processes. Metals with low ionization energies ( $<900$  kJ/mol) and small electronegativities ( $<1.6$ ) are potential candidates to electron dope or negatively charge CNTs since they can readily donate electrons. Both Group I and II metals could be used, however all Group I metals spontaneously undergo exothermic dissolution in water. Since the CNTs are to be used as electrodes in aqueous solutions these metals are not acceptable choices. Low atomic number, Group II metals such as beryllium or magnesium have larger ionization energies, making them less susceptible to reaction with water and are therefore better candidates.

To controllably n-dope CNTs with beryllium or magnesium, these metals can be evaporated onto the CNT surfaces, avoiding sputter processes. However, as can be seen below in Figure 3.19, the vapor pressure of beryllium is too low for beryllium to be practically used. Magnesium has much higher vapor pressures and is more readily evaporated. For example, at 800 K the vapor pressure of Be is  $\sim 10^{-7}$  mTorr, while the vapor pressure of Mg is  $\sim 100$  mTorr. When contacted with the CNTs, it was hypothesized that the magnesium would donate its electrons to defect sites due to the Pauling electronegativity difference between Mg and C, 1.31 and 2.55 respectively. Excess magnesium will most likely form on the surface of the CNTs as well, but could be removed by reacting with  $\text{HCl}_{(aq)}$  as shown below:



To determine the effects of  $\text{HCl}_{(aq)}$ , CNTs without Mg deposition were treated with  $\text{HCl}_{(aq)}$  and used for a control. Treated CNTs were subject to critical point drying (CPD) after exposure to  $\text{HCl}_{(aq)}$  and subsequently checked through Raman Spectroscopy and electrochemistry.

Similar to the CVD based  $\text{H}_2$  protocol described earlier, the chamber was initially evacuated to below 80 mTorr. Subsequently, Ar gas was used to fill the chamber until the desired pressure was reached and then allowed to flow for 10 min. The chamber was then heated to the desired temperature and Mg was allowed to evaporate for the

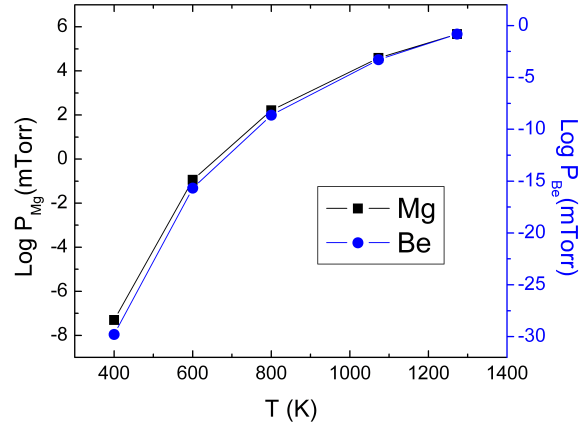


**Figure 3.19:** Vapor pressure profiles of Be(●) and Mg(■) as a function of temperature.

set period of time. Once the deposition was completed, the furnace was turned off, the throttle valve shut, and the Ar flow increased to 350 SCCM until atmospheric pressure was reached. Ar was allowed to flow until the furnace temperature was less than 50 °C.

**Table 3.8:** Magnesium Deposition Variables

Process Parameter	Range
Temperature (°C)	350, 415
time (min)	10
Ar Pressure (Torr)	5, 10
Ar Flow (SCCM)	100, 350

### 3.6 The Influence of Defects as Determined Through Raman Spectroscopy

In the following sections the Raman spectroscopy results will be presented for the different treatments. As the CNTs are exposed to ions in the plasma, H<sub>2</sub> gas, and evaporated Mg, structural changes were represented by the changes in the first order G, D, and D' peaks as well as second order harmonic and combination peaks. In this work, the focus was placed only on the three first order peaks. To determine the peak widths, heights, and positions the Raman spectral data were fitted using a Lorentzian function.

For one peak, the Lorentzian function was defined as[16]:

$$y = y_0 + y_p \frac{\omega^2}{4(x - x_c)^2 + \omega^2} \quad (3.7)$$

where  $y_0$  is the baseline y-offset in counts,  $y_p$  is the peak counts,  $x_c$  is the peak position in  $\text{cm}^{-1}$ ,  $\omega$  is the full-width-at-half-maximum in  $\text{cm}^{-1}$ , and  $x$  is the wavenumber in  $\text{cm}^{-1}$ . The area under the curve can also be defined in terms of  $y_p$ , where:

$$A = \frac{y_p \pi \omega}{2} \quad (3.8)$$

A macro in Microsoft Excel was written to perform the baseline subtraction and deconvolution of the D, G and D' peaks. The Levenberg-Marquardt algorithm for non-linear least squares fitting was used to minimize the error between the fitted function and the actual data. The  $\chi^2$  error function was normalized to the number of degrees of freedom and was used to determine the error of the fit as it provides an estimate of the confidence of the fitting that can be generally applied to many functions. The macro also stepped through different starting peak positions, performed the fitting deconvolution, and calculated the overall best fit to eliminate any error based on the starting peak positions. A typical Raman spectra is shown in Figure 3.20a and a first order fitted spectra is shown in Figure 3.20b.

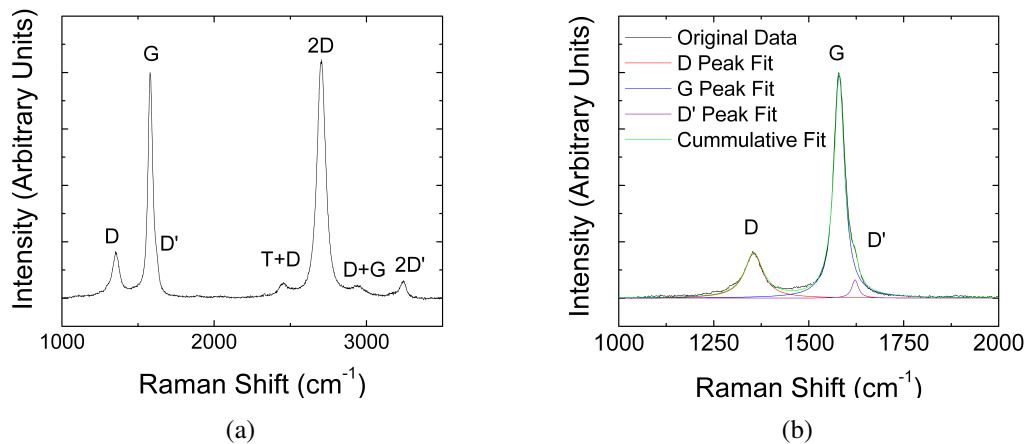


**Figure 3.20:** (a) Full Raman spectrum of as produced CNTs. (a) First order fitted Raman spectra of as produced CNTs. The peak assignments reflect those found in the literature.



Several relationships were used to quantify structural and electronic changes in treated CNTs. Monitoring changes in the peak positions provides insight on charge transfer and doping of the CNTs, while the peak intensities provide information about the amount of polarizability. An empirical relationship was developed by Tuinstra and Koenig that relates the ratio of the D peak intensity to the G peak intensity ( $\frac{I_D}{I_G}$ ) and the average distance between defects ( $L_a$ ), where  $L_a \propto \left(\frac{I_G}{I_D}\right)$ . [81] Similarly,  $\frac{I_{D'}}{I_G}$  can be used to monitor the relative number of edge-plane-like defects. By taking the ratio of  $\frac{I_D}{I_G}$  to  $\frac{I_{D'}}{I_G}$  the correlation of the D peak to the D' peak could be investigated.

The general radial expansion or contraction of hexagonal rings (Figure 3.15a) that defines the D peak, may also be pertinent to the D' peak, but is restricted to vibrations occurring near the edge-plane. In graphite the D peak position and intensity for the armchair configuration of the edge plane is strongly dependent on the D' peak, as shown in Figure 3.21. The zig-zag configuration also shows a dependence of the D peak on the D' peak, yet it is much less pronounced. [20] The dependency between the D and D' peaks could be used to determine if edge-plane-like defects are being created with treatment or if the new defects are not edge-plane. Definitive intensity relationships between the D and D' peaks cannot be formed since the two vibrational modes are distinct with respect to which  $\kappa$  points are involved. [82]

### 3.6.1 Structural Differences in As Produced CNTs

As mentioned in Chapter 2 and illustrated in Section 3.3, the growth conditions for CNTs can have a dramatic effect on the relative number of defects and CNT morphology. Changes in the Raman spectra can therefore be used to determine CNT characteristics. The majority of this work was done with hollow type CNTs grown with a feed gas mixture of ethylene, hydrogen, and argon, but prior work used an acetylene and argon feed gas mixture. Typical fitted Raman spectra for AP CNTs are shown in Figure 3.22 that demonstrate the differences in the Raman spectra based on the carbon source.

A range of defect densities (0.3-0.8) were measured for all AP CNTs as a result from the inability to completely reproduce the growth conditions associated with the CVD process. To illustrate the dependence of the peak positions and widths on the

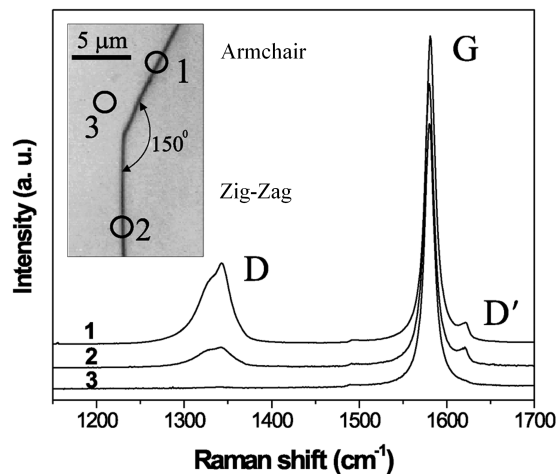


**Figure 3.21:** Diagram illustrating the impact of edge-plane orientation on the D peak and the total defect density. Labels 1 and 2 correspond to the armchair and zig-zag configurations respectively, and label 3 corresponds to the basal plane of graphite. The figure was adapted from Cancando et al.[20]

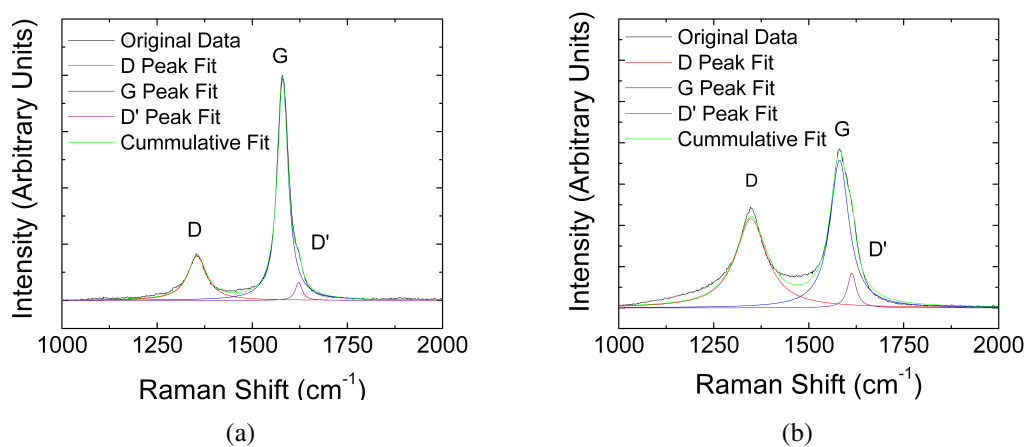


**Figure 3.22:** Raman spectra of first order peaks of AP CNTs growth with (a) ethylene and (b) acetylene carbon sources.

defect density,  $x$  and  $\omega$  were plotted with respect to  $\frac{I_D}{I_G}$ . Several significant similarities and differences exist between the CNTs grown with acetylene and ethylene. Both AP CNTs exhibit similar peak positions for the G, D, and D' peaks of  $\sim 1578 \text{ cm}^{-1}$ ,  $\sim 1347 \text{ cm}^{-1}$ ,  $\sim 1610 \text{ cm}^{-1}$  over their respective ranges of  $\frac{I_D}{I_G}$ .

Significant differences however exist between the peak widths and intensity ratios, shown in Figure 3.23. The CNTs grown with acetylene have total ( $\frac{I_D}{I_G}$ ) and edge-plane-like ( $\frac{I_{D'}}{I_G}$ ) intrinsic defect densities that are  $\sim 75\%$  and  $\sim 140\%$  greater, respectively, as illustrated in Figures 3.23e and 3.23f. Therefore, the use of acetylene as the carbon source results in non-uniform growth and consequently higher intrinsic defect concentrations. The increased peak widths, shown in Figures 3.23c and 3.23d, also indicate non-uniformity in the growth that results in increased bond disorder.

As indicated in Section 3.3, bamboo type CNTs (BCNTs) have periodic edge planes that give BCNTs their unique physical shape, indicating that BCNTs could have relatively large intrinsic defect densities, as illustrated in Figure 3.24a.

For BCNTs, both the D and G peak widths and positions differ significantly from those measured for hollow type CNTs. The larger  $\omega$  is attributed to the larger number of non-energetically uniform intrinsic defects, which was also seen with HCNTs grown with acetylene compared to ethylene, where  $\omega$  for HCNTs grown with acetylene was larger than HCNTs grown with ethylene. The non-uniformity in the energy of intrinsic defects results from the dynamic nature of the BCNT growth mechanism, that ideally would result in a periodic formation of compartments along the CNT axis. However, the compartment spacings are experimentally determined via TEM in Section 2.3 to not be ideally periodic. The lack of periodicity increases the distribution of bond vibrational energies, which corresponds to an increase in  $\omega$ . The up-shifts in the peak positions are also directly related to the greater number of edge-planes in BCNTs. Edge-planes are inherently more energetic than the basal planes due to the occurrence of dangling bonds at the edge-planes and the inclusion of edge-planes in BCNTs increases the probability that phonons will propagate into edge-planes, decreasing the propagation length. Both the increase in bond energies at the edge-plane and smaller propagation lengths, increases the frequency of vibration that is interpreted through an up-shift in the Raman peak position. The D' peak could not be resolved due to large  $\omega_G$ , which caused the G

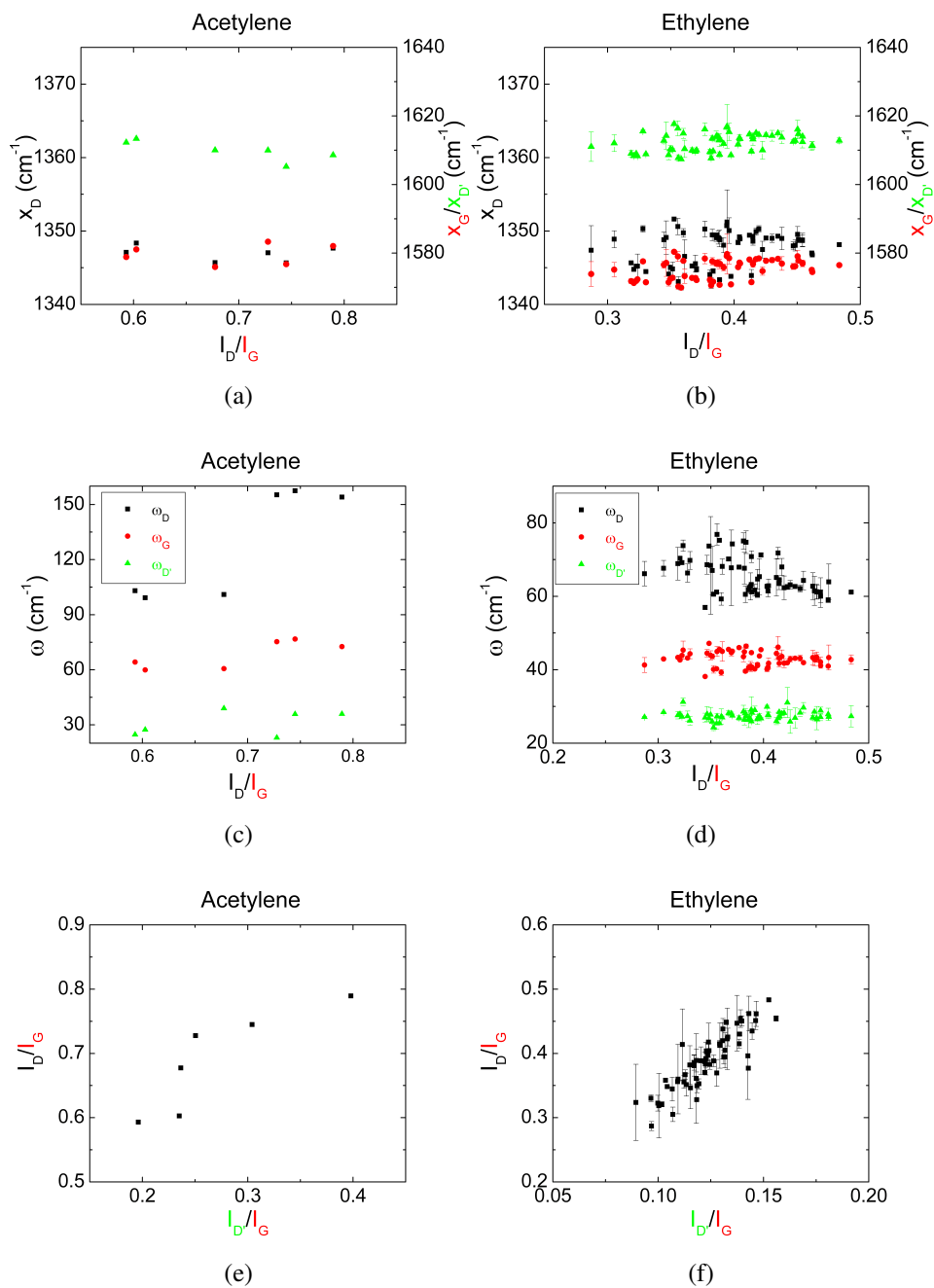


**Figure 3.23:** G (red), D (black), D' (green) peak positions for HCNTs grown with (a) acetylene and (b) ethylene carbon sources. Peak widths with respect to (c) acetylene and (d) ethylene carbon sources. Comparison of edge plane defects to all defects for CNTs growth with (e) acetylene and (f) ethylene carbon sources.

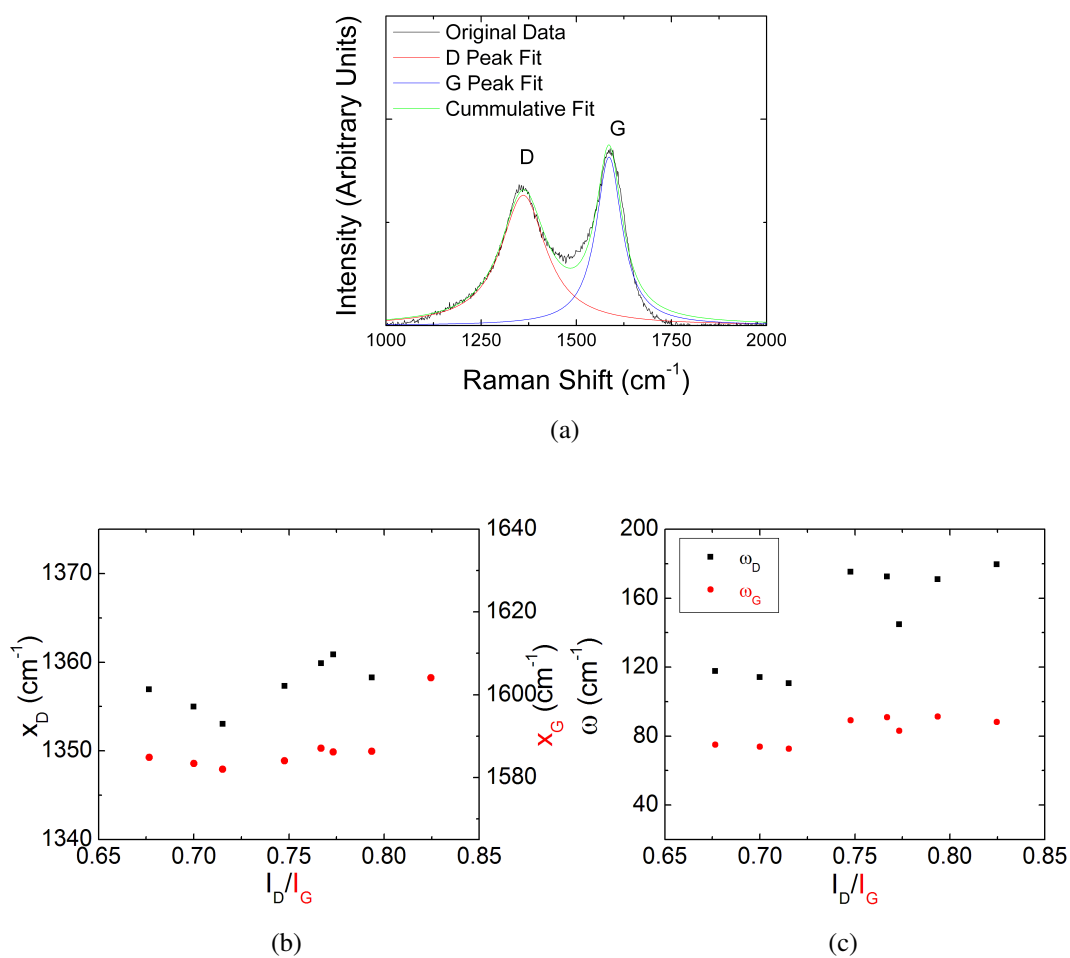


**Figure 3.24:** (a) Fitted Raman spectra of a typical BCNT. The D' peak could not be resolved. (b) G (red) and D (black) peak positions and (c) peak widths for BCNTs growth with an acetylene and ammonia mixture.

peak to mask any indication of the D' peak.

Sections 3.6.2.2 and 4.3.1 will demonstrate that BCNTs may be good electrodes for electrochemical experiments due to a large number of intrinsic defects, but cannot be defectively tailored and will therefore were not the main focus of this work.

## **3.6.2 Generating Defects with Argon Plasma**

### **3.6.2.1 Tailoring Defects in Hollow CNTs**

Argon plasma was initially used to create defects in CNTs since the ionic species in the plasma are limited to  $\text{Ar}^+$  and  $\text{Ar}^+$  has a strong affinity for electrons as indicated by its relatively large first ionization potential of  $\sim 1500$  kJ/mol. The combination of these two factors makes Ar plasma an ideal candidate to create positively charged defects. With Ar irradiation, defects are created by removing electrons from C-C bonds, sputtering carbon atoms in the CNT lattice, or a combination of both. By changing the plasma density and the ion velocity the mechanism involved in defect generation could be explored. As described in Table 3.2, various RIE and ICP powers, pressures, and exposure times were used to explore how induced defects are dependant on the process parameters.

Efforts to increase the plasma density and therefore increase the effectiveness of plasma irradiation were first done by increasing the gas pressure. However, as indicated in Figures 3.25a and 3.25b, the peak positions and widths are independent of pressure for a range of ICP/RIE powers. The ineffectiveness of pressure is hypothesized to result from an increased number of recombination events. At higher pressures a proportionally greater number of gas molecules can be excited. However, the increased number of gas molecules also increases the probability of recombination events, reducing the lifetime of the ionic species and preventing a greater number of ions from being accelerated at the CNTs. Reducing the excitation lifetime therefore hinders implementing changes in the gas pressure to increasing the concentration of induced defects in CNTs.

In contrast to changes in pressure, increases in the ICP power, RIE power, and time increase defect concentration in a predictable way. General changes in the G, D, and D' peak positions and widths can be understood by evaluating how these parameters change with respect the defect density,  $\frac{I_D}{I_G}$ . Changing the defect density can affect all

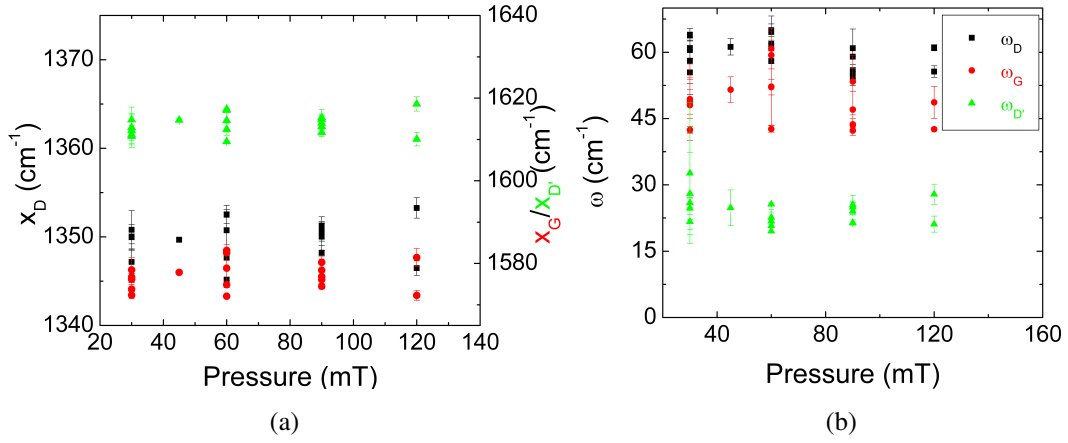


**Figure 3.25:** (a) G (red), D (black), and D' (green) peak positions ( $x$ ) and (b) peak full width half maximum values  $\omega$  for several RIE (50-150 W) and ICP (0-50 W) powers and 60 s exposure time.

vibrational modes since introducing new defects creates new scattering sources. For Ar plasma treated CNTs, a  $\sim 100\%$  increase in  $\frac{I_D}{I_G}$  results in an up-shift in all peak positions and an increase in  $\omega_G$ . The G, D, and D' peak positions increase by  $\sim 15 \text{ cm}^{-1}$ ,  $\sim 10 \text{ cm}^{-1}$ , and  $\sim 10 \text{ cm}^{-1}$ , respectively, and also change in width by  $\sim 20 \text{ cm}^{-1}$ ,  $\sim 8 \text{ cm}^{-1}$ , and  $\sim -10 \text{ cm}^{-1}$ , respectively. These changes in  $x$  and  $\omega$  indicate a non-uniform decrease in long range order. The loss of long range order increases all peak positions, while the non-uniformity of defect introduction increases the distribution of phonon energies associated with the G peak.[16, 74, 75]. The slight increase in  $\omega_D$  indicates that, in general, new defects are energetically non-uniform, contrasting the increased uniformity of edge-plane-like defects.

The linear relationship between  $\frac{I_{D'}}{I_G}$  and  $\frac{I_D}{I_G}$  and y-intercept of  $\sim 0$ , shown in Figure 3.26c, indicate that new defects are most likely the result of  $\text{Ar}^+$  ions creating edge-plane-like defects. When  $\frac{I_{D'}}{I_G} \sim 0$ ,  $\frac{I_D}{I_G}$  is also  $\sim 0$  and no defects exist. Therefore, any increase in  $\frac{I_D}{I_G}$  results from increases in  $\frac{I_{D'}}{I_G}$  and thus defects originating on or near edge planes. The linear relationship between  $\frac{I_{D'}}{I_G}$  and  $\frac{I_D}{I_G}$  indicates that new edge-plane-like defects affect the total defect concentration monotonically. However, the absolute concentration of edge-plane-like defects compared to the total defect concentration cannot

be determined, as previously mentioned in the beginning of Section 3.6, since no definitive relationship between the D and D' peak intensity can be formed.

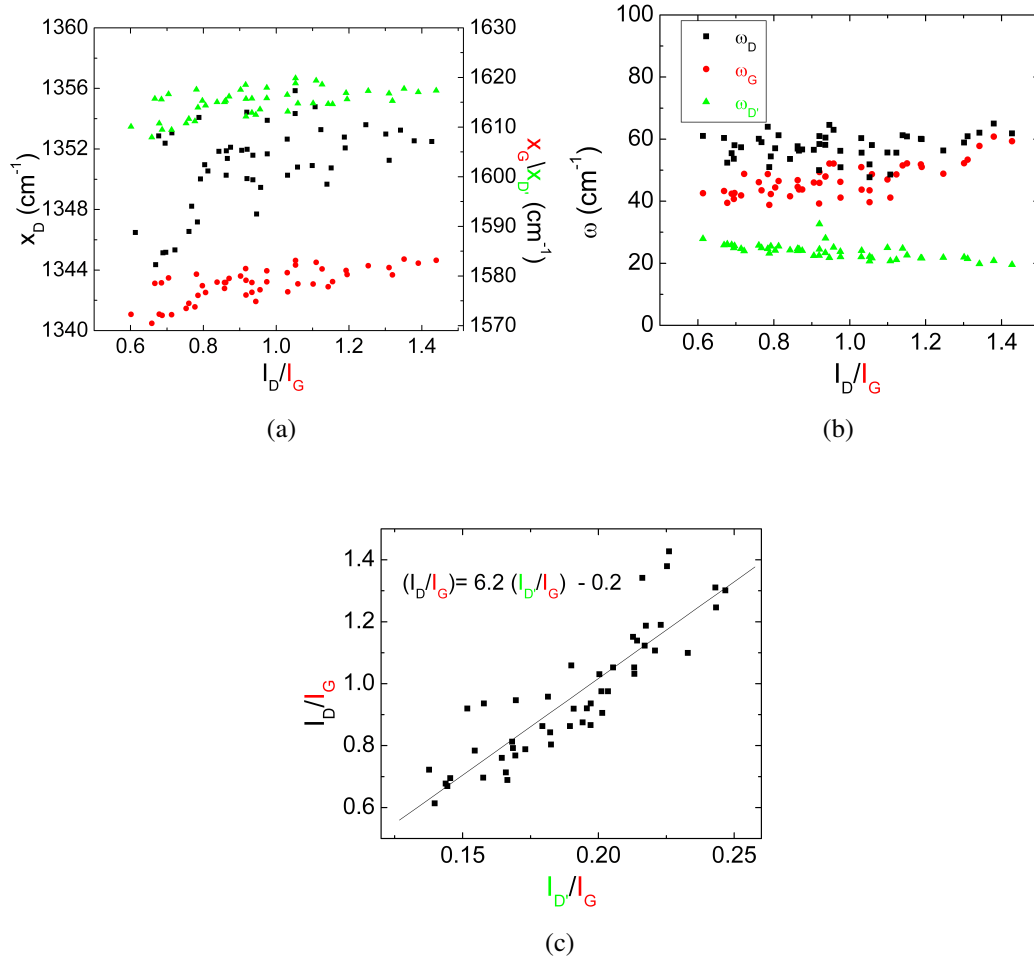


**Figure 3.26:** G (red), D (black), and D' (green) (a) peak positions ( $x$ ), (b) peak full width half maximum values ( $\omega$ ), and (c) relative edge plane density for all RIE and ICP powers, exposure times, and pressures used as a function of defect density.

The sputtering of the CNTs has important implications for both the G and D peak parameters in addition to effects on the D' peak. Defects created through sputtering confine zone center ( $\Gamma$ ) phonons associated with the G peak by changing the phonon propagation length and amount of  $\pi$  bond conjugation.[16, 81, 83] If carbon atoms are removed by sputtering, dangling bonds consisting of unpaired electrons are created.



These unpaired electrons no longer contribute to  $\pi$  conjugation and the bond lengths of surrounding bonds decrease.[84, 85] The reduction in bond lengths causes an upward dispersion of the phonon wave vectors near  $\Gamma$  (Figure 3.9a) to include higher energy phonons, yielding an up-shift in peak positions, as shown in Figures 3.15 and 3.26a. The D and D' peaks are similarly affected by sputtering, as changes in the bond lengths at edge-plane-like defects will change the symmetry of the ring contraction/expansion vibrational modes.

In spite of the general trends seen for the G, D, and D' peak positions shown in Figure 3.26, the creation of edge-plane-like defects has different effects on the peak widths that are unique to increases in either RIE or ICP power. The dependence of the peak widths on RIE or ICP power indicates that although edge-plane-like defects are being generated as a result of increases in both RIE and ICP, differences exist in the uniformity of defect creation that depend on the density of the plasma. Figure 3.27 illustrates the effects of changing the RIE power on the peak parameters. As can be seen in Figure 3.27d, the increase in edge-plane-like density as a function of total defect density is abrupt and an upper limit of  $\sim 1.1$  for  $\frac{I_D}{I_G}$  is obtained. The lack of change in the defect density with increasing RIE power up to 150 W occurred for all times (30-90 s) and ICP (0, 50 W) powers investigated. Therefore it appears that attempting to increase the DC bias, and thus ion velocity, through increases in RIE power as described through Equation (3.5) is not necessarily effective for argon plasmas.

As shown in Figures 3.27b and 3.27c, changes in the D and D' peak positions up-shift by  $\sim 2\text{-}3\text{ cm}^{-1}$  and peak widths contract by  $\sim 4\text{ cm}^{-1}$ , while the G peak position up-shifts by  $\sim 2\text{-}3\text{ cm}^{-1}$  and peak width expands by  $\sim 2\text{-}8\text{ cm}^{-1}$ . The up-shifts in the G, D, and D' peaks indicate bond contractions, while the narrowing of the D and D' peak widths to the same extent results from a greater uniformity between defects. The total defect density also appears to be linearly dependent on the edge-plane-like defect concentration as indicated in Figure 3.27d, where the y-intercept of  $\sim 0$  demonstrates that without edge-plane-like defects no defects would exist. It is therefore believed that Ar plasma irradiation sputters carbon atoms in the CNTs to introduce edge-plane-like defects, causing all peak positions to up-shift as a result of a loss of aromaticity ( $\pi$  conjugation). The reduction of both the D and D' peak widths results from an in-

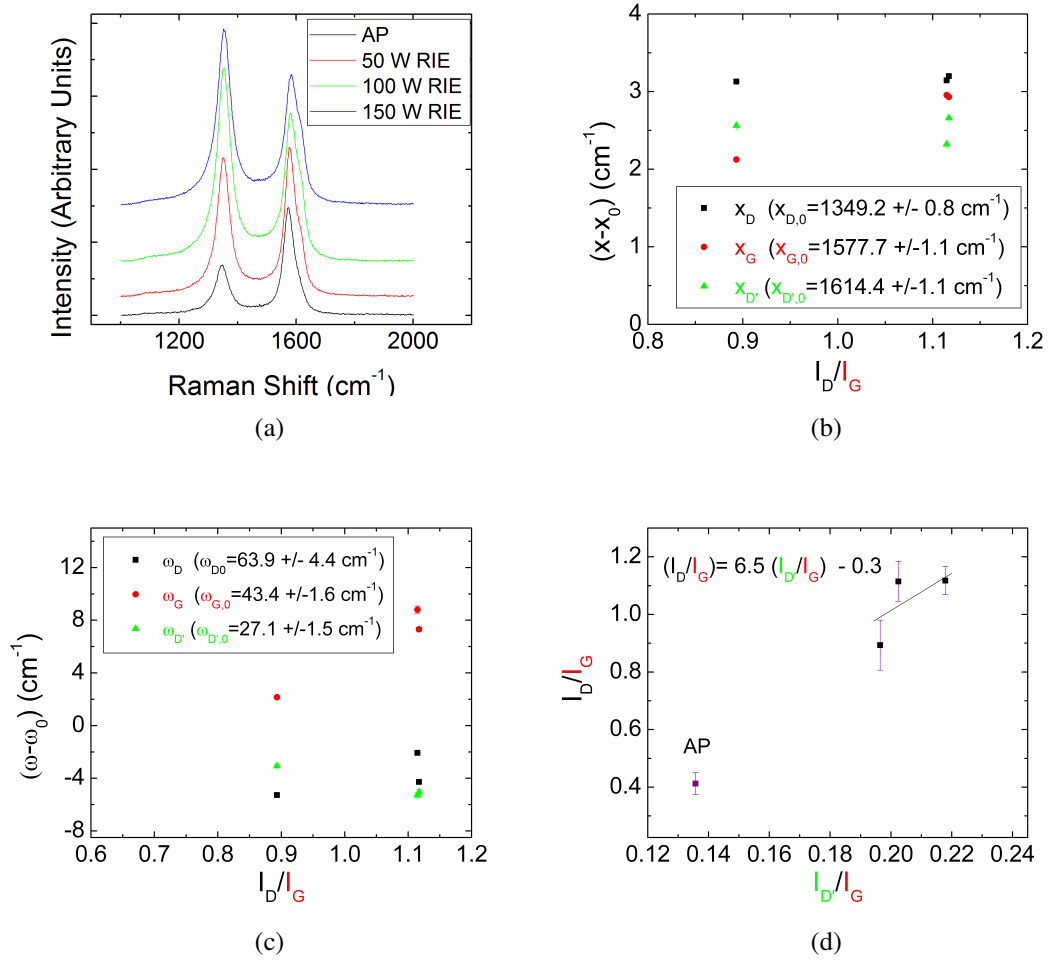


**Figure 3.27:** (a) Typical Raman spectra for CNTs exposed to Ar plasma with differing RIE powers. The RIE power was incrementally increased from 50 to 150 W in 50W intervals. The exposure time for all samples was 60 s, with a pressure of 60 mTorr. (b) Peak position shifts, (c) change in peak shifts for the G (red), D (black), and D' (green) peaks, and (d) intensity ratios for the different RIE powers. The reference value for the various parameters was calculated by taking the average and standard deviation of all AP samples.

creased uniformity of defects since all new defects are believed to be edge-plane-like. Furthermore, the broadening of the G peak indicates that the new defects are randomly introduced into the CNTs, affecting the propagation lengths of the phonons associated with the G peak unequally, as indicated in Figure 3.28.

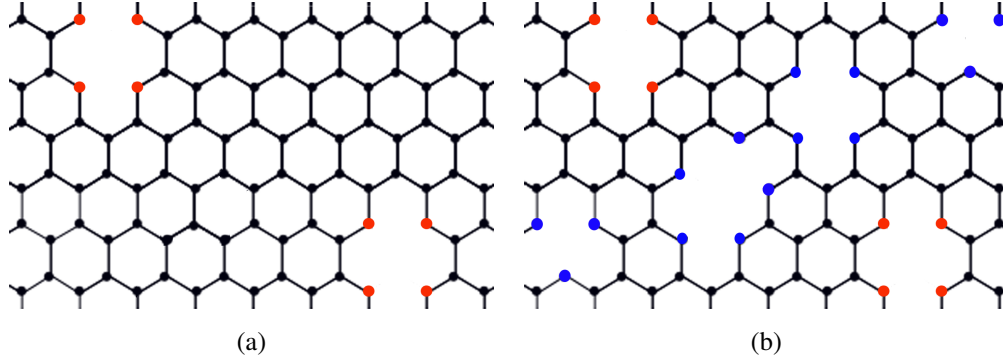


**Figure 3.28:** Illustrative diagram describing the random formation of edge-plane-like defect in CNTs as a result of changing the RIE power, where the red atoms in (a) depict initial defect locations and the blue atoms in (b) illustrate new defect locations as a result of carbon sputtering.

Changes in the peak characteristics resulting from changes in the ICP power are similar to changes in RIE power, yet some distinct features exist that indicate possible differences in the randomness of induced defect locations. As was seen with changing the RIE power, Figure 3.29d illustrates that increases in the total defect density is dependent on the density of edge-plane-like defects as measured through changes in  $\frac{I_D}{I_G}$  and  $\frac{I_{D'}}{I_G}$ , respectively. However, unlike with changes in the RIE power, changing the ICP power results in a gradual increase in  $\frac{I_D}{I_G}$  with increases in  $\frac{I_{D'}}{I_G}$ . Changing ICP power could therefore be a more controllable way to introduce new defects, indicating the importance of plasma density on sputtering effects.

As with changes in RIE power, creating new defects by increasing ICP power also up-shifts all peak positions, indicating that the new defects cause bond contraction. The increase in peak position gradually increases from  $2 \text{ cm}^{-1}$  to  $6 \text{ cm}^{-1}$  with increases in  $\frac{I_D}{I_G}$  from 0.7 to 1.1, which is two times greater than for increases in RIE power for the same range of  $\frac{I_D}{I_G}$ . Furthermore, the G peak width does not change with increasing ICP power indicating that the energy distribution of the G vibrational mode does not change,

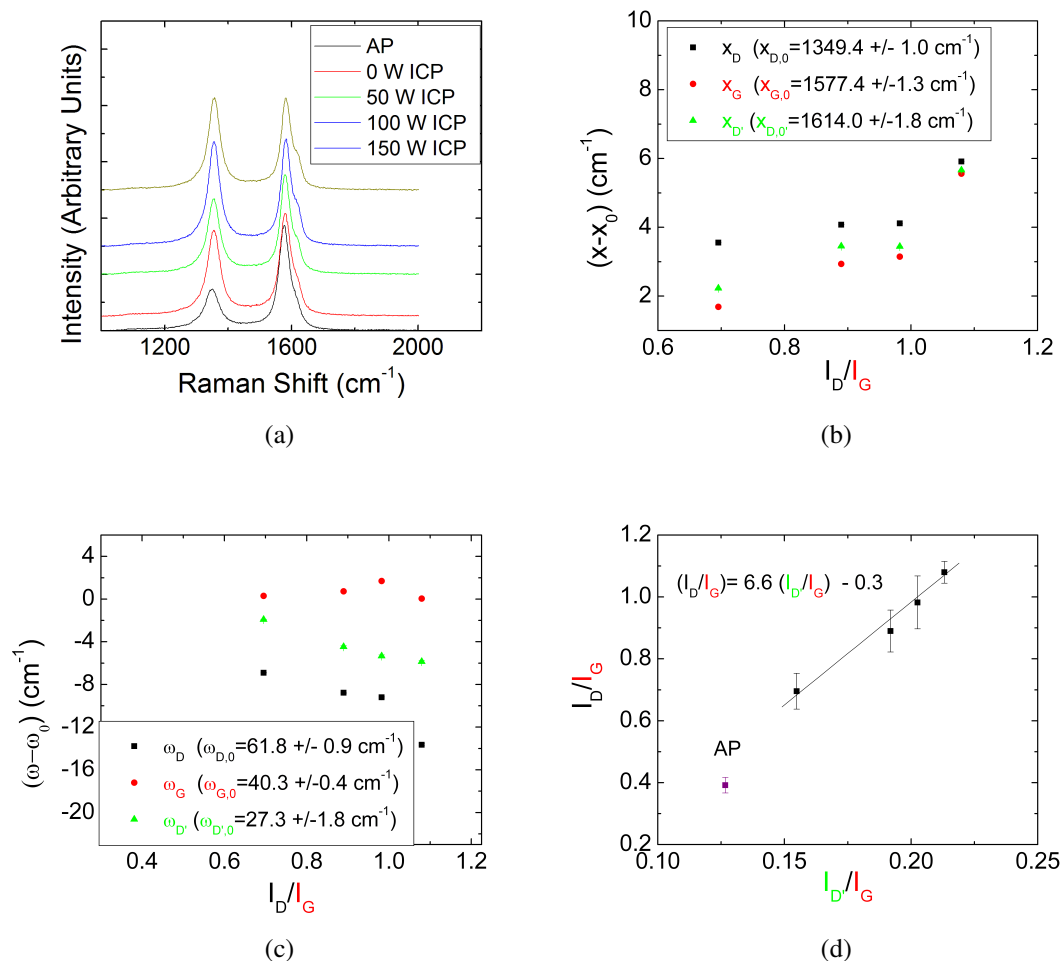


**Figure 3.29:** (a) Typical Raman spectra for CNTs exposed to Ar plasma with differing ICP powers. For all treated samples, the ICP power was incrementally increased from 0 to 150 W in 50W intervals, with a concurrent use of 50 W of RIE power. The exposure time for all samples was 60 s, with a pressure of 60 mTorr. G (red), D(black), and D' (green)(b) peak position shift, (c) change in peak width, and (d) intensity ratios for CNTs exposed to Ar plasma with differing ICP powers. The reference value for the various parameters was calculated by taking the average and standard deviation of all AP samples.

unlike the broadening of the G peak ( $\sim 6 \text{ cm}^{-1}$ ) seen with changes in RIE power. The D and D' peaks narrow by  $\sim 6\text{-}14 \text{ cm}^{-1}$  and  $\sim 2\text{-}6 \text{ cm}^{-1}$ , resulting in a greater uniformity in the energy distribution of induced defects. The narrowing of the D peaks is 233% greater than the peak narrowing with changes in RIE power, yet the D' peak narrowing is approximately the same. The up-shifts in all peak positions and the narrowing of the D and D' peaks, along with the dependence of  $\frac{I_D}{I_G}$  on  $\frac{I_{D'}}{I_G}$  indicates that new defects are energetically uniform edge-plane-like defects that cause contractions in the average bond lengths due to loss of aromaticity, as seen with changes in RIE power.

The larger increase in peak shifts coupled with no broadening of the G peak and a greater contraction of the D peak indicates that increasing the plasma density through increases in ICP power results in a difference in how defects are created in CNTs. Since the narrowing of  $\omega_D$  is 233% greater and the G peak width does not change for changes in ICP power compared to RIE power, it is believed that newly induced defects are more uniformly distributed along the CNT with increases in the plasma density. If energetically similar defects are uniformly distributed along the CNTs, the total energy distribution of defects would decrease with increases in the number of induced defects. The effect that this process would have on the G vibrational mode would also be minimal since the all phonons associated with the G peak would be affected equally. For instance, if induced defects are evenly distributed along the CNTs (Figure 3.30) such that the majority of bonds contract equally, the energy distribution of the G peak vibrational frequencies would not change, yet the average bond vibrational frequency ( $\bar{\omega}$ ) would increase.

Changes in the Raman spectra may also be explained by the addition of  $\text{Ar}^+$  ions. If  $\text{Ar}^+$  ions would be added to the CNTs, the positively charged ions would withdraw electron density away from the CNTs, but remain intercalated in or be on the surface of the CNTs to retain charge neutrality. The removal of electron density would cause an up-shift in the peak positions since the bonds lengths would effectively shorten and changes in the peak widths would change to the degree of defect energy uniformity. To investigate whether argon remained on or was intercalated in the CNTs, EDS was used.

For AP CNTs, only carbon was found with the EDS experiments. After argon plasma exposure, only carbon and oxygen were found. The amount of oxygen compared

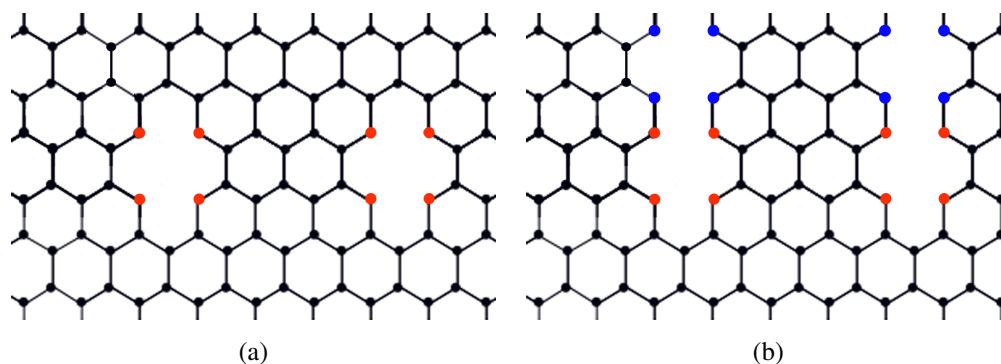


**Figure 3.30:** Illustrative diagram describing non-random edge-plane-like defect formation in CNTs as a result of changing the ICP power, where the red atoms in (a) depict the initial defect locations and the blue atoms in (b) illustrate new defect locations.

to carbon was determined to be  $\sim 0.027 : 1$  and its presence in the defective CNTs most likely arises from the exposure of the new defects in the CNTs to oxygen in air.[86] Given the absence of Ar in the EDS spectra, the changes in the Raman spectra upon Ar plasma exposure are believed to result from physically damaging the CNTs.

### 3.6.2.2 Ineffectiveness of Inducing Defects in Bamboo CNTs

As mentioned previously in Section 3.6.1, BCNTs have high intrinsic defect concentrations. The quantity and type of these defects is important in determining the ability to tune the defect density as was accomplished with HCNTs. A direct comparison of the impact that Ar plasma exposure has on the peak parameters is shown in Figure 3.31.

As can be seen in Figures 3.31b and 3.31c, the G peak is up-shifted and broadens with increasing exposure times similar to what was observed with HCNTs, while the D peak position does not change in any predictable way and the width remains relatively constant. Furthermore, Figure 3.31d illustrates that increasing the exposure time beyond 60 s is relatively ineffective for creating new defects in BCNTs. These two phenomena are believed to result from the high intrinsic defect concentration of BCNTs that prevents the tuning of BCNT defect density to the same extent as HCNTs. A similar trend is also apparent in electrochemical experiments to be described later in Chapter 4, Section 4.3.1.

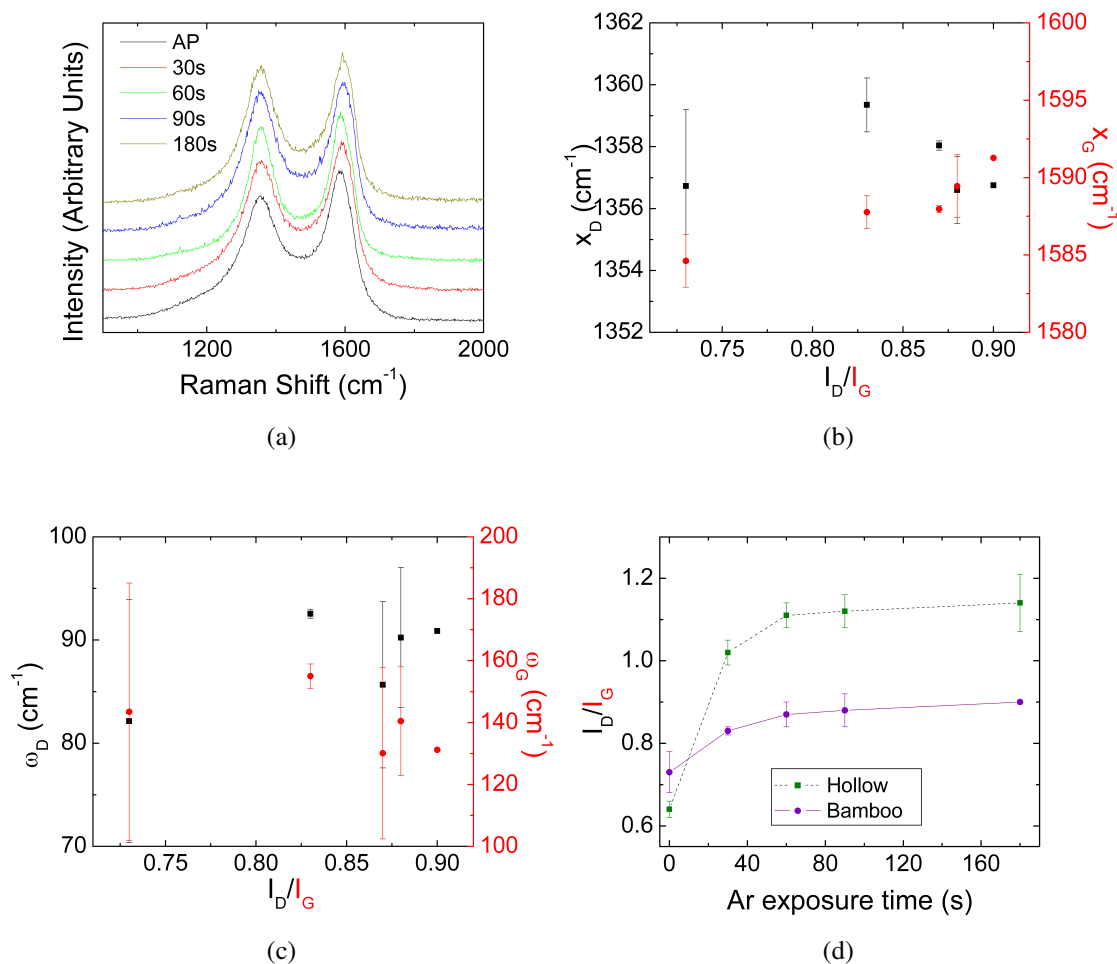


**Figure 3.31:** (a) Typical spectra of BCNTs exposed to Ar plasma as a function of exposure time. The pressure and RIE power used were 30 mTorr and 100 W, respectively. Changes in the D (black) and G (red) peak (b) positions and (c) widths with respect to the defect density. (d) Comparison of the changes in  $I_D/I_G$  with increases in Ar exposure time between HCNTs and BCNTs.

### 3.6.3 Passivating Effects of Hydrogen

To investigate the effects of ion mass on the ability to create defects in HCNTs, hydrogen plasma was used and the results compared to argon plasma exposure. In addition to sputtering, exposure to hydrogen plasma can also result in hydrogenation reactions between the plasma species and the conjugated  $\pi$  bonds.[87] If defect sites are created as a result of ion sputtering, these defects would cause bonds in the CNTs to shorten as a result of a loss in the degree of  $\pi$  bond conjugation, while also forming dangling bonds. The unpaired electrons in dangling bonds are more reactive than bound electrons and are thus more susceptible to undergo reactions with hydrogen. Sputtering as a result of hydrogen plasma exposure and then subsequent reactions between the species in the plasma and dangling bonds, therefore can give rise to changes in the Raman spectra and electrochemical activity of defects not observed with Ar plasma treatments.

#### 3.6.3.1 Hydrogen Plasma Irradiation: Simultaneous Defect Formation and Passivation

Similar to the experiments with argon plasma, the effects of RIE and ICP power were investigated. However, unlike with argon the gas pressure affects the species in the plasma as previously shown in Figure 3.17. To minimize the number of species present, the gas pressure was maintained at 10 mTorr resulting in the dominant presence of  $H_2^+$  ions. Several distinct features arise from reactions between hydrogen and defect sites. As shown in Figure 3.32d,  $\frac{I_D}{I_G}$  increases with increasing  $\frac{I_{D'}}{I_G}$ . The relatively gradual nature of the increase in  $\frac{I_D}{I_G}$  for  $H_2$  treatments compared to Ar plasma treatments for similar RIE powers is most likely results from the difference in mass between the two ions. The less massive hydrogen ions would require much larger velocities than the argon ions to gain enough momentum to displace carbon in the CNTs.

The differences between argon and hydrogen plasma exposure becomes more apparent when investigating the changes in the G, D, and D' peak positions and widths. For hydrogen plasma treated CNTs the G, D, and D' peak positions down-shift by  $\sim 1\text{ cm}^{-1}$ ,  $\sim 1\text{ cm}^{-1}$ , and  $\sim 1\text{-}3\text{ cm}^{-1}$ , respectively, with increasing defect concentration. The down-shift in the peak positions indicates that bonds in the CNTs are becoming longer,



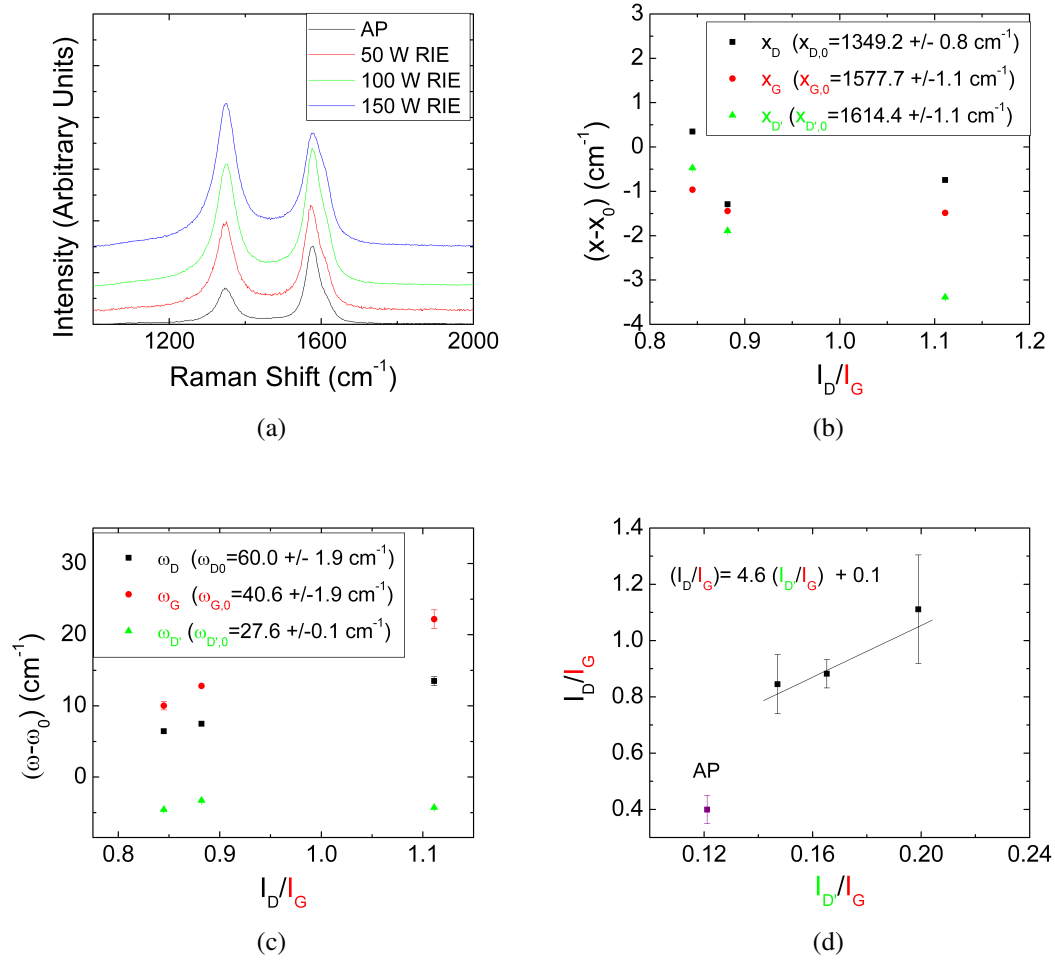


**Figure 3.32:** (b) Typical Raman spectra for CNTs exposed to H<sub>2</sub> plasma with differing RIE powers. The RIE power was incrementally increased from 0 to 150 W in 50W intervals. The exposure time for all samples was 60 s, with a pressure of 10 mTorr. G (red), D (black), and D' (green) (b) peak position shift, (c) change in peak width, and (d) intensity ratios for CNTs exposed to H<sub>2</sub> plasma. The reference value for the various parameters was calculated by taking the average and standard deviation of all AP samples.

opposite of what was observed for argon plasma treatments. The G and D peaks also broaden by  $\sim 10\text{-}20\text{ cm}^{-1}$  and  $\sim 6\text{-}15\text{ cm}^{-1}$ , respectively, indicating a decrease in energy uniformity of the G and D vibrational modes. Conversely, the D' peak narrows by  $\sim 5\text{ cm}^{-1}$  and therefore the phonons associated with the D' peak become more energetically uniform. The parallel between the changes in the G and D peaks, instead of the D and D' peaks, and the increase in  $\frac{I_{D'}}{I_G}$  indicates that the induced defects are distinctly different from the edge-plane-like defects created through Ar plasma exposure.

If edge-plane-like defects are created through sputtering with hydrogen ions, the formation of dangling bonds and subsequent localization of electron density and bond contraction is expected as demonstrated previously with Ar plasma treatments. However, with hydrogen plasma treatments the dangling bonds can react with species in the hydrogen plasma to passivate the dangling bonds. Therefore the up-shift in the peak positions associated with a loss of  $\pi$  bond conjugation can be counteracted by reactions with the dangling bonds. As a result of the reactions with the dangling bonds, the energy of the D' vibrational mode will decrease as indicated through a down-shift in the peak position.

Reactions between hydrogen species in the plasma and the CNT however are not limited to dangling bonds formed through sputtering. The slight decrease in the G and D peak positions and the broadening of the G and D peak widths indicate that both of these vibrational modes become less energetic and less energetically uniform with the introduction of defects. A similar effect was seen between glassy carbon and graphite, where both the G and D peak widths are significantly broader for glassy carbon compared to graphite, yet the peak positions remain essentially unaffected.[16]

If the ICP power is changed for a fixed RIE power of 50 W and exposure time of 60 s similar trends in the G, D, and D' peaks and widths are seen compared to changes in the RIE power, as seen in Figure 3.33. With changes in ICP power, the G and D' peaks down-shift  $\sim 0.5\text{ cm}^{-1}$  and the D peak up-shifts by  $\sim 0.5\text{ cm}^{-1}$ . The lack of definitive change in the D and G peaks for changes in both RIE and ICP power, indicates that hydrogen plasma treatment does not change the vibrational energies of these phonon modes significantly. Furthermore, the G and D peaks broaden by  $\sim 5\text{-}15\text{ cm}^{-1}$  and  $\sim 5\text{-}8\text{ cm}^{-1}$ , respectively, while the D' peak narrows by  $\sim 3\text{-}6\text{ cm}^{-1}$ . The changes in  $\omega$

for all peaks is approximately equal for RIE and ICP treatments, demonstrating the importance of hydrogen based reactions with the CNTs and compared to increases in the plasma density. Since no distinct differences in the peak positions and widths can be made between changes in RIE and ICP power and changes in the D and G peak parallel each other, it is believed that the reactions between hydrogen and the CNTs are the dominant way in which defects are created in the CNTs and bond contraction as a result of sputtering is passivated by these reactions.

### 3.6.3.2 Hydrogen Reactivity in Thermal CVD

To ensure the validity of the passivation of defects in CNTs with hydrogen, CNTs were exposed to hydrogen gas in the CVD reactor at several temperatures. Such a method of hydrogen exposure has the benefit of low kinetic energy, enabling the distinction between reactions between the CNTs and hydrogen and reactions coupled with sputtering induced resulting from plasma processes. In the plasma processes, the kinetic energy of the hydrogen ions are approximately  $10^{-6}$  J as calculated through using the velocity ( $v$ ) in Equation (3.4), whereas in the CVD methods the kinetic energy of the hydrogen atoms are  $\sim 10^{-20}$  J as calculated through  $\frac{3}{2}k_B T$ . To monitor the effects of increasing the temperature, without the presence of hydrogen, several wafers with CNTs were heated to the maximum temperature under investigation in a pure Ar feed gas stream to be used as references to distinguish between the effects of heating in the Ar atmosphere and exposure to hydrogen.

For the reference CNTs and CNTs exposed to hydrogen, slight up-shifts in all peak positions of  $\sim 0.5 \text{ cm}^{-1}$  as well as a broadening of all peaks of  $\sim 1 \text{ cm}^{-1}$  is observed, as illustrated in Figure 3.34. Since the up-shifts in the peak positions are seen for the reference CNTs and those exposed to  $\text{H}_2$ , the changes in the peak position are attributed to the heating of the CNTs in Ar. However, unlike for the CNTs only exposed to Ar gas,  $\frac{I_D}{I_G}$  and  $\frac{I_{D'}}{I_G}$  decrease with increasing temperature for CNTs exposed to  $\text{H}_2$ . The reduction in both  $\frac{I_D}{I_G}$  and  $\frac{I_{D'}}{I_G}$  indicates that hydrogen is reacting with the CNTs to reduce the edge-plane-like defect concentration and subsequently the total defect concentration. This behavior contrasts that of CNTs exposed to  $\text{H}_2$  plasma, where exposure to the plasma increases the number of defects. Therefore it is believed that the energies associated with ions in the plasma are large enough to damage the CNTs to create more defects,

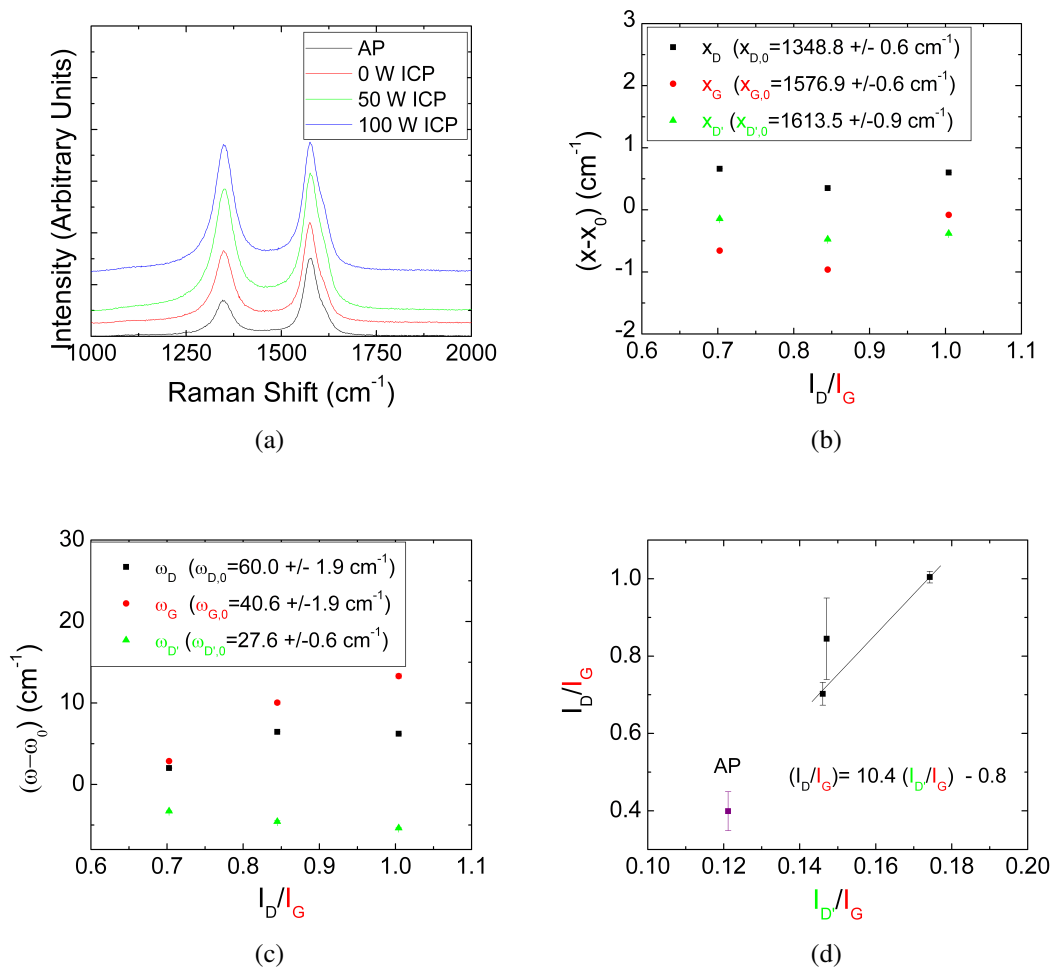


**Figure 3.33:** (a) Typical Raman spectra for CNTs exposed to H<sub>2</sub> plasma with differing RIE powers. The ICP power was incrementally increased from 0 to 100 W in 50W intervals with a RIE power of 50W. The exposure time for all samples was 60 s, with a pressure of 10 mTorr. G (red), D (black), and D' (green) (b) peak position shift, (c) change in peak width, and (d) intensity ratios for CNTs exposed to H<sub>2</sub> plasma. The reference value for the various parameters was calculated by taking the average and standard deviation of all AP samples.

yet the reactivity between hydrogen and the CNTs at the defect sites cause the difference in changes in  $\omega$  observed between CNTs exposed to Ar and H<sub>2</sub> plasmas.

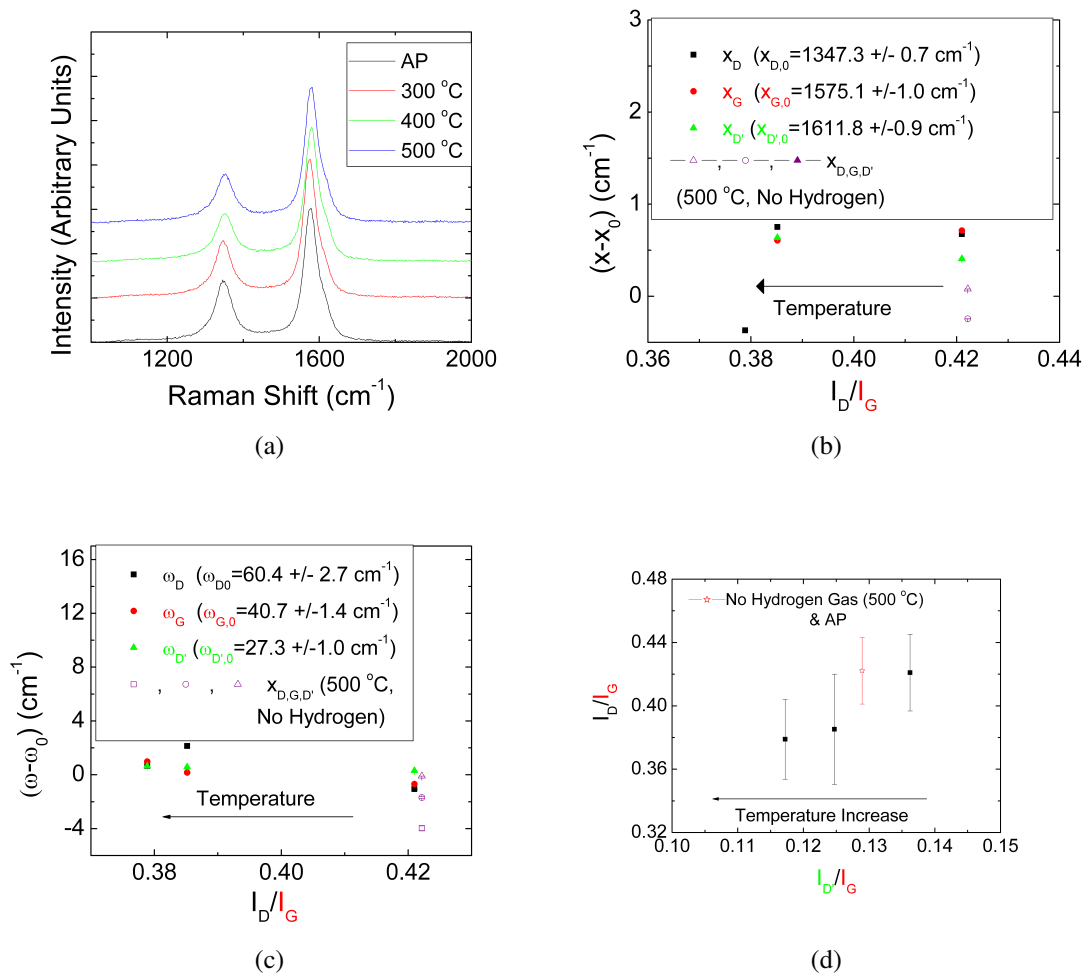


**Figure 3.34:** G (red), D (black), and D' (green) (b) peak position shift, (c) change in peak width, and (d) intensity ratios for CNTs exposed to H<sub>2</sub> plasma. The RIE power was incrementally increased from 0 to 150 W in 50W intervals. The exposure time for all samples was 60 s, with a pressure of 10 mTorr. The reference value for the various parameters was calculated by taking the average and standard deviation of all AP samples.

### 3.6.4 Influence of Chlorine Ion Charge State on Defects

Like hydrogen, chlorine can potentially react with the CNTs, while also sputtering the CNTs. Chlorine plasma chemistry allows for the predominance of either positively or negatively charged ions through control of the reactor pressure and power, as described in Section 3.5.1. The most important operational regimes are the low pressure (10 mTorr), high power (300 W) regime and high pressure (240 mTorr), low power (50 W) regimes, as these represent instances when positively and negatively charged ions are predominantly present, respectively. When  $\text{Cl}^-$  is the most concentrated ion in the plasma interactions between the CNT and  $\text{Cl}^-$  may result in  $\text{Cl}^-$  donating electron density to the CNT, effectively lengthening bonds in the CNT and subsequently causing the peak positions to down-shift. Conversely, when  $\text{Cl}^+$  is the most concentrated ion it may abstract electron density from the CNTs, shortening bond lengths and thus cause an up-shift in the peak positions.

To determine if chlorine reacts for both pressure/power regimes, EDS measurements were performed on the CNTs with a typical spectra shown in Figure 3.35.

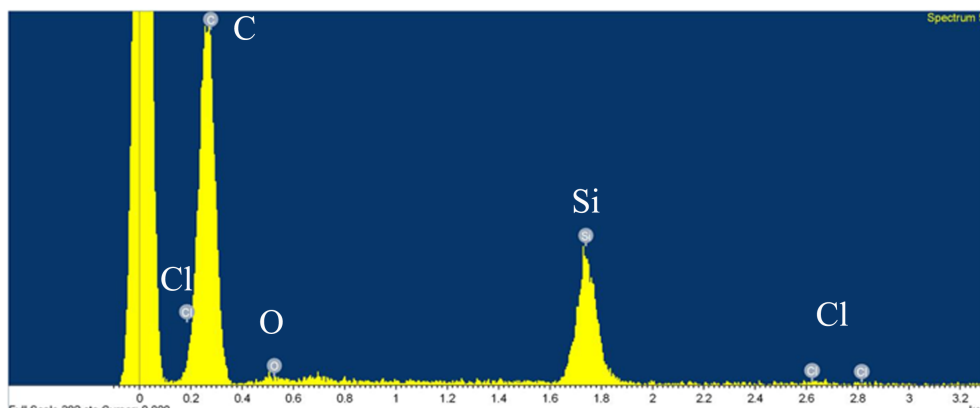


**Figure 3.35:** EDS spectra of CNTs exposed to  $\text{Cl}_2$  for 180 s at 240 mTorr and a RIE power of 50 W.

From Figure 3.35, it appears that chlorine is indeed reacting with the CNTs. However, the relative atomic percent of chlorine with respect to carbon is approximately constant ( $\sim 0.5\%$ ) for all treatments and times investigated. Since the amount of chlorine does change with increasing exposure time, it appears that interactions between the

CNTs and chlorine are limited and independent of changes in the defect density, where changes in defect density will be illustrated in the following paragraphs.

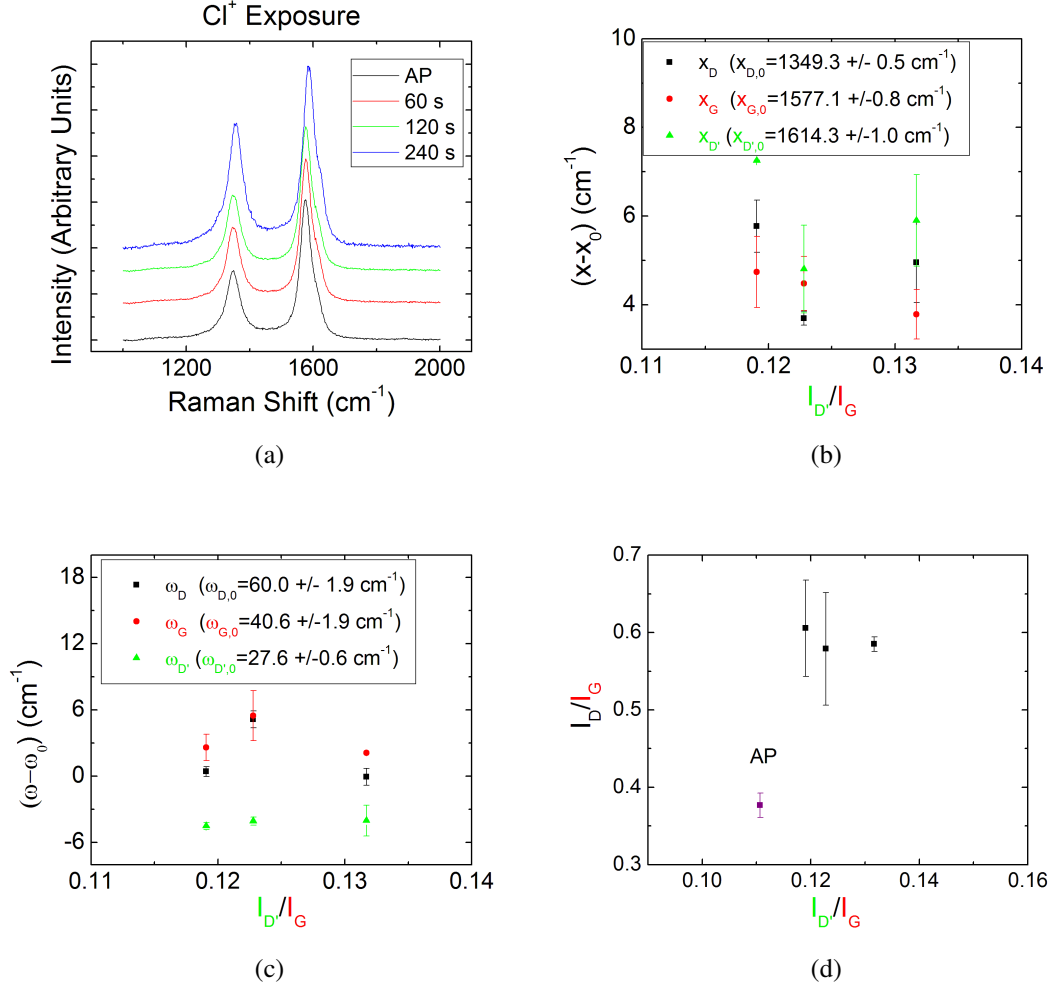


**Figure 3.36:** (a) Typical Raman spectra for a total power of 200 W at a pressure of 10 mTorr. (b) Peak position shift, (c) change in peak width for the G (red), D (black), and D' (green) peaks, and (d) intensity ratios for CNTs exposed to  $\text{Cl}^+$  ions in the plasma. The exposure times were 60, 120, and 240 s.

For the  $\text{Cl}^+$  dominated regime illustrated in Figure 3.36, all peaks up-shift by  $\sim 4\text{-}6 \text{ cm}^{-1}$ , with an increase in  $\frac{I_{D'}}{I_G}$ , to indicating a contraction of bonds resulting from the creation of edge-plane-like defects. However, unlike with  $\text{H}_2$  and Ar plasma, the increase in  $\frac{I_{D'}}{I_G}$  is not accompanied by an increase in  $\frac{I_D}{I_G}$ . Since  $\frac{I_D}{I_G}$  does not change it is

believed that the reactions between  $\text{Cl}^+$  are localized to the edge-plane-like defects and that changes in  $\frac{I_{D'}}{I_G}$  result largely from these reactions, whereas in Ar and  $\text{H}_2$  plasmas the increase in  $\frac{I_{D'}}{I_G}$  results from sputtering of the CNTs. The slight broadening of G and D peaks of  $\sim 0.5 \text{ cm}^{-1}$ , compared to the narrowing of the D' peak of  $\sim 5 \text{ cm}^{-1}$ , further indicates that  $\text{Cl}^+$  reactions are limited to the edge-plane-like defects, since the narrowing of the D' peak indicates that the energy distribution of D' mode vibrations becomes smaller with increasing number of edge-plane-like defects.

For the  $\text{Cl}^-$  dominated regime illustrated in Figure 3.37, a decrease in  $\frac{I_{D'}}{I_G}$  and  $\frac{I_D}{I_G}$  is observed in conjunction with a decrease in  $\omega_{D'}$ . The narrowing of the D' peak width and the reduction  $\frac{I_D}{I_G}$  is believed to result from reactions between  $\text{Cl}^-$  and the CNTs at edge-plane-like defects, where electron density is donated to the CNTs, contrasting the effects observed with  $\text{Cl}^+$  exposure, where electron density may be removed from the CNTs. If electrons are donated to the CNTs from  $\text{Cl}^-$ , bonds in the CNTs would be expected to become less stiff, resulting in a down-shift in the peak positions. However, as illustrated in Figure 3.37b, the peak positions up-shift with  $\text{Cl}^-$ . The up-shift in  $x$  is believed to result from the relative electronegativity difference between chlorine and carbon, since chlorine's electronegativity is 0.61 greater than carbon on the Pauling scale. Therefore, although  $\text{Cl}^-$  may donate electron density to the CNTs, the donation is limited due to the electronegativity difference between the two atoms.

### 3.6.5 n-Doping Through Magnesium Deposition

Plasma treatments that result in the formation of edge-plane-like defects through the atomic removal of carbon in CNTs generally cause up-shifts in the peak positions resulting from a loss in  $\pi$  bond delocalization and subsequent bond contraction. As illustrated with  $\text{Cl}_2$  and  $\text{H}_2$  plasma treatments, changes in the electron density of bonds may also result from chemical reactions between the CNTs and the plasma gases, such as hydrogenation reactions. To create n-type CNTs without removing carbon atoms, electropositive adatoms must be added to the CNTs such that the kinetic energy of the adatoms does not exceed the bond energies in the CNTs. Low kinetic energy processes can be accomplished by exposing the CNTs to heated gases as explained in Section 3.6.3.2 or dissolving the CNTs in liquefied metals. As explained in Section 3.5.2, such addition is ideally performed through Group I metal intercalated into the graphitic lat-



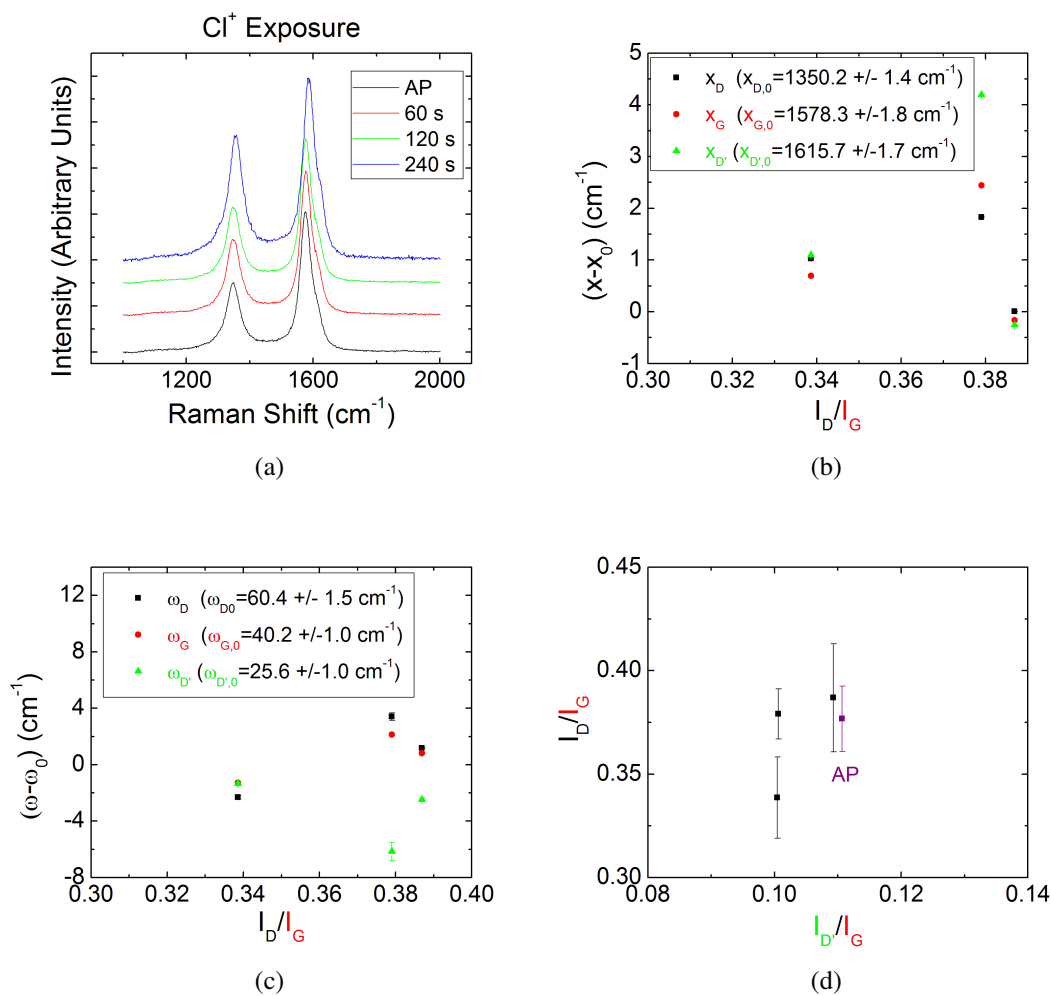


**Figure 3.37:** (a) Typical Raman spectra for a total power of 50 W at a pressure of 240 mTorr. (b) Peak position shift, (c) change in peak width for the G (red), D (black), and D' (green) peaks, and (d) intensity ratios for CNTs exposed to  $\text{Cl}^-$  ions in the plasma. The exposure times were 60, 120, and 240 s.

tice. Unfortunately, these metals are moisture sensitive.

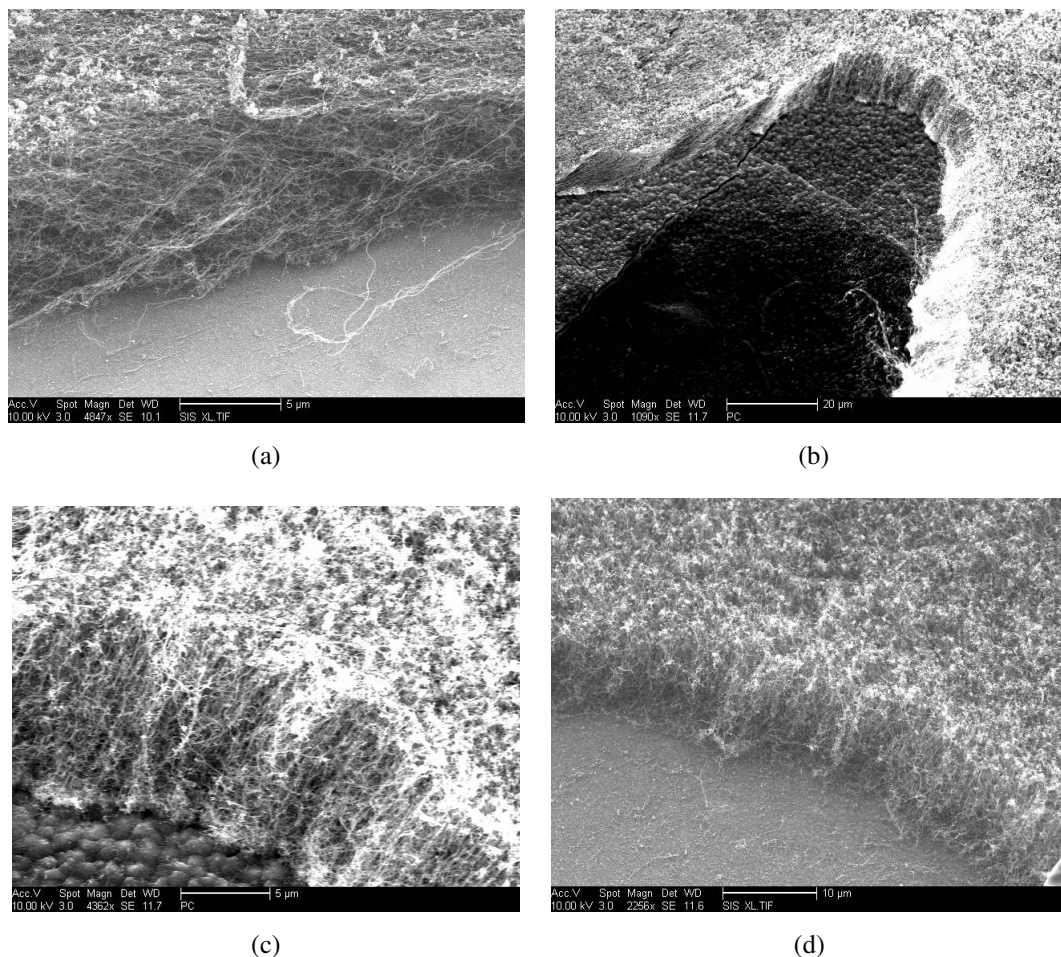


**Figure 3.38:** SEM images of a wafer (a) prior and (b) post Mg deposition. Image (c) is a higher magnification image illustrating the presence of deposited Mg metal on the CNTs and Si wafer. (d) illustrates the successful removal of excess Mg from the Si wafer.

Magnesium was instead evaporated onto the CNTs in the CVD reactor. Figure 3.38 shows SEM images of the CNT wafers before and after Mg deposition. To remove excess metal, the wafer was dipped into 5 mM  $\text{HCl}_{aq}$  for 90 min, dissolving excess Mg. The CNTs were then subsequently washed several times with DI water. Figure 3.38d shows the results of removing excess Mg after the wafer was rinsed and critical point dried (CPD) with  $\text{CO}_2$ . As can be seen in the figure, no excess metal appears to coat the wafer surface. Acid washing however adds complexity to the process since reactions between  $\text{H}^+$  and functional groups present on the CNTs or other impurities

may be misinterpreted as originating from Mg deposition. To explore the effects of exposing the CNTs to HCl, CNTs that did not have Mg deposited on them were used as standards and subjected to the same experimental procedures as the Mg coated CNTs.

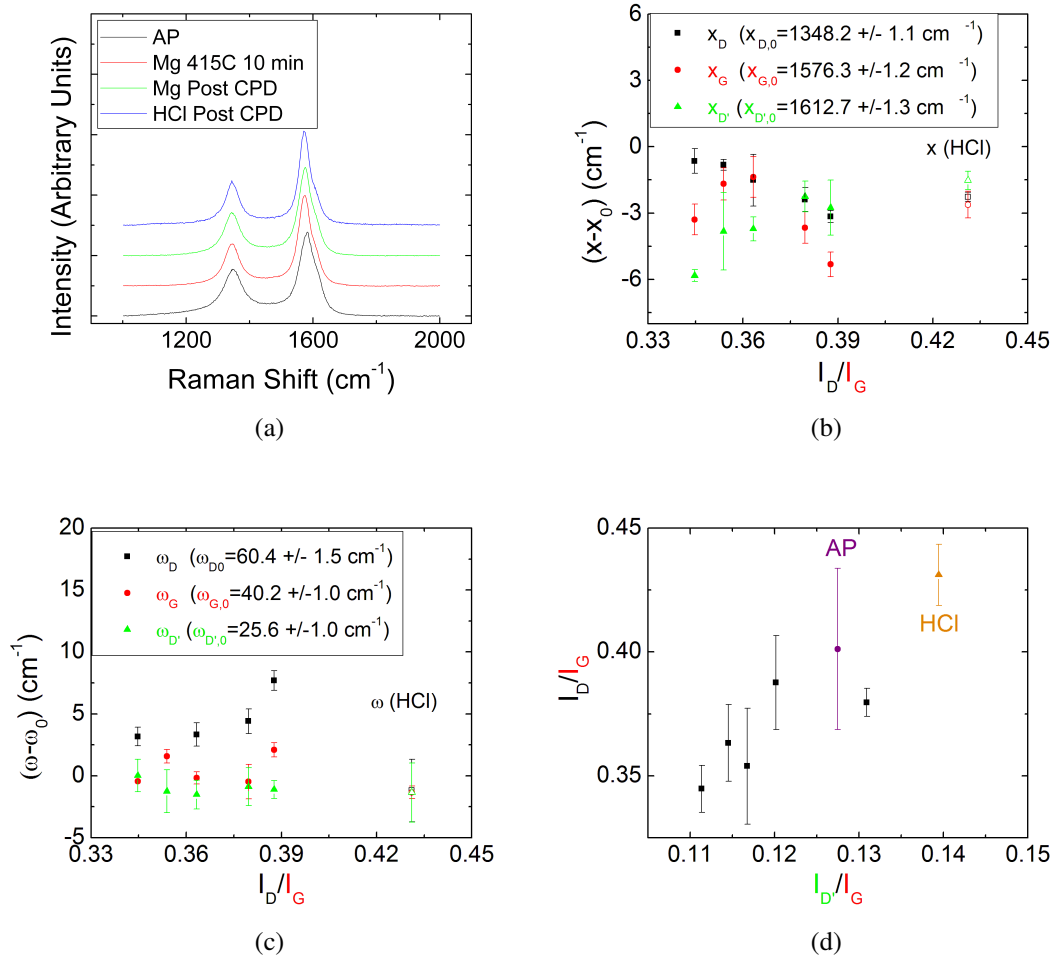


**Figure 3.39:** (a) Typical Raman spectra of CNTs treated with Mg, Mg + HCl + CPD, and HCl + CPD. (b) Peak position shift, (c) change in peak width for the G (red), D (black), and D' (green) peaks, and (d) intensity ratios for CNTs exposed to Mg vapor at different temperatures and total pressures. The error bars indicated the standard deviation between different trials.

As can be seen from Figure 3.39d exposure to HCl increases the edge-plane-like defect density as well as down-shifts all peak positions by  $\sim 2 \text{ cm}^{-1}$ . Since no

known reactions between HCl and CNTs exist, the increase in edge-plane defect density is attributed to reactions between HCl and exposed Fe catalyst. The dissolution of Fe could expose edge-planes and thus increase the defect density of the CNTs.

With Mg exposure, all peak positions down-shift and the number of total and edge-plane-like defects is reduced as indicated through the reduction of  $\frac{I_{D'}}{I_G}$  from  $\sim 0.128$  to  $\sim 0.115$ . The down-shift of the peak positions is indicative of electron donation to the CNTs by Mg, where electron poor or strained carbon bonds react with such that Mg may donate electrons and relieve local strain or stabilize electron poor regions. A similar phenomenon was observed by Choi et al., where dissolved metals were reduced at defective sites, indicating a higher reactivity of defect sites relative to non-defective sites.[7] Furthermore, since the D' peak narrows by  $\sim 2 \text{ cm}^{-1}$ , while the D peak broadens by  $\sim 4 \text{ cm}^{-1}$ , it appears that Mg is not preferentially reacting at edge-plane-like defects, since the energy distribution of D' vibrational modes decreases while other defects encompassed by the D vibrational modes increases.

### 3.7 Summary of Treatment Effects on Raman Spectroscopy

A large variety of processing parameters have been evaluated to create defects in CNTs with differing effects. Initially, argon plasma was used to create p-type CNTs as this gas has the least complicated plasma chemistry of the gases used. The results from these tests illustrate that utilizing different process variables such as changes in RIE or ICP power to change the plasma density effect the distribution of defects along the CNTs. Up-shifts in the peak positions and broadening of the G peak, in conjunction with the increase in the edge-plane-like defect density, most likely result from a loss in  $\pi$  bond conjugation that leads to bond contractions.

When hydrogen is used in plasma processes, dangling bonds that result from sputtering the CNTs can react with the hydrogen, passivating them. Changes in the D and G peak positions are thus minimal, yet the distribution of energy associated with the D and G vibrational modes increases as a result of hydrogen reactivity with the CNTs. To confirm the reactivity between hydrogen and CNTs, hydrogen was used in molecular form in the CVD processes. Molecular hydrogen treatment in the CVD reactor reduced the defect density, indicating that hydrogen reacts at defects in CNTs.

Chlorine plasma treatments were then explored to evaluate the effects of ion

charge state, where low power/high pressure favors the formation of negatively charged ions and high power/low pressure favors the formation of positively charged ions. Negatively charged ions are however difficult to manipulate with the current experimental setup, since during the plasma processes a negative bias forms on the electrode where the CNTs are placed and thus positively charged ions are accelerated at the electrode. Nevertheless, it appears as if new defects are generated through reactions with the CNTs for  $\text{Cl}^-$  and  $\text{Cl}^+$  ions, as realized through changes in both  $\frac{I_{D'}}{I_G}$  and  $\frac{I_D}{I_G}$ .

Finally Mg, was hypothesized to n-dope the CNTs. Exposure to Mg resulted in the down-shifts of all peak positions as well as the reduction of  $\frac{I_{D'}}{I_G}$  and  $\frac{I_D}{I_G}$ , indicating that Mg reacted at defects and donated electrons to the CNTs. However, more sophisticated experimental designs are needed to better determine the dependencies on deposited Mg concentration.

Chapter 3, in part, is a reprint of the material as it appears in “Defect engineering of the electrochemical characteristics of carbon nanotube varieties”, in Journal of Applied Physics, v.108, n.3, pp.034308, 2010, Hoefler, M. A.; Bandaru, P. R. The dissertation author was the primary investigator and author of this paper.

## 4 Electrochemistry

### 4.1 Background

Three complementary electrochemical techniques were used in this work: (1) Cyclic voltammetry (CV), (2) electrochemical impedance spectroscopy (EIS), and (3) cyclic constant current chronopotentiometry or galvanostatic charging and discharging (GALV). Cyclic voltammetry was used to study diffusion and electron transfer kinetics at the CNT electrode, where the current response to an applied DC voltage is measured. Electrochemical impedance spectroscopy utilizes small scale AC perturbations to equilibrium to separate different physical processes involved in charge transfer. By comparing CV and EIS, a comprehensive study of the diffusion and kinetic based processes in charge transfer can be obtained. Galvanostatic charging was to monitor how CNT capacitor devices perform in a practical application. With these three methods, it will be shown that defects are the reactive sites for charge transfer and that shifts in the peak positions of the Raman spectra correspond to changes in the diffusion and charge transfer processes. This chapter therefore provides a methodology to demonstrate the improvements in electrochemical performance of defective CNTs, which translate into improved electrochemical capacitor performance.

#### 4.1.1 Fundamentals of Cyclic Voltammetry

Cyclic voltammetry involves investigating the effects of perturbing the system away from equilibrium by applying a triangular waveform potential between two electrodes, as shown in Figure 4.1a. The rate of change of voltage versus time is called the scan rate ( $\nu$ ). When applying the potential, the current response of the system is measured with respect to the potential as illustrated in Figure 4.1b for a one electron transfer process. In Figure 4.1,  $E_\lambda$  is the switching voltage at time  $t_\lambda$ ,  $i_{p,a}$  and  $i_{p,c}$  are the anodic and cathodic currents, respectively,  $n$  is the number of electrons transferred, and  $E^{0'}$  is the formal reduction potential of the oxidized species O being reduced to the reduced species R:



The shape of the curves plotted in Figure 4.1b results from competing diffusion and kinetic processes. If at time  $t_0$  and potential  $E_0$  (point A), O is the abundant species

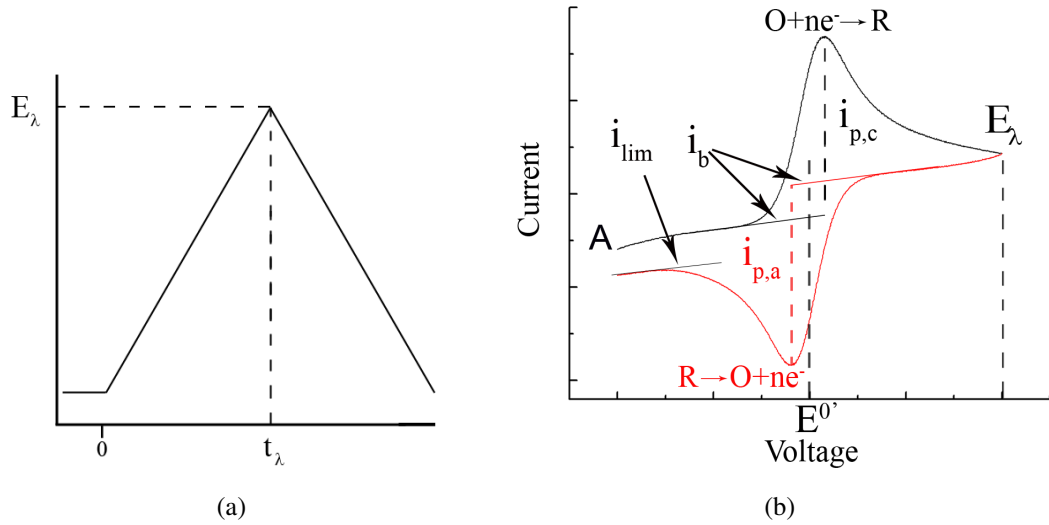


**Figure 4.1:** (a) CV triangular waveform. (b) Current response to triangular waveform for a one  $e^-$  transfer.  $i_b$  and  $i_{lim}$  are the baseline and limiting currents, respectively.

and the potential is decreased until  $E_\lambda'$ , at some potential close to  $E^{0'}$  the reduction of O to R will begin to occur. As the potential decreases further past  $E^{0'}$ , O begins to reduce more rapidly and a diffusion layer builds at the surface of the working electrode. Once the diffusion layer becomes sufficiently thick such that the diffusion of O to the working electrode is equal to the diffusion of R away from the electrode, a peak current is reached at a potential  $E_p$ . The difference between  $E_p$  and  $E^{0'}$  is known as the overpotential and is proportional to the resistance of the system, which will be explained later. Past  $E_p$ , the diffusion of R away from the working electrode is sufficiently large to impede diffusion of O to the electrode, which depletes at the electrode surface. As a result of the differing diffusion rates between O and R, the current begins to decay to the limiting current  $i_{lim}$ . The current decay is defined through the Cottrell equation:

$$i = \frac{nFAC_j D_j}{\delta} \quad (4.2)$$

where  $n$  is the number of electrons transferred,  $F$  is Faraday's constant,  $A$  is the electrode surface area,  $C_j$  is the bulk concentration of species  $j$ ,  $D_j$  is the diffusion coefficient of species  $j$ , and  $\delta$  is the diffusion layer thickness. The limiting current will be explicitly defined in Equation (4.12), but represents the point at which no faradaic reactions occur

at the electrode surface.

In many CV experiments  $E_\lambda$  is reached prior to reaching  $i_{lim}$ , thus once  $E_\lambda$  is reached R begins to diffuse to the electrode. Close to  $E^{0'}$ , R begins to oxidize to O until a peak current is attained. As before, the current again decays until the limiting current is achieved or the potential is increased to  $E_\lambda$ .

The peak current ratio ( $|i_{p,c}/i_{p,a}|$ ) and peak separation ( $\Delta E_p$ ) in the voltammogram can be used to determine the reversibility of the oxidation-reduction reaction. To understand how  $|i_{p,c}/i_{p,a}|$  and  $\Delta E_p$  are determined by the reversibility of electron transfer the flux equations must be solved. For electrodes exhibiting reversible electron transfer, semi-infinite linear diffusion boundary conditions are applied, where the time scale of the experiment is shorter than the time needed to obtain steady state. Furthermore, charge transfer kinetics are assumed to be fast, such that the reverse reaction does not affect charge transfer kinetics, and charge transfer follows Nerstian behavior such that the instantaneous voltage (E) always obeys[22].

$$E = E^{0'} + \frac{RT}{nF} \ln \frac{C_O(0,t)}{C_R(0,t)} \quad (4.3a)$$

$$E = E_i - \nu t \quad (4.3b)$$

where R is the universal gas constant, T is temperature,  $C_{O/R}(0,t)$  is the concentration of O/R at the electrode surface, and  $E_i$  is the initial voltage. The other useful boundary conditions are defined by[22]:

$$\frac{\partial C_O(x,t)}{\partial t} = D_O \frac{\partial^2 C_O(x,t)}{\partial x^2} \quad (4.4a)$$

$$\frac{\partial C_R(x,t)}{\partial t} = D_R \frac{\partial^2 C_R(x,t)}{\partial x^2} \quad (4.4b)$$

$$C_O(x,0) = C_O^* \quad (4.4c)$$

$$C_R(x,0) = 0 \quad (4.4d)$$

$$\lim_{x \rightarrow \infty} C_O(x,t) = C_O^* \quad (4.4e)$$

$$\lim_{x \rightarrow \infty} C_R(x,t) = 0 \quad (4.4f)$$



where  $D_O$  and  $D_R$  are the diffusion coefficients of O and R, respectively, and  $C_O^*$  is the bulk concentration of O. The flux balance can be written as[22]:

$$D_O \left( \frac{\partial C_O(x,t)}{\partial t} \right)_{x=0} + D_R \left( \frac{\partial C_R(x,t)}{\partial t} \right)_{x=0} = 0 \quad (4.5)$$

Utilizing the boundary conditions and the flux relationship, it can be shown through the use of Laplace transforms that the current at any point in the CV curve is defined by[22, 88]:

$$i = nFAC_O^* \sqrt{\pi D_O \sigma} \chi(\sigma t) \quad (4.6a)$$

$$\sigma t = \left( \frac{nF}{RT} \right) \left( E - E^{0'} - \frac{RT}{nF} \ln \sqrt{\frac{D_R}{D_O}} \right) \quad (4.6b)$$

where R is the universal gas constant, T is temperature, E is the instantaneous voltage, and  $\sigma t$  is a dimensionless parameter needed to solve the Laplace transform. The function  $\chi(\sigma t)$  must be solved numerically and when a maximum current is obtained, Equation (4.6a) can be rewritten for reversible electron transfer as:

$$i_p = 0.4463 \sqrt{\frac{F^3}{RT}} n^{3/2} A D_O^{1/2} C_O^* v^{1/2} \quad (4.7a)$$

$$i_p = (2.69 \times 10^5) n^{3/2} A D_O^{1/2} C_O^* v^{1/2} \text{ at } 25^\circ \text{C} \quad (4.7b)$$

which is the Randles-Sevcik equation.[89] The potential for which the current reaches a peak value is defined as follows:

$$E_p = E^{0'} + \frac{RT}{nF} \ln \sqrt{\left( \frac{D_R}{D_O} \right)^\gamma} - \gamma 1.109 \frac{RT}{nF} \quad (4.8)$$

where  $\gamma$  is +1 for the anodic sweep and -1 for the cathodic sweep. Using Equation (4.8) and assuming the  $D_O = D_R$ , the peak separation can be defined as follows:

$$\Delta E_p = E_{p.c} - E_{p.a} \quad (4.9a)$$

$$\Delta E_p = \frac{2.3RT}{nF} \quad (4.9b)$$

$$\Delta E_p \approx \frac{59}{n} \text{ mV at } 25^\circ \text{C} \quad (4.9c)$$

From  $\Delta E_p$  the standard rate constant ( $k^\circ$ ) can be determined. The relationship between  $\Delta E_p$  and  $k^\circ$  is derived from the special case when equilibrium is achieved and  $C_O^* = C_R^*$ . In this instance, the forward and reverse reactions of Equation (4.1) occur at equal rates and  $k_f = k_r$ . The forward and reverse rate constants can be defined through:

$$k_f = k^\circ \exp\left[-\alpha \frac{F}{RT}(E - E^{0'})\right] \quad (4.10a)$$

$$k_r = k^\circ \exp\left[(1 - \alpha) \frac{F}{RT}(E - E^{0'})\right] \quad (4.10b)$$

and the current can be defined through:

$$i = nFA[k_f C_O(0, t) - k_r C_R(0, t)] \quad (4.11)$$

Substituting Equation (4.10) into Equation (4.11) the current can be defined through:

$$i = F A k^\circ \left[ C_O(0, t) e^{\frac{-\alpha F}{RT}(E - E^{0'})} - C_R(0, t) e^{\frac{(1-\alpha)F}{RT}(E - E^{0'})} \right] \quad (4.12)$$

where  $i = i_{lim}$  when  $|E - E_p| \gg 1$ . By rearranging Equation (4.12)  $k^\circ$  can be defined through [90, 91]:

$$k^\circ = 2.18 \left( \frac{D\beta F v}{RT} \right)^{1/2} \exp\left[-\frac{\beta^2 n F}{RT}(E_{p,a} - E_{p,c})\right] \quad (4.13)$$

where  $\beta$  is the complementary to the charge transfer coefficient ( $\alpha$ ). The charge transfer coefficient is a measure of the symmetry of the energy barrier upon reaction and  $\alpha$  of 0.5 can be approximated for most systems. [22]

Reversible electron transfer is therefore defined by three important relationships: (1)  $i_p$  is proportional to  $C$  and  $\sqrt{v}$ , (2)  $|\frac{i_{p,a}}{i_{p,c}}| \approx 1$ , and (3)  $n\Delta E_p$  is not a function of scan rate or concentration. [22]

For irreversible systems, the equations governing electron transfer can also be derived, yet the boundary conditions are different than those of reversible systems. Irreversibility can arise from several factors, including adsorption of the redox couple onto the electrode or coupled homogeneous reactions, which prevent the reverse reaction from occurring. An example of CV illustrating an adsorption process, in which currents diminish with successive voltage sweeps is shown in Figure 4.2.

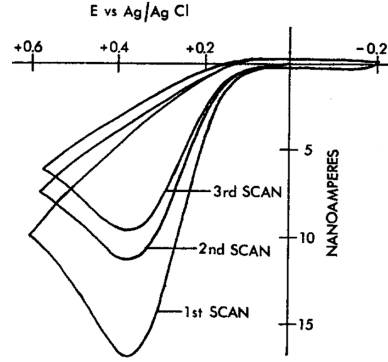


**Figure 4.2:** CV illustrating irreversible electron transfer and adsorption of the redox couple during the anodic sweep, adapted from Kissinger et al.[21, 22]

For an irreversible one-step, one-electron transfer reaction, the reaction is defined through:



where no reverse reaction is possible. The nerstian boundary condition given by Equation (4.3) is therefore replaced by[22]:

$$i = FAD_O \left[ \frac{\partial C_O(x,t)}{\partial x} \right]_{x=0} = k_f(t)C_O(0,t) \quad (4.15a)$$

$$\text{where} \quad (4.15b)$$

$$k_f(t) = k^\circ \exp \left[ \frac{-\alpha F}{RT} (E_i - E^{0'}) \right] e^{\frac{F}{RT} \alpha \nu t} \quad (4.15c)$$

Using the Laplace transform and a numerical solution to the partial differential flux equation  $i_p$  and  $E_p$  for irreversible systems can be defined through[22, 88]:

$$i_p = (2.99 \times 10^5) \alpha^{1/2} A C_O^* D_O^{1/2} \nu^{1/2} \quad (4.16a)$$

$$E_p = E^{0'} - \frac{RT}{nF} \left[ 0.780 + \ln \frac{D_O^{1/2}}{k^\circ} + \ln \sqrt{\frac{\alpha F \nu}{RT}} \right] \quad (4.16b)$$

As can be seen from Equations (4.16a) and (4.16b),  $i_p$  is once again proportional to  $C_O^*$  and  $\sqrt{\nu}$ . However,  $E_p$  is now dependent on  $\nu$  unlike in reversible systems, where the peak position is independent of scan rate.

For quasi-reversible systems, electron transfer kinetics of the forward(reverse) reaction are not sufficiently facile and the reverse(forward) reaction must be taken into account. For a one-step, one-electron transfer the reaction can be defined through:



and the following boundary condition is applied to the flux equation[22, 23]:

$$D_O \left[ \frac{\partial C_O(x,t)}{\partial x} \right]_{x=0} = k^\circ e^{\frac{-\alpha F}{RT}(E-E^{0'})} \left( C_O(0,t) - C_R(0,t) e^{\frac{F}{RT}(E-E^{0'})} \right) \quad (4.18)$$

Just as with reversible and irreversible electron transfer systems, the flux equation must be solved numerically and the resulting equations for  $i$  and  $E_p$  are defined through[22, 23]:

$$i = FA \sqrt{\frac{D_O F \nu}{RT}} C_O^* \Psi(E) \quad (4.19a)$$

$$E_p = E^{0'} + \frac{RT}{nF} \ln \sqrt{\left( \frac{D_R}{D_O} \right)} - \Xi(\Lambda, \alpha) \frac{RT}{F} \quad (4.19b)$$

$$\Lambda = k^\circ \sqrt{\frac{RT}{DF\nu}} = k^\circ \sqrt{\frac{RTt}{DF(E_i - E)}} \quad (4.19c)$$

where  $\Psi(E)$  is illustrated in Figure 4.3a, and  $\Xi(\Lambda, \alpha)$  is illustrated in Figure 4.3b.  $\Psi$  and  $\Xi$  are dimensionless functions of voltage and thus scan rate through Equation (4.19c), that are needed to numerically solve the partial differential flux equation. Therefore, for quasi-reversible systems  $i_p$  is not proportional to  $\sqrt{\nu}$  since  $\Psi$  is dependent on  $\nu$  through  $\Lambda$  and  $E_p \propto \frac{1}{\sqrt{\nu}}$ .

By using the above relationships between  $i_p$  and  $E_p$  and scan rate and concentration, the electron transfer process at a specific electrode can be categorized as either reversible, quasi-reversible, or irreversible. In addition to a reaction's reversibility, capacitance information can also be gathered from a CV current-voltage plot. As can be seen in Figure 4.1b, the anodic and cathodic peak currents are considered with respect to the their respective baseline currents ( $i_b$ ). The baseline current results from charge migration from the bulk solution to the surface of the electrode, which subsequently

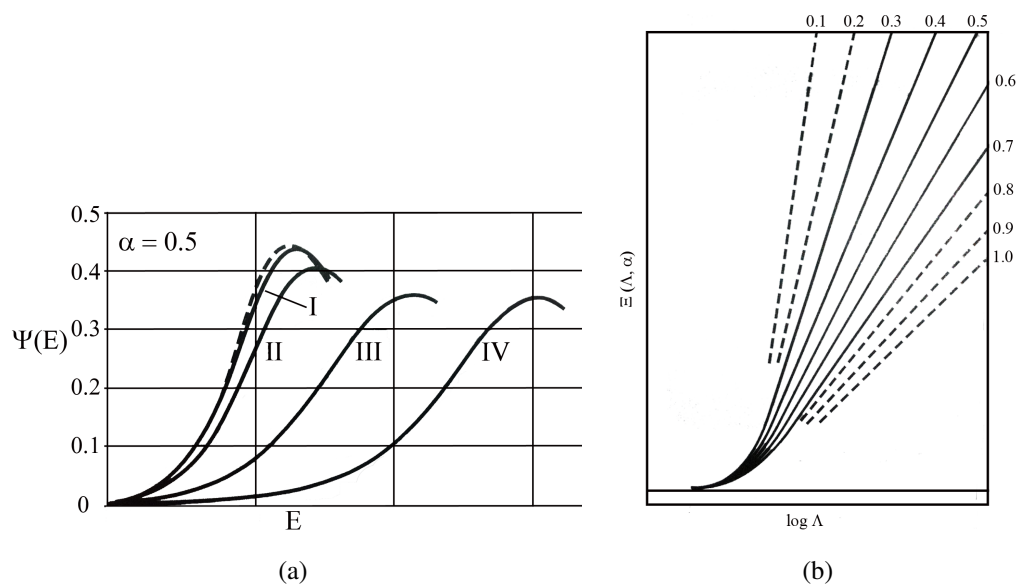


**Figure 4.3:** (a)  $\Psi$  as a function of  $E$ . Dashed lines indicate reversibility and the Roman Numerals represent different scan rates, where I, II, III, and IV correspond to  $\Lambda = 10$ , 1, 0.1, and 0.01, respectively. (b)  $\Xi$  as a function of  $\log(\Lambda)$  for different values of  $\alpha$ . Dashed lines indicate total irreversibility. Illustrations originally published by Matsuda et al. and Bard et al.[22, 23]

causes ions to stack preferentially near the surface of the electrode based on the electrode polarity as shown in Figure 4.4.

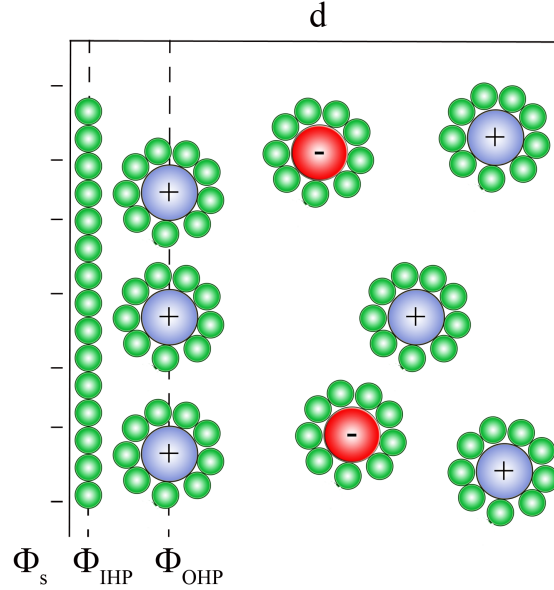


**Figure 4.4:** Illustration of the double-layer, where  $d$  indicates the distance from the electrode surface.  $\Phi$  indicates the potential at the surface(s), inner Helmholtz plane (IHP), and outer Helmholtz plane (OHP). Past the OHP, the diffuse layer begins, which extends into the bulk solution. The smaller (green) circles are solvent molecules.

The first two layers of ions are called the inner (IHP) and outer (OHP) Helmholtz planes, respectively, where ions of the IHP are termed specifically adsorbed and are not solvated. Ions of the OHP are nonspecifically adsorbed and are screened through solvation. Since the ions are stacked near the surface of the electrode, but are separated from the electrode surface by a distance ( $d$ ), the electric double-layer behaves capacitively. A first order approximation of the capacitive effects of the electric double-layer was made through implementing the parallel plate capacitor model, where the double-layer capacitance ( $C_{dl}$ ) per unit surface area ( $A$ ) is defined through:

$$\frac{C_{dl}}{A} = \frac{\epsilon \epsilon_0}{d} \quad (4.20)$$

where  $\epsilon$  is the dielectric constant and  $\epsilon_0$  is the permittivity of free space.

The double-layer current and thus  $C_{dl}$  can be determined near  $E_\lambda$ . If  $E_\lambda$  is sufficiently far away from the peak potential such that the diffusion layer is relatively thick, the switching potential represents the voltage where the double-layer restructures itself due to a change in the electrode polarity. For instance, when the electrode polarity changes from (+) to (-), negatively charged ions in the IHP and OHP are repelled electrostatically by the (-) charge on the electrode, while positively charged ions are attracted. In the limiting case of  $E_\lambda \gg E_p$ ,  $i_{dl}$  can be approximated by difference between the baseline current ( $i_b$ ) and the limiting current ( $i_{lim}$ ) as defined by:

$$C_{dl} = \frac{i_{dl}}{Av} = \frac{|i_b - i_{lim}|}{2Av} \quad (4.21)$$

Strictly speaking  $C_{dl}$  is dependent on the applied potential through  $i_{lim}$  and the Helmholtz model does not hold. However, if the capacitance is large and the potential range under investigation is relatively small  $C_{dl}$  can be approximated to be independent of voltage over a specific range. In this work, the Helmholtz model was assumed to be acceptable since the variation in observed capacitance over the implemented voltage ranges was negligible.

The capacitance associated with the faradaic peak current can also be determined in CV experiments. The faradaic capacitance is not a capacitance in the typical sense, since it due to non-transient currents associated with charge transfer. This capacitance is also termed a pseudocapacitance ( $C_p$ ) and is defined through:

$$C_p = \frac{|i_p|}{v} \quad (4.22)$$

where  $i_p$  is graphically determined as the difference between the actual current ( $i_T$ ) and the baseline current at the peak potential as indicated in Figure 4.1b and defined through:

$$i_p = i_T - i_b \quad (4.23)$$

where the linear nature of  $i_b$  represents the limiting case of no change in the diffusion layer current near the peak potential. However,  $i_b$  is comprised of  $i_{dl}$  and  $i_{lim}$ . Due to difficulties in graphically separating  $i_{dl}$  and  $i_{lim}$  near the peak potentials, the  $i_p$  can be slightly overestimated. The inability to accurately calculate  $i_{dl}$  and  $i_{lim}$  graphically is not only important at the peak potentials but also becomes important at relatively large

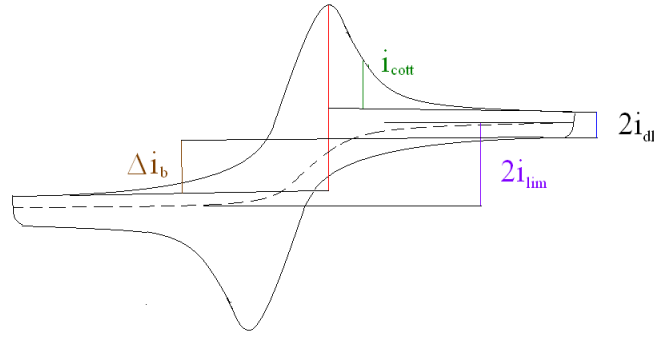


**Figure 4.5:** Illustrative CV curve demonstrating how the experimental CV curves were used to measure the difference components of the total current.

redox couple concentrations and large scan rates. If  $i_{lim} \gg i_{dl}$  or  $E_\lambda \not\gg E_p$  such that either O or R is not completely exhausted at the working electrode surface, it becomes extremely difficult to directly determine  $i_b$  with respect to  $i_{lim}$  and thus  $C_{dl}$  from a single CV plot.

To determine  $C_{dl}$ , a different approach was therefore implemented. If (1)  $i_{dl}$  for O and R are equal and the Helmholtz model holds, (2)  $E_\lambda \gg E_p$ , and (3)  $|i_{lim}|$  is equal for the anodic and cathodic sweeps as determined when  $i_b$  for both sweeps are parallel as illustrated in Figure 4.5, the difference between oxidation and reduction baseline curves can then subsequently be used to determine  $i_{dl}$  through:

$$2i_{lim} = \Delta i_b + 2i_{dl} \quad (4.24a)$$

$$i_T = \Delta i_b + 2i_{dl} + i_{cott} \quad (4.24b)$$

where Equation (4.2) can be substituted for  $i_{cott}$  and  $i_T - \Delta i_b$  is rewritten as  $i_B$  to give:

$$i_B = \frac{nFAC_j^*D_j}{\delta} - 2i_{dl} \quad (4.25)$$

where  $\delta$  is the diffusion layer thickness. Utilizing the definition of  $\delta$ :

$$\delta = \sqrt{\pi D_j t} \quad (4.26)$$

and approximating time as  $(\frac{\Delta V}{\nu})$ , where  $\Delta V$  is the voltage difference between  $E_\lambda$  and  $E_p$ , Equation (4.25) can be rewritten as:



$$i_B = nFAC_j^* \sqrt{\frac{D_j \nu}{\pi \Delta V}} - 2i_{dl} \quad (4.27)$$

By dividing Equation (4.27) by the scan rate,  $i_B$  and  $i_{dl}$  can be rewritten as capacitances:

$$C_B = 2nFC_j^* A \sqrt{\frac{D_j}{\nu \pi \Delta V}} - 2C_{dl} \quad (4.28)$$

Therefore if the plots of  $C_B$  as a function of  $\frac{1}{\sqrt{\nu}}$  or  $C_j^*$  are linear,  $C_{dl}$  can be determined by the y-intercept.

#### 4.1.2 Electrochemical Impedance Spectroscopy (EIS): Equivalent Circuit Design

Another method of determining the capacitance of the system is through electrochemical impedance spectroscopy. In EIS, a constant dc potential ( $E_{dc}$ ) is applied to the system as well as a small amplitude ac signal ( $\dot{E}_{ac}$ ) at various frequencies as shown in Figure 4.6a. The applied dc potential is used to set the surface concentrations of O and R, while  $\dot{E}_{ac}$  is used to induce small perturbations to equilibrium. Since  $\dot{E}_{ac}$  and the resulting current ( $\dot{I}_{ac}$ ) are out of phase with each other (Figure 4.6b) due to capacitances, such as  $C_{dl}$  and  $C_p$ , information about which electrochemical processes are occurring can be gathered by plotting the modulus and phase ( $\phi$ ) of the impedance ( $Z$ ) at a number of different frequencies (Figure 4.6c). The impedance and phase angle are defined as follows:

$$\dot{E} = Z\dot{I} \quad (4.29a)$$

$$Z = Z_{real} - jZ_{imag} \quad (4.29b)$$

$$\phi = \tan^{-1} \left( \frac{-Z_{imag}}{Z_{real}} \right) \quad (4.29c)$$

Using the features of Figure 4.6c and knowledge of the electrochemical system, an equivalent circuit consisting of a combination of circuit elements can be constructed to model the frequency response of the system. To verify the validity of the model, the experimental data can be non-linearly fit to minimize the error between the curves predicted by the model and the experimental data. As mentioned previously, the two critical electrochemical processes that are under investigation in this work are the double-layer

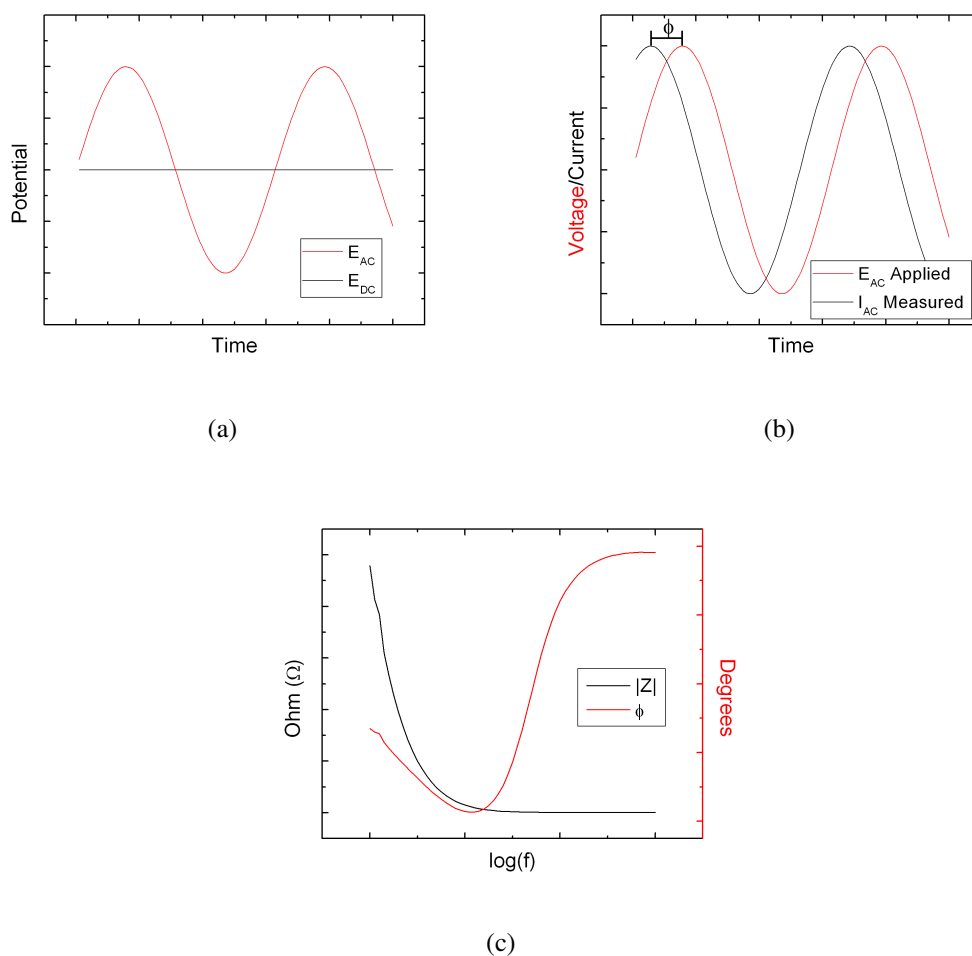


**Figure 4.6:** (a) The waveform of the applied dc and ac signals. (b) The resulting ac current response to the ac applied potential, indicating the phase shift between the two. (c) Example of frequency response for  $|Z|$  and  $\phi$  of an electrochemical system.

and the faradaic contributions to the total current, where the system can be modelled with a Randles circuit shown in Figure 4.7.

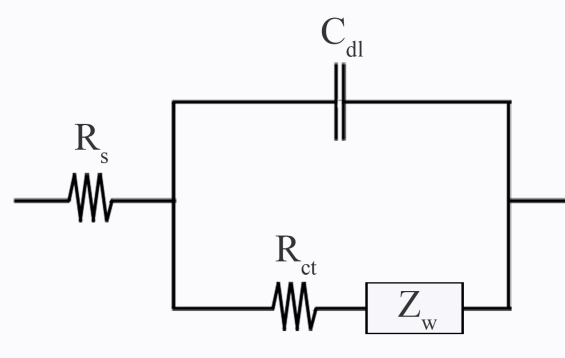


**Figure 4.7:** The equivalent circuit of the electrochemical system under investigation.  $R_s$  is the solution resistance,  $R_{ct}$  is the charge transfer resistance,  $C_{dl}$  is the double-layer capacitance,  $Z_w$  is the Warburg impedance.

The Warburg impedance ( $Z_w$ ) introduced in Figure 4.7 represents the diffusion process associated with the faradaic current. This process has both capacitive and resistive components and is modelled through[22]:

$$Z_w = \frac{\sigma}{\sqrt{\omega}}(1 - j) \quad (4.30a)$$

$$\sigma = \frac{RT}{n^2 F^2 A \sqrt{2}} \left( \frac{1}{C_O^* \sqrt{D_O}} + \frac{1}{C_R^* \sqrt{D_R}} \right) \quad (4.30b)$$

If the charge transfer kinetics are relatively fast,  $R_{ct} \rightarrow 0$  and thus  $\phi$  for the faradaic impedance ( $Z_f$ ) approaches  $45^\circ$ , where:

$$Z_f = R_{ct} + Z_w \quad (4.31a)$$

$$Z_f = R_{ct} + \frac{\sigma}{\sqrt{\omega}}(1 - j) \quad (4.31b)$$

$$\phi = \tan^{-1} \left( \frac{\frac{\sigma}{\sqrt{\omega}}}{R_{ct} + \frac{\sigma}{\sqrt{\omega}}} \right) \quad (4.31c)$$

For quasi-reversible and irreversible systems,  $R_{ct}$  becomes appreciably large and significantly contributes to  $Z_f$ . Changes in  $Z_f$  are also dependent on  $\frac{C_O^*}{C_R^*}$  through the

applied DC offset voltage. For instance, when  $C_O^*$  ( $C_R^*$ ) is appreciably larger than  $C_R^*$  ( $C_O^*$ ),  $\sigma$  varies such that diffusion of  $C_R^*$  ( $C_O^*$ ) to the electrode can be hindered.

For the circuit model illustrated in Figure 4.7, the frequency response of the system can be defined analytically. The real ( $Z_{real}$ ) and imaginary ( $Z_{imag}$ ) parts of the impedance can therefore be separated as follows:

$$Z_{real} = R_s + \frac{R_{ct} + \frac{\sigma}{\sqrt{\omega}}}{(C_{dl}\sigma\sqrt{\omega} + 1)^2 + \omega^2 C_{dl}^2 (R_{ct} + \frac{\sigma}{\sqrt{\omega}})^2} \quad (4.32a)$$

$$Z_{imag} = \frac{\omega C_{dl} (R_{ct} + \frac{\sigma}{\sqrt{\omega}})^2 + \frac{\sigma}{\sqrt{\omega}} (C_{dl}\sigma\sqrt{\omega} + 1)}{(C_{dl}\sigma\sqrt{\omega} + 1)^2 + \omega^2 C_{dl}^2 (R_{ct} + \frac{\sigma}{\sqrt{\omega}})^2} \quad (4.32b)$$

To best understand how  $Z$  responds to changes in frequency, the high and low frequency limits are first investigated. As  $\omega \rightarrow \infty$ , the Warburg impedance becomes negligible compared to  $R_{ct}$  and the equivalent circuit presented in Figure 4.7 is reduced to that of Figure 4.8a and  $Z_{real}$  and  $Z_{imag}$  are simplified to:

$$Z_{real}(\omega \rightarrow \infty) = R_s + \frac{R_{ct}}{1 + (\omega C_{dl} R_{ct})^2} \quad (4.33a)$$

$$Z_{imag}(\omega \rightarrow \infty) = \frac{\omega C_{dl} R_{ct}^2}{1 + (\omega C_{dl} R_{ct})^2} \quad (4.33b)$$

$$\left(Z_{real} - R_s - \frac{R_{ct}}{2}\right)^2 + Z_{imag}^2 = \left(\frac{R_{ct}}{2}\right)^2 \quad (4.33c)$$

As can be deduced from Equations 4.33a and 4.33b, if  $R_{ct} \approx 0$ , then at high frequencies,  $Z_{real}$  is dominated by  $R_s$  and  $Z_{imag} \approx 0$ . The phase angle is therefore approximately  $0^\circ$  for kinetically facile systems, when a relatively high frequency ac input potential is used.

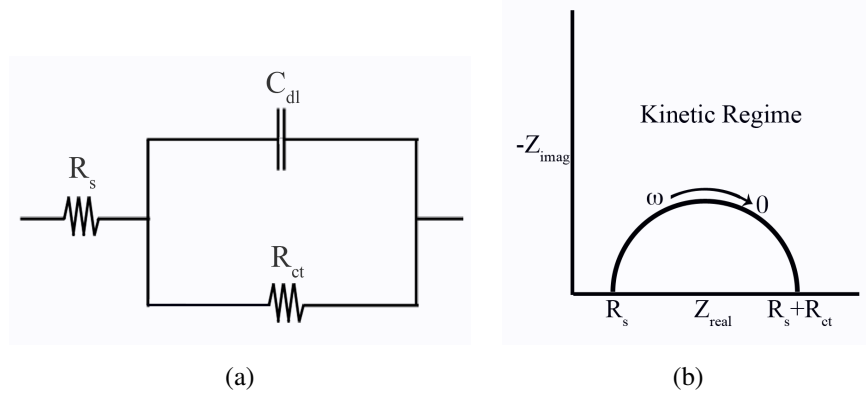


**Figure 4.8:** (a) The equivalent circuit as  $\omega \rightarrow \infty$ . (b) Nyquist plot of the equivalent circuit shown in (a).

When  $\omega \rightarrow 0$ , the equivalent circuit model is dominated by the  $Z_W$  and the frequency response is diffusion-controlled. The real and imaginary forms of the impedance are as follows and are graphically shown in Figure 4.9.

$$Z_{real}(\omega \rightarrow 0) = R_s + R_{ct} + \frac{\sigma}{\sqrt{\omega}} \quad (4.34a)$$

$$Z_{imag}(\omega \rightarrow 0) = \frac{\sigma}{\sqrt{\omega}} + 2\sigma^2 C_{dl} \quad (4.34b)$$

$$Z_{imag} = Z_{real} - R_s - R_{ct} + 2\sigma^2 C_{dl} \quad (4.34c)$$

At sufficiently low frequencies,  $Z_{real}$  is dominated by diffusion processes ( $\sigma$ ) and  $\phi = 45^\circ$ . If  $\phi$  is experimentally measured to be  $\approx 45^\circ$  below a certain frequency, diffusion processes determine the EIS response for the specific frequency range. The transition between the kinetic and diffusion dominated regimes is termed the knee frequency ( $f_{knee}$ ). The knee frequency represents the frequency at which the system transitions from resistive to capacitive behavior and  $|Z_{imag}|$  increases as  $\omega \rightarrow 0$ . If the knee frequency is increased, the time constant ( $\frac{1}{f_{knee}}$ ) for charging and discharging cycles is reduced. Time constant reduction is desirable especially for large capacity capacitors, since the full capacity can be discharged relatively more quickly. Time constant reduction also indicates a transition from battery-like behavior to conventional capacitor behavior, since the time associated for charge transfer in a battery is can be much longer than for charge transfer in a capacitor.

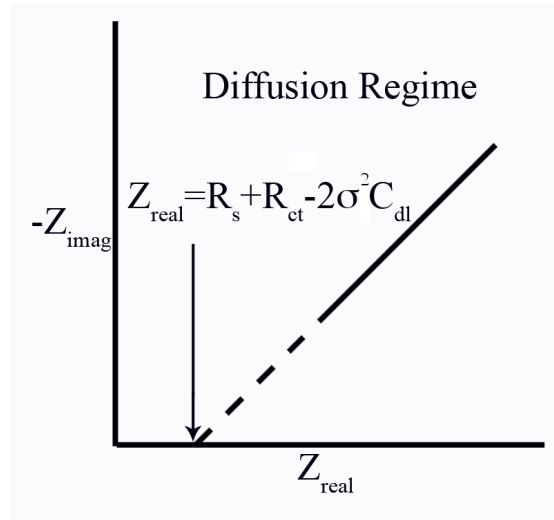


**Figure 4.9:** Nyquist plot of when  $\omega \rightarrow 0$  (diffusion limited regime). The intercept can be used to determine  $R_s$ ,  $R_{\text{ct}}$ ,  $\sigma$  and  $C_{\text{dl}}$ .

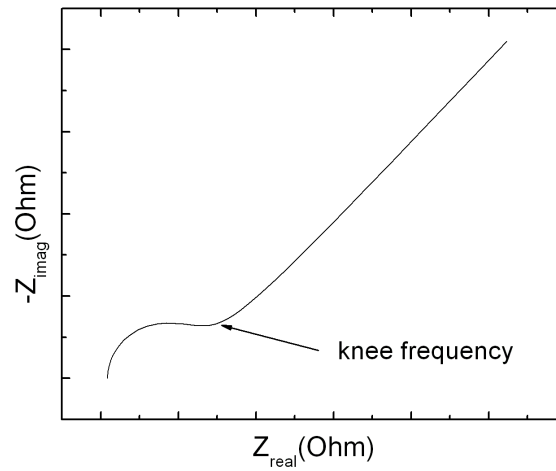


**Figure 4.10:** Nyquist plot indicating the knee frequency, where the kinetic regime transitions to the diffusion regime.

If  $|\phi|$  continues to increase from  $45^\circ$  to  $90^\circ$  below the knee frequency, as with many purely double-layer capacitors, the equivalent circuit model in Figure 4.7 is no longer valid. A  $90^\circ$  phase angle is representative of an ideally polarizable capacitor and therefore the Warburg impedance can be replaced with a capacitor ( $C_p$ ). When  $Z_W$  is replaced with  $C_p$  the Nyquist plot exhibits a more purely capacitive frequency response as shown in Figure 4.11.

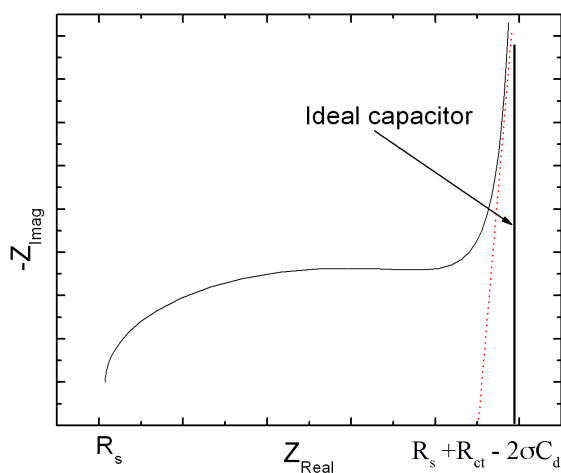


**Figure 4.11:** Nyquist plot where  $Z_W$  is replaced by  $C_p$ , but remains in series with  $R_{ct}$  to demonstrate a transition to ideal capacitor behavior.

By utilizing EIS at different DC voltages the importance of diffusion on  $C_p$ ,  $C_{dl}$ ,  $R_{ct}$ , and  $R_s$  can be determined. Each of these values is also affected by the solvent-solute system, electrode geometry, and electrode-redox couple interactions, thus it characterizes how the physical and electrical properties of electrodes affect their electrochemical performance.

### 4.1.3 Chronopotentiometry

As with EIS, chronopotentiometry provides complementary information to CV, but the system is measured in response to a input current. The input current drives reactions at the electrode surface and the potential of the system is measured. When a constant current is sourced for a particular time then reversed for a second time period

as shown in Figure 4.12, the chronopotentiometric technique is termed constant current cyclic chronopotentiometry (GALV).

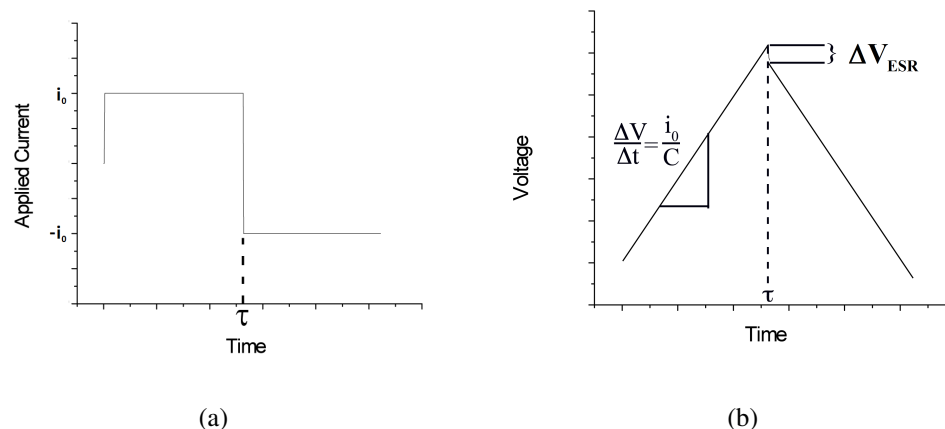


**Figure 4.12:** (a) Square waveform used for cyclic constant current chronopotentiometry. (b) Resulting voltage response to current waveform for an ideally polarizable capacitor in series with a resistor. ESR is the equivalent series resistance and is calculated experimentally by  $R_{ESR} = \frac{V_{ESR}}{|i_1 - i_2|}$ . In electrolytic capacitors,  $R_{ESR}$  is a combination of the current collector resistance,  $R_s$ ,  $R_{ct}$ , and contact resistance at the terminal leads. The value of  $R_{ESR}$  is critical for high power applications since large resistances can lead to heating and expansion of the electrolyte, causing the capacitor to fail.

If the current is sourced in such a way that electrons flow into the solution, O is reduced at a constant rate at the electrode surface. The time associated with the reaction can be termed the transition time ( $\tau$ ) and is a function of the diffusion coefficients and surface concentrations of O and R, as shown in Equation (4.35). Once the surface concentration of O is exhausted, the magnitude of the measured potential increases rapidly until another reduction potential is reached, resulting in a step-like function for the measured potential. Since ideally polarizable electrodes exhibit only linear behavior as shown in Figure 4.12b, ideal behavior can be assessed by monitoring the slope of the potential as a function of time.

Analogous to  $i_p$  and the instantaneous current in CV,  $\tau$  and the measured voltage ( $V$ ) can be assessed analytically by using the semi-infinite linear diffusion boundary conditions and the flux equations, as explained in Section 4.1.1. In all systems where a



constant current ( $i_{source}$ ) is sourced,  $\tau$  can be defined as:

$$\tau = \left( \frac{nFAC_j^* \sqrt{\pi D_j}}{2i_{source}} \right)^2 \quad (4.35)$$

where  $j$  denotes the oxidized or reduced species of the redox couple, which is known as the Sand equation.[22]

Since capacitance can be defined as:

$$C = \frac{i}{\Delta V / \Delta t} \quad (4.36)$$

as shown in Figure 4.12b, the voltage window ( $\Delta V$ ) and time associated with charging ( $\Delta t$ ) play critical roles in the capacitance of an electrode. For purely double-layer capacitors,  $\Delta V$  is determined by the point at which the solvent undergoes electrolysis and is therefore characteristic of the solvent. For instance, the breakdown voltage for aqueous solutions is approximately 0.9 V, where as organic solutions typically have much larger breakdown voltages,  $\sim 2.7$  V.[92] When a redox couple is added to the solvent-solute system, the current supplied drives faradaic reactions at the electrode surface until the surface concentration is depleted. The voltage at which this occurs is dependent on the reversibility of the system as shown in Figure 4.13a, where the following equations were used to define the measured potential with respect to one-step, one-electron transfer processes for reversible, irreversible, and quasi-reversible systems. The voltage window therefore depends on the solvent system and the reversibility of electron transfer.

$$V = E^{0'} - \frac{RT}{2nF} \ln \left( \frac{D_O}{D_R} \right)^m + \frac{RT}{nF} \ln \left( \frac{\sqrt{\tau_j} - \sqrt{t}}{\sqrt{t}} \right)^m \quad (\text{Reversible}) \quad (4.37a)$$

$$V = E^{0'} - \frac{RT}{\alpha F} \ln \left[ \frac{2k_j^0}{\sqrt{\pi D_j}} \right] + \frac{RT}{\alpha F} \ln \left[ m(\sqrt{\tau_j} - \sqrt{t}) \right] \quad (\text{Irreversible}) \quad (4.37b)$$

$$V = E^{0'} + \frac{RT}{F} \ln \frac{C_O^*}{C_R^*} - \frac{RT}{F} i_{source} \left[ \frac{2\sqrt{t}}{FA\sqrt{\pi}} \left( \frac{1}{C_O^* \sqrt{D_O}} + \frac{1}{C_R^* \sqrt{D_R}} \right) + \frac{1}{i_0} \right] \quad (\text{Quasi-reversible}) \quad (4.37c)$$

where  $t$  is time and  $m$  is an integer corresponding to the current direction. When electrons are supplied to the solution,  $m = +1$  and  $j = O$  when electrons flow from the

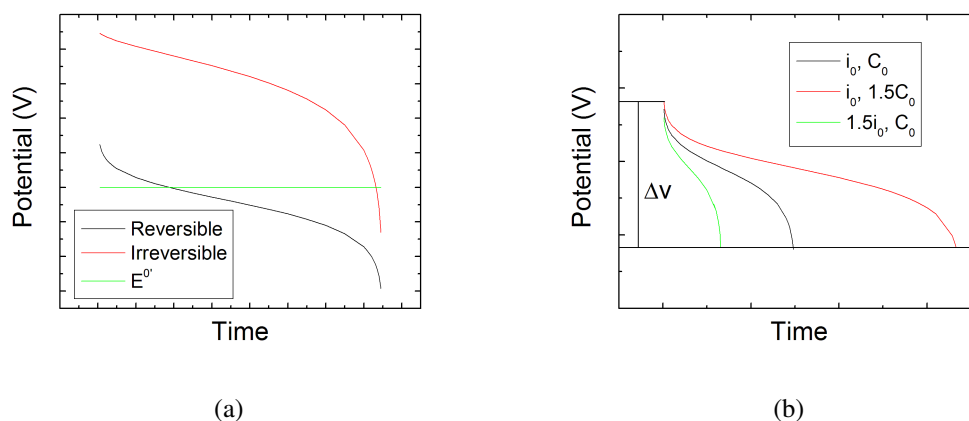


**Figure 4.13:** (a) Measured potential as a function of time for reversible and irreversible systems with reference to  $E^0$ . (b) Measured potential as a function of time, concentration, and source current for reversible systems.

solution to the electrode,  $m = -1$  and  $j = R$ . The exchange current,  $i_0$ , is defined as:[22]

$$i_0 = F A k^\circ C_O^{*(1-\alpha)} C_R^{*\alpha} \quad (4.38)$$

Figure 4.13b illustrates how changing  $C_j^*$  and  $i_{source}$  do not change  $\Delta V$ , but change how much time is needed to span  $\Delta V$ , as explained through Equation (4.35). The voltage window is therefore independent of the redox couple for a given degree of reversibility, while  $\Delta t$  is dependent upon  $C_j^*$  and  $i_{source}$ .

Assuming that  $\Delta V$  is fixed for a given solvent,  $C_p$  can be defined for chronopotentiometric systems as:

$$C_p = \frac{i_{source}\tau}{\Delta V} \quad (4.39)$$

since  $\tau$  is the time associated with faradaic reactions. Furthermore, using Equation (4.35) to replace  $\tau$  in Equation 4.39, Equation 4.39 can be rewritten as:

$$C_p = \frac{(nFAC_j^* \sqrt{\pi D_j})^2}{4i_{source}\Delta V} \quad (4.40)$$

where a maximum  $C_p$  can be obtained with relatively small source currents and when the  $C^*$  is maximized.

## 4.2 Experimental Setup

### 4.2.1 Cyclic Voltammetry

As mentioned in Section 4.1.1, many experimental parameters can be used to characterize electron transfer at the electrode surface using CV. In this work, CV experiments were carried out using a PCI4-300 potentiostat from Gamry Instruments, which has a current resolution of 1 fA and a voltage resolution of 1  $\mu$ V. For electrode characterization experiments a three electrode setup was used as shown in Figure 4.14. The electrodes used were a (1) saturated calomel reference electrode (SCE), a (2) platinum wire as the counter electrode (CE), and a (3) working electrode (WE). The advantage of using this setup compared to a two electrode cell design, where the reference electrode and counter electrode are combined into one electrode, is that the voltage of the reference electrode can be fixed and is not changed by the flow of electrical current, as can be the case with a two electrode setup.

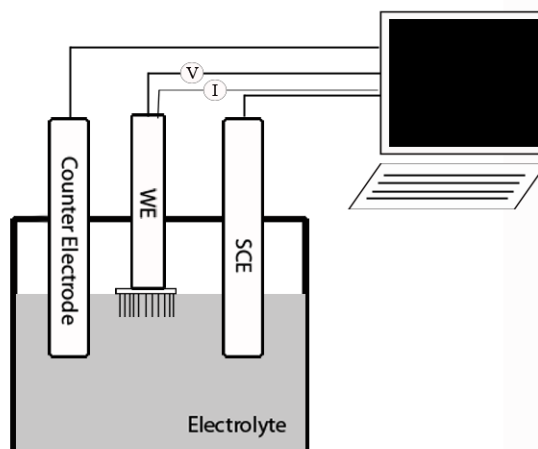


**Figure 4.14:** Experimental CV setup used for working electrode (WE) characterization. The counter electrode used was a Pt wire and reference electrode was a saturated calomel electrode (SCE).

The working electrode consisted of a platinum wire for diagnostic checks or an array of CNTs on a Si wafer. Carbon nanotube electrodes were made by first growing CNTs on n-doped Si wafers with a resistivity of 1-10 m $\Omega$ cm as described in Chapter

2. On the other side of the wafer, a contact pad consisting of 10 nm of titanium and 60 nm of silver was deposited using electron beam evaporation. The contact pad was positioned at the center of the wafer with a side length of 0.5 cm. A copper wire was then soldered to the contact pad with indium solder, resulting in a contact resistance of  $< 1\Omega$ . Care was taken to only expose only the CNT side of the wafer to the solvent, as the exposure of Ag or the solder to the solution during CV scans would result in metal dissolution, creating undesired redox peaks. Furthermore, a bare Si wafer was tested to verify that no electrochemical activity resulted from Si in the voltage window tested.

The majority of experiments were conducted with solutions of potassium ferricyanide ( $K_3Fe(CN)_6$ ), an inner-sphere redox couple, in aqueous potassium chloride (KCl). Ruthenium hexamine trichloride ( $Ru(NH_3)_6Cl_3$ ), an outer-sphere redox couple, in  $KCl_{(aq)}$  was another redox couple used. The denotation of outer and inner sphere is used to describe how electron transfer occurs, where outer sphere electron transfer involves the transfer of the electron through the space separating the redox centers, whereas the electron in inner sphere electron transfer occurs along a chemical bridge. The two different redox couples were used to determine any influence of adsorption of the redox couple onto the electrode. All materials used were of 98% or higher purity and purchased from Sigma-Aldrich. Potassium chloride was used as the supporting electrolyte to conduct the current and was typically 100 times more concentrated than that of the redox couple. Table 4.1 shows all of the concentration values used. Multiple scan rates in addition to several concentrations were also used to determine the reversibility of the reactions. The scan rates used in this work were 5, 10, 25, 50, 100, and 200 mV/s. All CV spectra were taken between 5-50 times to monitor any cycle dependencies.

**Table 4.1:** CV Concentrations

Redox Couple	[mM]	Salt	[M]	Solvent
$K_3Fe(CN)_6$	0.5, 3, 5, 6, 10, 25, 50, 100, 300, 600	KCl	0.5, 1.0, 3.0	$H_2O$
$Ru(NH_3)_6Cl_3$	0.5, 3, 6, 10	KCl	1.0	$H_2O$

Before CNTs were used as the working electrode, each supporting electrolyte-redox couple system was tested as a control with a Pt working electrode to ensure that the

potentiostat was properly calibrated. All Pt electrodes were also polished with micro-bead metal polish provided by Gamry Instruments before every use. The polished electrodes were then cleaned with Alconox detergent dissolved in deionized water (DI) and sonicated for 2 min to ensure that the polish was fully removed.

When constructing CNT based devices, all diagnostic checks were also performed prior to device construction and testing. Unlike with the electrode characterization tests, only two terminals exist on the capacitor devices, as illustrated in Figure 4.15. The CE and reference (Ref) electrical leads were thus attached to one another and then to one terminal lead. The two electrical leads for the WE, one of which is used only for electrical current (I) and the other for voltage measurements (V), were attached to one another and then attached to the other terminal lead.

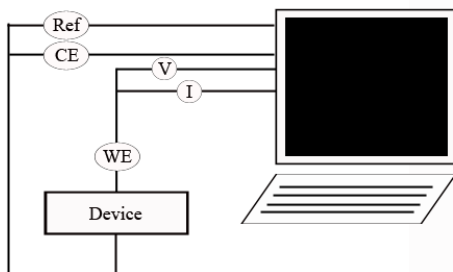


**Figure 4.15:** Experimental two electrode setup used for device characterization. The reference (Ref) and counter electrode (CE) leads were electrically connected and attached to one capacitor electrode and the working electrode (WE) leads were connected to the second capacitor electrode.

### 4.2.2 Electrochemical Impedance Spectroscopy

All EIS measurements were taken after several CV measurements, therefore redox couple and supporting electrolyte concentration dependencies were also investigated, in addition to a variety of DC and AC voltages. AC voltages ranged from 5-20  $mV_{RMS}$ . DC offset voltages were typically set to the open circuit potential (OCP) to minimize  $R_{ct}$ . The OCP was measured by monitoring the potential during a 10 min time period with no current flow, where all electrodes were placed in solution. To measure surface concentration effects for O and R species of the redox couple, DC offset poten-

tials of  $E^{0'} \pm 1.5\Delta E_p$  were used, which ensures that reverse reactions are not present.

For EIS experiments where only one CNT electrode was being characterized the frequency range used was 10 kHz to 10 mHz. When a device was being tested the frequency range was 100 kHz to 1 mHz.

### 4.3 Effects of Defects on Electrochemistry

To establish a concrete understanding of the redox couple system the three-electrode setup shown in Figure 4.1b was employed. For initial calibration, a platinum electrode was used for the working electrode and the counter electrode. Figure 4.16 illustrates the change in the CV curves for different scan rates and different concentrations. After approximating the baseline and solving for the peak currents and positions, as illustrated in Figure 4.1b, the reversibility of the system can be evaluated.

If the reactions between the redox couple and the Pt working electrode are reversible,  $|\frac{i_{pc}}{i_{pa}}| = 1$ ,  $\Delta E_p$  is not a function of  $\nu$ , and  $i_p$  follows the Randles-Sevcik equation (Equation 4.7a). As shown in Figure 4.17,  $i_p$  is linear with concentration and square-root of the scan rate. The non-zero y-intercept indicates that the baseline fitting of the peaks is not ideal or an adsorbate exists at the surface of the electrode.[22] However, since the y-intercepts are relatively small compared to the peak current and are independent of the redox couple, the error most likely results from approximating the true baseline. The peak current ratios and peak separations are shown in Table 4.2, where the peak current ratios can also be deduced from the slopes in Figure 4.17. Since (a) the peak separation is not a function of scan rate, (b) the peak current ratios are approximately 1 for all scan rates and concentrations, and (c) the peak current is proportional to redox couple concentration and the square-root of the scan rate, reversible behavior is observed.

In addition to providing information about the reversibility of the charge transfer process, the slopes of the plots in Figures 4.17 can also be used to determine  $A\sqrt{D}$ . If  $D$  is accurately known the effective area of the working electrode can be determined. For each redox couple in 1.0 M KCl<sub>aq</sub>, the diffusion coefficient for the oxidized and reduced species have been experimentally determined to be relatively equal.[93, 94] Using the average value for  $D$ , the effective area for the Pt working electrode was determined and shown in Table 4.2. As can be seen in the table and given the specified area of the Pt electrode to be 0.075 cm<sup>2</sup>, the average error in  $A_{effective}$  is approximately 5.7 %. The

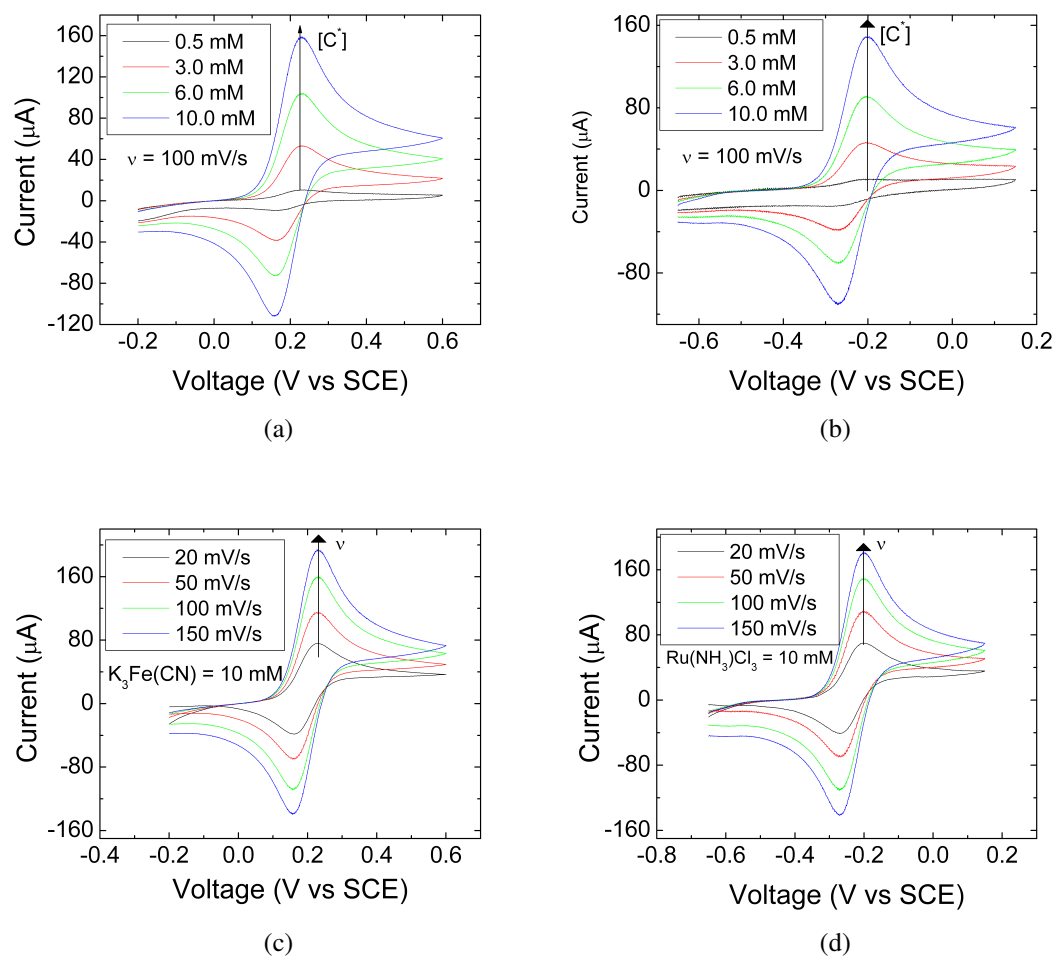


**Figure 4.16:** CV plots as a function of concentration and scan rate for (a), (c) potassium ferricyanide and (b), (d) ruthenium hexaamine trichloride in 1.0 M  $\text{KCl}_{aq}$ , respectively. Pt was the working electrode.

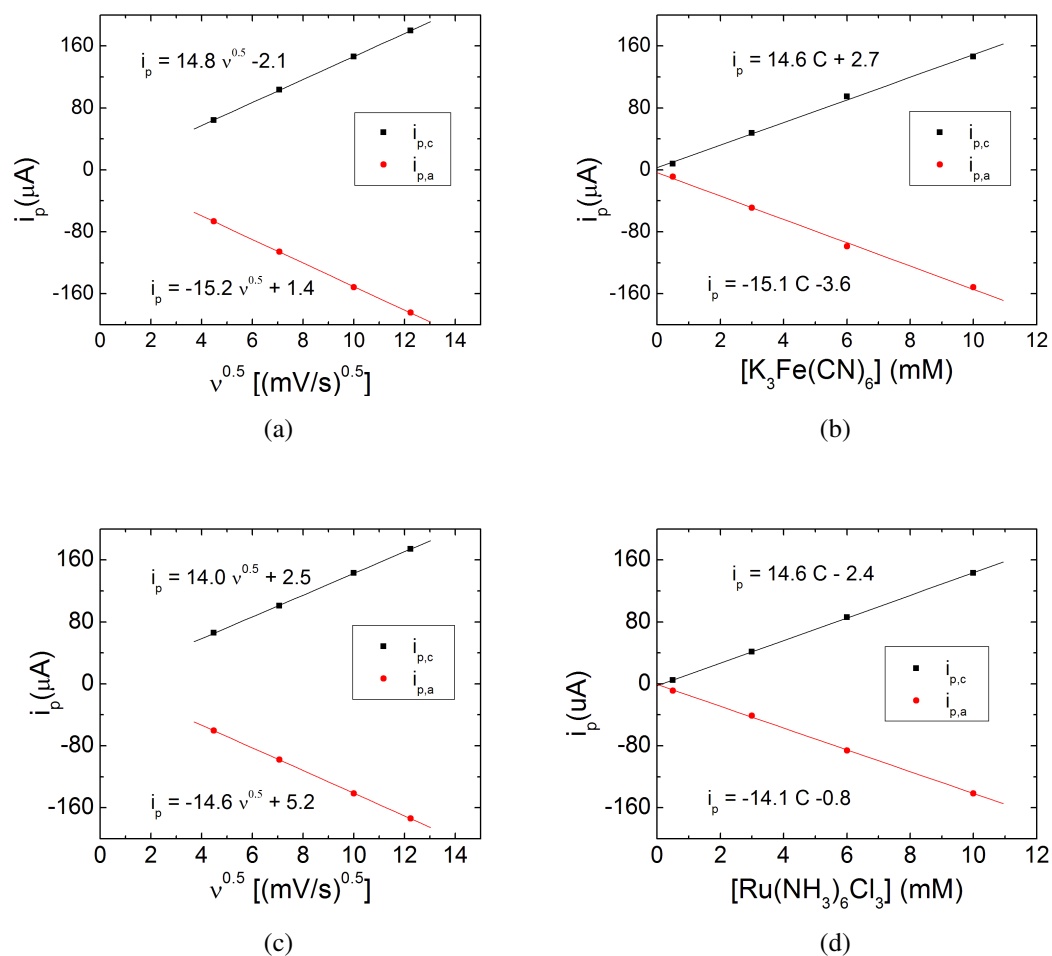


**Figure 4.17:** Plots of  $i_p$  as functions of scan rate and redox couple concentration to determine reversibility. (a) and (b) are for potassium ferricyanide. (c) and (d) are for ruthenium hexaamine trichloride.



good agreement between the experimental and manufacturers specified area, implies that both  $D_{O,R}$  and  $A$  are reasonably accurate.

**Table 4.2:** Redox Couple Performance

Redox Couple	Avg $ \frac{i_{p,c}}{i_{p,a}} $	Avg $\Delta E_p$ (mV)	D ( $\frac{cm^2}{s}$ )	$A_{effective}$ ( $cm^2$ )
$K_3Fe(CN)_6$	$0.97 \pm 0.02$	$73.0 \pm 2.6$	$6.8 \times 10^{-6}$ [93]	$0.0677 \pm 0.0033$
$Ru(NH_3)_6Cl_3$	$0.99 \pm 0.05$	$72.7 \pm 1.8$	$3.89 \times 10^{-6}$ [94]	$0.0756 \pm 0.0056$

### 4.3.1 Influence of Intrinsic Defects on Electron Transfer Kinetics

Prior to testing CNT electrodes, any potential effects on the baseline or faradaic currents from the contact pad coming into contact with the solution or the Si wafer were explored. This was a necessary step to ensure that neither of these factors could falsely skew any data that would be attributed to treatments done on the CNTs. As demonstrated in Figure 4.18, the Si wafer showed no redox activity in the potential window of -0.75 to 0.75 and the current was negligible compared to both the Pt standard electrode and the CNT electrode. This voltage window was chosen because it includes the  $E^0$  potentials for  $K_3Fe(CN)_6$  and  $Ru(NH_3)_6Cl_3$  and thus ensures that Si would exhibit no redox activity whether  $K_3Fe(CN)_6$  or  $Ru(NH_3)_6Cl_3$  was used as the redox couple.

Since the Si wafer does not exhibit any redox activity, the next step to characterize reactions with the CNT electrodes was to determine if they were sensitive to the redox couple used. The reversibility of AP CNTs grown with acetylene was monitored for potassium ferricyanide and ruthenium hexaamine trichloride redox couples in 1.0 M KCl, as can be seen from Figure 4.19.

From these CV plots, the peak capacitances were experimentally determined and plotted as functions of  $\frac{1}{\sqrt{\nu}}$  and  $[C]$  as defined through Equations (4.7) and (4.22) to form:

$$C_p = (2.69 \times 10^5) n^{3/2} A D_O^{1/2} C_O^* \nu^{-1/2} \quad (4.41)$$

The peak positions were also experimentally determined and plotted as a function of  $\nu$ . Both of the comparisons were used to determine whether or not reversible

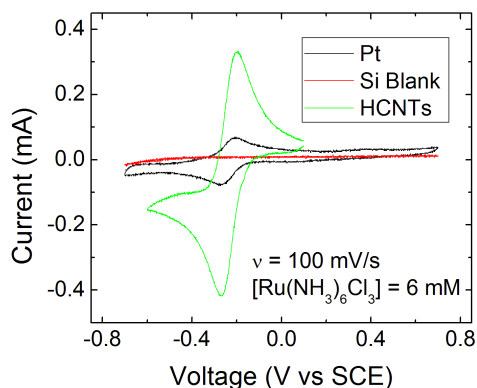


**Figure 4.18:** The redox couple was 6 mM ruthenium hexaamine trichloride in 1 M KCl, where a scan rate of 100 mV/s was used.

electron transfer was observed, as shown in Figure 4.20. As can be deduced from these plots, the peak capacitance follows the trends described by Equation (4.41) and  $\Delta E_p$  is independent of the scan rates greater than 40 mV/s, therefore electron transfer is reversible at HCNTs electrodes for both redox couples. The slight increase in the peak separation compared to the ideal value of 59 mV for one electron transfer described by Equation (4.9c), indicates that there is some non-ideality in the reaction processes as observed in most electrochemical redox reactions.[95]

The intrinsically large defect density of BCNTs has a significant impact on their electrochemical properties. An important structural feature of these types of CNTs is the high intrinsic edge-plane character, that appears to prevent any significant structural changes from occurring in the BCNTs upon Ar plasma exposure detailed in Section 3.6.1 and Figure 3.31. As can also be seen in Figure 4.21 the CV scans and therefore  $C_p$  and  $C_{dl}$  do not change significantly with increased irradiation times. Hollow CNTs were treated and tested in the identical manner as BCNTs to illustrate and emphasize the effects of CNT morphology on electron transfer kinetics.

With increasing Ar irradiation,  $C_p$  for the HCNTs gradually increases, while for BCNTs  $C_p$  does not appear to show any dependence, shown in Figure 4.21d. The initial reactive site density of BCNTs therefore appears to determine the electrochemical response. The lack of change in the electron transfer kinetics shown in Figure 4.22 through changes in  $\Delta E_p$  also indicates the dominance of the intrinsic edge plane defects.

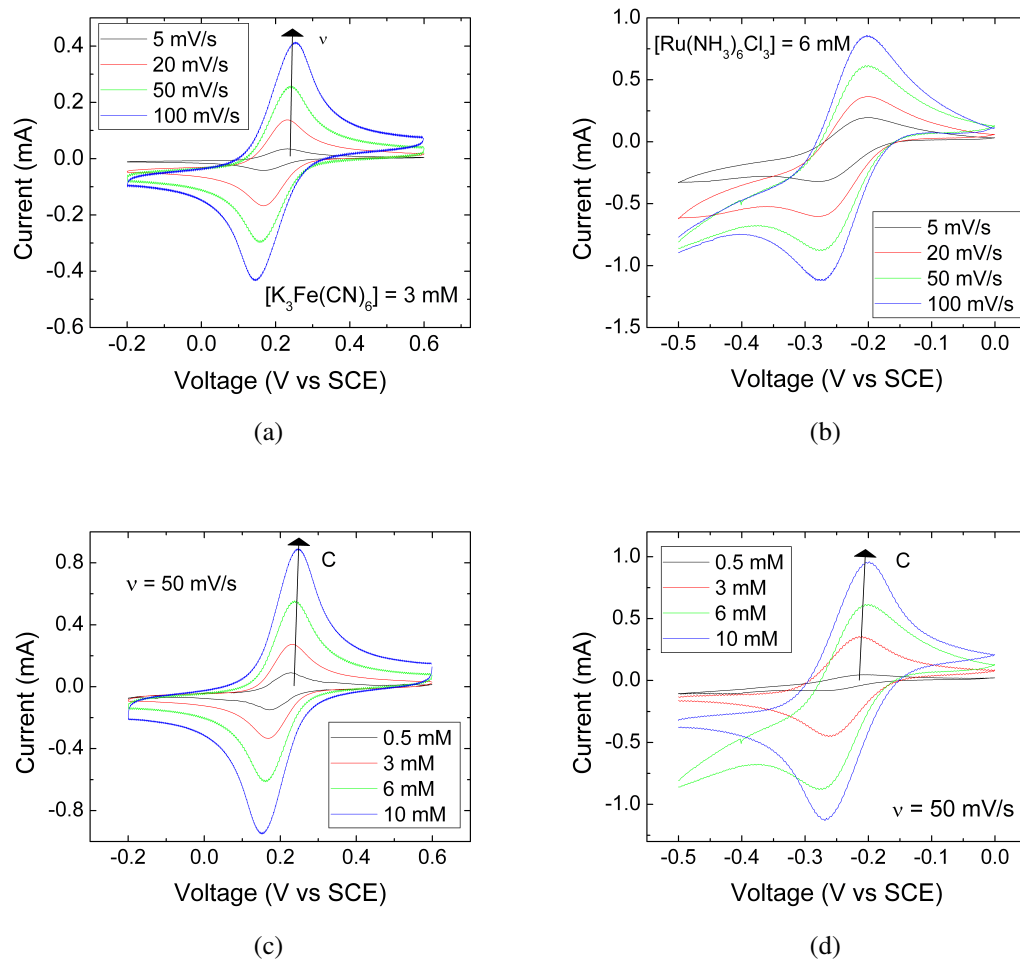


**Figure 4.19:** CV plots for AP CNTs with respect to scan rate for (a) potassium ferricyanide and (b) ruthenium hexaammine trichloride. CV plots with respect to changes in the concentration of (c) potassium ferricyanide ( $K_3Fe(CN)_6$ ) and (d) ruthenium hexaammine trichloride ( $[Ru(NH_3)_6Cl_3]$ ). The supporting electrolyte was 1.0 M KCl for all solutions.

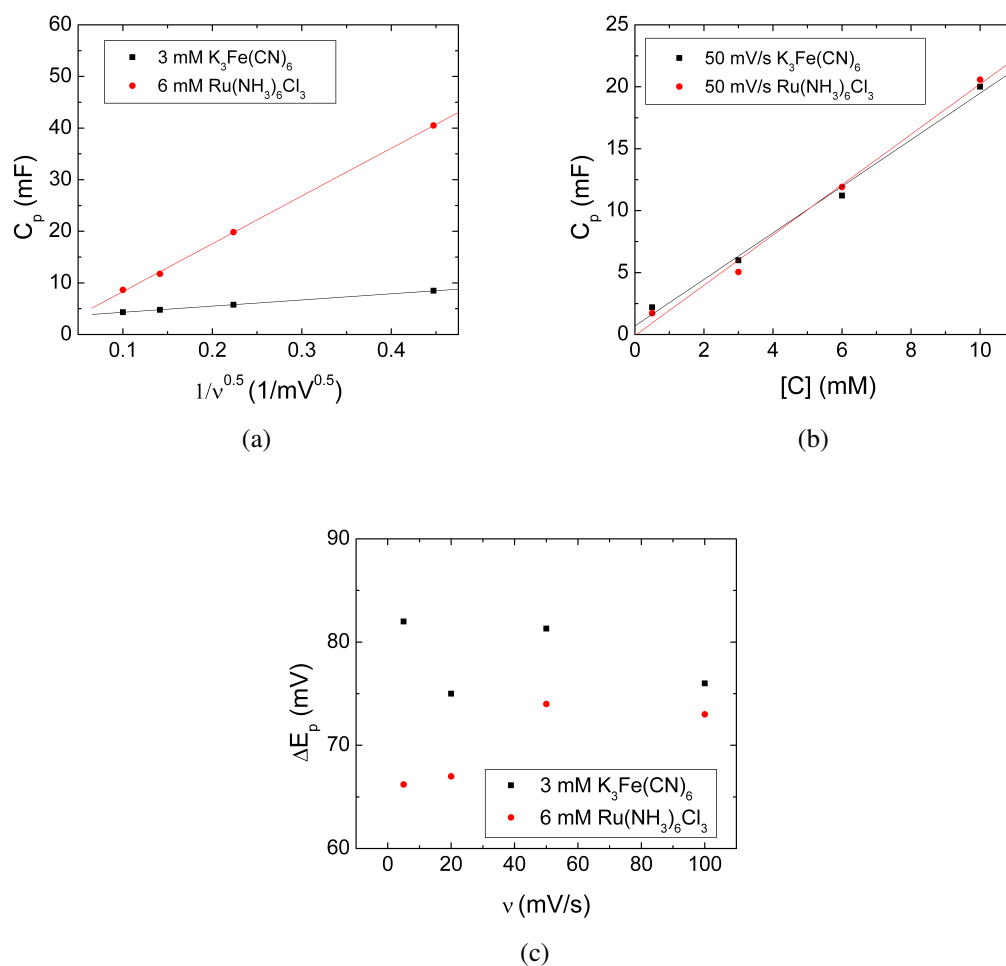


**Figure 4.20:** Peak capacitances as functions of (a) the inverse of the square-root of the scan rate and (b) redox couple concentration.  $\Delta E_p$  as a function of (c) scan rate to determine reversibility.

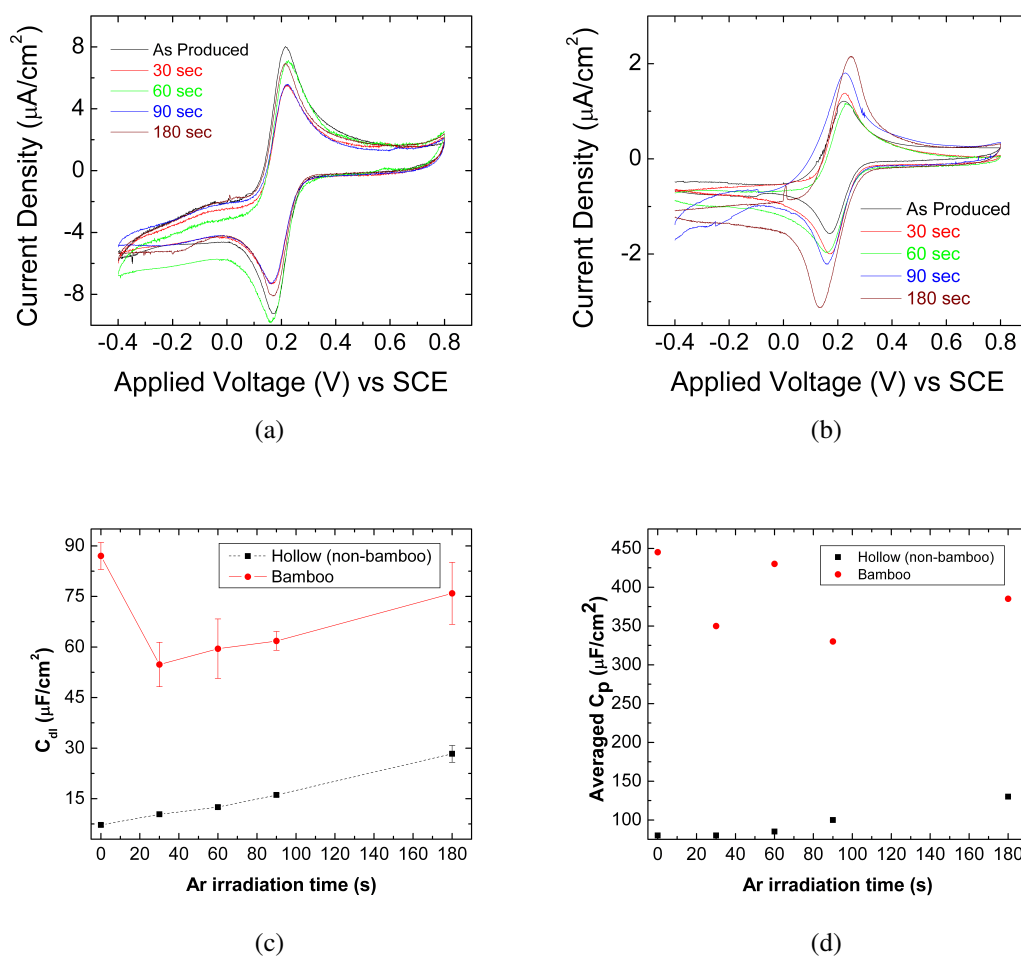


**Figure 4.21:** CV plots of (a) BCNTs and (b) HCNTs with respect to different argon irradiation times, illustrating the changes in the current normalized to the total surface area of the CNTs. The potassium ferricyanide concentration was 3mM in 1 M KCl and the scan rate was 20 mV/s. Changes in (c) double-layer and (d) peak capacitances for BCNTs and HCNTs as a function of RIE irradiation time. The RIE experimental conditions were 30 mTorr, 100 W, with a gas flow rate of 30 SCCM.

The average standard rate constant ( $k_{avg}^{\circ}$ ) was calculated for BCNTs through Equation (4.13) and was determined to be  $2.0 \pm 0.2 \times 10^{-3}$  cm/s. This value of  $k_{avg}^{\circ}$  is taken as the nominal value for edge-plane-like defects since the intrinsic defect density of BCNTs originates from the periodic edge-planes composing the structure of the CNTs. The significant increase in  $\Delta E_p$  for HCNTs at long exposure times may be the result of either increased CNT resistance due to damage induced through defect generation or changes in the double-layer upon charging due to doping. A possible explanation as to which scenario is more probable can be explained by charging the CNTs without sputtering as well as sputtering the CNTs with a subsequent passivation of dangling bonds. Both of these scenarios will be explored in later sections.

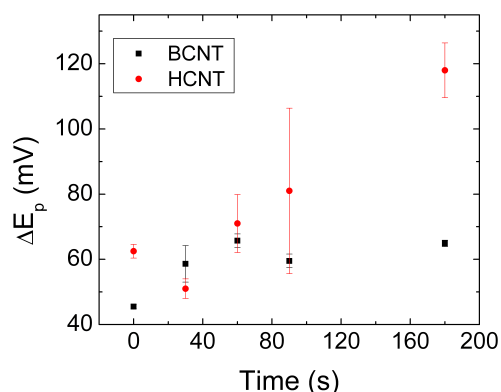


**Figure 4.22:** The effects of Ar plasma irradiation time on electron transfer kinetics are evident for HCNTs and comparatively minute for BCNTs when 3mM of potassium ferricyanide is used with a scan rate of 20 mV/s.

### 4.3.2 Defect Manipulation in Hollow Carbon Nanotubes

Hollow CNTs behave differently than BCNTs since the number of defects intrinsic to HCNTs is less, as illustrated with the Raman spectra presented in Sections 3.6.1 and 3.6.2.2. Since the defect density in HCNTs can increase in HCNTs with Ar and H<sub>2</sub> plasma exposure, the performance of the CNTs should increase with increasing defect density as it is believed that the defect sites act as reaction sites.[96] The following sections will explain in detail the effects of different treatments on the electrochemical performance of CNTs and correlate those changes to the changes observed in the Raman

spectra.

### 4.3.2.1 Increasing Reaction Site Density Through Argon Plasma Irradiation

The first step in understanding how Ar plasma exposure affects the electrochemical performance of HCNTs, is to determine the reversibility of electron transfer at the CNT electrode. A typical data set for Ar treatments as a function of RIE power is illustrated in Figure 4.23.

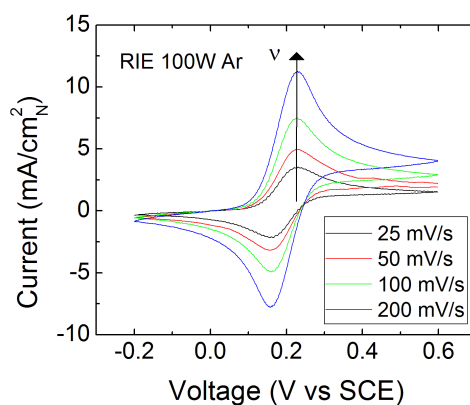


**Figure 4.23:** CV scans as a function of scan rate for a HCNT working electrode treated with Ar plasma at 100W RIE. N denotes the nominal area of 0.25 cm<sup>2</sup>.

For all Ar plasma treated samples, the peak capacitances and peak positions were plotted against  $\frac{1}{\sqrt{v}}$  and  $v$  as described by Equation (4.9) and (4.7) and, respectively, to determine the reversibility as a function of treatment. The results of the CV analysis are illustrated in Figure 4.24.

As can be seen from Figure 4.24, for both RIE and ICP treatments, the average  $C_p$  scales with the inverse of the square root of the scan rate in accordance with the Equation (4.41), the peak current ratio is approximately unity, and  $\Delta E_p$  is not independent of scan rate. The increased peak separation at higher scan rates is indicative of kinetic limitations compared to the scan rate. Furthermore,  $\Delta E_p$  deviations from the ideal value of 59 mV indicate changes in  $R_{ct}$ , mass transfer resistance, or changes in the electrode resistance. Decreases in  $\Delta E_p$  below 59 mV most likely indicate that the redox couple is adsorbed onto the CNT electrode and thus the mass transfer resistance

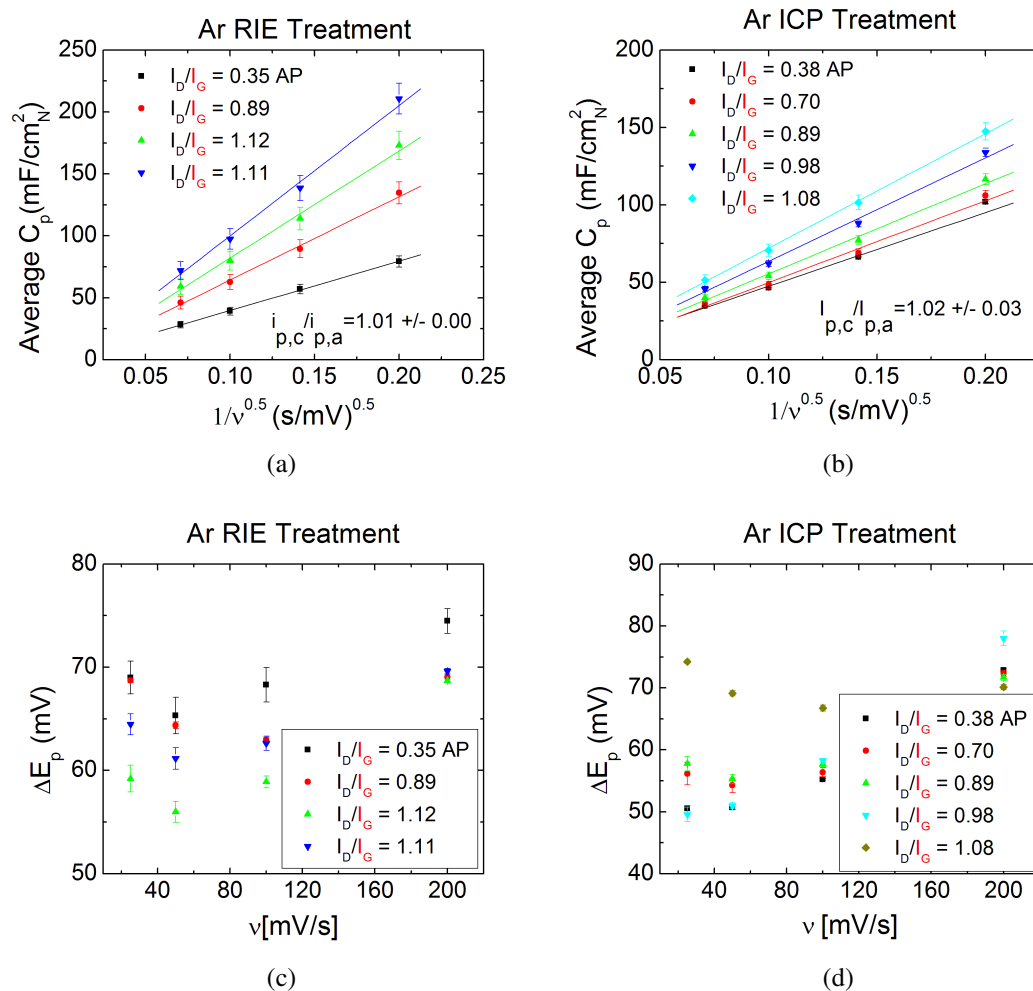


**Figure 4.24:** Plots of  $C_p$  normalized to the nominal area (0.25 cm<sup>2</sup>) as functions of  $\frac{1}{\sqrt{v}}$  for Ar plasma exposure using (a) RIE only and (b) 50W RIE with ICP. (c) and (d) illustrate the shifts in the peak positions with RIE and ICP treatments, respectively. The redox couple used is potassium ferricyanide. The error bars in the figure represent the standard deviation between different trials.



is reduced. Conversely, increases in  $\Delta E_p$  to values greater than 59 mV upon Ar plasma irradiation could arise from increase in the electrode resistance arising from damaging the CNTs through increases in the defect density, increases in  $R_{ct}$  through changes in the defect energy, or through increases in the mass transfer resistance upon charging the CNTs. Charging the CNT electrodes could change the density of ions near the surface of the electrode thus affecting the diffusion of the electroactive species to the electrode. For Ar irradiated CNTs, increases in  $\Delta E_p$  at a given scan rate are hypothesized to come from increases in the electrode resistance or changes in the density of the double-layer.

Several important features of the plots in Figure 4.24 include the increase in the slope in Figures 4.24a and 4.24b and the increases in  $C_p$  with increases in defect density at a given scan rate. As demonstrated with Pt at the beginning of this section, increases in the slope indicates that  $A$  is changing with treatment. However, unlike with the Pt working electrode which has a well defined planar surface area and exhibits ideal, reversible kinetics, the CNT working electrode has a more complicated geometry since the effective surface area of the CNTs may change upon treatment due to increases in number of reaction sites. As the CNTs become more damaged, the vibrational modes in the CNT become more energetic as indicated by the up-shifts in the peak positions of the Raman spectra shown in Section 3.6.2. The increase in energy of the bond vibrations also indicates that they have increased the reactivity. The effects of changing the CNT characteristics upon Ar treatment is also evident in the increased wettability of the CNTs post Ar treatment shown in Figure 4.25. The increase in  $A$  therefore could be attributed to an increase in CNT wetting. However, this is not believed to be the case since if the CNTs were not wettable prior to the electrochemistry experiments, no electrochemistry experiments could be conducted since the CNT electrode would not contact the solution. To wet the CNTs, they were first rinsed with acetone, then rinsed with DI water, and rinsed with 1.0 M  $\text{KCl}_{aq}$  prior to dipping them into solution.

To verify the increases in  $A$  observed in CV experiments,  $A$  was also calculated through EIS experiments with Equation (4.30b), where  $\sigma$  is calculated from the non-linear regression analysis to fit the impedance data in Figure 4.26 to the circuit shown in Figure 4.7. There is a substantial difference in  $A$  depending on the electrochemical experiment, either CV or EIS as shown in Table 4.3. However, these differences can

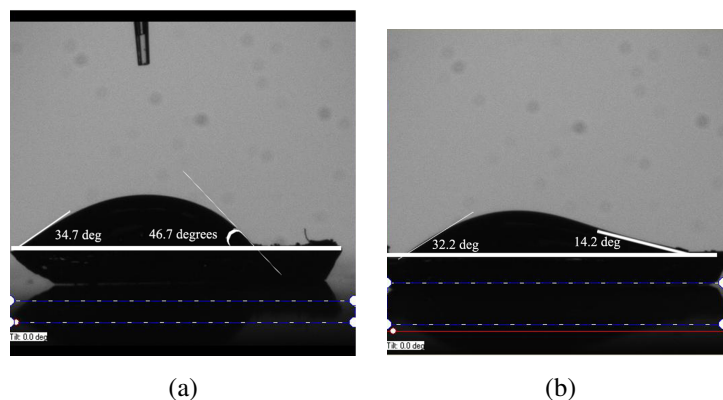


**Figure 4.25:** Contact angle measurements with Ar plasma exposed CNTs. The exposure time for (a) was 30 s, and for (b) was 180s. The difference in the wetting angle in (a) is believed to result from non-uniform Ar plasma exposure of the CNT wafer.

be explained by the state of the system in both experiments. In CV,  $A$  is taken at large voltage deviations from equilibrium and the diffusion layer becomes sufficiently thick to impede faradaic reactions. In EIS experiments, the DC offset voltage was maintained at the open circuit potential, which is the formal potential. The concentration of the oxidized and reduced species of the redox couple are therefore maintained at their equilibrium values and the diffusion layer thickness that forms results from the AC voltage signal. Since the AC voltage polarity changes sinusoidally, the diffusion layer does not have enough time to become as thick as DC based CV experiments as illustrated through Equation (4.26), thus it is negligible in comparison. When the DC offset potential was set to values other than 0, both redox species do not diffuse to and from the electrode as in equilibrium. Diffusion however is impeded as indicated by the non-zero  $R_{ct}$ , which is accompanied by increases in  $A$  to values similar to those determined through CV. The increase in  $A$  with changes in the DC bias illustrates the importance of faradaic reactions on  $A$  through diffusion of the electroactive species to the electrode. Furthermore, the changes in  $A$  with changes in RIE and ICP power are similar between CV and EIS experiments although the  $\frac{A}{A_N}$  ratios are quite different, indicating that the changes in  $A$  upon treatment are indeed real.  $A_N$  is the nominal geometric area of the electrodes,  $\sim 0.25 \text{ cm}^2$ .

The extent to which the different treatments affect both the peak and double-layer

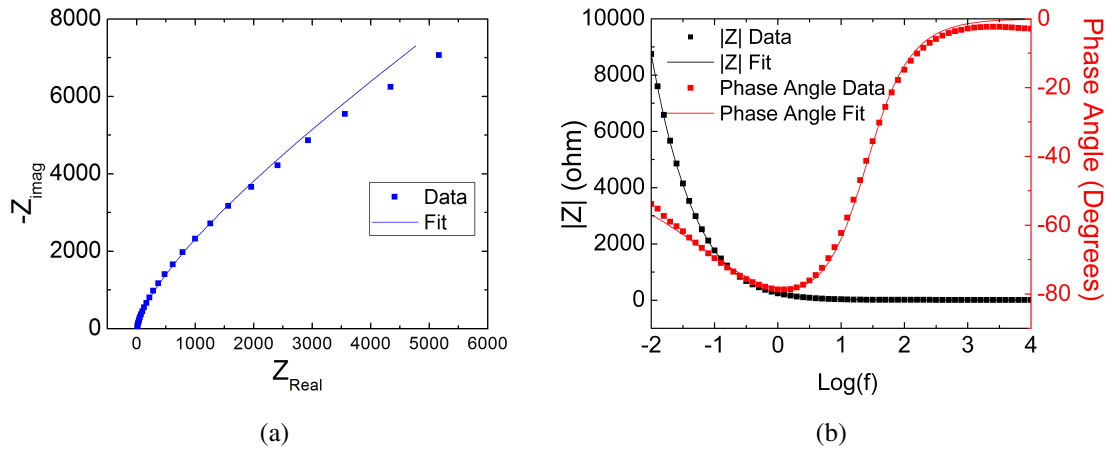


**Figure 4.26:** Typical Nyquist (a) and (b) Bode plots for Ar plasma treated CNTs with an  $5 \text{ mV}_{RMS}$  AC signal and a DC offset of 0 V with respect to the open circuit voltage.

**Table 4.3:** EIS and  $V_d$  Analysis: Ar Plasma

RIE/ICP Power (W)	DC <sub>off</sub> (V)	C <sub>dl</sub> (mF)	R <sub>ct</sub> (Ohm)	R <sub>s</sub> (Ohm)	EIS $\frac{A}{A_N}$	CV $\frac{A}{A_N}$
AP	0	$0.10 \pm 0.02$	0	$11.8 \pm 0.7$	0.12	3.5
50/0	0	$1.14 \pm 0.38$	0	$12.4 \pm 0.7$	0.14	5.8
100/0	0	$3.32 \pm 1.14$	0	$12.4 \pm 0.5$	0.18	6.6
150/0	0	$5.20 \pm 1.76$	0	$11.6 \pm 0.0$	0.22	9.1
AP	0	$0.43 \pm 0.10$	0	$12.4 \pm 1.5$	0.12	4.4
AP	-0.37	$0.44 \pm 0.14$	$(3.3 \pm 0.2) \times 10^3$	$11.8 \pm 0.1$	1.1	4.4
AP	-0.42	$0.60 \pm 0.13$	$(1.6 \pm 0.3) \times 10^3$	$11.6 \pm 0.2$	2.3	4.4
50/0	0	$1.44 \pm 0.49$	0	$12.9 \pm 0.8$	0.31	4.5
50/50	0	$1.48 \pm 0.50$	0	$12.6 \pm 0.4$	0.50	5.0
50/100	0	$3.08 \pm 1.03$	0	$11.8 \pm 0.4$	0.63	5.8
50/150	0	$0.68 \pm 0.23$	0	$13.6 \pm 1.0$	0.55	6.5

capacitance is illustrated in Figure 4.27.

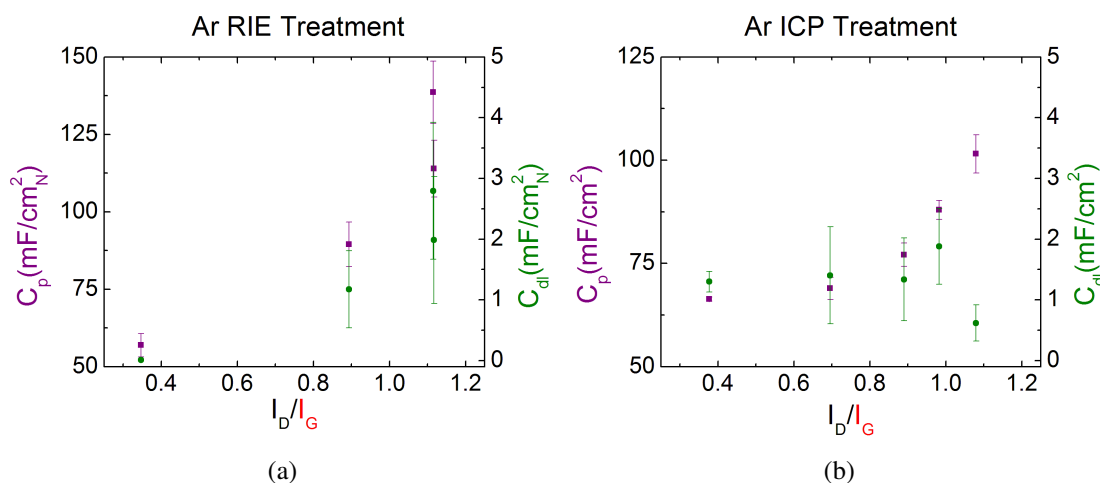


**Figure 4.27:** Peak and double-layer capacitance normalized to the nominal wafer ( $A_N = 0.25 \text{ cm}^2$ ) area for (a) RIE Ar treatments and (b) ICP Ar treatments. The scan rate and potassium ferricyanide concentration were 50 mV/s and 10 mM, respectively.

Since  $C_p$  increases with increasing  $I_D/I_G$ , the induced defects are hypothesized to act as reaction sites. Increasing RIE power however, appears to increase  $C_p$  and  $C_{dl}$  by 37 % and 250 %, respectively, more than changes in ICP power at similar defect densities. The greater sensitivity to RIE treatment can be correlated to changes in the Raman spectra shown in Figures 3.27 and 3.29. The most apparent difference between the RIE and ICP treatments is the difference in changes of the G and D peak widths. For RIE treatments the G and D peak widths change by  $\sim 8 \text{ cm}^{-1}$  and  $\sim 4 \text{ cm}^{-1}$ , respectively, while for ICP treatments the peak widths change by  $\sim 0 \text{ cm}^{-1}$  and  $\sim 12 \text{ cm}^{-1}$ , respectively. These trends in peak width may be the result of the way defects are introduced into the CNTs. It is believed that increasing the plasma density through changes in ICP power induces energetically uniform defects that are not randomly introduced. The defects originating from RIE treatment, conversely, appear to add randomly to the CNTs and thus increase the disorder of the G vibrational mode, as indicated by the increase in the G peak width. The increased disorder of defects introduced through changes in RIE power therefore appears to enhance the effects of a greater number of defects.

To determine the effects of defects and disorder of introduced defects on the

rate of electron transfer, the standard rate constant ( $k^\circ$ ) was calculated from  $\Delta E_p$  using Equation (4.13) and the nominal diffusion coefficient values given in Table 4.2 for all scan rates. The average  $k^\circ$  was then determined over the scan rate range, so that the effect of scan rate on  $\Delta E_p$  would be minimized. Since reactions can occur at all defects and non-defect sites,  $k^\circ$  can be subdivided into contributions from non-edge-plane-defects ( $D^*$ ), edge-plane-like defects ( $D'$ ) and the basal plane (B) such that:

$$k^\circ = k_{D^*}^\circ x_{D^*} + k_{D'}^\circ x_{D'} + k_B^\circ x_B \quad (4.42)$$

where:

$$x_{D^*} + x_{D'} + x_B = 1 \quad (4.43)$$

To determine the influence of edge-plane concentration on  $k^\circ$ ,  $k^\circ$  was plotted as a function of  $\frac{I_{D'}}{I_G}$ , where  $\frac{I_{D'}}{I_G}$  was used to approximate  $x_{D'}$ . At  $\frac{I_{D'}}{I_G} = 0$ , no edge-planes exist and all of the reactivity can be accounted for by non-edge-plane-like defects and the basal plane. Furthermore,  $k^\circ$  is reduced to:

$$k^\circ = k_{D^*}^\circ x_{D^*} + k_B^\circ x_B \quad (4.44)$$

Using  $k_B^\circ = 10^{-9}$ ,  $k_B^\circ x_B$  can be approximated as 0 and Equation (4.44), which represents the y-intercept in Figure 4.28, can be further reduced to:[96]

$$k^\circ = k_{D^*}^\circ x_{D^*} \quad (4.45)$$

As shown in Figure 4.28, the slopes of the trendlines have different signs depending on whether or not RIE or ICP power was changed. However, the negative slope of -1.12 for ICP treatments is not believed to be accurate since it must be non-zero as defined through Equation (4.42). The slope for changes in ICP power is therefore approximated as 0. Edge-plane-like defects originating from changes in ICP power thus do not contribute to faster electron transfer, while those originating from RIE changes increase the rate of electron transfer. Furthermore, the similarity in  $k^\circ$  at  $\frac{I_{D'}}{I_G} = 0$  for both RIE and ICP Ar treatments indicates that non-edge-plane-like defects have a similar affect on kinetics and the concentration of such defects is approximately equal.

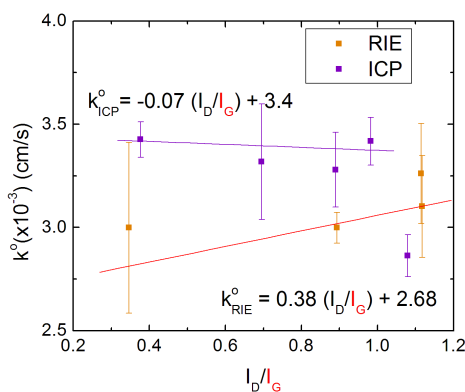


**Figure 4.28:** Determination of the non-edge-plane contribution to the average  $k^\circ$  for ICP and RIE Ar plasma treatments.

### 4.3.2.2 Influence of Hydrogen Treatments on Charge Transfer Kinetics

Hydrogen plasma has the potential to create defects in CNTs through the removal of carbon as well as react with dangling bonds. Section 3.6.3.1 showed that the changes in the peak positions and widths for the D peak were similar to those of the G peak in the Raman spectra. This phenomenon is hypothesized to result from the passivation of dangling bonds created by the removal of carbon atoms during plasma exposure. To investigate whether passivation occurs, CNT electrodes subjected to hydrogen plasma treatment were tested electrochemically through CV, shown in Figure 4.29.

Figures 4.30a and 4.30b illustrate the results of the CV analysis with respect to scan rate. As can be seen from these plots,  $C_p$  follows the dependency on scan rate as determined by Equation (4.41). The peak separation also increases with scan rate, indicating some quasi-reversible behavior.

The most significant difference between Ar and H<sub>2</sub> plasma treatments is the change in  $C_p$  and  $C_{dl}$  with increases in  $I_D/I_G$ . As shown in Figure 4.27, when exposed to Ar plasma the increase in  $I_D/I_G$  is accompanied by increases  $C_p$  and  $C_{dl}$ . Furthermore, Figures 4.24a and 4.24b illustrate an increase in the effective surface area  $A$  as depicted by an increase in slope. However, upon H<sub>2</sub> plasma exposure,  $C_p$  and  $C_{dl}$  decrease with increases in  $I_D/I_G$  as shown in Figure 4.31 and  $A$  decreases as shown in Figures 4.30a and

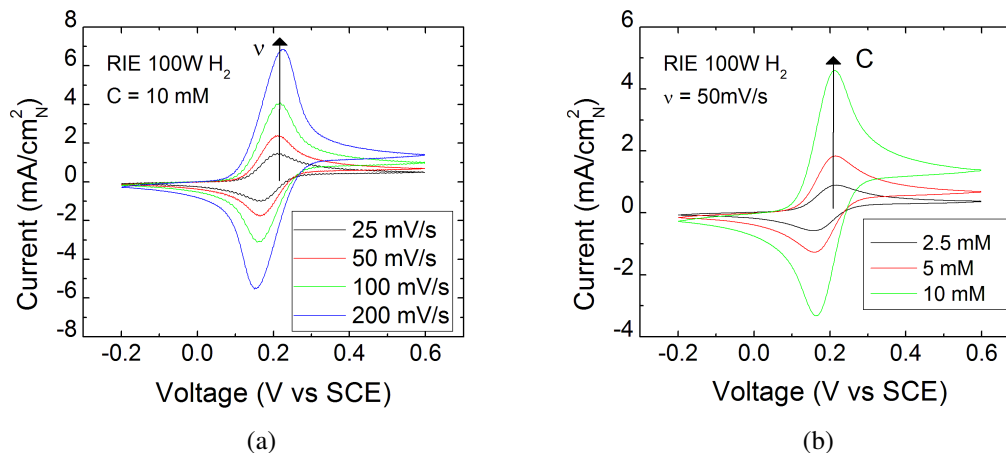


**Figure 4.29:** CV scans as a function of (a) scan rate and (b)  $K_3Fe(CN)_6$  concentration for a HCNT working electrode treated with  $H_2$  plasma at 100W RIE. N denotes the nominal area of  $0.25 \text{ cm}^2$ .

4.30c, where decreases in the slope indicate reductions in  $A$ . The decreases in  $C_p$ ,  $C_{dl}$ , and  $A$  most likely result from defect passivation. When the unpaired electrons comprising dangling bonds react with  $H_3^+$  ions in the plasma defect site reactivity decreases due to an increase in bond stability. Since the changes in the Raman peak positions are small upon hydrogen plasma treatment as explained previously in Section 3.6.3, decreases in  $\Delta E_p$  with increasing hydrogen plasma treatment are hypothesized to originate from a reduction of  $R_{ct}$  or the mass transfer resistance through changes in the ion concentration of the double-layer.

To verify these conclusions,  $A$  and  $R_{ct}$  were calculated from EIS experiments and compared to the values obtained through CV measurements. Bode and Nyquist plots for the  $H_2$  exposure are shown in Figure 4.32 were used to determine the values of  $C_{dl}$ ,  $\sigma$ ,  $R_s$  and  $R_{ct}$  by non-linearly fitting the experimental data to impedance equation based on the circuit diagram shown in Figure 4.7. The results of the EIS experiments and comparison of the experimentally determined value of  $A$  to the nominal value of  $0.25 \text{ cm}^2$  are shown in Table 4.4.

As with the Ar plasma results,  $A$  determined from EIS was much smaller in magnitude than when determined from the CV scans. Unlike before,  $V_d$  increases with

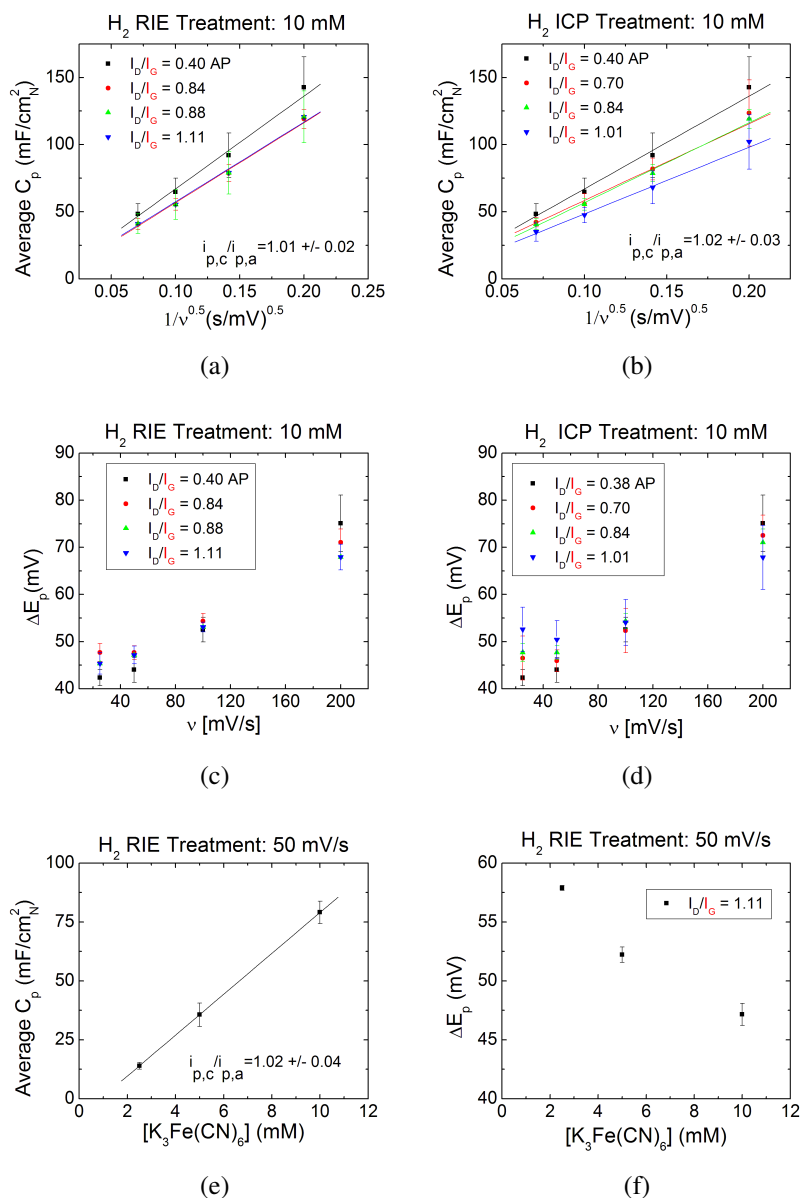


**Figure 4.30:** Plots of  $C_p$  normalized to the nominal area (0.25 cm<sup>2</sup>) as functions of  $\frac{1}{\sqrt{v}}$  for H<sub>2</sub> plasma exposure using (a) RIE only and (b) 50W RIE with ICP. (c) and (d) illustrate the shifts in the peak positions with RIE and ICP treatments, respectively. The redox couple used is 10 mM  $K_3Fe(CN)_6$  in 1.0 M KCl. (e) and (f) illustrate the dependence of  $C_p$  and  $\Delta E_p$  on concentration for RIE treated CNTs. The error bars in the figure represent the standard deviation between different trials.



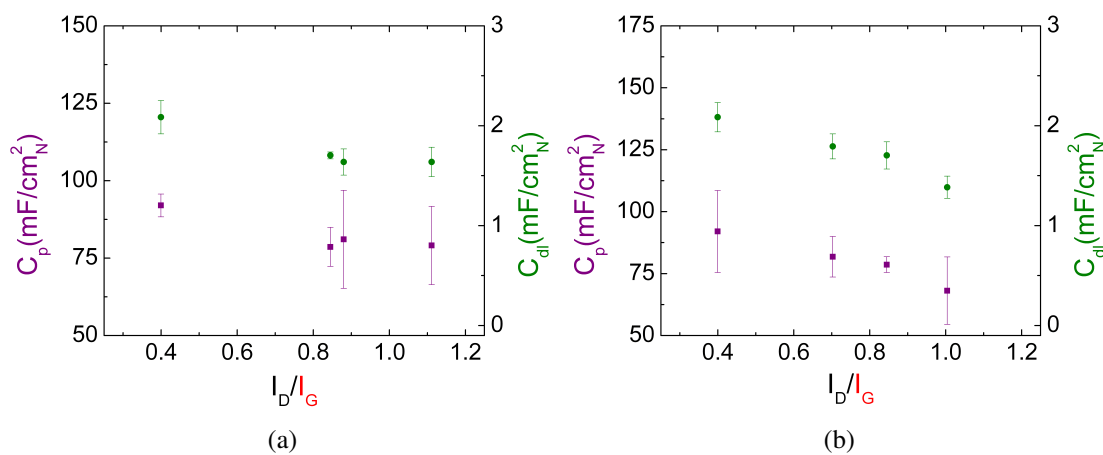


**Figure 4.31:** Peak and double-layer capacitance normalized to the nominal wafer (N) area ( $0.25 \text{ cm}^2$ ) for (a) RIE H<sub>2</sub> treatments and (b) ICP H<sub>2</sub> treatments. The scan rate and potassium ferricyanide concentration were 50 mV/s and 10 mM, respectively.

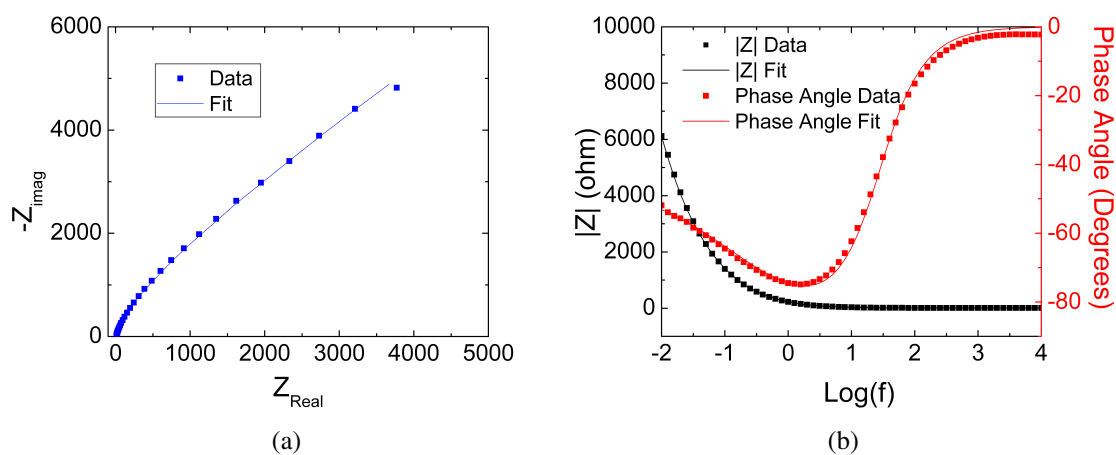


**Figure 4.32:** Typical Nyquist (a) and (b) Bode plots for H<sub>2</sub> plasma treated CNTs with an  $5 \text{ mV}_{RMS}$  AC signal and a DC offset of 0 V with respect to the open circuit voltage.

**Table 4.4:** EIS and  $V_d$  Analysis:  $H_2$  Plasma

RIE/ICP Power (W)	$DC_{off}$ (V)	$C_{dl}$ (mF)	$R_{ct}$ (Ohm)	$R_s$ (Ohm)	EIS $\frac{A}{A_N}$	CV $\frac{A}{A_N}$
AP	0	$0.25 \pm 0.02$	0	$9.8 \pm 0.4$	0.01	3.0
50/0	0	$0.52 \pm 0.07$	0	$11.0 \pm 0.9$	0.04	2.6
100/0	0	$0.29 \pm 0.06$	0	$10.2 \pm 0.5$	0.03	2.6
100/0	0.6	$0.13 \pm 0.08$	$(3.1 \pm 0.7) \times 10^{-2}$	$10.1 \pm 0.6$	0.01	2.6
150/0	0	$0.30 \pm 0.01$	0	$9.6 \pm 0.0$	0.52	2.4
AP	0	$0.25 \pm 0.02$	0	$9.8 \pm 0.4$	0.01	3.0
50/0	0	$0.46 \pm 0.05$	0	$10.3 \pm 0.4$	0.03	2.6
50/50	0	$0.52 \pm 0.07$	0	$11.0 \pm 0.9$	0.04	2.6
50/100	0	$3.91 \pm 0.40$	0	$10.1 \pm 0.2$	0.55	2.2

increasing number of defects when determined from EIS, but decreases when calculated from CV. This apparent difference in the results however can be explained by setting the  $DC_{off}$  potential to a potential other than the equilibrium potential. When this is done ( $DC_{off} = 0.6$  V) the determined value for  $A$  decreases, illustrating the importance of the surface concentration and diffusion layer on  $A$ . For CNT electrodes exposed to  $H_2$  the reduction in  $A$  appears to be correlated to the reduction in reactive sites that results from passivating dangling bonds. When only the open circuit potential is used and the effects of faradaic reactions are reduced, the increase in  $A$  can be attributed to the sputtering of the CNT electrodes.

The standard rate constant for defects was also calculated for RIE and ICP  $H_2$  treatments as shown in Figure 4.33. The small magnitude of the slopes indicate that new edge-plane-like defects do not increase reaction kinetics, which is attributable to the passivation of dangling bonds at edge-plane carbons. Furthermore, the y-intercept values are similar to those calculated for the Ar plasma exposed samples, indicating that the non-edge-plane-like defects contribute equally to  $k^\circ$  and is thus likely to be a function of the intrinsic defects.

It is hypothesized that if hydrogen was indeed reacting with the defect sites, a similar effect would be seen with CNTs exposed to hydrogen exposure in the CVD

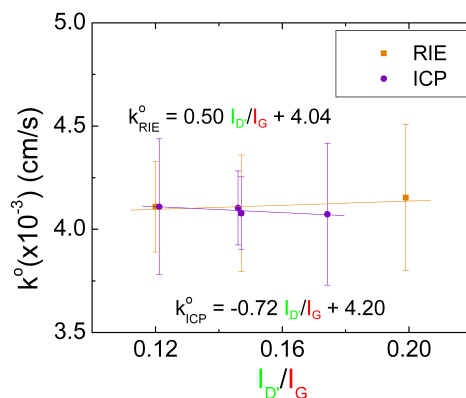


**Figure 4.33:** Determination of the non-edge-plane contribution to the average  $k^\circ$  for ICP and RIE  $H_2$  plasma treatments.

reactor. Some evidence of defect passivation was observed when analyzing the Raman data presented in Chapter 3, Section 3.6.3.2. The impact that defect passivation has on the electrochemical performance of the CNTs however is even more pronounced as in Figure 4.34.

As shown in Figure 4.34b, all CNTs that were exposed to  $H_2$  gas in the CVD reactor displayed decreased peak capacitance. In fact, the reduction of  $C_p$  and  $C_{dl}$  is far greater than that seen for hydrogen plasma in Figure 4.30. For HCNs treated with hydrogen in the CVD reactor, a 12 % reduction in  $\frac{I_D}{I_G}$  results in a 65 % reduction in  $C_p$  and a 89 % reduction in  $C_{dl}$  evaluated at 50 mV/s. However, HCNs treated with hydrogen ions in the plasma using changes in the ICP power, a 250 % increase in  $\frac{I_D}{I_G}$  results in a 24 % reduction in  $C_p$  and a 34 % reduction in  $C_{dl}$  evaluated at 50 mV/s. For plasma treated samples, the difference in reduction of  $C_p$  and  $C_{dl}$  with defect passivation is partially offset by the formation of new defects from sputtering the CNTs. From evaluating  $x$  and  $\omega$  from the Raman spectra for these CNTs, it was not expected that the impact of defect passivation would be so great on the electrochemical performance of the CNTs since the changes in  $x$  and  $\omega$  were relatively small,  $<1$  %. However, realizing that the standard rate constant of the basal plane of graphite is  $\sim 10^7$  times smaller than that of the edge-plane, it would seem that a strong reduction in  $C_p$  would be expected if defects are indeed the charge transfer sites. By reducing the number of reaction sites with hydrogen passivation,  $C_p$  and  $C_{dl}$  are reduced.

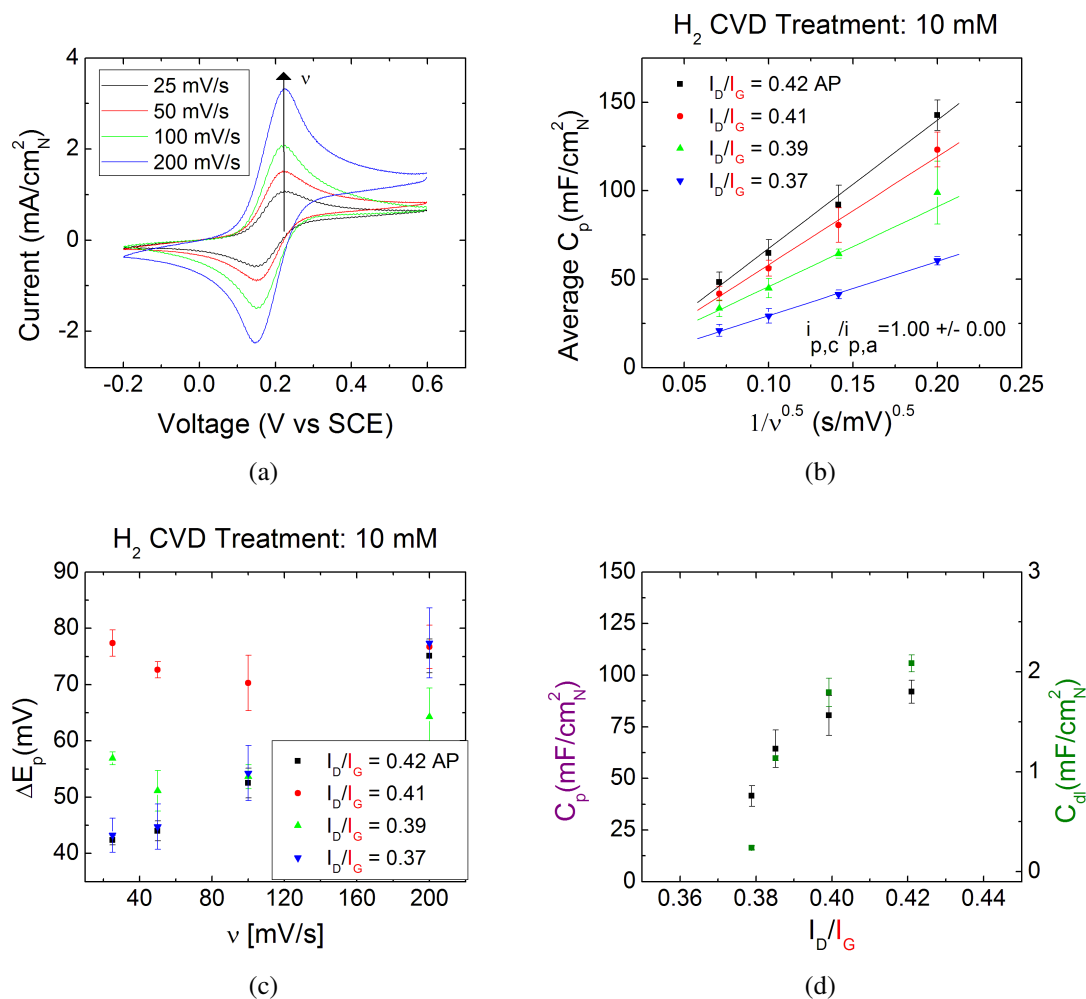


**Figure 4.34:** (a) CV scans as a function of scan rate for a HCNT working electrode treated with H<sub>2</sub> gas in the CVD reactor at 300 °C. (b) Plots of  $C_p$  normalized to the nominal area (0.25 cm<sup>2</sup>) as a function of  $\frac{1}{\sqrt{v}}$ . (c) illustrates the shifts in the peak positions with scan rate. (d) illustrate the dependence of  $C_p$  and  $C_{dl}$  on defect density at 50 mV/s. The error bars in the figure represent the standard deviation between different trials.

### 4.3.2.3 Effects of Chlorine Plasma Reactions at Defects on Reaction Kinetics

Chlorine plasma exposure allowed for the generation of both positive and negatively charged Cl ions through control of the applied RIE and ICP power and pressure. However, in the present experimental setup only positively charged ions can be accelerated towards the CNTs during the processing steps. Any kinetic effects are therefore minimized when negatively charged ions were generated and any defects generated were most likely the result of chlorine reacting with the CNTs as described in Section 3.6.4. The results of generating negatively charged chlorine ions is shown in Figure 4.35.

The CNT electrodes treated with  $\text{Cl}^-$  exhibit quasi-reversible behavior similar to all plasma treated CNTs, where  $C_p$  behaves according to Equation (4.41),  $|\frac{i_{p,c}}{i_{p,a}}| \approx 1$ , yet  $\Delta E_p$  exhibits some dependence on scan rate. The lack of change in the peak capacitance with different treatments is presumably due to lack of significant change in the defect density. Consequently,  $A$  does not change and remains  $\sim 2$  times larger than the nominal value, further indicating that only specific defects are the reaction sites as discussed in Section 4.3.2.2.

The effects of generating positively charged ions in the plasma appear to be similar to those seen for the Ar and  $\text{H}_2$  plasma treatments. Once again  $|\frac{i_{p,c}}{i_{p,a}}| \approx 1$  and the increases in  $C_p$  appear to follow Equation (4.41). For these samples, the change in  $\Delta E_p$  did not show any definitive trends with changes in the scan rate, shown in Figure 4.36, indicating that charge transfer appears to be reversible. The difference between these samples and the other plasma treatment CNTs appears is the origin of defect formation. For Ar treated samples, for instance, new defects resulting from the removal of carbon atoms through sputtering. However, for  $\text{Cl}^+$  treated samples new defects are hypothesized to result from reactions between  $\text{Cl}^+$  and the CNTs, therefore the 230 % increase in  $C_p$  at 25 mV/s results from reactions and not the formation of dangling bonds associated with carbon atom removal.

The influence of ion polarity on rate transfer becomes apparent when calculating  $k^\circ$ , as shown in Figure 4.37. For  $\text{Cl}^-$  treatments,  $k^\circ$  increases with increasing edge-plane-like defect concentration, indicating that contribution to  $k^\circ$  from the new defects becomes increasingly important. The y-intercept for  $\text{Cl}^-$  treatments indicates that

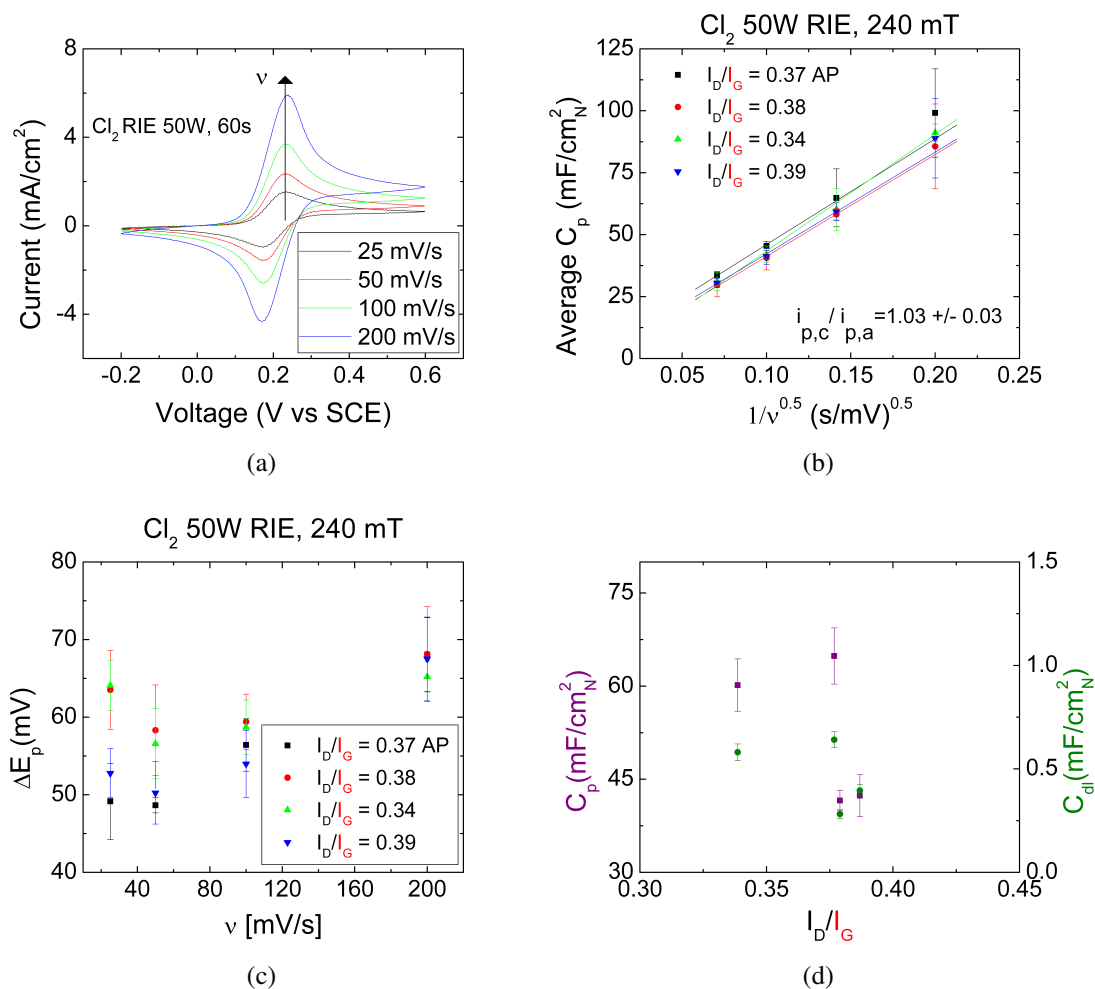


**Figure 4.35:** (a) CV scans as a function of scan rate for a HCNT working electrode treated with  $\text{Cl}_2$  plasma with a RIE power of 50 W at 240 mT for times of 60, 120, and 240 s. (b) Plots of  $C_p$  normalized to the nominal area ( $0.25 \text{ cm}^2$ ) as a function of  $\frac{1}{\sqrt{v}}$ . (c) illustrates the shifts in the peak positions with scan rate. (d) illustrate the dependence of  $C_p$  and  $C_{dl}$  on defect density at 50 mV/s. The error bars in the figure represent the standard deviation between different trials.

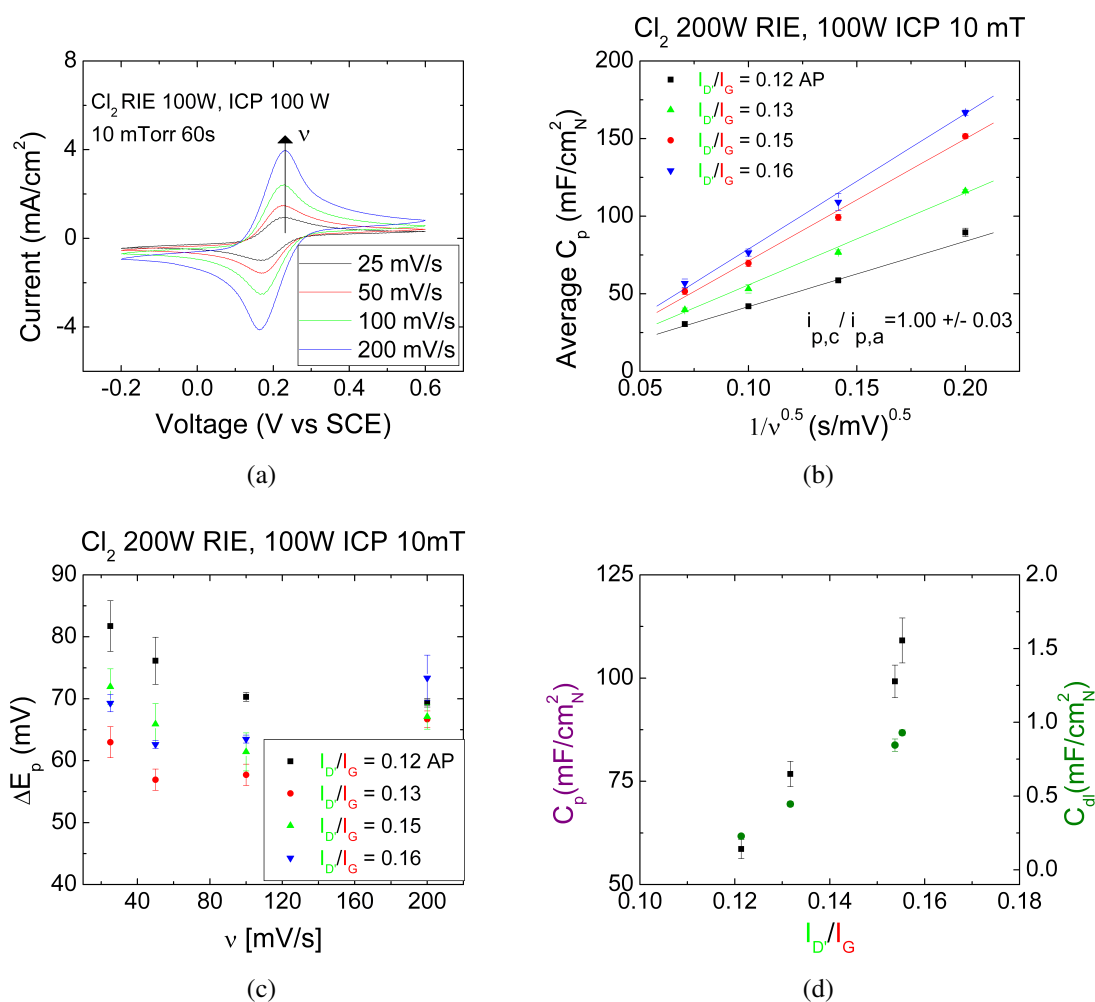


**Figure 4.36:** (a) CV scans as a function of scan rate for a HCNT working electrode treated with  $\text{Cl}_2$  plasma with a RIE power of 200 W and an ICP power of 100 W at 10 mT for times of 60, 120, and 240 s. (b) Plots of  $C_p$  normalized to the nominal area ( $0.25 \text{ cm}^2$ ) as a function of  $\frac{1}{\sqrt{v}}$ . (c) illustrates the shifts in the peak positions with scan rate. (d) illustrate the dependence of  $C_p$  and  $C_{dl}$  on edge-plane-like defect density at 50  $\text{mV}/\text{s}$ . The error bars in the figure represent the standard deviation between different trials.

the intrinsic defects contribute similarly to  $k^\circ$  as observed previously for Ar and  $H_2$ . Conversely, for  $Cl^+$  treatments  $k^\circ$  is much more dependent on  $\frac{I_{D'}}{I_G}$  and the y-intercept is 50 % smaller than the average y-intercept value. The reduction in the y-intercept ( $k^\circ_{D*} x_{D*}$ ) coupled with the increase in the slope indicates that  $Cl^+$  is reacting with intrinsic defects to form edge-plane-like defects, since a reduction in the non-edge-plane-like defect density would decrease  $x_{D*}$  and highlight the importance of charge transfer at edge-plane-like defects.

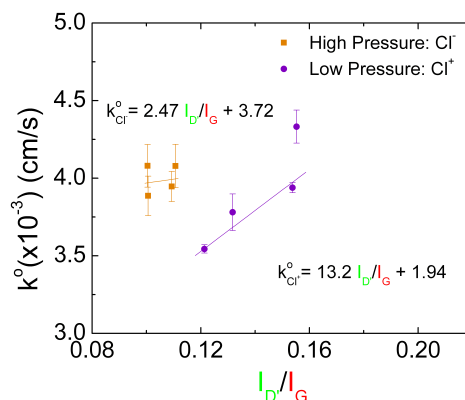


**Figure 4.37:** Determination of the non-edge-plane contribution to the average  $k^\circ$  for ICP and RIE  $Cl_2$  plasma treatments.

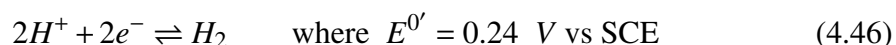
#### 4.3.2.4 Effects of Magnesium Deposition on Double-Layer Capacitance

As demonstrated with the Raman spectra in Section 3.6.5, changes in the CNTs were limited to down-shifts in all peak positions. Down-shifts are typically associated with an increase in  $sp^3$  character or an addition of electron density that lowers bond energy. In the case of magnesium evaporation onto the CNTs, Mg is hypothesized to donate electrons to the CNTs, acting as a n-type dopant. Since the deposition process involves relatively low kinetic energy, the number of defects formed through atomic displacement does not increase. In fact, Mg addition reduces  $\frac{I_D}{I_G}$  and  $\frac{I_{D'}}{I_G}$ , thus the peak capacitances is not expected to increase. Indeed the reduction in  $\frac{I_D}{I_G}$  upon Mg exposure causes a reduction in  $C_p$  as seen in Figures 4.38b and 4.38d. Another important feature of these figures, is the lack of significant change in  $C_p$  for the HCl treated samples,



even though  $\frac{I_p}{I_G}$  increased from  $\sim 0.40$  to  $\sim 0.43$  as illustrated in Figure 3.39d. New defects generated through HCl exposure therefore do not contribute to  $C_p$ . Furthermore,  $C_p$  scales accordingly to  $\frac{1}{\sqrt{v}}$  and  $\frac{i_{p,c}}{i_{p,a}} \approx 1$ . The similarity in all aspects presented in Figure 4.38 of the HCl treated sample and the AP sample indicates that HCl does not produce any substantial changes in the electro-reactivity of the CNTs. The reduction in the peak capacitance for the Mg treated sample is likely caused by the reduced number of effective defects.

The most significant aspects of Mg addition are the changes in the shape of the CV curves, as well as the substantial increase in  $\Delta E_p$  depending on the scan rate. As the scan rate is increased the peaks become distorted and a redox peaks are observed near 0.45 V for the cathodic sweep and -0.1 V for the anodic sweep. Therefore  $E^{0'}$  for this redox couple is  $\sim 0.275$  compared to the SCE. The new peaks are attributed to molecular hydrogen formation from residual acid, which has the following reduction reaction:



Aside from the  $H_2$  redox peaks, no other new peaks are observed indicating that reactions with any residual Mg are not observed. The substantial increase in  $\Delta E_p$  from  $\sim 50$  mV to  $\sim 300$  mV at a scan rate of 200 mV/s is therefore hypothesized to result from changes in the CNT resistance,  $R_{ct}$ , or an increase in the mass transfer resistance due to changes in concentration profiles near the surface of the electrode. Increases in any of these resistances would require a greater potential to be applied at the electrode to induce redox reactions, thus increasing  $\Delta E_p$ .

Since the Mg process involves only the evaporation of the metal onto the CNTs, it is unlikely that atomic displacement occurs in the CNTs and thus the resistance of the CNTs should not change. To measure any effects on  $R_{ct}$  and diffusion, EIS was performed at the open circuit voltage shown in Figure 4.39.

The impedance behavior of the Mg treated CNTs is quite different than that previously observed. At low frequencies the system behaves more like an ideal capacitor as indicated by the vertical line in the Nyquist plot. For electrolytic charge transfer processes this transition can be described by the transition away from a semi-infinite diffusion layer model to a bounded diffusion layer model, where diffusion the process occurs

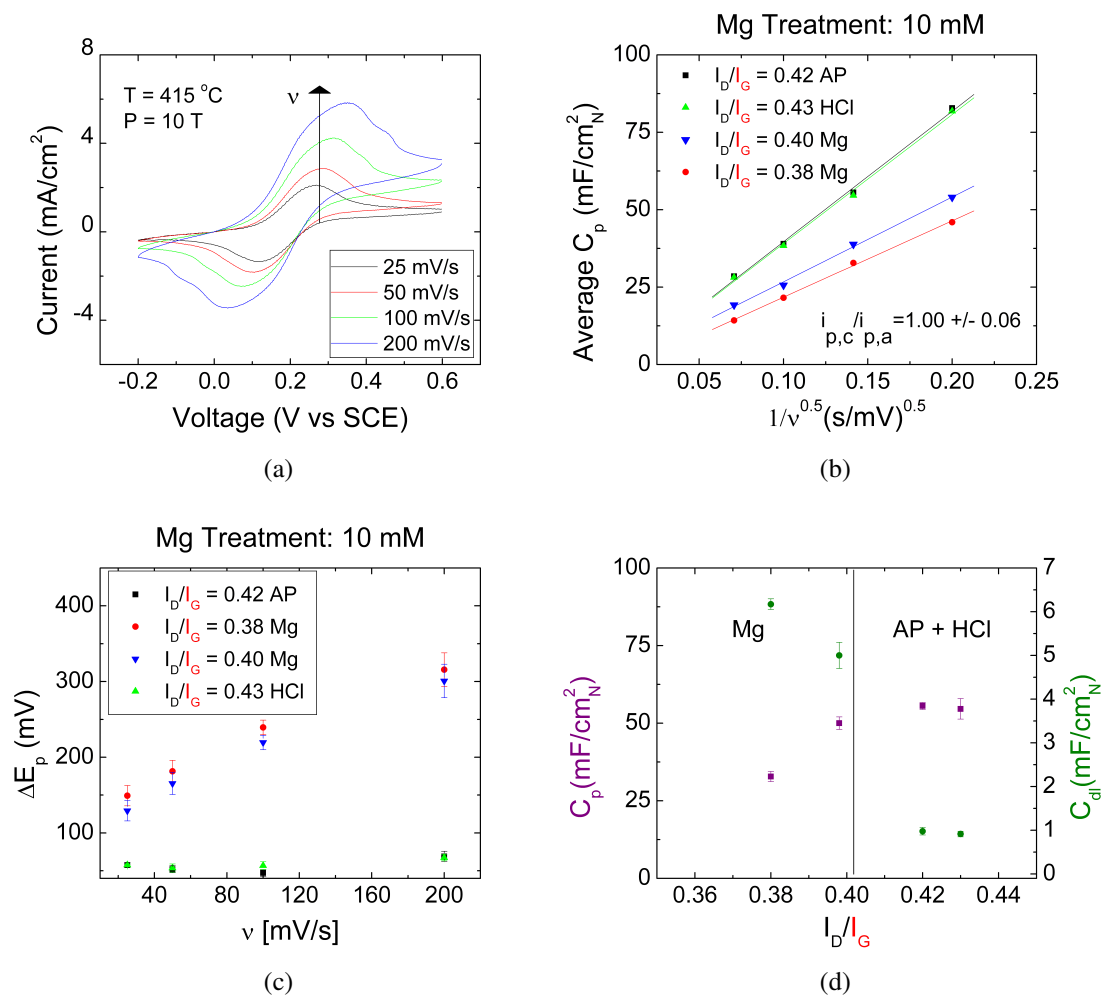


**Figure 4.38:** (a) CV scans as a function of scan rate for a HCNT working electrode treated with Mg evaporated at  $415\text{ }^{\circ}\text{C}$  and a total pressure of 10 Torr. (b) Plots of  $C_p$  normalized to the nominal area ( $0.25\text{ cm}^2$ ) as a function of  $\frac{1}{\sqrt{v}}$ . (c) illustrates the shifts in the peak positions with scan rate. (d) illustrate the dependence of  $C_p$  and  $C_{dl}$  on defect density at 50 mV/s. The error bars in the figure represent the standard deviation between different runs on the same substrate.

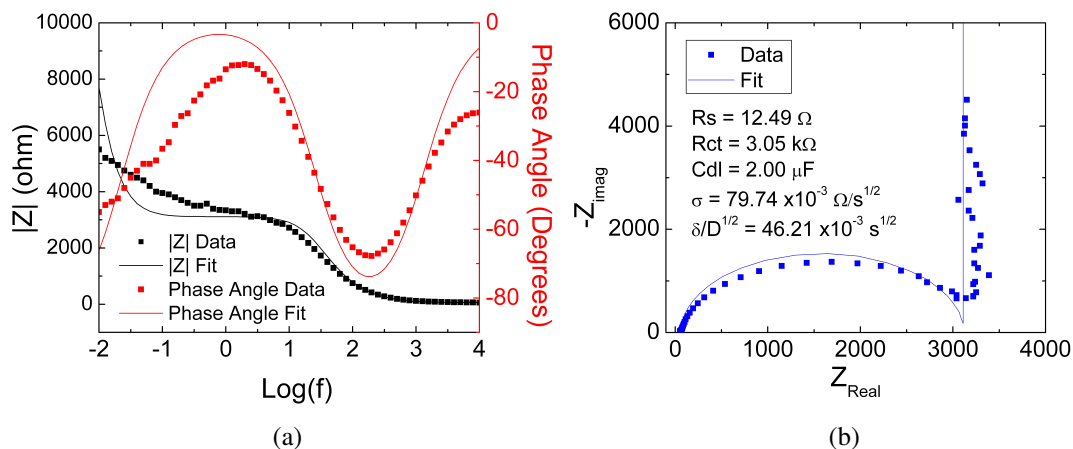


**Figure 4.39:** (a) Bode and (b) Nyquist plots of a typical Mg exposed CNTs in 10 mM potassium ferricyanide with DC bias of 0 V versus the open circuit potential and a AC voltage of 5 mV<sub>RMS</sub>. The circuit model for these fits was similar to that of Figure 4.7, yet the Warburg element was replaced with a bounded Warburg element.

totally within the diffusion layer ( $\delta$ ) and charge transfer at low frequencies does not occur.[97] This bounded diffusion model implies that Mg deposition results in changes in the diffusion processes that dictate how charge transfer and diffusion occurs at the electrode. The bounded diffusion layer model is called a bounded Warburg impedance and is defined as:

$$Z = \left[ \frac{\sqrt{2}\sigma}{\sqrt{j\omega}} \right] \tanh\left( \frac{\delta}{\sqrt{D}} \sqrt{j\omega} \right) \quad (4.47)$$

where  $\sigma$  is the diffusion layer thickness. Using the bounded Warburg impedance model instead of the semi-infinite diffusion model and a nominal  $D$  for  $K_3Fe(CN)_6$ , the diffusion layer thickness is calculated to be 120  $\mu\text{m}$  by fitting the data through non-linear regression analysis to determine  $\frac{\delta}{\sqrt{D}}$ . This value for  $\delta$  is quite close to that calculated from Equation (4.26), which is  $\sim 150 \mu\text{m}$ , indicating that diffusion is restricted to within  $\delta$ . Since no charge transfer occurs at low frequencies,  $R_{ct}$  and  $C_{dl}$  increase when the frequency is low enough such that the system responds as if a DC bias is applied. This hypothesis appears to be supported by nearly 6-fold increase in the double-layer capacitance with Mg exposure as shown in Figure 4.38d.

Finally, if  $k^\circ$  is plotted with respect to the the edge-plane defect concentration as in Figure 4.40 a sharp decrease in  $k^\circ$  is observed as a result of the increase in  $\Delta E_p$ . When extrapolating to  $\frac{I_{D'}}{I_G} = 0$ ,  $k^\circ$  approaches approximately zero, which is equivalent to  $k^\circ$  of the basal plane rate constant of  $\sim 10^{-9}$ . It is hypothesized that Mg can stabilize defects such that the defects become inactive for electron transfer.

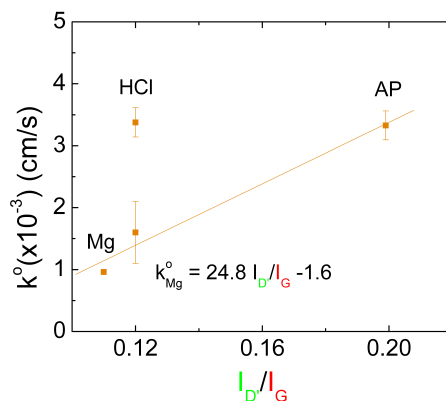


**Figure 4.40:** Determination of the non-edge-plane contribution to the average  $k^\circ$  for Mg treatment.

## 4.4 Summary of Electrochemical Performance

The electrochemical performance of CNTs can be understood through changes in the peak currents and peak positions with respect to changes in scan rate and redox couple concentration. All CNT electrodes tested, exhibit reversible behavior with respect to the peak currents by behaving in accordance to the Randles-Sevcik equation and have a peak current ratio of approximately unity. However, for the systems to demonstrate complete reversibility, they must also show no change in  $\Delta E_p$  with changes in scan rate. For the majority of CNTs,  $\Delta E_p$  did increase for any scan rate greater than 100 mV/s, characteristic of quasi-reversible electron transfer kinetics.

The reasons why the CNTs display quasi-reversible behavior is not directly evident, although the geometry of the CNTs may play a key role in the performance of the CNTs. Utilizing Equation (4.41) for  $C_p$  as determined through CV and EIS spectroscopy, the effective surface area  $S$  can be determined. For all CNT samples under investigation, the CNT separation of  $\sim 100$  nm is much smaller than the diffusion length

on the order of micrometers as calculated through Equation (4.26), where  $t$  is determined by  $\frac{\Delta V}{v}$ . The CNTs electrodes therefore act as macro-like electrodes. However, for all treated CNTs that exhibited increases in  $C_p$ ,  $A$  also increased. Similarly, decreases in  $C_p$  were also accompanied by a decrease in  $A$ . If the projected area of the electrode does not change,  $A$  should remain constant and independent of the experimental setup. Since  $A$  does not remain constant, the surface area of the CNTs is better defined as an active surface area dictated by the number of defect reaction sites.

The variety of different treatments confirmed many of the initial observations gained through Raman spectroscopy. Of these, one clear trend exists with regards to all treatment types: the area of the CNTs available for faradaic reactions to occur is determined by the number of defect sites that can be used as reaction sites. This is explicitly shown when comparing Ar and H<sub>2</sub> plasma treatments. In the case of Ar, both  $C_{dl}$  and  $C_p$  increase proportionally with defect density, while with H<sub>2</sub> plasma increases in the number of defects does not increase  $C_p$ . The difference between the two treatments is explained through the differences in the Raman spectra, where Ar plasma exposure increases the number of dangling bonds, while hydrogen plasma treatment allows for hydrogen ions to passivate the dangling bonds, rendering them electrochemically inert.

The reactivity of molecular hydrogen with the CNTs becomes evident when examining the treatment of CNTs in the CVD reactor with hydrogen gas. Upon exposure the heated H<sub>2</sub> gas, the defect density decreases as monitored through Raman spectroscopy. When the treated CNTs are subsequently used as electrodes,  $C_p$  and  $C_{dl}$  decrease rapidly. Decreases in  $C_p$  were also observed with Mg treatment, but with increased  $C_{dl}$ . It is hypothesized that the addition of Mg affects the surface concentration profiles through the addition of electron density to the CNTs. By n-doping the CNTs, the double-layer may become more compact since the increase in electron density needs to be balanced to maintain charge neutrality. By increasing the concentration of ions near the surface of the CNT electrode  $C_{dl}$  increases. However, the larger concentration of ions near the surface also increases the charge transfer resistance since the separation between the electroactive species and the electrode would increase.

Chapter 4, in part, is a reprint of the material as it appears in “Defect engineering of the electrochemical characteristics of carbon nanotube varieties”, in Journal of

Applied Physics, v.108, n.3, pp.034308, 2010, Hoefer, M. A.; Bandaru, P. R. The dissertation author was the primary investigator and author of this paper.

## 5 CNT Based Capacitor Design and Implementation

The goal of characterizing how defects can be manipulated and created in CNTs is to evaluate how such changes in the CNT structure and electronic properties can be utilized for electrochemical capacitors. Since devices usually have operating restrictions that are often not explored during initial testing, such as elevated temperatures or restrictions on total volume, it is not until prototypes are made that the true performance of CNTs based electrodes can be evaluated. This is especially true with CNTs, as many early predictions of potential applications have yet to be realized, since incorporating CNTs into current devices while maintaining or achieving the theoretical limits of performance is difficult.

Many research groups have implemented CNTs into electrolytic capacitors. The vast majority of these electrodes are formed from free CNTs that are mixed with a paste or gel to provide support and electrical contact to a current collector.[98–106] In this work, CNT based capacitors were assembled according to the schematic illustrated in Figure 5.1 such that the devices utilized a configuration similar to the initial experiments. The major difference between this configuration and that utilized in the 3-electrode setup for initial testing, is the separation of the electrodes by the separator. The separator is a porous membrane used to prevent the net migration of ions to either electrode.

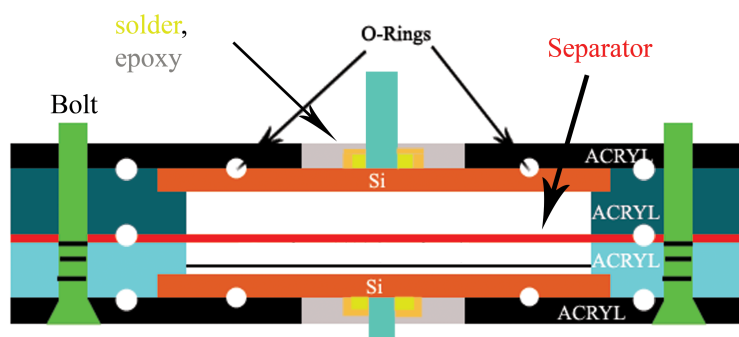


**Figure 5.1:** Schematic of CNT capacitor based device. All materials used were non-metallic to prevent the capacitor from short circuiting, and silicon O-rings were used at all joints to prevent the leakage of electrolyte onto the back contact pad and out of the cell. ACRYL denotes acrylic.

This approach to capacitor design was implemented since several key problems that plague typical electrolytic capacitor design can be avoided. For example, typical de-

signs are comprised of a suspended electrode material that is then subsequently bound to a current collector, both of which can lead to contact resistances greater than 1 Ohm due to poor electrical contact between the CNTs and the current collector. High contact resistances prevent the flow of current and also cause heating of the device leading to premature failure. Furthermore, bundling of CNTs leads to poor faradaic performance as ions can become trapped during cycling, similar to what has been observed for activated carbons and polymer electrodes.[92, 107] By using the growth and defect inducing schemes described in Chapters 2 and 3 it was hypothesized that typical problems associated with peak capacitance decay over lifetime cycling tests could be minimized as the geometry of the CNTs on the Si wafer provides better penetration of the solvent. Also the contact resistance between the current collector (n-doped Si wafer) could be minimized as intimate electrical contact is maintained between the CNTs and the wafer through the catalyst islands that reside on the inside of the multi-walled CNTs.

## 5.1 Testing Methods for Exploring Pseudocapacitance Longevity

All characterization methods used previously with CNT samples were also implemented with the CNT based capacitor devices. In addition to these tests, additional galvanostatic tests described in Section 4.1.3 and outlined in Table 5.1 were also done. Multiple source current magnitudes were used that included 1  $\mu\text{A}$ , 10  $\mu\text{A}$ , 100  $\mu\text{A}$ , 1 mA, and 10 mA. In these experiments, the current was sourced with the same waveform shown in Figure 4.12a. The time for which the current was sourced was set with the Gamry software so that the desired voltage range was realized, where the voltage range is limited by the breakdown voltage of the solvent. The voltage window was limited to  $\pm 0.8\text{V}$  for aqueous solutions, which is smaller than the required voltage of 1.229 V and 1.358 V with respect to the standard hydrogen electrode for water hydrolysis and chlorine gas formation, respectively. For acetonitrile solutions, the dielectric breakdown voltage is  $\sim 3\text{ V}$  therefore the voltage window was restricted to  $\pm 2.5\text{ V}$ .

The effects of redox couple and supporting electrolyte concentration on  $\tau$  and  $R_{ESR}$  were also investigated and summarized in Table 4.1. Additional experiments were also designed to characterize changes of the device upon cycling. To accomplish the cycling tests, the Gamry software was programmed to execute a series of electrochemical tests as shown in Table 5.1. The entire control sequence was looped between 1 and 10



times, for a maximum total of 10,000 galvanostatic cycles. The upper and lower voltage bounds in Table 5.1 are the peak positions of the reduction and oxidation waves.

**Table 5.1:** Capacitor Cycling Characterization

Step	Test	Parameters
1	CV	$\nu = 25, 50, 100, 200 \text{ mV/s}$ $\Delta V = (\text{Voltage Window}) \text{ V}$
2	Delay	15 min
3	EIS	DC = 0 V vs OCP $f = 1 \text{ mHz} - 100 \text{ kHz}$
4	Delay	15 min
5	EIS	DC = $V_{\text{lowerbound}} + 0.1 \text{ V}$ $f = 1 \text{ mHz} - 100 \text{ kHz}$
6	Delay	15 min
7	EIS	DC = $V_{\text{upperbound}} - 0.1 \text{ V}$ $f = 1 \text{ mHz} - 100 \text{ kHz}$
8	Delay	15 min
9	GALV	$\pm i = 1 \mu\text{A}, 10 \mu\text{A}, 100 \mu\text{A}, 1 \text{ mA or } 10 \text{ mA}$ $\Delta V = (\text{Voltage Window}) \text{ V}$ Cycles = 1000

## 5.2 Device Characterization Results

### 5.2.1 Influence of Source Current on Pseudocapacitance

Initial tests were performed to determine how the device would respond to changes in the magnitude of the source current. Ideally, changes in the magnitude of the source current would not change the capacitance of an electrode, if reactions at the electrode are faster than the flux of ions to the surface of the electrode. As mentioned in Chapter 4, Section 4.3, at scan rates greater than 100 mV/s an increase in  $\Delta E_p$  is observed corresponding to quasi-reversible behavior. A similar effect is illustrated in Figure 5.2b. When source currents larger than 1 mA are implemented, the reaction

rate could not support the flux of ions dictated by the input source current as indicated through increases in  $\frac{dV}{dt}$ . Using the definition of capacitance:

$$C = \frac{i}{\frac{dV}{dt}} \quad (5.1)$$

and the capacitance ( $C$ ) calculated from the CV plot in Figure 5.2a of  $\sim 10$  mF in addition to a source current ( $i$ ) of 1 mA,  $\frac{dV}{dt}$  can be calculated near  $E^{0'}$ , since  $E^{0'}$  corresponds to voltages at which redox reactions occur. The experimentally observed  $\frac{dV}{dt}$  when 1 mA current is used was calculated to be approximately 100 mV/s, which is also approximately the scan rate at which deviations in  $\Delta E_p$  were observed.

The lack of symmetry of the CV curve and the galvanostatic curves could result from an unequal amount of CNTs on both wafers or from unequal redox couple concentrations at both electrodes. Differences in CNT mass would result in differing numbers of reaction sites and thus a reduction in  $C_p$ . An inequality in redox couple concentration would similarly affect  $C_p$ . Both of these scenarios were experimentally observed by either (1) diluting to concentration of  $K_3Fe(CN)_6$  in only one half of the capacitor device or (2) intentionally removing CNTs from one electrode.

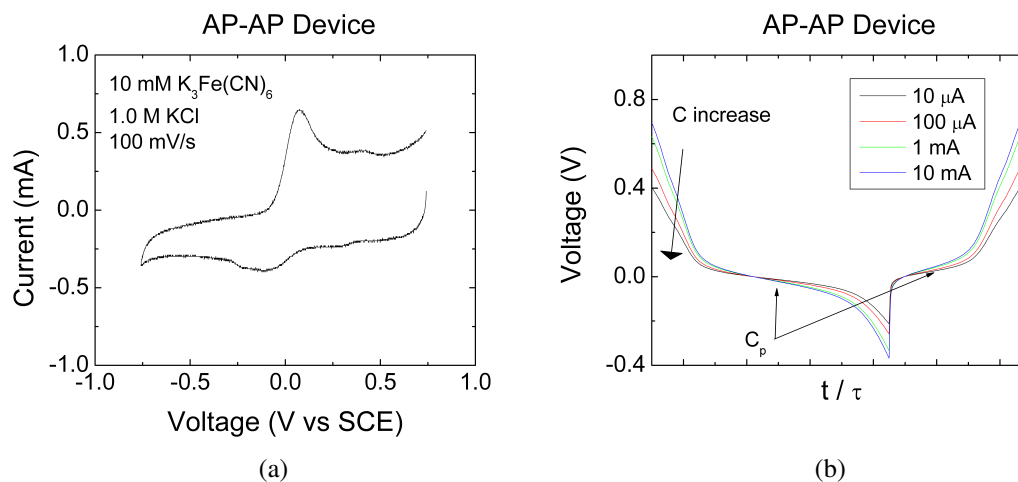


**Figure 5.2:** (a) CV plot for the AP-AP CNT capacitor device. (b) Galvanostatic plots for the same CNT device as a function of different source currents after 1000 cycles.  $\tau$  is the time associated with faradaic reactions described by Equation (4.35).

The cyclability of the CNT electrodes was also performed as a function of source

current as shown in Figure 5.3. The initial changes in the average capacitance most likely originate from concentration gradients existing across the separator, leading to differences in the capacitance of both electrodes comprising the capacitor. The average capacitance was calculated by:

$$C_{avg} = \frac{C_{+i} + C_{-i}}{2} \quad (5.2)$$

The capacitance of the devices does not degrade significantly with the number of cycles up to the maximum of 10,000 cycles, which is major problem with activated carbon supercapacitors due to ion trapping.[92, 107] It is thus hypothesized that the vertical orientation of the CNTs allows for unimpeded diffusion of ions between the CNTs.

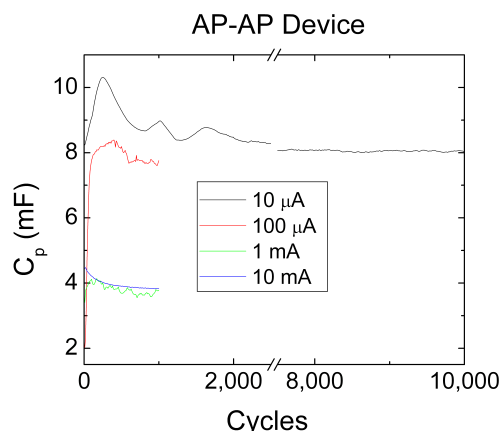


**Figure 5.3:** CNT capacitor performance with respect to the number of cycles for different source currents.  $[K_3Fe(CN)_6] = 10 \text{ mM}$  in  $1.0 \text{ M KCl}$

### 5.2.2 Increasing Capacitance with Concentration

In many instances, the input current for a capacitor will be variable therefore designing a capacitor based on an input current is not necessarily the most comprehensive design strategy. As shown through Equation (5.1), where  $t$  can be replaced by  $\tau$  defined through Equation (4.35), the only ways of increasing the contribution of  $C_p$  to the total capacitance that are independent of the current used are through increasing the redox couple concentration or increasing the area of the electrode. However, if capacitor is restricted in size, increasing the redox couple concentration is the only method to increase  $C_p$ . Figure 5.4 illustrates the effects of increasing the  $K_3Fe(CN)_6$  concentration on  $i_p$

(5.4a) and  $\tau$  (5.4b), which can also be determined through Equations (4.7b) and (4.35), respectively. As can be seen in Figure 5.4a, no redox reactions are observed when the concentration of  $K_3Fe(CN)_6$  is 0 as expected. Adding  $K_3Fe(CN)_6$  to the 1.0 M solution of KCl does produce Fe based redox reactions, yet the two electrodes do not perform equally as evidenced through differences in  $i_p$  for the anodic and cathodic sweeps. Since the CV curves are not symmetric, charge transfer at one electrode is affected either by having less number of reaction sites or the concentration of  $K_3Fe(CN)_6$  is not equal on both sides of the separator. Furthermore, increasing the  $K_3Fe(CN)_6$  concentration from 3 mM to 6 mM does not result in twice the peak current as expected through Equation (4.7b). Since  $i_p$  does not increase proportionally to  $C$ , it is hypothesized that mass transfer to the electrode is impeded when a scan rate of 100 mV/s is used, resulting in a decrease in the surface concentration of  $K_3Fe(CN)_6$ .

Changes in the galvanostatic plot shown in Figure 5.4b also illustrate dependencies on the concentration of  $K_3Fe(CN)_6$ . When no  $K_3Fe(CN)_6$  is present, any increase in the voltage results from charging of the double-layer. However, upon addition of  $K_3Fe(CN)_6$ , definitive changes in the time associate with charging result, i.e. the time needed to span the voltage window of -0.8 V to 0.8 V. These increases are the direct result of faradaic reactions at the electrode, as further evidenced by the increase in the charging time upon doubling the  $K_3Fe(CN)_6$  concentration. The lack of symmetry between positive and negative changes in voltage results from the effectiveness of the electrodes to conduct electricity as mentioned previously with reference to Figure 5.4a.

Since  $C_p$  is a function of redox couple concentration, one method to maximize the capacitance would be to increase the concentration of the redox couple until the solubility limit is achieved. However one drawback from this approach is a potential increase in  $R_s$ . In electrochemical experiments, the purpose of the supporting electrolyte is to increase the conductivity of the solution and prevents net ion migration to the electrodes, therefore the concentration of the supporting electrolyte should be more concentrated than the redox couple. For  $K_3Fe(CN)_6$  and KCl in water, the solubility limits are 1.49 M and 4.54 M, respectively, which is smaller than the concentration ratios used during the characterization experiments of typically 100:1 for KCl: $K_3Fe(CN)_6$ .

Figure 5.5 outlines the effect of high  $K_3Fe(CN)_6$  concentration on both  $i_p$  in CV

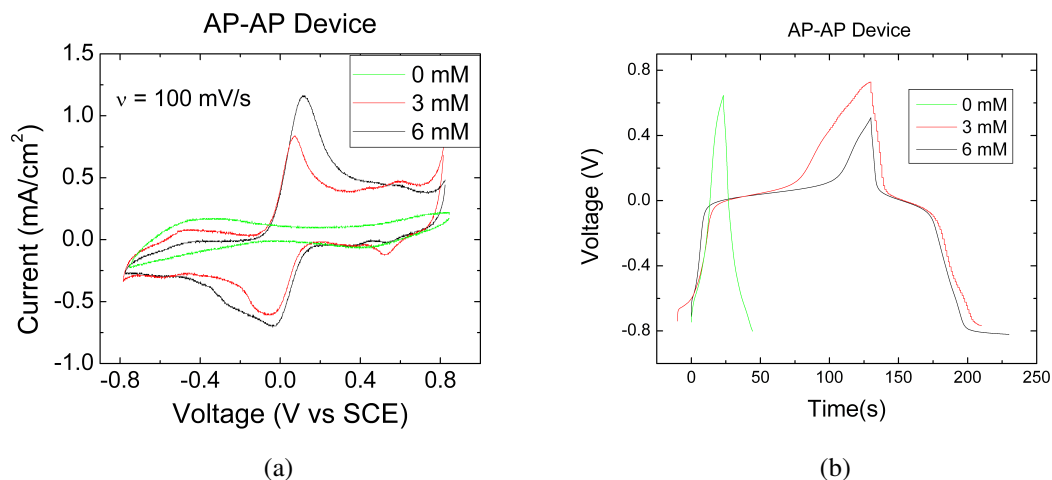


**Figure 5.4:** (a) CV plots for a CNT capacitor device comprised of two as produced (AP) CNT electrodes at different  $K_3Fe(CN)_6$  concentrations in 1.0 M KCl. (b) Galvanostatic plots for the same CNT capacitor device as a function of  $K_3Fe(CN)_6$  concentration after 1000 cycles, when a current of 1 mA is sourced.

experiments and  $\tau$  in galvanostatic experiments for a AP-AP CNT device. When the concentration of  $K_3Fe(CN)_6$  is increased to 100 mM in 1.0 M KCl to from 6 mM in Figure 5.4a,  $i_p$  increases from  $\sim 1.2 \frac{\text{mA}}{\text{cm}^2}$  to  $\sim 20 \frac{\text{mA}}{\text{cm}^2}$ , as predicted by the Randles-Sevcik equation. Consequently, the capacitance of the device is increased to  $\sim 363 \frac{\text{mF}}{\text{cm}^2}$  for a 1 mA source current, as shown in Figure 5.5b. Furthermore, as can be seen in Figure 5.5c,  $\Delta E_p$  increases by a factor of  $\sim 2.6$ , equivalent to a 25 % reduction in  $k^\circ$  calculated through Equation (4.13). Changes in  $\Delta E_p$  induced through changes in  $K_3Fe(CN)_6$  concentration are important to characterize since  $\Delta E_p$  indicates how well the CNT capacitor will perform with high current loads.

### 5.2.3 Performance Increases through Defect Manipulation

The final tests performed on the CNT devices were those on Ar treated CNTs to evaluate if the increase in performance observed for single CNT electrodes corresponds to increased performance when used in a device configuration as well. The results from the galvanostatic and impedance experiments are shown Figure 5.6

As can be seen in Figure 5.6a the time taken to span the voltage window was

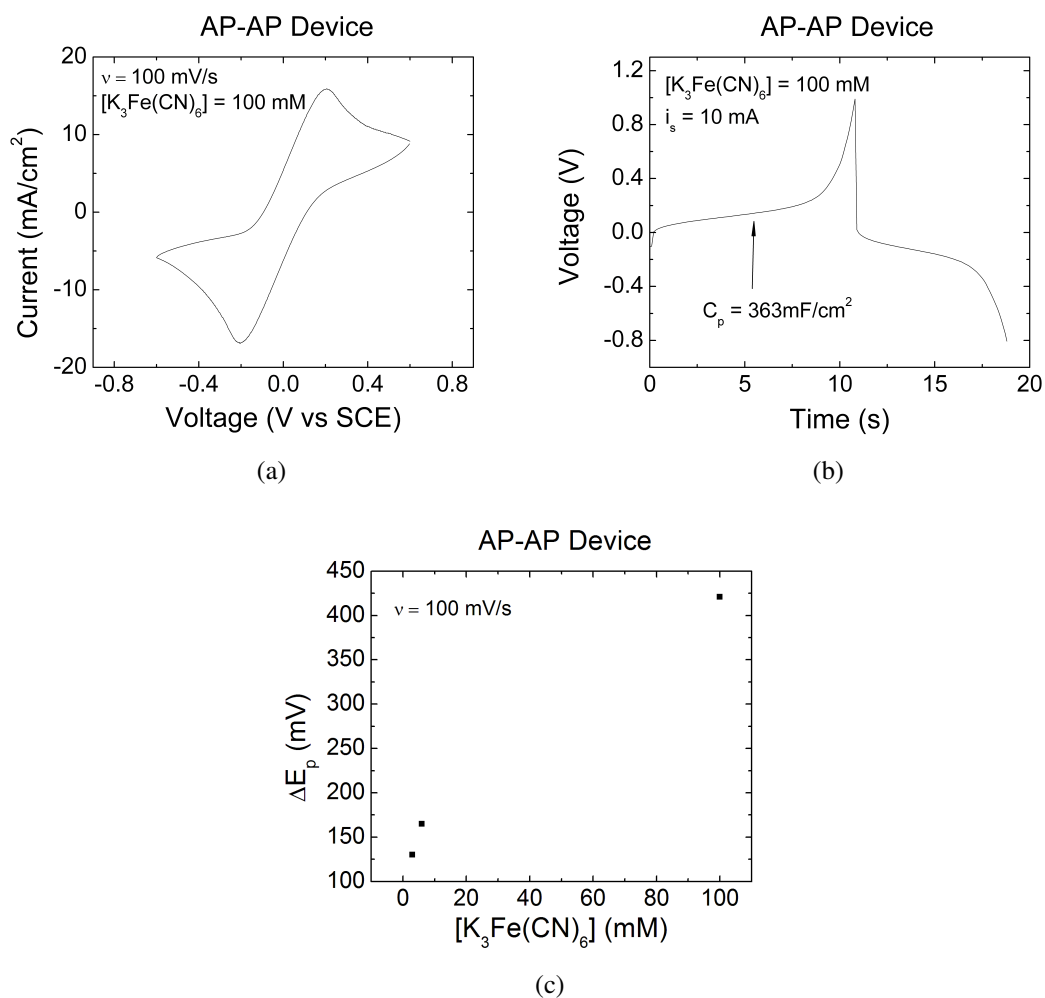


**Figure 5.5:** (a) CV and (b) galvanostatic plots for a AP-AP CNT capacitor device at 100 mM  $\text{K}_3\text{Fe}(\text{CN})_6$  concentration after 1000 cycles with a source current of 10 mA. (a) Plot of peak separation as a function of redox couple concentration, illustrating the effects of high redox couple concentration.

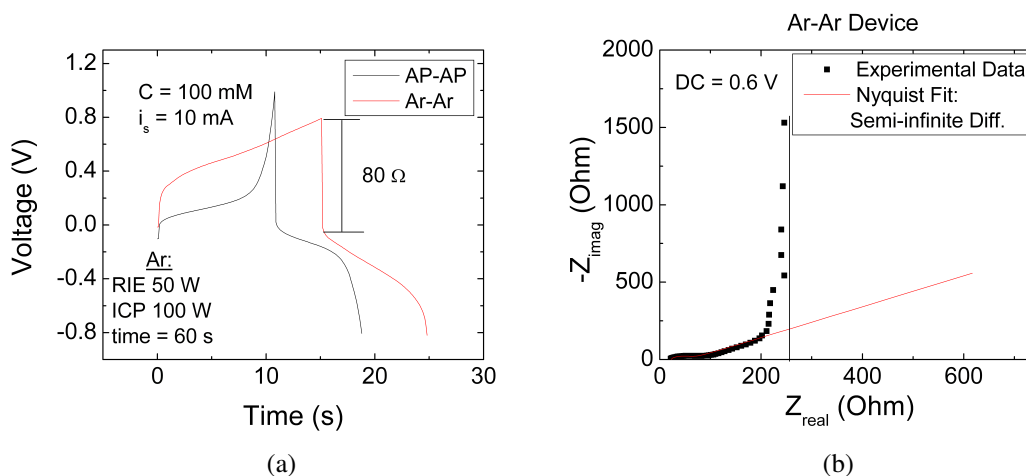


**Figure 5.6:** (a) Galvanostatic plot after 2000 cycles illustrating the effects of Ar plasma exposure for  $[K_3Fe(CN)_6] = 100 \text{ mM}$  and a source current of 10 mA. (b) Nyquist plot of the Ar-Ar CNT device for  $[K_3Fe(CN)_6] = 100 \text{ mM}$  and a  $DC_{offset}$  of 0.6 V.

extended through treatment of the CNT electrodes with Ar plasma, which increased the number of defects and subsequently allowed for a greater number of reactions to occur. If the overall capacitance is calculated, using the full voltage range of 0.8 V, the AP CNT device has a capacitance of  $138 \frac{\text{mF}}{\text{cm}^2}$ , where the Ar treated CNT device has a capacitance of  $192 \frac{\text{mF}}{\text{cm}^2}$  corresponding to an increase of  $\sim 40 \%$ , which is similar to increases in  $C_p$  seen for single wafers for the given exposure parameters discussed in Section 4.3.2.1. The IR drop was determined to be approximately  $80 \Omega$ , which is comprised of the contact resistance, resistance of the electrode,  $R_s$ , and  $R_{ct}$ .

To understand the changes in the galvanostatic plots, EIS was implemented and shown in Figure 5.6b. From the EIS spectra,  $R_s$  and  $R_{ct}$  were determined to be  $22 \Omega$  and  $38 \Omega$ , respectively. A non-zero DC bias voltage was chosen since the concentration of the redox couple was only 1/10th the concentration of the supporting electrolyte, which can have a major impact on  $R_{ct}$ . Comparing  $R_{ct} + R_s$  to the IR drop seen in Figure 5.6a, it appears as if the source for the large voltage drop results from increases in the electrode resistance upon Ar treatment, since the soldered contact between the Si wafer and the attached wire had a resistance less than  $1 \Omega$ .

Another interesting aspect of the Nyquist plot in Figure 5.6b is the transition

to the bounded Warburg impedance circuit element at low frequencies. This behavior has been observed for Mg treated samples seen in Figure 4.39. The similarity between the Mg treated CNTs and Ar treated samples when the concentration of  $K_3Fe(CN)_6$  is increased to 100 mM, may result from an increase in the mass transport of the O/R near the electrode surface arising from increased charge density in the case of Mg treated CNTs and high  $K_3Fe(CN)_6$  concentrations for the present case. This phenomenon may also explain the increase in  $\Delta E_p$  shown in Figure 5.5c.

### 5.3 Summary and Conclusions of CNT Capacitor Performance

Preliminary tests done with CNT electrodes appear promising for several reasons: (a) the capacitance be improved by at least 40 % and (b)  $C_p$  does not degrade significantly up to 10,000 cycles. Further increases in the capacitance beyond the results presented in this work are also feasible through increases in the redox couple until the solubility limit, which could maximize  $i_p$  and subsequently  $C_p$ . The ability to tailor the number of defects also allows for increased faradaic contributions to the total capacitance. Increasing the number of defects also has the added benefit of increasing the number of reaction sites per the same initial volume of starting material, i.e. the effective/contributing area is increased.

Some significant obstacles may also exist, namely the large voltage drop at the switching time in the galvanostatic experiments shown in Figure 5.6a. Ideally, this potential drop would approach zero, indicating no electrical resistance to charge migration. Since this is not the case, these resistances could heat the electrolyte at large source currents, leading to device failure. The contact and solution resistances therefore must be minimized for CNT electrodes to be viable alternatives to electrode materials presently used.



## 6 Conclusions and Potential Future Work

In this work, CNTs were successfully fabricated via a thermal CVD process. The influence of the carbon feed stock and other processing parameters were investigated with respect to structural changes that impact the electrocatalytic ability of the CNTs. To understand exactly what role defects play in electrochemical processes a number of different treatments were employed and monitored through Raman spectroscopy, electrochemistry, and microscopy techniques.

Different CNT morphologies offer differing degrees of susceptibility to post growth processes. Bamboo type CNTs are intrinsically more defect and the defect density is not as easily changes as of hollow type CNTs, where the defect density can be tailored much more readily. The immunity of BCNTs to treatments is believed to result from their high intrinsic defect density and morphological structure, which is defined by a relatively high percentage of edge planes. The edge planes are believed to be the source of the fast electron kinetics associated with CNTs, where the standard rate constant is seven orders of magnitude higher for the edge plane relative to the basal plane. Therefore, high defect density would imply an improved electrocatalytic ability.

As was indicated by the difference in electrochemical performance of Ar and H<sub>2</sub> plasma treated CNT electrodes, the total defect density does not necessarily accurately predict an increase in the electron transfer kinetics. Even within the scope of these two treatment processes, slight differences in the Raman spectra and electrochemical performance occurs whether RIE or ICP power is applied. The dependence on which type of RF source is used appears to indicate a difference in the way atoms, ions, and molecules in the plasma impinge the CNTs. Another possible explanation for the differences in the Raman spectra may be linked to the orientation of the edge plane, either armchair or zigzag, which could not be resolved in this work since the CNTs were characterized on an ensemble basis.

In addition to plasma based treatments, less kinetically energetic processes were used to determine the influence of kinetics and potential n and p type doping of the CNTs. Initial results appear to indicate that Cl<sup>-</sup> and Mg exposure may lead to the n-doping of CNTs at defect locations. The most apparent indication of this phenomenon is the relative changes in the double-layer and pseudocapacitances and impedance spectroscopy of Mg treated CNT electrodes, with respect to one another. This phenomenon

is very exciting as n-type CNTs are inherently difficult to create due to the reactivity of currently used dopant metals and the subsequent p-doping of the CNTs upon exposure with air. The use of Mg to n-dope CNTs appears to avoid both of these pitfalls and therefore should be explored further.

Finally, the use of CNT electrodes in capacitor devices was explored. The vertical alignment of the CNTs relative to the current collector allows for the free flow of ions between the CNTs giving the redox couple maximum mobility. The intimate electrical contact between the current collector and the CNTs also makes them ideal candidates for electrochemical capacitor implementation, since the CNTs can carry large currents with little impact on the CNTs themselves due to their structural robustness. These two features coupled together result in key features such as the long cycle lifetime of the pseudo capacitance, where up to 10,000 cycles with minimal decreases in the overall capacitance has been observed. The improvements seen with single CNT electrodes can also be translated to CNT devices allowing for significant improvements over as produced CNTs.

The vast majority of electrochemical tests described in this work involved the use of aqueous solvents. The benefits of aqueous solvents are the ease of use, relatively high ion conductivities, and well established reaction kinetics. Aqueous solutions however have relatively small dielectric breakdown voltages, which limit the energy density as described through:

$$\xi = \frac{CV^2}{2m} \quad (6.1)$$

where  $m$  is the mass,  $C$  is capacitance, and  $V$  is the voltage window. Organic solvents offer much larger breakdown voltages, yet have lower conductivities reducing the power density. The interplay between power and energy density and the solvent system, needs to be explored to realize the full electrochemical potential of CNT electrodes. Future experiments would therefore involve refinements in the solvent system to increase the voltage window while maintaining high conductivity through large solubility limits of dissolved salts at room temperature and redox couple choice to elucidate any performance trends.

## Bibliography

- [1] Michele Meo and Marco Rossi. Prediction of young's modulus of single wall carbon nanotubes by molecular-mechanics based finite element modelling. *Composites Science and Technology*, 66(11):1597 – 1605, 2006.
- [2] Mukul Kumar and Yoshinori Ando. Chemical vapor deposition of carbon nanotubes: A review on growth mechanism and mass production. *Journal of Nanoscience and Nanotechnology*, 10(6):3739–3758, 2010.
- [3] Ming Lin, Joyce Pei Ying Tan, Chris Boothroyd, Kian Ping Loh, Eng Soon Tok, and Yong-Lim Foo. Dynamical observation of bamboo-like carbon nanotube growth. *Nano Letters*, 7(8):2234–2238, 2007.
- [4] F. Banhart, J. Kotakoski, and A. Krashenninnikov. Structural defects in graphene. *ACS Nano*, 5(1):26–41, 2010.
- [5] J. Robertson L. Li, S. Reich. Defect energies in graphite: Density-functional calculations. *Physics Review B*, 72(18):184109, 2005.
- [6] M. Lusk, D. Wu, and L. Carr. Graphene nanoengineering and the inverse stone-thrower-wales defect. *Physical Review B*, 81:155444, Apr 2010.
- [7] H. Choi, M. Shim, S. Bangsaruntip, and H. Dai. Spontaneous reduction of metal ions on the sidewalls of carbon nanotubes. *Journal of the American Chemical Society*, 124(31):9058–9059, 2002.
- [8] Y. Sun, F. Kefu, Y. Lin, and W. Huang. Functionalized carbon nanotubes: Properties and applications. *Accounts of Chemical Research*, 35(12):1096–1104, 2002.
- [9] Y. Zhao and J. Fraser Stoddart. Noncovalent functionalization of single-walled carbon nanotubes. *Accounts of Chemical Research*, 42(8):1161–1171, August 2009.
- [10] M. Zhang and J. Li. Carbon nanotube in different shapes. *Materials Today*, 12(6):12 – 18, 2009.
- [11] P. Bandaru, S C. Daraio, and A. Rao Jin. Novel electrical switching behaviour and logic in carbon nanotube y-junctions. *Nature Materials*, 4(9):663–666, September 2005.
- [12] N. Rodriguez, A. Chambers, and R. Baker. Catalytic engineering of carbon nanostructures. *Langmuir*, 11(10):3862–3866, 1995.
- [13] Teri Wang Odom, Jason H. Hafner, and Charles M. Lieber. *Topics in Applied Physics*, volume 80. Springer Berlin / Heidelberg, 2010.
- [14] Steven G. Louie. *Topics in Applied Physics*, volume 80. Springer Berlin / Heidelberg, 2010.

- [15] M. Dresselhaus, G. Dresselhaus, R. Saito, and A. Jorio. Raman spectroscopy of carbon nanotubes. *Physics Reports*, 409(2):47 – 99, 2005.
- [16] J. Robertson. Diamond-like amorphous carbon. *Materials Science and Engineering: R: Reports*, 37(4-6):129 – 281, 2002.
- [17] S. Nunomura and M. Kondo. Characterization of high-pressure capacitively coupled hydrogen plasmas. *Journal of Applied Physics*, 102(9):093306, 2007.
- [18] Kouichi Ono, Mutumi Tuda, Hiroki Ootera, and Tatsuo Oomori. Electron cyclotron resonance plasma etching of si with  $c_{12}$ : plasma chemistry and mechanisms. *Pure and Applied Chemistry*, 66(6):1327–1334, 1994.
- [19] Ellen Meeks and Jong Won Shon. Modeling of plasma-etch processes using well stirred reactor approximations and including complex gas-phase and surface reactions. *IEEE Transactions on Plasma Science*, 23:539–549, 1995.
- [20] L. Cancando, M. Pimenta, B. Neves, M. Dantas, and A. Jorio. Influence of the atomic structure on the raman spectra of graphite edges. *Physical Review Letters*, 93:247401, Dec 2004.
- [21] Peter T. Kissinger, Jonathan B. Hart, and Ralph N. Adams. Voltammetry in brain tissue - a new neurophysiological measurement. *Brain Research*, 55(1):209 – 213, 1973.
- [22] Allen Bard and Larry Faulkner. *Electrochemical Methods: Fundamentals and Applications 2nd ed.* New York: John Wiley & Sons, 2001.
- [23] Hiroaki Matsuda and Yuzo Ayabe. Zur theorie der randles-sevcikschen kathodenstrahl-polarographie. *Zeitschrift fuer Elektrochemie, Berichte der Bunsengesellschaft fuer physikalische Chemie*, 59(6):494–503, 1955.
- [24] Hideyuki Kazumi and Kazutami Tago. Analysis of plasma chemical reactions in dry etching of silicon dioxide. *Japan Journal of Applied Physics*, 34(4B):212–2131, April 1995.
- [25] U. Kelkar, M. Gordon, L. Roe, and Y. Li. Diagnostics and modeling in a pure argon plasma: Energy balance study. *Journal of Vacuum Science & Technology A: Vacuum, Surfaces, and Films*, 17(1):125–132, 1999.
- [26] Osamu Fukumasa, Ryohei Itatani, Setsuo Saeki, Katashi Osaki, and Satoshi Sakiyama. Wall effects on the percentage of atomic ions in a hydrogen plasma. *Physics Letters A*, 100(4):186 – 190, 1984.
- [27] Min-Feng Yu, Oleg Lourie, Mark J. Dyer, Katerina Moloni, Thomas F. Kelly, and Rodney S. Ruoff. Strength and breaking mechanism of multiwalled carbon nanotubes under tensile load. *Science*, 287(5453):637–640, 2000.

- [28] Seunghun Hong and Sung Myung. Nanotube electronics: A flexible approach to mobility. *Nature Nanotechnology*, 2(4):207–208, 2007.
- [29] Kenji Hata, Don N. Futaba, Kohei Mizuno, Tatsunori Namai, Motoo Yumura, and Sumio Iijima. Water-assisted highly efficient synthesis of impurity-free single-walled carbon nanotubes. *Science*, 306(5700):1362–1364, 2004.
- [30] R. Lacerda, A. Teh, M. Yang, K. Teo, N. Rupesinghe, S. Dalal, K. Koziol, D. Roy, G. Amaratunga, W. Milne, M. Chhowalla, D. Hasko, F. Wyczisk, and P. Legagneux. Growth of high-quality single-wall carbon nanotubes without amorphous carbon formation. *Applied Physics Letters*, 84(2):269–271, 2004.
- [31] Don Futaba, Kenji Hata, Takeo Yamada, Kohei Mizuno, Motoo Yumura, and Sumio Iijima. Kinetics of water-assisted single-walled carbon nanotube synthesis revealed by a time-evolution analysis. *Physical Review Letters*, 95:056104, Jul 2005.
- [32] Lingbo Zhu, Yonghao Xiu, Dennis W. Hess, and Ching-Ping Wong. Aligned carbon nanotube stacks by water-assisted selective etching. *Nano Letters*, 5(12):2641–2645, 2005.
- [33] YeoHeung Yun, Vesselin Shanov, Yi Tu, Srinivas Subramaniam, and Mark J. Schulz. Growth mechanism of long aligned multiwall carbon nanotube arrays by water-assisted chemical vapor deposition. *The Journal of Physical Chemistry B*, 110(47):23920–23925, 2006.
- [34] Chao Hsun Lin, Hui Lin Chang, Chih Ming Hsu, An Ya Lo, and Cheng Tzu Kuo. The role of nitrogen in carbon nanotube formation. *Diamond and Related Materials*, 12(10-11):1851 – 1857, 2003. Proceedings of the 8th International Conference on New Diamond Science and Technology.
- [35] Lingbo Zhu, Jianwen Xu, Fei Xiao, Hongjin Jiang, Dennis W. Hess, and C.P. Wong. The growth of carbon nanotube stacks in the kinetics-controlled regime. *Carbon*, 45(2):344 – 348, 2007.
- [36] Qingwen Li, Xiefei Zhang, Raymond DePaula, Lianxi Zheng, Yobhao Zhao, Lilian Stan, Terry Holesinger, Paul Arendt, Dean Peterson, and Yuntian Zhu. Sustained growth of ultralong carbon nanotube arrays for fiber spinning. *Advanced Materials*, 18(23):3160–3163, 2006.
- [37] Ge Li, Supriya Chakrabarti, Mark Schulz, and Vesselin Shanov. Growth of aligned multiwalled carbon nanotubes on bulk copper substrates by chemical vapor deposition. *Journal of Materials Research*, 24:2813–2820, 2009.
- [38] Christian P. Deck and Kenneth Vecchio. Growth mechanism of vapor phase cvd-grown multi-walled carbon nanotubes. *Carbon*, 43(12):2608 – 2617, 2005.

- [39] T. de los Arcos, F. Vonau, M. Garnier, V. Thommen, H. Boyen, P. Oelhafen, M. Düggelin, D. Mathis, and R. Guggenheim. Influence of iron-silicon interaction on the growth of carbon nanotubes produced by chemical vapor deposition. *Applied Physics Letters*, 80(13):2383–2385, 2002.
- [40] Christian P. Deck and Kenneth Vecchio. Prediction of carbon nanotube growth success by the analysis of carbon– – –catalyst binary phase diagrams. *Carbon*, 44(2):267 – 275, 2006.
- [41] Qi-Gao Zhu, Hiroshi Iwasaki, Ellen Williams, and Robert Park. Formation of iron silicide thin films. *Journal of Applied Physics*, 60(7):2629–2631, 1986.
- [42] I. Lebedeva, A. Knizhnik, A. Gavrikov, A. Baranov, B. Potapkin, S. Aceto, P. Bui, C. Eastman, U. Grossner, D. Smith, and T. Sommerer. First—principles based kinetic modeling of effect of hydrogen on growth of carbon nanotubes. *Carbon*, 49(7):2508 – 2521, 2011.
- [43] Wei Chen, Xiulian Pan, Marc-Georg Willinger, Dang Shen Su, and Xinhe Bao. Facile autoreduction of iron oxide/carbon nanotube encapsulates. *Journal of the American Chemical Society*, 128(10):3136–3137, 2006.
- [44] Y. Wang, J. Lin, C. Huan, and G. Chen. Synthesis of large area aligned carbon nanotube arrays from  $C_2H_2 - H_2$  mixture by rf plasma-enhanced chemical vapor deposition. *Applied Physics Letters*, 79(5):680–682, 2001.
- [45] Cinar Öncel and Yuda Yürüm. Carbon nanotube synthesis via the catalytic cvd method: A review on the effect of reaction parameters. *Fullerenes, Nanotubes and Carbon Nanostructures*, 14(1):17–37, 2006.
- [46] Kohei Mizuno, Kenji Hata, Takeshi Saito, Satoshi Ohshima, Motoo Yumura, and Sumio Iijima. Selective matching of catalyst element and carbon source in single-walled carbon nanotube synthesis on silicon substrates. *The Journal of Physical Chemistry B*, 109(7):2632–2637, 2005.
- [47] Nikhil Das, Ajay Dalai, Jafar S. Soltan Mohammadzadeh, and John Adjaye. The effect of feedstock and process conditions on the synthesis of high purity cnts from aromatic hydrocarbons. *Carbon*, 44(11):2236 – 2245, 2006.
- [48] Minjae Jung, Kwang Yong Eun, Young-Joon Baik, Kwang-Ryeol Lee, Jin-Koog Shin, and Sung-Tae Kim. Effect of  $NH_3$  environmental gas on the growth of aligned carbon nanotube in catalytically pyrolyzing  $c_2H_2$ . *Thin Solid Films*, 398-399:150–155, 2001.
- [49] Feng Ding, Kim Bolton, and Arne Rosèn. Molecular dynamics study of bamboo-like carbon nanotube nucleation. *Journal of Electronic Materials*, 35:207–210, 2006. 10.1007/BF02692437.

- [50] A. Krasheninnikov, P. Lehtinen, A. Foster, and R. Nieminen. Bending the rules: Contrasting vacancy energetics and migration in graphite and carbon nanotubes. *Chemical Physics Letters*, 418(1-3):132 – 136, 2006.
- [51] J. Ma, D. Alfe, A. Michaelides, and E. Wang. Stone-wales defects in graphene and other planar  $sp^2$ -bonded materials. *Physics Review B*, 80:033407, 2009.
- [52] M. Yoon, S. Han, G. Kim, S. Lee, S. Berber, E. Osawa, J. Ihm, M. Terrones, F. Banhart, J.C. Charlier, N. Grobert, and D. Tománek H. Terrones, P. Ajayan. Zipper mechanism of nanotube fusion: Theory and experiment. *Physical Review Letters*, 92:075504, Feb 2004.
- [53] C. Kiang, M. Endo, P. Ajayan, G. Dresselhaus, and M. Dresselhaus. Size effects in carbon nanotubes. *Physical Review Letters*, 81:1869–1872, Aug 1998.
- [54] P. Lehtinen, A. Foster, A. Ayuela, A. Krasheninnikov, and R. Nieminen K. Nordlund. Magnetic properties and diffusion of adatoms on a graphene sheet. *Physical Review Letters*, 91:017202, 2003.
- [55] A. Pasquarello O. Yazyev. Metal adatoms on graphene and hexagonal boron nitride: Towards rational design of self-assembly templates. *Physical Review B*, 82:045407, Jul 2010.
- [56] A. Krasheninnikov, P. Lehtinen, A. Foster, P. Pyykkö, and R. Nieminen. Embedding transition-metal atoms in graphene: Structure, bonding, and magnetism. *Physical Review Letters*, 102:126807, Mar 2009.
- [57] Joseph F. AuBuchon, Li-Han Chen, Andrew I. Gapin, and Sungho Jin. Opening of aligned carbon nanotube ends via room-temperature sputter etching process. *Journal of Applied Physics*, 97(12):124310, 2005.
- [58] Gang Wu, Yong-Sheng Chen, and Bo-Qing Xu. Remarkable support effect of swnts in pt catalyst for methanol electrooxidation. *Electrochemistry Communications*, 7(12):1237 – 1243, 2005.
- [59] S. Agrawal, M. Raghuveer, H. Li, and G. Ramanath. Defect-induced electrical conductivity increase in individual multiwalled carbon nanotubes. *Applied Physics Letters*, 90(19):193104, 2007.
- [60] S. Picozzi, S. Santucci, L. Lozzi, L. Valentini, and B. Delley. Ozone adsorption on carbon nanotubes: The role of stone–wales defects. *The Journal of Chemical Physics*, 120(15):7147–7152, 2004.
- [61] Kin Tak Lau, Mei Lu, and David Hui. Coiled carbon nanotubes: Synthesis and their potential applications in advanced composite structures. *Composites Part B: Engineering*, 37(6):437 – 448, 2006.

- [62] Yufeng Zhao, Richard E. Smalley, and Boris I. Yakobson. Coalescence of fullerene cages: topology, energetics, and molecular dynamics simulation. *Phys. Rev. B*, 66:195409, Nov 2002.
- [63] A. V. Krasheninnikov and F. Banhart. Engineering of nanostructured carbon materials with electron or ion beams. *Nature Materials*, 6(10):723–733, 2007.
- [64] A. V. Krasheninnikov and K. Nordlund. Ion and electron irradiation-induced effects in nanostructured materials. *Journal of Applied Physics*, 107(7):071301, 2010.
- [65] A.M. Rao, S. Bandow, E. Richter, and P.C. Eklund. Raman spectroscopy of pristine and doped single wall carbon nanotubes. *Thin Solid Films*, 331(1-2):141 – 147, 1998.
- [66] A. M. Rao, P. C. Eklund, Shunji Bandow, A. Thess, and R. E. Smalley. Evidence for charge transfer in doped carbon nanotube bundles from raman scattering. *Nature*, 388(6639):257–259, July 1997.
- [67] B. Elman, M. Shayegan, M. Dresselhaus, H. Mazurek, and G. Dresselhaus. Structural characterization of ion-implanted graphite. *Physical Review B*, 25:4142–4156, Mar 1982.
- [68] R. Saito, T. Takeya, T. Kimura, G. Dresselhaus, and M. S. Dresselhaus. Finite-size effect on the raman spectra of carbon nanotubes. *Physical Review B*, 59:2388–2392, Jan 1999.
- [69] Noriaki Hamada, Shin-ichi Sawada, and Atsush Oshiyama. New one-dimensional conductors: Graphitic microtubules. *Physical Review Letters*, 68:1579–1581, Mar 1992.
- [70] K. Sato, R. Saito, J. Jiang, G. Dresselhaus, and M. S. Dresselhaus. Discontinuity in the family pattern of single-wall carbon nanotubes. *Phys. Rev. B*, 76:195446, Nov 2007.
- [71] J. W. Mintmire and C. T. White. Universal density of states for carbon nanotubes. *Physical Review Letters*, 81:2506–2509, Sep 1998.
- [72] Philip Kim, Teri W. Odom, Jin-Lin Huang, and Charles M. Lieber. Electronic density of states of atomically resolved single-walled carbon nanotubes: Van hove singularities and end states. *Physical Review Letters*, 82:1225–1228, Feb 1999.
- [73] Gen Katagiri, Hideyuki Ishida, and Akira Ishitani. Raman spectra of graphite edge planes. *Carbon*, 26(4):565 – 571, 1988.
- [74] Yan Wang, Daniel Alsmeyer, and Richard McCreery. Raman spectroscopy of carbon materials: structural basis of observed spectra. *Chemistry of Materials*, 2(5):557–563, 1990.



- [75] C. Underhill, S.Y. Leung, G. Dresselhaus, and M.S. Dresselhaus. Infrared and raman spectroscopy of graphite-ferric chloride. *Solid State Communications*, 29(11):769 – 774, 1979.
- [76] R. Al-Jishi and G. Dresselhaus. Lattice-dynamical model for alkali-metal graphite intercalation compounds. *Physical Review B*, 26:4523–4538, Oct 1982.
- [77] M. Dresselhaus and G. Dresselhaus. Intercalation compounds of graphite. *Advances in Physics*, 30(2):139–326, 1981.
- [78] J. Parker, D. Feldman, and M. Ashkin. Raman scattering by silicon and germanium. *Physical Review*, 155:712–714, Mar 1967.
- [79] Jim McVittie. Tutorial on using rf to control dc bias. May PEUG Mtg 2007.
- [80] Xiangdong Yao, Chengzhang Wu, Aijun Du, Jin Zou, Zhonghua Zhu, Ping Wang, Huiming Cheng, Sean Smith, and Gaoqing Lu. Metallic and carbon nanotube-catalyzed coupling of hydrogenation in magnesium. *Journal of the American Chemical Society*, 129(50):15650–15654, 2007.
- [81] F. Tuinstra and J.L. Koenig. Characterization of graphite fiber surfaces with raman spectroscopy. *Journal of Composite Materials*, 4:492, 1970.
- [82] R. Saito, A. Jorio, A. G. Souza Filho, G. Dresselhaus, M. S. Dresselhaus, and M. A. Pimenta. Probing phonon dispersion relations of graphite by double resonance raman scattering. *Physical Review Letters*, 88:027401, Dec 2001.
- [83] S. Osswald, V. Mochalin, M. Havel, G. Yushin, and Y. Gogotsi. Phonon confinement effects in the raman spectrum of nanodiamond. *Physical Review B*, 80:075419, Aug 2009.
- [84] G. Jungnickel, D. Porezag, T. Frauenheim, M. Heggie, W. Lambrecht, B. Segall, and J. Angus. Graphitization effects on diamond surfaces and the diamond/graphite interface. *Physica Status Solid A*, 154:109, 1996.
- [85] A. Fasolino, J. Los, and M. Katsnelson. Intrinsic ripples in graphene. *Nature Materials*, 6:858–861, 2007.
- [86] Philip Collins, Keith Bradley, Masa Ishigami, and A. Zettl. Extreme oxygen sensitivity of electronic properties of carbon nanotubes. *Science*, 287(5459):1801–1804, 2000.
- [87] R. Besser, X. Ouyang, and H. Surangelikar. Hydrocarbon hydrogenation and dehydrogenation reactions in microfabricated catalytic reactors. *Chemical Engineering Science*, 58(1):19 – 26, 2003.

- [88] R. Nicholson and I. Shain. Theory of stationary electrode polarography for a chemical reaction coupled between two charge transfers. *Analytical Chemistry*, 37(2):178–190, 1965.
- [89] J. Randles. A cathode ray polarograph. part ii. -the current-voltage curves. *Transactions of the Faraday Society*, 44(0):327–338, 1948.
- [90] R. J. Klingler and J. K. Kochi. Electron-transfer kinetics from cyclic voltammetry. quantitative description of electrochemical reversibility. *Journal of Physical Chemistry*, 85(12):1731–1741, 1981.
- [91] Irma Lavagnini, Riccarda Antiochia, and Franco Magno. An extended method for the practical evaluation of the standard rate constant from cyclic voltammetric data. *Electroanalysis*, 16(6):505–506, 2004.
- [92] Patrice Simon and Yury Gogotsi. Materials for electrochemical capacitors. *Nat Mater*, 7(11):845–854, November 2008.
- [93] S. J. Konopka and Bruce McDuffie. Diffusion coefficients of ferri- and ferrocyanide ions in aqueous media, using twin-electrode thin-layer electrochemistry. *Analytical Chemistry*, 42(14):1741–1746, 1970.
- [94] Amy T. Beisler, Kathleen E. Schaefer, and Stephen G. Weber. Simple method for the quantitative examination of extra column band broadening in microchromatographic systems. *Journal of Chromatography A*, 986(2):247 – 251, 2003.
- [95] J. M. Nugent, K. S. V. Santhanam, A. Rubio, and P. M. Ajayan. Fast electron transfer kinetics on multiwalled carbon nanotube microbundle electrodes. *Nano Letters*, 1(2):87–91, 2001.
- [96] Craig Banks, Gregory G. Wildgoose Trevor J. Davies, and Richard G. Compton. Electrocatalysis at graphite and carbon nanotube modified electrodes: edge-plane sites and tube ends are the reactive sites. *Chemical Communications*, 7:829–841, 2005.
- [97] Fritz Scholz, editor. *Electroanalytical Methods: Guide to Experiments and Applications*. Springer; 2nd ed., 2010.
- [98] O. Barbieri, M. Hahn, A. Herzog, and R. Kötz. Capacitance limits of high surface area activated carbons for double layer capacitors. *Carbon*, 43(6):1303 – 1310, 2005.
- [99] Elzbieta Frackowiak and Francois Béguin. Carbon materials for the electrochemical storage of energy in capacitors. *Carbon*, 39(6):937 – 950, 2001.
- [100] J. Chen, W. Li, D. Wang, S. Yang, J. Wen, and Z. Ren. Electrochemical characterization of carbon nanotubes as electrode in electrochemical double-layer capacitors. *Carbon*, 40(8):1193 – 1197, 2002.

- [101] E. Frackowiak, K. Metenier, V. Bertagna, and F. Béguin. Supercapacitor electrodes from multiwalled carbon nanotubes. *Applied Physics Letters*, 77(15):2421–2423, 2000.
- [102] Kuanping Gong, Feng Du, Zhenhai Xia, Michael Durstock, and Liming Dai. Nitrogen-doped carbon nanotube arrays with high electrocatalytic activity for oxygen reduction. *Science*, 323(5915):760–764, 2009.
- [103] V. Khomenko, E. Raymundo-Piñero, E. Frackowiak, and F. Béguin. High-voltage asymmetric supercapacitors operating in aqueous electrolyte. *Applied Physics A: Materials Science & Processing*, 82:567–573, 2006. 10.1007/s00339-005-3397-8.
- [104] Xi miao LIU, Rui ZHANG, Liang ZHAN, Dong hui LONG, Wen ming QIAO, Jun he YANG, and Li cheng LING. Impedance of carbon aerogel/activated carbon composites as electrodes of electrochemical capacitors in aprotic electrolyte. *New Carbon Materials*, 22(2):153 – 158, 2007.
- [105] R. A. H. Niessen, J. de Jonge, and P. H. L. Notten. The electrochemistry of carbon nanotubes. *Journal of The Electrochemical Society*, 153(8):A1484–A1491, 2006.
- [106] P. L. Taberna, P. Simon, and J. F. Fauvarque. Electrochemical characteristics and impedance spectroscopy studies of carbon-carbon supercapacitors. *Journal of The Electrochemical Society*, 150(3):A292–A300, 2003.
- [107] A. Laforgue, P. Simon, J. F. Fauvarque, M. Mastragostino, F. Soavi, J. F. Sarrau, P. Lailier, M. Conte, E. Rossi, and S. Saguatti. Activated carbon/conducting polymer hybrid supercapacitors. *Journal of The Electrochemical Society*, 150(5):A645–A651, 2003.